Distributions and perturbations of the marine dissolved cobalt cycle in a changing ocean

Rebecca Jane Chmiel

B.A., Colby College, 2017

Submitted to the Department of Earth, Atmospheric and Planetary Sciences in partial fulfillment of the requirements for the degree of

Doctor of Philosophy

at the

MASSACHUSETTS INSTITUTE OF TECHNOLOGY

and the

WOODS HOLE OCEANOGRAPHIC INSTITUTION

February 2023

Signature of Author_____

Joint Program in Oceanography/Applied Ocean Science and Engineering
Massachusetts Institute of Technology
and Woods Hole Oceanographic Institution
January 2, 2023

Certified by_____

Dr. Makoto A. Saito
Thesis Supervisor
Woods Hole Oceanographic Institution

Accepted by_____

Dr. Edward A. Boyle
Chair, Joint Committee for Chemical Oceanography
Massachusetts Institute of Technology

Distributions and perturbations of the marine dissolved cobalt cycle in a changing ocean

by

Rebecca Jane Chmiel

Submitted to Joint Program in Oceanography/Applied Ocean Science and Engineering, Massachusetts Institute of Technology & Woods Hole Oceanographic Institution on January 2, 2023 in partial fulfillment of the requirements for the degree of Doctor of Philosophy in the field of in Marine Biogeochemistry

Abstract

Cobalt is a necessary nutrient for many marine phytoplankton, but its hybrid-type nature results in small marine inventories that make it one of the scarcest bioactive trace metals in the oceans. This study examines the marine dissolved cobalt cycle in two regions: the Pacific Ocean and Antarctic coastal seas. In the North Pacific, elevated cobalt stoichiometries among phytoplankton were linked to nitrogen, iron and phosphate stress protein biomarkers at the boundaries of oceanographic provinces and upwelling zones, providing insight into the flexibility of cobalt stoichiometry. In both regions, perturbations to the marine cobalt cycle were either predicted or observed; in the equatorial Pacific, the dissolved cobalt inventory was predicted to increase by up to 28% due to the expansion of oxygen minimum zones in a warmer ocean, while in the Antarctic, melting ice shelves have the potential to shift the nutrient regime from iron limitation towards zinc and vitamin B_{12} limitation, resulting in higher cobalt demand and a lower dissolved cobalt inventory. When the global cobalt cycle was estimated throughout four of Earth's systems (the lithosphere, biosphere, hydrosphere and the anthroposphere – the human environment), it was determined that the scale of the cobalt flux through the anthroposphere is only one order of magnitude lower than the inventory of the entire hydrosphere (10^9 mol Co yr^{-1} and 10^{10} mol Co, respectively), revealing a vulnerability to anthropogenic perturbation of the marine cobalt inventory through human mining, use and disposal of cobalt if appropriate pollution abatement, disposal and recycling infrastructure is not established. In light of observed and predicted changes to cobalt biogeochemistry, this research suggests that the marine cobalt cycle is particularly vulnerable to anthropogenic perturbation from both global climate change and pollution due to its low ocean inventory and interconnection to other nutrient biogeochemical cycles.

Thesis Supervisor: Dr. Makoto A. Saito
Title: Senior Scientist, Marine Chemistry and Geochemistry Department, Woods Hole Oceanographic Institution

The ocean is a desert with its life underground and a perfect disguise above.

– Dewey Bunnell, “A Horse with No Name”

Acknowledgments

This work, like all scientific endeavors, could only be achieved through the support and collaboration of many, many scientists, administrators and friends. My work in the Saito Lab was supported by several National Science Foundation grants, including awards for the GEOTRACES GP15 program (OCE-1736599, OCE-1756138, OCE-1657781 and OCE-1736601), the CICLOPS expedition via the Office of Polar Programs (OPP-1643684, OPP-1644073 and OPP-1643845), and the CLIO Biogeochemical AUV project (OCE-1924554 and OCE-1658067), as well as funding from the Watson Foundation.

I feel extremely fortunate to have found myself in the Saito Lab for the last half decade. Mak has been an incredible advisor, mentor and inspiration to me, and I'll always be grateful for the trust he placed in me as a young scientist. Mak challenged me to consider the big picture and to trust myself and my data when I got too in the weeds of research. He taught me that the best things to bring to sea are tools and scrap wood – after the seasick meds – to fix any problems that arose with improvisation and creative thinking. I will carry these lessons with me throughout all my future career and life endeavors.

The Saito Lab seems to only accumulate compassionate, resourceful and encouraging people to work beside, and I am so grateful to have met, sailed with and learned from all of them. It has been wonderful to work with all the inspirational scientists that have passed through the lab, both past and present. Three lab heroes need to be thanked first and foremost: Dawn Moran, Matt McIlvin and Paloma Lopez; you've been amazing people to work and sail with, and thank you for being there for me to bother when something was going wrong. A heartfelt thank you to the other JP students in the lab; Noelle Held, who supported me in my early grad school years when I most needed it, Annaliese Meyer and Emily Burdige, incredible oceanographers who are so fun to be around, Deepa Rao, whose python matplotlib code forms the backbone of almost every figure presented here, and Riss Kellogg, my absolutely wonderful labmate, cohort-mate and roommate – we did it! Thank you also to all the post-docs and post-bacs of the Saito Lab who have been supportive friends and mentors at sea, in the lab, and facing down an empty word doc: Natalie Cohen, Maggi Brisbin, Mike Mazzotta, Vero Oldman, Jaci Saunders, Ichiko Sugiyama and Dominique Kelly. Special thanks to Natalie, a wonderful friend and mentor who I convinced to join me in Tahiti to pick up 8 containers of samples in overweight checked bags, and Jaci, whose knowledge of proteomic and bioinformatic pipelines knows no bounds, and neither does her patience.

I would like to thank my thesis committee: Matt Charette, Steph Dutkiewicz and Al Tagliabue for their thoughtful questions, attentiveness and support over the past few years, as well as my defense chair Heather Kim. Beyond the direct contributions you have made to this dissertation, you served as incredible role models of scientists and I feel very lucky to have worked with you.

There are many amazing scientists, co-authors and administrators that I worked with outside of the Saito Lab that dedicated significant time and energy working with me over the course of my graduate studies. Thank you to my co-authors Nate Lanning, Allison Laubach, Jong-Mi Lee, Jess Fitzsimmons, Mariko Hatta, Bill Jenkins, Phoebe Lam, Chris Dupong, Josh Espinoza, Tyler

Goepfert, Nick Hawco and Reiner Schlitzer. Thank you to the science party, marine techs, captain and crew of the RVIB Nathaniel B. Palmer during the CICLOPS expedition, of the R/V Roger Revelle during the GEOTRACES GP15 expedition, and of the R/V Atlantic Explorer during the AE1913 expedition. And a huge thank you to the MIT/WHOI Joint Program deans and admins, especially Julia Westwater, Kris Kipp, Tricia Nesti, Lea Fraser, Ann Tarrant, Meg Tivey, Christine Charette and Mary Zawoysky – you guys rock, and the care and love you've put into supporting the students in this program has really made all the difference.

Thank you so much to my friends and family, who supported me throughout my time at MIT and WHOI, both locally and from afar. Thank you to the entire Sunfish cohort – your fast friendship and support has meant the world to me over the past few years – and friends Jule, Jen, Lydia, Emman, Alia, Ben, Jay, Lauren, Kevin, Adrian, Ellen, Jess, Fiona, Jing, Kalina, Nastasia, Stewart, Jordan, Caitlyn and Tyler. Lastly, a huge thank you to my family: Mom and Dad, you've always supported my education and drive for knowledge and travel, and always welcomed me home at the end of it; and Tracy and Matt, you're the best. Love you all.

Table of Contents

Chapter 1.

Introduction

1.1 Motivation: why study the marine biogeochemistry of trace metals?

Transition metals play critical roles in the metabolisms of life on Earth. Their reactivity and their diverse potential for oxidation and reduction make them ideal nonorganic reaction centers in organic molecules. Many proteins use transition metals such as iron (Fe), zinc (Zn), manganese (Mn) and cobalt (Co) as cofactors in enzymatic processes, utilizing the unique reaction properties of transition metals to perform necessary metabolic functions within the organism (Lippard and Berg, 1994). Many transition metals are consequently essential nutrients for an organism to live and grow in an environment, and when an organism is limited in its ability to acquire necessary metal nutrients, its growth and ability to thrive in that environment will also be limited.

Metals are known to limit plankton growth in vast regions of the marine environment (Moore et al., 2013). Many metal nutrients are present at trace dissolved concentrations in seawater due to their incorporation into inorganic mineral particles that sink to form deep ocean sediments (Bruland and Lohan, 2003). Uptake by plankton also keeps dissolved bioactive metal concentrations low, particularly in the upper ocean where nutrient uptake by phytoplankton can create regions of extremely low metal micronutrient concentrations (Bruland et al., 1994; Bruland and Lohan, 2003). In this way, the distribution and biogeochemical cycling of bioactive trace metals can exert control over marine productivity and ocean carbon (C) sequestration when the availability of dissolved nutrients is insufficient to support microbial growth (Moore et al., 2013; Sunda, 2012). This is notably the case for Fe across large regions of the oceans, including portions of the Southern, equatorial Pacific and North Pacific Oceans; low sources of Fe from aerosol dust and continental shelves, as well as deep ocean upwelling transporting abundant macronutrients like phosphorus (P) and nitrogen (N) to the surface ocean create an environment where dissolved Fe (dFe) concentrations are drawn down by microbial blooms to levels that limit additional phytoplankton productivity (Arrigo et al., 2008; Behrenfeld et al., 1996; Kolber et al., 1994; Mann and Chisholm, 2000; Martin et al., 1990). The resulting Fe limitation can be species-dependent,

allowing microbes with flexible Fe metabolisms to survive while organisms that require higher amounts of Fe to be selected against in the microbial community (La Roche et al., 1996; Thompson et al., 2011).

In order to understand and quantify ocean productivity and the carbon cycle, we must first understand the interconnection between the biogeochemical cycles of carbon and essential trace metal nutrients. Constraining the uptake and cycling processes of trace metals will allow for more accurate modeling and predictions of the marine biological carbon sink whereby fixed organic carbon associated with marine phytoplankton and other organisms is sequestered in the deep ocean and seafloor sediments, acting as a sink of carbon from the atmosphere (Sunda, 2012). As global climate change continues to significantly disrupt the global carbon cycle, it is more important than ever to constrain bioactive trace metal nutrient cycles and broaden our understanding of how they will affect and be affected by climate change throughout the oceans.

1.2 The marine cobalt cycle

Cobalt (Co) is an essential metal micronutrient for marine life, and many microorganisms have either an absolute metabolic requirement for or a flexible use capability of Co (Saito et al., 2002; Sunda and Huntsman, 1995). Co is utilized as the metallic co-factor in the corrin ring center of the vitamin B_{12} (cobalamin) molecule, used in many metabolisms for the biosynthesis of methionine (Warren et al., 2002). The trace metal is also used as a co-factor in some forms of carbonic anhydrases, a metalloenzyme that concentrates CO_2 in preparation for photosynthesis, where it can substitute for other trace metal nutrients like Zn and cadmium (Cd) (Kellogg et al., 2020; Price and Morel, 1990; Roberts et al., 1997; Sunda and Huntsman, 1995). A culture study by Hawco (2020) suggested that *Prochlorococcus*, a marine cyanobacterium, contains a higher Co metal use efficiency than is explained by these known metabolic functions, indicating that Co may play additional roles in the metabolisms of marine microbes that are currently unknown (Hawco et al., 2020).

Co is also one of the scarcest metal micronutrients in the marine environment, and is often present in the dissolved phase (dCo) in the tens of picomolar range (1×10^{-12} mol L^{-1}). The low dissolved inventory of dCo, particularly in the surface ocean, has led to predictions of Co co-limitation of phytoplankton productivity in some regions of the ocean (Browning et al., 2017; Moore et al., 2013), while the Co-containing vitamin B_{12} has been observed to be a co-limiting

nutrient some phytoplankton bloom communities (Bertrand et al., 2007; Gobler et al., 2007; Sanudo-Wilhelmy et al., 2006). The scarcity of Co in the marine environment is due to the metal's hybrid-type geochemistry, indicating that its distribution in the water column is influenced by both biological uptake in the surface ocean and scavenging to oxide particles in the mesopelagic and deep ocean (Bruland and Lohan, 2003; Noble et al., 2008). Co scavenging is microbially mediated by manganese oxidizing bacteria (Moffett and Ho, 1996; Tebo et al., 1984), and represents a major sink of Co in the oxic oceans, shuttling Co from the dissolved to the particulate phase, where it sinks to the seafloor as sediment (Hawco et al., 2018; Noble et al., 2008, 2017). Together, the processes of biological uptake and scavenging keep dCo concentrations low throughout the majority of the pelagic oceans and contribute to Co's short marine residence time of ~130 years (Hawco et al., 2018).

The marine biogeochemical Co cycle (Fig. 1) tracks the movement of Co in, out and through the oceans. The major sources of Co to the oceans include rivers and estuaries, continental margin sediments, hydrothermal inputs and aerosol dust deposition, both natural and anthropogenic, and the major sinks of Co include the sinking of particulate Co into ocean sediments, both as un-remineralized plankton biomass and as mineral particles via oxide scavenging (Dulaquais et al., 2014a; Hawco et al., 2016, 2018; Noble et al., 2017). Internal Co cycling processes include those that move Co between the dissolved and particulate phases, like biological uptake, remineralization and the incorporation and dissolution of Mn-oxide particles.

The biogeochemical processes of the Co cycle can be illuminated by analyzing the dCo vs. dPO_4^{3-} relationship; both dCo and dPO_4^{3-} are associated with biological uptake and remineralization, and so the two nutrients tend to be coupled in regions like the surface ocean where dCo distributions are primarily controlled by these biological processes. When dCo distributions become influenced by other processes, like abiotic inputs from dust and continental margins or scavenging to Mn-oxides, the dCo vs. dPO_4^{3-} relationship will become more decoupled. Vector space (Fig. 2) can be used to describe the directionality of Co cycling processes on the dCo vs. dPO_4^{3-} relationship, which tends to be linear in the surface ocean and exhibits a slope that is dictated by phytoplankton uptake and remineralization stoichiometry. Below the surface ocean in mesopelagic and deep waters, the co-occurrence of both remineralization and scavenging processes creates a net vector sum to the lower right, where deep water exhibit high dPO_4^{3-} and low dCo concentrations. This analysis technique will be used several times throughout this

dissertation to investigate major processes influencing the distribution of Co in a region, as well as the stoichiometry of Co uptake in microbial communities.

Dissolved Co in the marine environment can be described as existing in two major categories: as a labile, or "free", Co(II) species with weakly bound ligands, and as a Co(III) species that is strongly bound to organic ligands with a stability constant (K_s) greater than $10^{16.8}$ (Saito et al., 2005). Organic ligand complexes with the Co(II) species are typically negligent in the marine environment because the metal–ligand bonds have a higher affinity to more abundant divalent cations like Ni(II) (Baars and Croot, 2014). Of the two dissolved species, labile dCo is considered to be more bioavailable to phytoplankton and Mn-oxidizing bacteria than Co(III), and tends to be depleted in the surface ocean (Bown et al., 2012).

The biological uptake of Co via a microbial cell's divalent metal membrane transport systems is often influenced by the presence and metabolic requirements of other essential cation micronutrients like Zn and cadmium (Cd). Zn, Cd and Co share the same charge and a similar atomic radius, which often means that they are difficult to distinguish from one another in the "eyes" of a membrane uptake protein, and often share transport systems (Sunda and Huntsman, 1992). As such, the uptake of Co is influenced by the environmental concentration of other metals like dZn, which tend to be orders of magnitude more abundant than dCo, as well as the affinity of each metal for the ligands associated with the membrane transport system (Irving and Williams, 1948; Sunda and Huntsman, 1992, 1995). In environments with low dZn concentrations where phytoplankton are experiencing Zn-stress, Co and Zn's shared divalent transporter may be upregulated by plankton, and so the uptake of Co would be expected to increase in regions of Zn-stress (Browning et al., 2017). Plankton with the ability to substitute Co for Zn in their metalloproteins could then gain a competitive edge in low-dZn environments (Kellogg et al., 2020; Saito et al., 2002).

Until relatively recently, the speciation and distribution of dCo and many other trace metals in the oceans remained largely undetermined and unconstrained. In the late 1980s and into the early 2000s, new electrochemical methods to detect low marine dCo concentrations and its chemical speciation were developed (Donat and Bruland, 1998; Ellwood and van den Berg, 2001; Saito and Moffett, 2001), allowing for the analysis of dCo profiles and speciation in different marine environments (Bown et al., 2011; Noble et al., 2013; Saito et al., 2005). Over the past decade, the international GEOTRACES program has greatly increased our understanding of basin-

scale trace metal distributions, funding expeditions aimed at documenting the presence and biogeochemistry of trace elements and isotopes and increasing the number of published dCo measurements by the thousands. Thanks to the GEOTRACES program, high-density, basin-scale transects of dCo distributions have dramatically improved our understanding of the dCo cycle in the Atlantic (Dulaquais et al., 2014b; Noble et al., 2017), Arctic (Bundy et al., 2020) and South Pacific Oceans (Hawco et al., 2016), and have worked to establish baseline dCo distributions throughout these regions of the global oceans.

1.3 Thesis structure and overview

This dissertation explores three relatively open questions in our understanding of the marine Co biogeochemical cycle: (1) how is dCo distributed in the oceans and why? (2) How is Co being used by marine microbes? And (3) How is the marine Co cycle changing in the Anthropocene?

Chapter 2 examines the distribution of dCo along the recent GEOTRACES GP15 expedition to the North and equatorial Pacific Ocean, a region that has not yet been widely characterized by the GEOTRACES program. Following in the footstep of previous studies that characterized dCo distributions and biogeochemical cycling on a basin-scale, this study helps to establish baseline dCo concentrations throughout the pelagic Pacific Ocean while also describing major dCo cycling processes like riverine sources, scavenging sinks, internal cycling in the Pacific oxygen minimum zones, and basin-scale advection. The dCo distributions are then compared to a marine Co biogeochemical model to consider how well our predictions of the Pacific Co cycle matched our observations.

Chapter 3 continues to investigate the Co cycle in the Pacific Ocean where 4 recent expeditions, including the GP15 expedition, have greatly expanded the number of dCo and particulate Co (pCo) samples analyzed in the basin. Throughout the global oceans, Co stoichiometry exhibits exceptionally high variability due to its flexible use in phytoplankton metabolisms. This chapter examines spatial trends in surface ocean Co ecological stoichiometry as they vary by orders of magnitude over the wide range of oceanographic nutrient provinces present in the Pacific Ocean. A surface transect of bacterial protein biomarkers establishes clear nutrient stress regimes in the Pacific, and helps to link Co ecological stoichiometry to microbial metabolisms.

Chapter 4 examines the dCo cycle in a new region, the coastal Antarctic seas south of the Pacific Ocean, where dCo distributions had previously been characterized in 2005/2006 and 2009, and recently appears to be significantly changing. The chapter describes dCo results from the recent 2017/2018 CICLOPS expedition to the Amundsen and Ross Seas, noting substantial changes to the inventories and speciation of dCo over the 12-year period, including a loss of the deep dCo inventory, lower labile dCo concentrations, and higher dCo uptake rates. A mechanism for the deep dCo inventory loss is proposed, along with a hypothesis that suggests a link between melting ice shelves and heightened Co uptake in Antarctic coastal seas.

Finally, Chapter 5 broadens our perspective of the Co cycle, investigating the global Co cycle in the Earth systems of the lithosphere, hydrosphere, biosphere and anthroposphere, the portion of the Earth's environment that is controlled by humans and human-made systems. Demand for Co has recently sharply increased due to Co's use as the cathode in lithium-ion batteries used in personal electronic devices and many electric vehicles. This brief perspective chapter aims to scale the Co cycle of the anthroposphere to that of the natural Earth spheres, putting the human use of Co into perspective with the rest of the global Co cycle.

References

Arrigo, K. R., van Dijken, G. L. and Bushinsky, S.: Primary production in the Southern Ocean, 1997-2006, J. Geophys. Res., 113, C08004, doi:10.1029/2007JC004551, 2008.

Baars, O. and Croot, P. L.: Dissolved cobalt speciation and reactivity in the eastern tropical North Atlantic, Mar. Chem., 173, 310–319, doi:10.1016/j.marchem.2014.10.006, 2014.

Behrenfeld, M. J., Bale, A. J., Kolber, Z. S., Aiken, J. and Falkowski, P. G.: Confirmation of iron limitation of phytoplankton photosynthesis in the equatorial Pacific Ocean, Lett. to Nat., 383, 508–511, 1996.

Bertrand, E. M., Saito, M. A., Rose, J. M., Riesselman, C. R., Lohan, M. C., Noble, A. E., Lee, P. A. and DiTullio, G. R.: Vitamin B12 and iron colimitation of phytoplankton growth in the Ross Sea, Limnol. Oceanogr., 52(3), 1079–1093, doi:10.4319/lo.2007.52.3.1079, 2007.

Bown, J., Boye, M., Baker, A., Duvieilbourg, E., Lacan, F., Le Moigne, F., Planchon, F., Speich, S. and Nelson, D. M.: The biogeochemical cycle of dissolved cobalt in the Atlantic and the Southern Ocean south off the coast of South Africa, Mar. Chem., 126(1–4), 193–206, doi:10.1016/j.marchem.2011.03.008, 2011.

Bown, J., Boye, M. and Nelson, D. M.: New insights on the role of organic speciation in the biogeochemical cycle of dissolved cobalt in the southeastern Atlantic and the Southern Ocean, Biogeosciences, 9, 2719–2736, doi:10.5194/bg-9-2719-2012, 2012.

Browning, T. J., Achterberg, E. P., Rapp, I., Engel, A., Bertrand, E. M., Tagliabue, A. and Moore, C. M.: Nutrient co-limitation at the boundary of an oceanic gyre, Nature, 551(7679), 242–246, doi:10.1038/nature24063, 2017.

Bruland, K. W. and Lohan, M. C.: Controls of trace metals in seawater, in Treatise on geochemistry, edited by H. D. Holland and K. K. Turekian, pp. 23–47, Elsevier., 2003.
Bruland, K. W., Orians, K. J. and Cowen, J. P.: Reactive trace metals in the stratified central North Pacific, Geochim. Cosmochim. Acta, 58(15), 3171–3182, doi:10.1016/0016-7037(94)90044-2, 1994.
Bundy, R. M., Tagliabue, A., Hawco, N. J., Morton, P. L., Twining, B. S., Hatta, M., Noble, A., Cape, M. R., John, S. G., Cullen, J. T. and Saito, M. A.: Elevated sources of cobalt in the Arctic Ocean, Biogeosciences, 17, 4745–4767, doi:https://doi.org/10.5194/bg-2020-84, 2020.
Donat, J. R. and Bruland, K. W.: Direct determination of dissolved cobalt and nickel in seawater by differential pulse cathodic stripping voltammetry preceded by adsorptive collection of cyclohexane-1,2-dione dioxime complexes, Anal. Chem., 60(3), 240–244, 1998.
Dulaquais, G., Boye, M., Middag, R., Owens, S., Puigcorbe, V., Buesseler, K., Masqué, P., Baar, H. J. W. and Carton, X.: Contrasting biogeochemical cycles of cobalt in the surface western Atlantic Ocean, AGU Publ., 1387–1412, doi:10.1002/2014GB004903, 2014a.
Dulaquais, G., Boye, M., Middag, R., Owens, S., Puigcorbe, V., Buesseler, K., Masque, P., de Baar, H. J. W. and Carton, X.: Contrasting biogeochemical cycles of cobalt in the surface western Atlantic Ocean, Global Biogeochem. Cycles, 28(12), 1387–1412, 2014b.
Ellwood, M. J. and van den Berg, C. M. G.: Determination of organic complexation of cobalt in seawater by cathodic stripping voltammetry, Mar. Chem., 75(1–2), 33–47, doi:https://doi.org/10.1016/S0304-4203(01)00024-X, 2001.
Gobler, C. J., Norman, C., Panzeca, C., Taylor, G. T. and Sañudo-Wilhelmy, S. A.: Effect of B-vitamins (B1, B12) and inorganic nutrients on algal bloom dynamics in a coastal ecosystem, Aquat. Microb. Ecol., 49(2), 181–194, doi:10.3354/ame01132, 2007.
Hawco, N. J., Ohnemus, D. C., Resing, J. A., Twining, B. S. and Saito, M. A.: A dissolved cobalt plume in the oxygen minimum zone of the eastern tropical South Pacific, Biogeosciences, 13(20), 5697–5717, doi:10.5194/bg-13-5697-2016, 2016.
Hawco, N. J., Lam, P. J., Lee, J. M., Ohnemus, D. C., Noble, A. E., Wyatt, N. J., Lohan, M. C. and Saito, M. A.: Cobalt scavenging in the mesopelagic ocean and its influence on global mass balance: Synthesizing water column and sedimentary fluxes, Mar. Chem., 201(March 2017), 151–166, doi:10.1016/j.marchem.2017.09.001, 2018.
Hawco, N. J., McIlvin, M. M., Bundy, R. M., Tagliabue, A., Goepfert, T. J., Moran, D. M., Valentin-Alvarado, L., DiTullio, G. R. and Saito, M. A.: Minimal cobalt metabolism in the marine cyanobacterium prochlorococcus, Proc. Natl. Acad. Sci., 117(27), 15740–15747, doi:10.1073/pnas.2001393117, 2020.
Irving, H. and Williams, R. J. P.: Order of stability of metal complexes, Nature, 162, 746–747, 1948.
Kellogg, R. M., McIlvin, M. R., Vedamati, J., Twining, B. S., Moffett, J. W., Marchetti, A., Moran, D. M. and Saito, M. A.: Efficient zinc/cobalt interreplacement in northeast Pacific diatoms and relationship to high surface dissolved Co : Zn ratios, Limnol. Oceanogr., 65(11), 2557–2582, doi:10.1002/lno.11471, 2020.
Kolber, Z. S., Barber, R. T., Coale, K. H., Fitzwater, S. E., Greene, R. M., Johnson, K. S., Lindley, S. and Falkowski, P. G.: Iron limitation of phytoplankton photosynthesis in the equatorial Pacific Ocean, Lett. to Nat., 371, 145–149, 1994.
Lippard, S. J. and Berg, J. M.: Principles of Bioinorganic Chemistry, University Science Books, Mill Valley, CA., 1994.

Mann, E. L. and Chisholm, S. W.: Iron limits the cell division rate of Prochlorococcus in the eastern equatorial Pacific, Limnol. Oceanogr., 45(5), 1067–1076, doi:10.4319/lo.2000.45.5.1067, 2000.
Martin, J. H., Fitzwater, S. E. and Gordon, R. M.: Iron deficiency limits phytoplankton growth in Antarctic waters, Global Biogeochem. Cycles, 4(1), 5–12, 1990.
Moffett, J. W. and Ho, J.: Oxidation of cobalt and manganese in seawater via a common microbially catalyzed pathway, Geochim. Cosmochim. Acta, 60(18), 3415–3424, doi:10.1016/0016-7037(96)00176-7, 1996.
Moore, C. M., Mills, M. M., Arrigo, K. R., Berman-Frank, I., Bopp, L., Boyd, P. W., Galbraith, E. D., Geider, R. J., Guieu, C., Jaccard, S. L., Jickells, T. D., La Roche, J., Lenton, T. M., Mahowald, N. M., Marañón, E., Marinov, I., Moore, J. K., Nakatsuka, T., Oschlies, A., Saito, M. A., Thingstad, T. F., Tsuda, A. and Ulloa, O.: Processes and patterns of oceanic nutrient limitation, Nat. Geosci., 6, 701–710, doi:10.1038/ngeo1765, 2013.
Noble, A. E., Saito, M. A., Maiti, K. and Benitez-Nelson, C. R.: Cobalt, manganese, and iron near the Hawaiian Islands: A potential concentrating mechanism for cobalt within a cyclonic eddy and implications for the hybrid-type trace metals, Deep. Res. Part II Top. Stud. Oceanogr., 55(10–13), 1473–1490, doi:10.1016/j.dsr2.2008.02.010, 2008.
Noble, A. E., Moran, D. M., Allen, A. E. and Saito, M. A.: Dissolved and particulate trace metal micronutrients under the McMurdo Sound seasonal sea ice: basal sea ice communities as a capacitor for iron, Front. Chem., 1, 25, doi:10.3389/fchem.2013.00025, 2013.
Noble, A. E., Ohnemus, D. C., Hawco, N. J., Lam, P. J. and Saito, M. A.: Coastal sources, sinks and strong organic complexation of dissolved cobalt within the US North Atlantic GEOTRACES transect GA03, Biogeosciences, 14(11), 2715–2739, doi:10.5194/bg-14-2715-2017, 2017.
Price, N. M. and Morel, F. M. M.: Cadmium and cobalt substitution for zinc in a marine diatom, Nature, 344(6267), 658–660, doi:10.1038/344658a0, 1990.
Roberts, S. B., Lane, T. W. and Morel, F. M. M.: Carbonic Anhydrase in the Marine Diatom Thalassiosira Weissflogii (Bacillariophyceae), J. Phycol., 33(5), 845–850, doi:10.1111/j.0022-3646.1997.00845.x, 1997.
La Roche, J., Boyd, P. W., McKay, R. M. L. and Geider, R. J.: Flavodoxin as an in situ marker for iron stress in phytoplankton, Nature, 382, 802–805, doi:10.1038/382802a0, 1996.
Saito, M. A. and Moffett, J. W.: Complexation of cobalt by natural organic ligands in the Sargasso Sea as determined by a new high-sensitivity electrochemical cobalt speciation method suitable for open ocean work, Mar. Chem., 75(1–2), 49–68, doi:10.1016/S0304-4203(01)00025-1, 2001.
Saito, M. A., Moffett, J. W., Chisholm, S. W. and Waterbury, J. B.: Cobalt limitation and uptake in Prochlorococcus, Limnol. Oceanogr., 47(6), 1629–1636, doi:10.4319/lo.2002.47.6.1629, 2002.
Saito, M. A., Rocap, G. and Moffett, J. W.: Production of cobalt binding ligands in a Synechococcus feature at the Costa Rica upwelling dome, Limnol. Oceanogr., 50(1), 279–290, 2005.
Sanudo-Wilhelmy, S. A., Gobler, C. J., Okbamichael, M. and Taylor, G. T.: Regulation of phytoplankton dynamics by vitamin B12, Geophys. Reseach Lett., 33, L04604, doi:10.1029/2005GL025046, 2006.
Sunda, W. G.: Feedback interactions between trace metal nutrients and phytoplankton in the ocean, Front. Microbiol., 3, 204, doi:10.3389/fmicb.2012.00204, 2012.

Sunda, W. G. and Huntsman, S. A.: Feedback interactions between zinc and phytoplankton in seawater, Limnol. Oceanogr., 37(1), 25–40, doi:10.4319/lo.1992.37.1.0025, 1992.
Sunda, W. G. and Huntsman, S. A.: Cobalt and zinc interreplacement in marine phytoplankton: Biological and geochemical implications, Limnol. Oceanogr., 40(8), 1404–1417, doi:10.4319/lo.1995.40.8.1404, 1995.
Tebo, B. M., Nealson, K. H., Emerson, S. and Jacobs, L.: Microbial Mediation of Mn(II) and Co(II) Precipitation at the O_2/H_2S Interfaces in Two Anoxic Fjords, Limnol. Oceanogr., 29(6), 1247–1258, 1984.
Thompson, A. W., Huang, K., Saito, M. A. and Chisholm, S. W.: Transcriptome response of high- and low-light-adapted Prochlorococcus strains to changing iron availability, ISME J., 5, 1580–1594, doi:10.1038/ismej.2011.49, 2011.
Warren, M. J., Raux, E., Schubert, H. L. and Escalante-Semerena, J. C.: The biosynthesis of adenosylcobalamin (vitamin B12), Nat. Prod. Rep., 19, 390–412, doi:10.1039/B108967F, 2002.

Figures

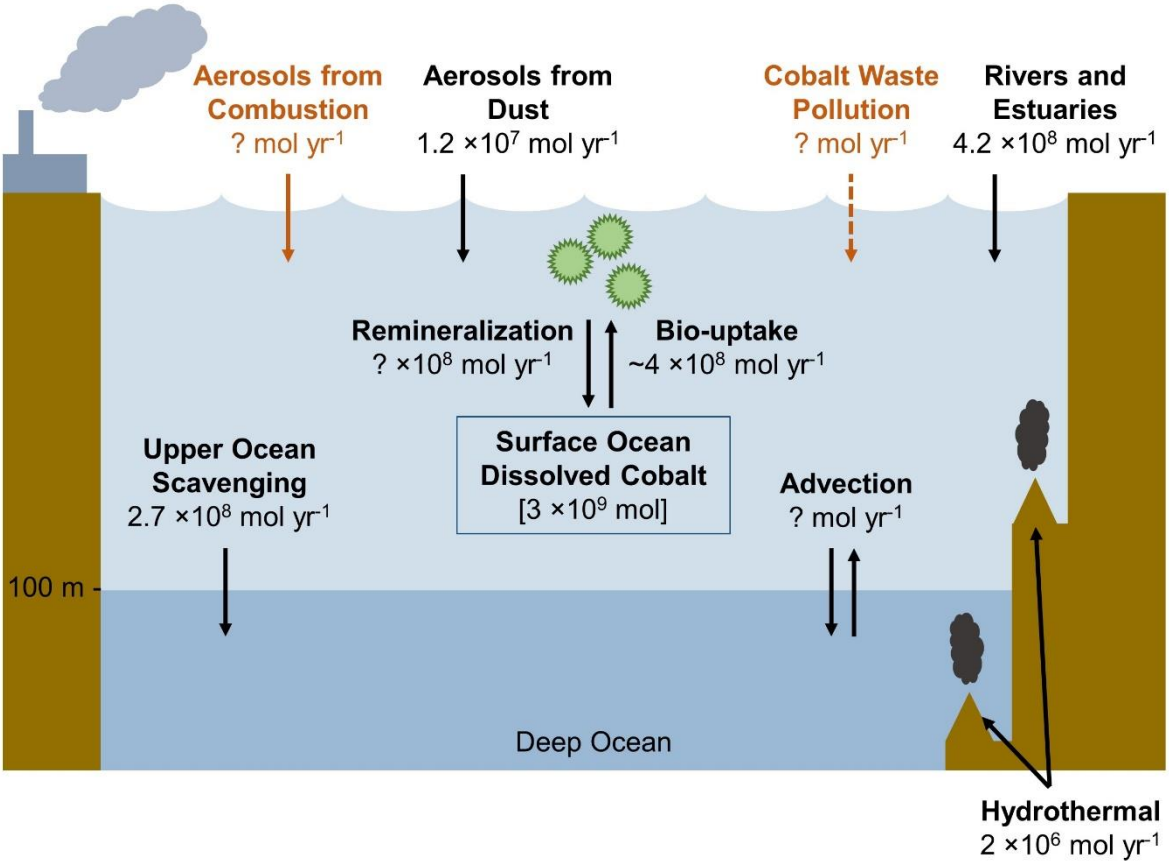

Figure 1. Schematic of Co fluxes within the surface ocean (depth ≤ 100 m), as presented in Chapter 5. Anthropogenic Co sources to the marine environment are shown in orange.

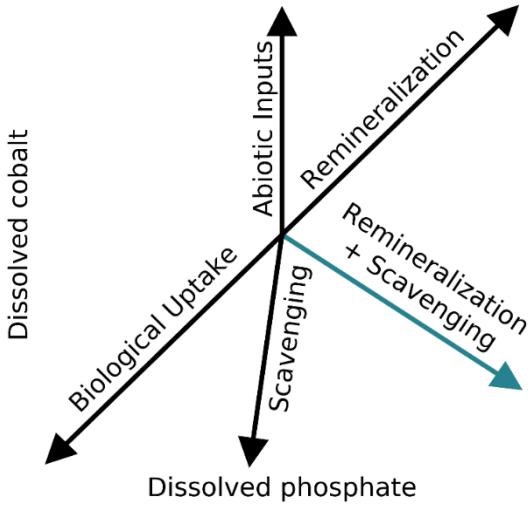

Figure 2. Vector schematic of the dCo vs. dPO_4^{3-} relationship, as presented in Chapter 3 and adapted from Noble et al (2008). The vectors depict the impact of major dCo biogeochemical processes in the oceans on dCo and dPO_4^{3-} concentrations. The blue line depicts the sum of the scavenging and remineralization vectors; both processes tend to dominate the dCo cycle below the mixed layer, resulting in intermediate and deep waters characterized by high dPO_4^{3-}, low dCo distributions.

Chapter 2.

Major processes of the dissolved cobalt cycle in the North and equatorial Pacific Ocean

This chapter was previously published in *Biogeosciences* by Copernicus Publications in 2022 and is reprinted here under the Creative Commons Attribution 4.0 License. © Authors 2022.

Chmiel, R., Lanning, N., Laubach, A., Lee, J.-M., Fitzsimmons, J., Hatta, M., Jenkins, W. J., Lam, P. J., McIlvin, M., Tagliabue, A. and Saito, M. A. (2022), Major processes of the dissolved cobalt cycle in the North and equatorial Pacific Ocean. Biogeosciences **19**: 2365–2395. https://doi.org/10.5194/bg-19-2365-2022.

2.1 Abstract

Over the past decade, the GEOTRACES and wider trace metal geochemical community has made substantial contributions towards constraining the marine cobalt (Co) cycle and its major biogeochemical processes. However, few Co speciation studies have been conducted in the North and equatorial Pacific Ocean, a vast portion of the world's oceans by volume and an important end-member of deep thermohaline circulation. Dissolved Co (dCo) samples, including total dissolved and labile Co, were measured at-sea during the GEOTRACES Pacific Meridional Transect (GP15) expedition along the 152° W longitudinal from 56° N to 20° S. Along this transect, upper-ocean dCo (σ_0<26) was linearly correlated with dissolved phosphate (slope = 82±3, µmol : mol) due to phytoplankton uptake and remineralization. As depth increased, dCo concentrations became increasingly decoupled from phosphate concentrations due to co-scavenging with manganese oxide particles in the mesopelagic. The transect revealed an organically bound coastal source of dCo to the Alaskan Stream associated with low-salinity waters. An intermediate-depth hydrothermal flux of dCo was observed off the Hawaiian coast at the Loihi Seamount, and the elevated dCo was correlated with potential xs^3He at and above the vent site; however, the Loihi Seamount likely did not represent a major source of Co to the Pacific basin. Elevated concentrations of dCo within oxygen minimum zones (OMZs) in the equatorial North and South Pacific were consistent with the suppression of oxidative scavenging, and we estimate that future deoxygenation could increase the OMZ dCo inventory by 18 % to 36 % over the next century. In Pacific Deep Water (PDW), a fraction of elevated ligand-bound dCo appeared protected from scavenging by the high biogenic particle flux in the North Pacific basin. This finding is counter to previous expectations of low dCo concentrations in the deep Pacific due to scavenging over thermohaline circulation. Compared to a Co global biogeochemical model, the observed transect displayed more extreme inventories and fluxes of dCo than predicted by the model, suggesting a highly dynamic Pacific Co cycle.

2.2 Introduction

Cobalt (Co) is a necessary inorganic micronutrient for many phytoplankton and other forms of marine life but is one of the scarcest essential bioactive metals in the surface ocean. Many cyanobacteria, such as *Synechococcus* and *Prochlorococcus*, have an absolute requirement of Co (Saito et al., 2002; Sunda and Huntsman, 1995), while other phytoplankton require vitamin B_{12} for methionine synthesis, which contains Co as a metallic cofactor (Bertrand et al., 2013). Many metalloenzymes also use Co as a cofactor, including some forms of eukaryotic carbonic anhydrases which can substitute Co for zinc (Zn) (Kellogg et al., 2020; Price and Morel, 1990; Sunda and Huntsman, 1995). The uptake of Co by marine plankton coupled with the scavenging of cobalt onto oxide particles in the mesopelagic ocean gives dissolved Co (dCo) a "hybrid-type" geochemistry, characterized by both nutrient uptake and scavenging processes (Bruland and Lohan, 2003; Noble et al., 2008), which contributes to Co's short residence time in the water column (~ 130 years) and keeps dCo at picomolar concentrations in the open oceans (Hawco et al., 2018; Saito and Moffett, 2002). Co has been predicted to be a co-limiting nutrient in some regions of the ocean, particularly areas with low Zn concentrations (Browning et al., 2017; Moore et al., 2013; Saito et al., 2002). Some of Co's biological influence is through vitamin B_{12}, which has been found to be a co-limiting nutrient in regions like the Antarctic coastal seas (Bertrand et al., 2007; Gobler et al., 2007; Sañudo-Wilhelmy et al., 2006).

Major sources of Co to the marine environment include rivers and estuaries, coastal sediments, hydrothermal inputs, and dust deposition (Dulaquais et al., 2014a; Hawco et al., 2016; Noble et al., 2017). Major sinks of Co primarily require dCo to be transformed to the particulate phase (pCo) via uptake by phytoplankton or lithogenic scavenging before it is removed from the water column by particle export. Dissolved Co is principally scavenged to manganese (Mn) oxides via a microbially mediated co-oxidation (Hawco et al., 2018; Moffett and Ho, 1996; Noble et al., 2017). Internal cycling processes act as major sources of dCo from particulate matter via biomass remineralization and the build-up of dCo in oxygen minimum zones (OMZs). Dissolved Co tends to be elevated in OMZs due to the combined processes of biomass remineralization below the photic zone, suppressed Mn oxide scavenging in the anoxic environment, remobilization of scavenged Co via Mn oxide reduction, and reduced ventilation and mixing of the water mass (Hawco et al., 2016; Noble et al., 2017). Inputs of dCo from OMZs have been shown to be higher than previously expected, representing ~ 27 % of the total marine Co flux (Hawco et al., 2018).

Comparatively, the hydrothermal and eolian dust fluxes are predicted to be <3 % of the total Co source flux (Hawco et al., 2018; Swanner et al., 2014).

Speciation determines the bioavailability of dCo for its major loss processes: uptake by phytoplankton and scavenging by Mn-oxidizing bacteria. Dissolved Co is present in both a labile, "free" Co(II) species and a ligand-bound, "complexed" species. Most if not all organically complexed dCo is predicted to be Co(III) due to its high binding stability with ligands. Ligand-bound Co(III) is a strongly inert fraction of the dCo pool with a conditional stability constant $>10^{16.8}$ (Saito et al., 2005). Organic Co(II)–ligand bonds are comparatively less stable since ligands have a higher affinity to divalent cations that are more abundant than Co such as Ni(II), making Co(II) ligand concentrations negligent (Baars and Croot, 2014). Labile dCo is considered to be more bioavailable to phytoplankton and Mn-oxidizing bacteria than the relatively inert ligand-bound dCo, but there is some evidence that cyanobacteria are able to produce extracellular organic ligands to stabilize ligand-bound dCo for uptake as a nutrient and to prevent its loss via scavenging (Bown et al., 2012; Saito et al., 2005).

The efforts of the GEOTRACES and wider biogeochemical community have greatly increased our understanding of the marine Co cycle on a basin-wide scale over the past decade, including in the Atlantic, Arctic, Southern Ocean, South Pacific and Mediterranean Sea (Bown et al., 2011, 2012; Bundy et al., 2020; Dulaquais et al., 2014a, b, 2017; Hawco et al., 2016; Noble et al., 2017). However, the distribution, sources and sinks of marine Co have not been widely characterized in the North and equatorial Pacific, leaving a vast section of the ocean understudied with regards to Co speciation and biogeochemical dynamics. The North Pacific Ocean is the largest ocean basin with the oldest, least ventilated deep-water mass that serves as the end-member for deep thermohaline circulation. Understanding the major biogeochemical features of the Co cycle in this basin, particularly within the Pacific deep end-member, is important to our understanding of the global Co cycle.

In this study, we examine the distribution of both total dissolved and labile dCo along the GEOTRACES GP15 Pacific Meridional Transect through the North and equatorial Pacific Ocean. This paper characterizes the major features present in the dCo GP15 transect and compares them to similar features found in other ocean basins where a higher density of dCo measurements has been reported. The observed dCo transect is then compared to output from a global biogeochemical Co model to assess and contextualize dCo features along the transect. This study area was

influenced by many relevant sources and sinks within the Co cycle, including coastal and riverine fluxes, OMZs, hydrothermal vents, oligotrophic subtropical gyres, and the aged deep Pacific end-member, providing an ideal snapshot into the Pacific Co cycle and a representative model of global Co biogeochemical processes.

2.3 Methods

2.3.1 Study area and dissolved trace metal sample collection

North and equatorial Pacific seawater samples were collected on the GP15 expedition as part of the US GEOTRACES program (RR1814 and RR1815; 18 September–24 November 2018). Dissolved seawater was sampled along a transect that mostly followed the 152° W meridian from 56° N to 20° S, traveling from the Gulf of Alaska to Hawaii (Leg 1) and on to Tahiti, French Polynesia (Leg 2; Fig. 1). Trace-metal-dissolved seawater samples were collected using a 24-bottle trace-metal-clean "GEOTRACES Carousel" (GTC) equipped with 12 L GO-FLO bottles (General Oceanics) on a titanium frame and a Kevlar cable, as described in Cutter and Bruland (2012). Seawater from the GO-FLO bottles was subsampled in a trace-metal-clean van under positive pressure. Surface water samples (~ 2 m depth) were collected from a trace-metal-clean towfish and pump while arriving at each station. Sampling locations included 25 full-depth stations and 10 demi stations where only the upper 1000 m was sampled. At Station 11, only a surface towfish sample was collected due to rough weather.

Dissolved Co subsamples were filtered using a 0.2 µm AcroPak capsule and stored until analysis at 4 °C in 60 mL low-density polyethylene (LDPE) bottles (Nalgene) that had been soaked for 1 week in Citranox, an acidic detergent; rinsed with Milli-Q water (Millipore); soaked for 2 weeks in 10 % trace-metal-grade HCl (Optima); and rinsed with lightly acidic Milli-Q water (<0.1 % HCl). All Co values presented here were analyzed at sea, with replicates of all samples taken for dCo analysis in the laboratory, if needed.

Macronutrient samples were analyzed at sea within 24 h of recovery by the Ocean Data Facility (ODF) at Scripps Institution of Oceanography. The nutrient and hydrographic dataset can be found on the Biological and Chemical Oceanography Data Management Office (BCO-DMO) website (Leg 1: https://www.bco-dmo.org/dataset/777951, last access: 3 May 2022; Leg 2: https://www.bco-dmo.org/dataset/824867, last access: 3 May 2022). Macronutrient

concentrations reported here have been converted from units of micromoles per kilogram (μmol kg^{-1}) to micromolar by multiplying each sample by its calculated in situ density.

The depth of the mixed layer was determined for each station as the first depth at which the difference between the potential density (σ_θ) and reference density (σ_{ref}) was greater than or equal to 0.125 kg m^{-3}, where σ_{ref} is the σ_θ at 10 m depth (Bishop and Wood, 2009; Ohnemus et al., 2017). In situ density, potential density and O_2 solubility used to calculated apparent oxygen utilization (AOU) were determined via the Gibbs SeaWater (GSW) Oceanographic Toolbox in Python (https://teos-10.github.io/GSW-Python/, last access: 22 April 2021) (Mcdougall and Barker, 2011).

2.3.2 Dissolved total and labile Co analysis

Dissolved cobalt was determined by cathodic stripping voltammetry (CSV) as originally described by Saito and Moffett (2001) and modified by Hawco et al. (2016) and Saito et al. (2010). Measurement occurred shipboard inside a trace-metal-clean plastic "bubble" within 1 week of sample collection using the Metrohm 663 VA and μAutolabIII systems equipped with a hanging mercury drop working electrode. The reagents used for this method included (1) 0.1 M dimethylglyoxime (DMG; Sigma Aldrich), (2) 0.5 M N-(2-hydroxyethyl)piperazine-N-(3-propanesulfonic acid) (EPPS; Sigma Aldrich) buffer, (3) 1.5 M $NaNO_2$ (Merck) and (4) a 25 pM $CoCl_2$ (Fisher Scientific) standard made in September 2018 for this expedition. The DMG reagent was purified via recrystallization, and the EPPS and $NaNO_2$ reagents were run through treated Chelex-100 resin columns (BioRad) to remove trace metal contaminates. The Chelex resin was prepared as described in Price et al. (1988, 1989), and reagents were purified as described in Saito and Moffett (2002).

For total dCo analysis, 0.2 μm filtered water samples were UV-irradiated in acid-washed quartz tubes for 1 h using a water-cooled UV irradiation system (Metrohm 705 UV Digestor) to destroy natural ligand-bound Co complexes. Then, 11 mL of sample seawater was aliquoted from the sample bottle into 15 mL acid-washed polypropylene vials, and 33 μL of the DMG reagent and 130 μL of the EPPS buffer was added to each vial. The samples were then processed on an autosampler (Metrohm 858 sample processor), which added 8.5 mL of the sample solution and 1.5 mL of the $NaNO_2$ reagent to a Teflon cup for electrochemical analysis. The mercury electrode performed a fast linear sweep from −1.4 to −0.6 V at a rate of 5 V s^{-1}, which reduced the Co bound

in the $Co(HDMG)_2$ complex from Co(II) to Co(0) and produced a Co reduction peak at −1.15 V with a height linearly proportional to the amount of dCo present in the sample. A standard addition curve was generated for each sample analyzed with four automated additions of the 25 pM $CoCl_2$ standard. A type-I linear regression of the standard curve allowed for the calculation of the initial amount of Co present in the sample, as described in Saito and Moffett (2001). Triplicate technical replicates were run on every sample to determine the precision of the method. Duplicate depths from different rosette casts were run when available.

Labile dCo analysis was identical to the total dCo method described above except the samples were not UV-irradiated prior to analysis to preserve the sample's ligands, and labile samples were allowed to equilibrate with the DMG and EPPS reagents overnight (~ 8 h) before CSV analysis. This equilibration step allows time for the labile dCo to bind to the DMG reagent via competitive ligand exchange ($K>10^{16.8}$) and thus is defined relative to its thermodynamic behavior (Saito et al., 2005). These labile dCo measurements are not necessarily comparable to dCo measurements that are performed using non-electrochemical methods, which are sometimes described as labile. In particular, inductively coupled plasma mass spectrometry (ICP-MS) measurements of dCo where samples are not UV-irradiated prior to analysis gives consistently different results than this electrochemical method, likely due to differences in Co complex adsorption and/or exchange kinetics with metal-binding resins. As a result, ICP-MS labile Co measurements tend to be somewhat offset compared to electrochemical labile Co measurements (unpublished data). This offset is not yet well understood, but it indicates that the two methods are measuring different pools of the dCo inventory, which should be considered before comparing dCo values analyzed with different methodologies. The purpose of mentioning the offset in this study is to clarify the distinction between the dCo analytical methods for those who will use this dataset in the future, particularly as part of the GEOTRACES intermediate data product (IDP).

Peak heights were determined by ElectroChemistry Data SOFTware (ECDSOFT) when possible, and manual measurement of peaks was used when peak detection was unsuccessful by the available software. This hybrid approach was employed because the most updated version of Metrohm software at the time, Nova 2.0, no longer supported manual peak-picking of individual samples, and ECDSOFT did not always detect peaks from samples with low dCo concentrations. A pairwise sample *t* test was performed to compare the differences between the manual analysis method and the digital ECDSOFT analysis method as determined by selected samples that were

analyzed using both methods (n=13, average difference = 0.9±2.7 pM). The two peak height analysis methods were found to be statistically equivalent (t=1.16, P=0.27).

The entire dCo dataset generated on the GEOTRACES GP15 expedition can be accessed online at https://www.bco-dmo.org/dataset/818383 (last access: 3 May 2022) (Leg 1) and https://www.bco-dmo.org/dataset/818610 (last access: 3 May 2022) (Leg 2).

2.3.3 Analytical blanks

Analytical blanks for each combination of reagent batches (a unique combination of DMG, EPPS and $NaNO_2$ reagents) were measured to determine background Co contamination due to reagent impurities. Blanks were prepared in duplicate or triplicate with UV-irradiated surface seawater passed through a treated Chelex-100 resin bead column (Bio-Rad) to remove metal contaminants, then UV-irradiated again to ensure no excess Co ligands were present. Averaged analytical blank values were subtracted from the measured Co values determined with the respective reagent batch.

For the four reagent batches used on GP15, the analytical blanks were found to be 9.44 ± 0.56 pM (n=3), 9.68 ± 0.40 pM (n=2), 0.04 ± 2.14 pM (n=2) and 6.28 ± 0.84 pM (n=2; Table 1). For the third reagent batch (0.04 pM blank), no blank value was subtracted from the determined Co values because the standard deviation was greater than the measured blank Co. An analytical limit of detection for this method was calculated from the 9.44 ± 0.56 pM blank (3× blank standard deviation where n≥3) to be 1.7 pM.

2.3.4 Intercalibration and internal standards

While processing samples at sea, duplicate GEOTRACES community intercalibration standards – either GSC2 or D1 – were run at least once every 2 weeks (Table 1). All intercalibration standards are stored acidified, so samples were carefully titrated directly before analysis with negligible volumes of ammonia hydroxide (NH_4OH) until they reached a pH of 7.5–8.2; then they were UV-irradiated and analyzed as a dCo sample. The D1 standard (44.0 ± 0.01 pM, n=2) was found to be within 1 standard deviation of the consensus value (46.6 ± 4.8 pM), and the GSC2 standard (82.8 ± 2.9, n=4) overlaps in its uncertainty range with the value reported in Hawco et al. (2016) (77.7 ± 2.4, 6.2 % difference). Additional GSC2 standards were run in the laboratory in August to November 2019 with a new reagent batch and displayed

dCo concentrations of 80.2 ± 6.2 pM (n=3). No official community consensus for dCo in GSC2 currently exists.

To validate the consistency of the instrument, an internal standard was analyzed at least once every other day dCo samples were measured. Two internal standard batches were used during the expedition: the first created from UV-irradiated surface North Pacific seawater (dCo = 55.9 ± 3.9 pM, n=18) and the second created from UV-irradiated South Atlantic water collected on the 2007 GAc01 CoFeMUG expedition (dCo = 15.5 ± 3.4 pM, n=7; Table 1). To ensure Co analysis was consistent while transitioning between internal standards, both standard batches were measured during an overlap period of 2 weeks (22 October–9 November 2018).

Station 35 of the GP15 expedition was a crossover station with the GEOTRACES GP16 expedition in 2013 and was located at the same latitude and longitude as GP16 Station 36 (10.5° S, 152° W). A comparison of their dCo profiles shows good agreement between the two stations (Fig. 2), although an independent t test of the deep-dCo values (≥ 2000 m) does show a significant offset (5 pM) between the two crossover station profiles (t = –4.9, P = 2.7 × 10^{-5}). The GP15 measurements showed a deep (≥ 2000 m) dCo signal of 24.0 ± 2.6 pM (n=15), and the GP16 measurements showed a slightly higher deep-dCo signal of 29.1 ± 3.5 pM (n=19). The GP16 profile from 2013 also had a larger mesopelagic maximum between 500 and 1000 m than the GP15 profile, which may be due to seasonal or annual variability in the remineralization signal in the South Pacific Gyre. The 5 pM offset may be due to a small analytical offset or oceanographic variability, possibly related to the higher mesopelagic dCo concentrations observed in the GP16 profile. Although the two profiles have a small statistical difference at depth, their substantial overlap and similarity of geochemical features are good indications that our measurement of dCo on the GP15 expedition was robust and oceanographically consistent.

2.3.5 Particulate metal and particulate organic carbon analysis

Samples for both particulate trace metal analysis and particulate organic carbon (POC) analysis were collected with dual-flow McLane Research in situ pumps (WTS-LV) at each full-depth station. Each McLane pump contained two filter holders: one outfitted with paired 1 µm quartz fiber (Whatman QMA) filters and 51 µm polyester prefilters (Sefar) and the other with paired 0.8 µm polyethersulfone (Pall Supor) filters and 51 µm polyester prefilters. Large particulate, total (LPT) samples were collected from the prefilters (>51 µm). Small particulate,

total (SPT) samples were collected from the QMA filters (1–51 µm) and Supor filters (0.8–51 µm), depending on sample type; SPT trace metal and lithogenic samples were collected from the Supor filters, while SPT POC samples were collected from the QMA filters.

Particulate trace metal samples, including particulate Co (pCo) and particulate Mn (pMn), were digested using hot refluxing with hydrofluoric and nitric acids and measured via high-resolution ICP-MS. Particulate aluminum (pAl) and titanium (pTi) concentrations were used as tracers for lithogenic particles and were used to calculate a lithogenic correction for pCo and pMn, where the corrected values represent excess trace metals unaccounted for by a lithogenic source. The Co : Ti ratio between potential lithogenic end-members was less variable (RSD ~ 27 %) than the Co : Al ratio (RSD ~ 64 %), so measured pTi was used for lithogenic Co correction together with a molar Co : Ti ratio of 0.00306, which was the median Co : Ti ratio of four potential lithogenic end-members: upper and bulk continental crust (Taylor and McLennan, 1995), mid-ocean ridge basalt (Gale et al., 2013), and ocean island basalt 0.0306 (Hémond et al., 1994). For Mn, the Mn : Al ratio was less variable (RSD ~ 36 %) than the Mn : Ti ratio (RSD ~ 48 %) between lithogenic end-members, so measured pAl together with a molar Mn : Al ratio of 0.0086, the median of the four lithogenic end-members as referenced above, was used to correct for lithogenic Mn. Total particulate values were calculated by summing the SPT and LPT values.

POC samples were analyzed via combustion in an elemental analyzer after fuming with HCl to remove particulate inorganic carbon. A particulate sampling and analysis procedure can be found in more detail in Xiang and Lam (2020).

2.3.6 Excess ^{3}He, dFe and dMn analysis at the Loihi Seamount

The collection, analysis and interpretation of helium (He) isotope and other noble gas samples along the GP15 transect and at the Loihi Seamount (Station 18.6) have been presented by Jenkins et al. (2020). Samples of ^{3}He, ^{4}He and Ne were collected from Niskin bottles on the Ocean Data Facility (ODF) CTD (conductivity–temperature–depth) rosette and not from the trace-metal-clean GEOTRACES CTD carousel (GTC) that supplied the dCo samples. Briefly, He isotopic ratios and abundances were determined by quantitative gas extraction and mass spectrometry as described in Jenkins et al. (2019). Dissolved He and neon (Ne) saturation anomalies were calculated as a function of temperature and salinity, and He isotope ratio anomalies were calculated relative to a marine atmospheric standard. The excess ^{3}He anomaly (xs^3He) was determined as

the ^{3}He unaccounted for by gas saturation, surface air injection, and diapycnal mixing (Jenkins et al., 2019).

The CTD cast discrepancy between the noble gas samples (ODF) and the dCo samples (GTC) is of particular note at the Loihi station because there was a clear offset in chemical composition between the two sampling casts, likely due to currents pushing the rosettes to differing locations within the heterogeneous vent environment of the seamount (see Sect. 2.5.3). The offset between the casts made a direct comparison between dCo and the xs^{3}He associated with hydrothermal sources in the Loihi Seamount impossible. Instead, we used dissolved Fe (dFe) and dissolved Mn (dMn) samples taken from both the GTC and the ODF casts to estimate a "potential ^{3}He anomaly" from the GTC cast, assuming the dFe : xs^{3}He and dMn : xs^{3}He ratios were consistent between the two casts. The ODF casts' trace metal : xs^{3}He ratios were used to infer the potential xs^{3}He concentration profile from GTC dFe and dMn concentrations. This calculation is explained in detail in Sect. 2.5.3.

This paper presents dFe and dMn data determined by flow injection analysis (FIA) for the ODF cast and ICP-MS for the GTC cast, as described in Jenkins et al. (2020). The two methods are in good agreement with each other, as shown in Fig. 3 of Jenkins et al. (2020).

2.3.7 Pairing GP15 samples with existing radiocarbon data

To estimate sample conventional radiocarbon age, sample locations along the GP15 transect were matched with existing radiocarbon data from the Global Ocean Data Analysis Project (GLODAP) v2, 2019 merged and adjusted data product for the Pacific Ocean (https://www.glodap.info/index.php/merged-and-adjusted-data-product/, last access: 21 June 2020) (Key et al., 2015; Olsen et al., 2016, 2019). GP15 sample locations were paired with the closest GLODAP sample locations containing Δ^{14}C data using their latitudinal, longitudinal and depth dimensions. Only GLODAP data points that were within 200 m depth and 500 km latitude–longitude distance from the original GP15 sample location were accepted. The conventional radiocarbon age of each deep sample (>3000 m) was calculated with the equation

$$\text{Radiocarbon Age} = -8033\ \text{yr} \times \ln(1 + (\Delta^{14}\text{C} + 67\ ‰)/1000) \quad (1)$$

where 8033 is the inverse of the ^{14}C decay constant (λ; 1.21×10^{-4} yr^{-1}), and −67 ‰ is subtracted from the $\Delta^{14}C$ value to correct for preformed $\Delta^{14}C$ in the North Atlantic such that the newly formed North Atlantic Deep Water (NADW) is reset to an age of ~ 0 years (Matsumoto, 2007). This radiocarbon age calculation has previously been used to calculate Co scavenging rates via thermohaline circulation (Hawco et al., 2018) and does not correct for the increase in anthropogenic radiocarbon due to nuclear weapons testing, the change in the atmospheric ^{14}C due to increased use of anthropogenic fossil fuels via the Suess effect, or the mixing and ventilation of NADW with Antarctic Bottom Water (AABW) during ocean circulation. The lack of correction for ventilation during AABW formation is acceptable because most of the $\Delta^{14}C$ and dCo in the deep Pacific is derived from NADW, not AABW (Hawco et al., 2018). The radiocarbon age calculated here is not the "natural" or "circulation" radiocarbon age and is only used to represent relative ages and ventilation of water masses in the deep Pacific Ocean.

2.3.8 Comparison to a cobalt biogeochemical model

The observational dCo concentrations from bottle samples along the GP15 transect were compared to the output of a published global Co biogeochemical model (Bundy et al., 2020; Richon and Tagliabue, 2021; Tagliabue et al., 2018). The Co model is embedded within the BYONIC version of the PISCES-v2 biogeochemical model (Richon and Tagliabue, 2021), which includes the simulation and circulation of a variety of tracers including dissolved phosphate (dPO_4), nitrate, ammonium, silicic acid, Fe, copper (Cu), Zn, Mn and O_2 as well as the resolution of different phytoplankton, zooplankton and particle pools. The Co biogeochemical model (Tagliabue et al., 2018) incorporates dCo, scavenged Co, diatom-associated Co, nanophytoplankton-associated Co, small particulate organic Co and large particulate organic Co. External input of Co is via dust, rivers and continental margins, with margin Co supply modulated by the overlying O_2 content. The model output was gridded on a $1^\circ \times 1^\circ$ latitude–longitude grid with 33 depth boundaries: 0, 10, 20, 30, 40, 50, 60, 70, 80, 90, 100, 110, 120, 135, 150, 175, 200, 250, 300, 500, 700, 1000, 1250, 1500, 2000, 2500, 3000, 3500, 4000, 4500, 5000 and 5500 m. Gridded points along the GP15 transect were extracted from the annual mean global model results and compared to the observed GP15 transect. In order to appropriately compare the two datasets, the dCo, O_2 and dPO_4 observed concentrations along the GP15 transect were binned on the same

grid as the model (1° × 1° latitude–longitude with 33 depth boundaries), and the values of any observed data points that occupied the same bin were averaged.

2.3.9 Regression analysis

All linear regressions presented in this paper were made using a two-way (type-II) linear regression, with the exception of the standard addition curves used to calculate dCo concentrations (Sect. 2.3.2). Two-way regressions are more suitable for stoichiometric analysis than one-way (type-I) regressions because they allow for error in the *x* parameter as well as the *y* parameter and as such do not assume dependence between the *x* and *y* axes. The algorithm for the two-way regression was written into MATLAB (lsqfitma.m) by Ed Peltzer circa 1995 (Glover et al., 2011) and was rewritten as a Python 3 function for this paper (available at https://github.com/rebecca-chmiel/GP15, last access: 3 May 2022).

2.4 Results

2.4.1 Hydrographic setting

The GEOTRACES GP15 expedition (Fig. 1) investigated a cross-section of the North and central Pacific basin that contained a wide range of ocean biogeochemical processes, including the North and South Pacific low-nutrient gyres, shelf- and riverine-associated sedimentary inputs along the Alaskan coast, hydrothermal vent inputs at the Hawaiian Loihi Seamount, and three oxygen minimum regions.

The GP15 transect crosses five major Pacific oceanographic provinces, including (1) the Alaskan coast (56–55° N; Stations 1–3), characterized by shallower depths, low-salinity surface waters and the coastal Alaskan Current (Reed, 1984; Stabeno et al., 1995); (2) the North Pacific subpolar gyre (54.6–44.5° N; Stations 4–9), an area of cyclonic upwelling and a high-nutrient, low-chlorophyll (HNLC) region generally considered to be iron (Fe)-limited (Boyd et al., 2004; Tsuda et al., 2005); (3) the North Pacific subtropical gyre (42–17.5° N; Stations 10–19), an anticyclonic oligotrophic gyre with low surface macronutrients and intermediate suboxic waters; (4) the equatorial Pacific (14.25° N–7.5° S; Stations 20–34), characterized by equatorial upwelling, subsurface equatorial currents, and the cross-sections of the eastern tropical North Pacific (ETNP) and eastern tropical South Pacific (ETSP); and (5) the South Pacific subtropical gyre (10.5–20° S;

Stations 35–39), an oligotrophic anticyclonic gyre that is generally macronutrient-limited, particularly for nitrogen (N) (Bonnet et al., 2008).

Three distinct oxygen minimum zones (OMZs) were present in the GP15 transect: the tail ends of the ETNP and ETSP OMZs, around 5–15° N and 2–10° S, respectively, and the intermediate waters of the North Pacific (Fig. 3c). OMZs are created by a combination of oxygen consumption, often via remineralization of organic carbon, and poor water mass ventilation that forms a "shadow zone" of sluggish, isolated water (Karstensen et al., 2008; de Lavergne et al., 2017). In the ETNP and ETSP, shadow zones are created by Ekman upwelling along eastern Pacific margins of North and South America (Czeschel et al., 2011; Karstensen et al., 2008); these OMZs are wider and more depleted in O_2 closer to the American continents where they are formed (Hawco et al., 2016; Stramma et al., 2008), and the GP15 transect captured a cross-section of the less O_2-depleted tailings of the OMZs. In contrast, the massive North Pacific OMZ is created by the abyssal overturning of Pacific Deep Water (PDW) traveling northward via thermohaline circulation. When the dense PDW reaches the North Pacific, it is upwelled to mid-depth waters (<2500 m) and returns southward along intermediate isopycnal boundaries, creating a shadow zone of low circulation in the above waters (1000–2500 m) (de Lavergne et al., 2017). The combination of the shadow zone and the remineralization of organic carbon from upwelling-fueled phytoplankton blooms in the North Pacific subpolar gyre (Nishioka et al., 2020; Sarmiento et al., 2004) creates a large OMZ that stretches across the North Pacific transect at intermediate depths. The three Pacific OMZs alter the redox state and biogeochemistry of trace metals contained within them.

2.4.2 Dissolved cobalt distributions in the Pacific Ocean

During the GP15 expedition, 1024 samples were analyzed at sea for Co, including 715 total dCo measurements (hereafter simply dCo) from 36 stations and 309 labile dCo measurements from 22 stations. The resulting longitudinal transect (Figs. 3, 4) represents the second-largest Pacific dataset of dCo speciation measurements, after the GEOTRACES GP16 dataset (Hawco et al., 2016).

Dissolved Co was depleted in the surface Pacific Ocean (Fig. 5) due to phytoplankton uptake and utilization. The towfish samples, the surface-most samples collected for dCo around 2 m depth, typically represented a dCo minimum in the profile. Towfish dCo values were lowest

in the North and South Pacific subtropical gyres, where average surface dCo reached near-zero values of 1.4 ± 2 pM (n=10) and 0.7 ± 2 pM (n=5), respectively. The surface dCo values were comparatively larger in the North Pacific subpolar gyre and equatorial Pacific, with average surface dCo values of 50 ± 31 pM (n=5) and 8 ± 8 pM (n=10), respectively. The only exception to the observed dCo surface minimum was on the Alaskan coast; Stations 1 and 2, the most coastal stations in the Gulf of Alaska, exhibited dCo maxima at the surface. The highest concentrations of dCo observed in the Pacific transect occurred in the towfish sample of Station 1, which contained a dCo maximum of 576 pM (Fig. 4). This value is 2 orders of magnitude larger than the lowest observed surface values in the transect, highlighting the large and dynamic range of dCo within the Pacific. At this station, dCo was highest in the surface ocean and decreased with depth, a profile typical of a scavenged-type element with a substantial coastal source in the surface ocean.

With the exception of the Alaskan coast and hydrothermally influenced stations, dCo profile maxima were observed in the mesopelagic ocean due to biomass-associated Co remineralization and re-dissolution. Excluding the Alaskan coast surface maxima, dCo maxima of 54 to 167 pM were observed in intermediate depths between 45 and 900 m (Fig. 6). This wide range of depths of the dCo remineralization maxima is associated with regional variation in mixed-layer depth and dCo build-up within OMZs. Within the poorly ventilated OMZ regions, elevated dCo plumes are formed when there is a source of dCo via remineralization in the mesopelagic but little to no loss of dCo via scavenging onto Mn oxide particles (see Sect. 2.5.4). The average dCo profile maximum was shallowest in the water column in the upwelling regions of the North Pacific subpolar gyre (76 ± 18 m, n=6) and the equatorial Pacific (210 ± 74 m, n=10), where the strongest influence from the North Pacific OMZ, ETNP and ETSP were located. In these regions, the dCo maxima were shallower than the dPO_4 maxima that represent the base of the nutricline, indicating that Co distribution within OMZs is somewhat decoupled from P remineralization, which is consistent with our understanding of elevated dCo in OMZs. In contrast, the average dCo profile maximum reached deeper depths in the North and South Pacific subtropical gyres (580 ± 150 m, n=10 and 425 ± 75 m, n=3, respectively) than in the regions affected by OMZs. These deeper mesopelagic dCo maxima follow a deepening nutricline in the subtropics, which is indicative of the downwelling environment, low biomass and high light penetration of the gyres.

Scavenging of dCo within and below the mesopelagic ocean created low concentrations of dCo in the ocean interior. In the deep Pacific (depth ≥2000 m) the average dCo concentration was

27 ± 11 pM (*n*=166), with large regions of the deep Pacific consistently under 25 pM dCo, particularly in the South Pacific. In contrast, the Atlantic Ocean has greater deep-dCo concentrations on average (Dulaquais et al., 2014a; Noble et al., 2017; Wyatt et al., 2021), with the North and South Atlantic basins displaying deep-dCo concentrations of 57 ± 12 pM (*n*=166) and 40 ± 9 pM (*n*=184), respectively (Schlitzer et al., 2018). On GP15, dCo exhibited a heterogeneous distribution within the deep ocean, often with clear vertical regimes of elevated dCo that extend from the mesopelagic to the seafloor. For example, dCo is elevated at the Equator (Station 29), at 17.5° N off the coast of Hawaii (Station 19), and in the North Pacific from 32–47° N (Stations 14–8). These vertical regimes of elevated dCo are reminiscent of POC export dynamics and likely represent the stabilization of deep dCo in a ligand-bound speciation. This vertical phenomenon is further explored in Sect. 2.5.6.

2.4.3 Labile dissolved cobalt

Labile dCo followed similar distribution patterns as dCo (Figs. 3b, 5b). Labile dCo was strongly depleted in the surface and deep interior Pacific Ocean and was elevated in OMZs, coastal regions, the Loihi Seamount and the highly remineralized mesopelagic. The surface ocean south of the subpolar gyre contained exceptionally low concentrations of labile dCo, with average surface towfish samples (~ 2 m depth) of the North Pacific subtropical gyre and equatorial Pacific displaying labile dCo values of 3 ± 5 pM (*n*=6) and 1 ± 3 pM (*n*=7), respectively. A total of 14 of the 21 surface towfish samples analyzed for labile dCo contained concentrations below the detection limit of 2 pM, including all three of the South Pacific subtropical gyre towfish samples. The deep interior Pacific (≥ 2000 m depth) also contained very low to undetectable concentrations of labile dCo, with an average concentration of 2 ± 5 pM and 43 of the 64 deep samples analyzed containing labile dCo concentrations below the detection limit. Like dCo, labile dCo was elevated in the mesopelagic, particularly in the cores of the tropical Pacific OMZ regions, where labile dCo reached a maximum of 49 pM in the ETNP and 56 pM in the ETSP. Labile dCo was depleted in the North Pacific OMZ compared to total dCo, indicating that a large portion of the dCo plume within that low-oxygen region was complexed by organic ligands.

The ratio of labile : total dCo in Pacific seawater was 0.33 ± 0.02 (R^2=0.55, *n*=237; Fig. 7) when data points affiliated with coastal waters (Station 1), OMZs ([O_2] <50 µmol kg^{-1}) and hydrothermal activity (Station 18.6, where depth >1100 m) were excluded because they exhibited

unique labile : total dCo ratios. This “background” Pacific ratio is identical to the ratio found in the South Pacific (0.33) on the GEOTRACES GP16 transect (Hawco et al., 2016). About two-thirds of dCo present in Pacific seawater existed in a strong ligand-bound speciation, likely as strong Co(III) complexes like vitamin B_{12} and similar biologically produced molecular species that are unable to exchange with strong ligands in experimental time frames. The other one-third of the dCo inventory existed as “free” or exchangeable, weakly bound Co(II) species that are considered more bioavailable and Mn-oxide-reactive (Baars and Croot, 2014; Saito et al., 2005). However, this 0.33 ratio was not consistent within all samples; of the 309 samples analyzed for labile dCo, 136 showed measurable total dCo but labile dCo values below the analytical limit of detection (2 pM), indicating near 100 % complexation. This caused the background seawater labile : total dCo slope to be depressed below the visual trend in higher labile and total dCo concentrations. Additionally, labile dCo values were found to be elevated compared to total dCo in the Loihi Seamount hydrothermal system and depressed with respect to total dCo near the Alaskan coast, indicating that the ratio of labile : total dCo varies among different dCo sources.

2.5 Discussion

2.5.1 The dCo and PO_4 relationship depicts Co advection, uptake, remineralization and scavenging

The advection of dCo is an important driver of dCo distributions throughout the Pacific. In the deep ocean, CDW carries dCo north from the Southern Ocean to the North Pacific basin via thermohaline circulation, then partially upwells the dCo in the North Pacific basin, forming PDW. To either side of the Equator, dCo is advected at intermediate depths within the ETNP and ETSP OMZs by the North Equatorial Current and South Equatorial Current, carrying elevated concentrations of dCo from the continental margins to the pelagic Pacific Ocean (see Sect. 2.5.4) (Hawco et al., 2016). However, dCo's relatively short residence time, especially in the upper ocean and mesopelagic, allows other, more vertical processes such as biological uptake, remineralization and scavenging to overlap with the dCo advection signal. This overlap of horizontal (advection) and vertical processes determines the Pacific dCo distribution observed along the GP15 transect.

An analysis of dCo : dPO_4 ratios allows us to distinguish between the role of dCo as a nutrient-type and scavenged-type element. When dCo is correlated with dPO_4, its distribution is primarily controlled by biological uptake and remineralization as a micronutrient, and when dCo

and dPO_4 are decoupled, its distribution is primarily controlled by additional processes acting upon the dCo concentrations such as scavenging to oxide particles or an abiotic dCo source. These processes affecting dCo distributions can be depicted in dCo : dPO_4 vector space, where Co- and PO_4-coupled processes like phytoplankton nutrient uptake and remineralization result in vectors with positive slopes and opposite directionality, while decoupled processes like abiotic inputs and scavenging result in more vertical vectors that primarily show change in dCo concentration (Fig. 8a) (Noble et al., 2008; Saito et al., 2017). Co scavenging is also primarily a biologically mediated process by oxidizing bacteria (Moffett and Ho, 1996), so biotic scavenging of dCo would in theory draw down a relatively small amount of dPO_4 via biological uptake. This is represented by a large negative dCo vector and a small negative dPO_4 vector, the sum of which is shown in Fig. 8a.

The dCo vs. dPO_4 relationship along the GP15 transect contained a relatively linear stoichiometry in the upper ocean and a "curl" towards the bottom right of the plot driven by mesopelagic and deep samples (Fig. 8b). The linear section in the upper ocean (0 to ~ 400 m) showed dCo distributions that were governed by phytoplankton uptake and remineralization, driving the coupling of dCo and dPO_4 ecological stoichiometry. The curl in the dCo vs. dPO_4 relationship occurred because of a shift in relative contributions of processes from remineralization to scavenging; the sum of the mesopelagic remineralization vector (increasing dCo and dPO_4) and the scavenging vector (decreasing dCo, little change in dPO_4) resulted in a vector sum towards the lower right, creating a curl towards low dCo and high dPO_4 in DPW. The decoupling of dCo and dPO_4 due to interior scavenging is a characteristic feature of Co's hybrid geochemistry and has been previously documented in the Pacific (Hawco et al., 2016), Atlantic (Noble et al., 2017; Saito et al., 2017) and Arctic oceans (Bundy et al., 2020). To this date, the Southern Ocean is the only major basin that does not display a strong dCo scavenging vector (Noble et al., 2013; Oldham et al., 2021; Saito et al., 2010). Below ~ 2500 m, the dCo vs. PO_4 relationship appeared to curl towards the origin. This phenomenon was driven by the mixing of water masses in the Pacific, namely the transition between the heavily remineralized PDW, characterized by exceptionally high dPO_4, and the abyssal CDW, which contained relatively less dPO_4 even at greater depths in the Pacific (Fig. 3d). Thus, both dCo and dPO_4 were relatively depleted within the CDW mass compared to the intermediate PDW mass, creating a deep Pacific "curl" towards the origin in the deep dCo vs. dPO_4 relationship. Note that mixing does not remove

dCo or dPO_4 from the system; the CDW and PDW masses simply contain different end-member dCo and dPO_4 concentrations.

To further explore the dCo vs. dPO_4 relationship with depth, sample points along the Pacific transect were divided into nine isopycnal bins by their potential density anomaly (σ_0), an analysis described in Hawco et al. (2018) (Fig. 9 and Table 2 in this paper). Each bin contained sample points within a σ_0 range of 0.25 kg m^{-3}, with the exception of the least dense bin, which contained all samples with σ_0<26 kg m^{-3}. Stations 1 and 2, the Alaskan coastal stations, were removed from this analysis since they exhibited a clear surface abiotic source vector and a negative upper-ocean dCo : dPO_4 correlation (see Sect. 2.5.2), indicating that the dCo : dPO_4 relationship was not primarily driven by uptake and remineralization. Dissolved Co and dPO_4 were positively correlated in the least dense bin (σ_0<26 kg m^{-3}; Fig. 9a), which represented the surface and upper ocean (depth range = 2–325 m, average depth = 84 ± 67 m). The dCo : dPO_4 slope was 82 ± 3 (µmol : mol; n=218, R^2=0.79), which is an estimate of the combined surface phytoplankton uptake stoichiometry and mesopelagic remineralization stoichiometry. This dCo : dPO_4 slope is comparable to the upper-ocean stoichiometry reported in the South Pacific (69, µmol : mol; R^2=0.89) (Hawco et al., 2016). In this study and the South Pacific study referenced, there appears to be one clear linear uptake and remineralization slope throughout the upper-ocean depth range. This is distinct from studies in the Atlantic Ocean where the upper dCo : dPO_4 ratio varies with depth, and dCo : dPO_4 slopes can be described as "accelerating" towards the surface ocean (Saito et al., 2017). High Atlantic dCo : PO_4 surface stoichiometry values have been reported up to 544 (µmol : mol; depth = 40–136 m, R^2=0.79) (Saito et al., 2017) and 560 (µmol : mol; depth = 5 m, R^2=0.63) (Saito and Moffett, 2002), an order of magnitude higher than those reported in the Pacific and deeper Atlantic (27–67, µmol : mol, up to 200–900 m depth) (Dulaquais et al., 2014b; Noble et al., 2017; Saito et al., 2017). The extraordinarily high ecological stoichiometry in Atlantic surface samples has been attributed to strong drawdown of dPO_4 in the upper ocean coupled with increased use of Co in metalloenzymes, which is hypothesized to substitute for Zn as a cofactor (Saito et al., 2017). This may be the case for alkaline phosphatase, an enzyme that cleaves phosphate groups from dissolved organic phosphorus molecules and is associated with P stress in phytoplankton (Cox and Saito, 2013; Quisel et al., 1996). Co has been shown to be the metallic cofactor for alkaline phosphatase in the hyperthermophile *Thermotoga maritima* (Wojciechowski et al., 2002), although Co substitution

for Zn in marine cyanobacterial alkaline phosphatase is currently unconfirmed. The Pacific Ocean, in contrast, broadly shows less evidence for P limitation and more evidence for N and Fe stress in the oligotrophic gyres (Bonnet et al., 2008; Saito et al., 2014) and Fe and other trace metal stress in the upwelling regions of the subpolar gyre and equatorial Pacific (Boyd et al., 2004; Coale et al., 1996; Moore et al., 2013; Tsuda et al., 2005; Ustick et al., 2021). This difference in extent of P stress in the Pacific basin compared to the Atlantic was likely the reason for the more linear relationship between dCo and dPO_4 throughout the upper Pacific Ocean.

As the σ_0 bins increased in density, the correlations (R^2) between dCo and dPO_4 concentrations became less significant (Fig. 9j), indicating that dCo concentrations were becoming decoupled from dPO_4 in the deep Pacific due to Co scavenging. In the second (b) and third (c) bins, the dCo : dPO_4 slopes (86 ± 14 and 86 ± 17 (µmol : mol), respectively) are similar to that of the least dense bin (82 ± 3, µmol : mol), but the slope error increases, and the R^2 value decreases at higher bin densities. Below the third density bin ($\sigma_0 \geq 26.5$ kg m^{-3}), the R^2 values of the correlations are extremely low, and the slope values should not be interpreted as meaningful. The deep-ocean density bins (Fig. 9g–i; average depths: 980 to 4144 m) displayed little dynamic range in dCo or dPO_4, indicating little to no significant remineralization or scavenging signatures across the deep ocean despite the wide depth range represented by these bins. These findings are consistent with other studies that show that Mn oxide formation and dCo scavenging primarily occur along sharp density gradients in the mesopelagic and are not as significant in the ocean's deep interior, where scavenging occurs at a slower rate (Hawco et al., 2018; Saito et al., 2017; Sunda and Huntsman, 1988).

2.5.2 The Alaskan coast as a source of ligand-bound dCo

In the coastal Gulf of Alaska at Stations 1 and 2, the dCo and labile dCo profile maxima occurred at the ocean surface (~ 2 m depth; Fig. 10c). This dCo distribution is similar to that of the Arctic Ocean, where high surface dCo concentrations of a similar magnitude and a scavenged-type profile have been attributed to riverine inputs from the surrounding continents and sedimentary inputs from the Arctic shelf (Bundy et al., 2020). The Station 1 towfish surface seawater sample contained the highest dCo and labile dCo measured in this study (576 and 102 pM, respectively) and displayed a noticeably low labile : total dCo ratio of 0.18, representing a source of predominantly ligand-bound, likely humic dCo to the surface water of the coastal Gulf of

Alaska. In vector dCo vs. dPO_4 space (Fig. 8a), this riverine input is represented by an upward abiotic source vector. Both dCo and labile dCo were negatively correlated with dPO_4 ($R^2 = 0.77$ and $R^2 = 0.57$, respectively) and salinity ($R^2 = 0.81$ and $R^2 = 0.60$, respectively; Fig. 10a, b). The correlation to salinity is a strong indication that dCo from a coastal freshwater end-member is mixing with the pelagic marine dCo inventory. This relationship is consistent with studies that found that riverine dCo was linearly coupled with salinity in the Arctic Ocean (Bundy et al., 2020), the Scheldt River estuary (Zhang et al., 1990), the Atlantic continental shelf off the northeastern US (Noble et al., 2017; Saito and Moffett, 2002) and the Amazon River output into the Atlantic (Dulaquais et al., 2014a). To estimate the dCo concentration of the riverine end-member, the linear dCo : salinity relationship was extrapolated to a salinity of 0, resulting in a dCo concentration of 13.3 ± 0.4 nM and a labile dCo concentration of 1.69 ± 0.09 nM. This estimation assumes riverine dCo is mixing conservatively, which is unlikely to be true since other processes like scavenging and uptake are expected to occur at river mouths and coastal environments (de Carvalho et al., 2021). The negative correlation with dPO_4 is striking since almost all other upper-ocean samples are positively correlated with dPO_4 in the surface ocean due to nutrient uptake and remineralization (Sect. 2.5.1). Here, the negative dCo : dPO_4 correlation is likely due to mixing as well; an end-member source of dCo at the surface with low dPO_4 is mixing with an open-ocean end-member that contains relatively lower dCo and higher dPO_4.

Particulate Co, pMn, and the lithogenic tracers pAl and pTi were all elevated at depth, in stark contrast to the surface dCo maximum (Fig. 10d–f). The deep particulate metal maxima indicate the presence of a shelf-derived particulate flux that is distinct from the dCo riverine surface flux. In the open ocean, dCo and pCo typically mirror each other in the upper water column (Noble et al., 2017), with biological uptake of Co resulting in low surface dCo and high surface pCo. The opposite distribution was observed at Station 1, suggesting that dCo and pCo at this coastal station are more strongly influenced by external inputs rather than internal cycling, with higher surface dCo due to fresh riverine inputs and increasing pCo with depth due to sedimentary particle flux. Fe has been observed to behave similarly along the Alaskan coast, where terrestrial- and glacial-derived dFe is transported by rivers to the surface coastal ocean (Crusius et al., 2011; Schroth et al., 2014), while the continental margins are a source of redox-sensitive pFe to the subsurface Gulf of Alaska (Lam et al., 2006; Lam and Bishop, 2008).

The Alaskan coast thus acts as a source of both dCo and pCo to the coastal Gulf of Alaska, delivering a flux of Co to the Alaskan Stream, a westward-flowing coastal current along southwestern Alaska and the Aleutian Islands (Reed, 1984; Stabeno et al., 1995). We observed little evidence that elevated dCo distributions were advected off the shelf into the pelagic Gulf of Alaska; instead, much of the dCo inputs observed at Stations 1 and 2 appear isolated from the coastline via transport within the Alaskan Stream, and elevated surface dCo was not observed at Station 3 or beyond. This mechanism could work to isolate the HNLC region of the subpolar gyre from trace metal sources along the Alaskan coast and within the Alaskan Stream.

2.5.3 Hydrothermalism and the Loihi Seamount

Elevated dCo concentrations were observed at the Loihi Seamount (Station 18.6; 18.91° N, 155.26° W), with a dCo maximum of 158 pM and a labile dCo maximum of 87 pM at a depth of 1290 m. This maximum corresponded to a greater labile : total dCo ratio (0.55) compared to background Pacific Seawater (0.33; Fig. 7). An elevated dCo and labile dCo signature has previously been observed in the Hawaiian Kīlauea eruption of 2018 (Hawco et al., 2020), confirming previously observed dCo signals in the vicinity (Noble et al., 2008) and in the near-field plumes of the Juan de Fuca Ridge and the Atlantic Mid-Ocean Ridge (Metz and Trefry, 2000; Noble et al., 2017).

He isotopic samples were collected from the Ocean Data Facility CTD (ODF) cast and not from the GEOTRACES CTD carousel (GTC) that the dCo samples were collected from. At the Loihi Seamount, the two CTD casts were completed at the sample station with latitudinal and longitudinal precision to within ~ 15 m and deployment within 1.5 h of each other. However, the casts appeared to sample different sections and/or locations within the hydrothermal plume, as indicated by anomalies in the dFe and dMn data collected from both casts. The GTC cast displayed trace metal (dCo, dFe, dMn) concentrations increasing towards the deepest sample at 1290 m, while trace metals (dFe, dMn) and xs^3He from the ODF cast displayed a shallower maximum around 1200–1250 m (Fig. 11a–d). This offset is likely attributable to slight changes in the wire angle of the CTD casts and/or the natural heterogeneity of the hydrothermal plume. The Loihi Seamount sampling station was located near the center of Pele's Pit, a collapsed volcanic pit ~ 200 m deep located towards the southern summit of the seamount. Pele's Pit contains several active hydrothermal vent fields within a radius of ~ 100 m of the Loihi station, and the casts likely

sampled a combined and heterogeneous hydrothermal signature from multiple vents (Clague et al., 2019; Jenkins et al., 2020).

The offset between the GTC and ODF casts means that the dCo data and xs^3He data could not be directly compared to show a hydrothermally associated dCo source from the vent system. Instead, the dFe and dMn profiles collected from both casts were used to calculate a "Potential xs^3He" signal from the GTC cast; the dFe : xs^3He and dMn:xs^3He ratios from the ODF cast, measured via FIA, were calculated to be 7.6 ± 0.7 mol : µmol and 0.66 ± 0.06 mol : µmol, respectively (Fig. 11f). Samples from above 750 m were excluded in order to isolate the hydrothermal relationships from unassociated upper-ocean processes. Then, the GTC profile dFe and dMn values, measured via ICP-MS, were multiplied by the dissolved metal : xs^3He ratio to find the potential xs^3He profile for the GTC cast (Fig. 11e). This estimation assumed that the dFe : xs^3He and dMn : xs^3He ratios were consistent between all vents in Pele's Pit and thus are comparable between the two casts. Although this assumption is a reasonable one to make within Pele's Pit since all potential vent locations within the pit are sourced from the same sub-seafloor magma reservoir (Clague et al., 2019), and the trace metal vs. xs^3He correlations at this station are reasonably linear (Fig. 11f; Jenkins et al., 2020, Fig. 4 therein), there is evidence to suggest trace metal hydrothermal ratios are more diverse and heterogeneous within vent fluids than previously expected (Kleint et al., 2019). Thus, any interpretation of the potential xs^3He results should be considered within the limitations of this assumption of consistent trace metal : xs^3He ratios between the two casts.

Dissolved Co was positively correlated with the potential ^{3}He anomaly at the Loihi Seamount (Fig. 11g). The Fe-derived and Mn-derived GTC dCo : potential xs^3He ratios were found to be similar to each other, with values of 6 ± 1 mol : mmol ($R^2 = 0.78$) from the Fe-derived estimate and 7 ± 2 mol : mmol ($R^2 = 0.71$) from the Mn-derived estimate. This correlation shows that there is a local dCo source from the Loihi Seamount that is clearly associated with hydrothermal activity and that the local dCo source is exported above the sill height of Pele's Pit ($\sim$ 1100 m) to the surrounding water column. The ^{3}He flux from the Loihi Seamount vent was estimated to be 10.4 ± 4 mol yr^{-1} during the GP15 expedition (Jenkins et al., 2020), suggesting a local Co flux of $6 \pm 3 \times 10^4$ mol Co yr^{-1} using the Fe-derived estimate or $7 \pm 3 \times 10^4$ mol Co yr^{-1} using the Mn-derived estimate. This local dCo source is one of the few hydrothermal Co flux observations that show transport of dCo from an active vent without directly sampling hot vent

fluids. The estimated Co flux would represent 3 % to 4 % of the global hydrothermal Co flux, which has been estimated to be $\sim 2 \times 10^6$ mol Co yr^{-1} (Swanner et al., 2014). This percentage is surprisingly high for one hydrothermal vent system, but it should be noted that the ^{3}He flux at the Loihi Seamount was also estimated to be ~ 2 % of the global deep hydrothermal flux (Jenkins et al., 2020) and that the majority of the hydrothermal dCo source is expected to be quickly scavenged.

The Loihi Seamount was the source of an eastward-flowing distal plume of elevated xs^3He that stretched across an estimated 1×10^{12} m^2 area of the Pacific basin (Jenkins et al., 2020). Even though the GP15 transect did not capture the full extent of this hydrothermal plume, xs^3He, dMn and dFe were found to be elevated at nearby stations (18, 19, and the Puna Ridge); when interpolated to the core plume depth of 1100 m, dFe and dMn showed a positive correlation with xs^3He at distal stations (Jenkins et al., 2020, Fig. 6 therein). In contrast, dCo concentrations interpolated to 1100 m from distal stations (14–25) showed little correlation with xs^3He (R^2= 0.28), indicating that hydrothermally associated dCo was not likely to have been transported far within the plume. Although it is difficult to make assumptions about a plume that was not thoroughly sampled by the expedition track, this finding is consistent with the hypothesis that the majority of hydrothermally sourced dCo is scavenged before it is able to be transported far on a basin scale.

Hydrothermal vents are notoriously heterogenetic, and the variations in vent fluid metal compositions between individual vents, ocean basins and over time contribute to a relatively unconstrained dCo hydrothermal flux. Hydrothermalism has been considered a negligible source of Co to the marine system since labile dCo is particularly susceptible to scavenging. It has been estimated that hydrothermal activity contributes only ~ 2.4 % of the total marine Co budget (Swanner et al., 2014). A more recent study to further constrain the global marine Co cycle adjusted this hydrothermal estimate to be only ~ 0.3 % of the total marine Co flux when other dCo sources were added or increased (Hawco et al., 2018). Here, we observed local vertical transport of dCo to the surrounding water column, but not horizontal transport of dCo to the greater Pacific basin. Our findings corroborate the evidence that dCo from Pacific hydrothermal inputs is likely relatively local and minor.

2.5.4 Elevated dCo in oxygen minimum zones

The phenomenon of elevated dCo in O_2-depleted regions has been documented throughout the global oceans, including in the North Atlantic, South Atlantic and South Pacific tropical OMZs (Baars and Croot, 2014; Hawco et al., 2016; Noble et al., 2012, 2017). These hotspots are created when there is a source of dCo to the mesopelagic via remineralization of sinking phytoplankton biomass and/or sedimentary flux processes but a suppressed sink of dCo via scavenging onto Mn oxide particles (Hawco et al., 2016). Manganese oxides are slow to form in OMZs due to the low-O_2 conditions, and the reductive dissolution of advected manganese oxide particles is favored (Johnson et al., 1996; Sundby et al., 1986). Thus, dCo is able to build up in low-O_2 regions within the mesopelagic and basin interior, creating plumes of dCo associated with OMZs (Hawco et al., 2016). As the elevated plume of dCo is advected to more oxic regions of the ocean, the dCo becomes vulnerable to oxic scavenging processes and can be quickly lost. Remaining elevated dCo then mixes with the surrounding oxic waters and forms a mixing line, creating a noticeable dCo : O_2 correlation at OMZ depths. The dCo : O_2 correlation observed in and around OMZs represents both this accumulation of dCo in low-oxygen waters and its advection and mixing into surrounding oxic waters.

Within the ETNP (Fig. 12b; Stations 20–25) and ETSP (Fig. 12c; Stations 29–34), dCo and O_2 are negatively correlated (R^2= 0.66 and 0.72, respectively; Table 3). This linear relationship suggests that dCo is advected from the cores of the tropical OMZs, where dCo from the continental margin is concentrated within the low-O_2 waters of the eastern boundary currents and then is transported westward through the pelagic Pacific. The dCo : O_2 slopes within the ETNP and ETSP (-0.72 ± 0.07 and 0.73 ± 0.06 μM : mol kg^{-1}, respectively) are higher than those observed in the North and South Atlantic, as well as those observed in the ETSP along the GP16 expedition transect (Table 3) (Baars and Croot, 2014; Hawco et al., 2016; Noble et al., 2012, 2017). However, the dCo : O_2 values observed along the GP15 transect cannot necessarily be extrapolated to the entire ETSP or ETNP because the transect only captures the tail ends of the equatorial OMZs, where the O_2 depletion and subsequent dCo enrichment are not as strong as they are further east along the margin of the Americas (Hawco et al., 2016). The higher dCo : O_2 slopes observed in this study may be attributed to the expedition track sampling along the boundary of the OMZs, where O_2 concentrations reach below 2 μmol kg^{-1}, but dCo concentrations rapidly decrease in the

surrounding oxic ocean. The persistence of the OMZ systems >5000 km from its core along the coast demonstrates the strength and geochemical influence of the tropical Pacific OMZs.

In contrast, the North Pacific OMZ showed little to no correlation between dCo and O_2 (R^2= 0.16), which was unexpected given the robust relationship of dCo and O_2 in OMZs observed throughout the world. Instead, the North Pacific OMZ displayed relatively consistent dCo concentrations between 20–40 pM in samples between 40–150 µmol kg^{-1} O_2 and a range of higher dCo concentrations where O_2 fell below 40 µmol kg^{-1} (Fig. 12a). The more complex relationship between dCo and O_2 in the North Pacific compared to the ETNP and ETSP suggests that multiple processes are affecting this relatively stagnant OMZ; the horizontal processes of advection and mixing likely drive the concentrations of dCo between 40–150 µmol kg^{-1}, while the more vertical processes of remineralization and scavenging likely drive the higher range of dCo concentrations at lower O_2 concentrations. These vertical processes are particularly visible in shallower samples where the OMZ intersects with the mesopelagic dCo maximum and its internal cycling source of dCo via remineralization (Fig. A1).

The North Pacific OMZ also lacks a single point source of dCo and pCo within its low-O_2 waters compared to the coastal Co sources from the eastern boundary margins that are advected westward within the equatorial OMZs. In the ETNP and ETSP, coastal sedimentary dCo inputs are protected from scavenging, and margin pCo inputs are available for reduction and remobilization within the low O_2 concentrations of the OMZ as this elevated dCo signal is advected from the coast to the pelagic ocean (Hawco et al., 2016). The North Pacific, in contrast, has a number of diffuse dCo sources from the surrounding continental margin and advection from the Kuroshio Extension current (Zheng et al., 2019), but there is little evidence that coastal sources are significantly transported to the pelagic North Pacific (Sect. 2.5.2). Additionally, the OMZ does not extend to the continental margin, and so any advected dCo source will be more vulnerable to loss via remineralization and scavenging as it travels between its coastal origin and the North Pacific OMZ. This lack of an intersection between the OMZ and a continental margin and the wide range of processes affecting dCo concentrations in this region are likely key reasons why we do not observe a simple linear correlation between dCo and O_2 in the North Pacific.

2.5.5 Implications of deoxygenation on the Pacific dCo inventory

The extent and intensity of Pacific OMZs have been increasing over the past 50 years due to global ocean warming, and OMZs are predicted to continue to expand throughout the next century (Matear and Hirst, 2003; Stramma et al., 2008). The waters surrounding OMZs are predicted to have the greatest O_2 loss rate; over a 50-year period, Stramma et al. (2008) estimated an O_2 loss trend ($\Delta O_2/\Delta t$) of -0.13 ± 0.32 µmol kg^{-1} yr^{-1} in the core of the equatorial Pacific OMZs (5° N to 5° S, 105 to 115° W), compared to a more negative $\Delta O_2/\Delta t$ of -0.19 ± 0.20 µmol kg^{-1} yr^{-1} farther west on the outskirts of the OMZs (5° N to 5° S, 165 to 175° W). Note that the $\Delta O_2/\Delta t$ estimates have a high error, which makes the prediction of future effects due to deoxygenation uncertain. The GP15 expedition passed between the locations of these two equatorial Pacific estimates, and it is reasonable to assume that $\Delta O_2/\Delta t$ within the equatorial OMZs at the longitude of the GP15 transect (152° W) falls somewhere between the two estimates.

Deoxygenation is expected to affect redox-sensitive trace element cycles in and around expanded OMZs. Compared to other trace metal cycles, the Co cycle may be notably affected by decreasing O_2 concentrations because of its exceptionally small dissolved inventory; expanding OMZs are predicted to increase the dCo inventory and decrease the Co scavenging flux, representing a significant perturbation to the marine Co cycle. In the next 100 years, the dCo inventory is estimated to increase by ~ 10 % in the South Atlantic OMZ (Noble et al., 2012) and by ~ 20 % in the North Atlantic OMZ (Noble et al., 2017).

Using the O_2 loss trends from Stramma et al. (2008) and the $dCo : O_2$ linear trends calculated above, we estimated the increase to the dCo inventory within the 152° W cross-sectional transect of the ETNP and ETSP over the next 100 years (Table 4). Assuming the linear relationship observed between $dCo : O_2$ will be constant over the next century, the dCo inventories within the equatorial Pacific OMZs are estimated to increase at a rate ($\Delta dCo/\Delta t$) of 0.068 to 0.11 pM yr^{-1}. To predict the effect of this rate of dCo change in the Pacific, the upper-ocean (≥ 1000 m) dCo inventory was estimated over the stations within the ETNP and ETSP via trapezoidal integration of dCo station profiles over depth and latitude. The estimated dCo inventories were determined within upper-ocean boxes of the Pacific with a width of 1 m, a depth of 1000 m, and a length equal to the distance between the northernmost and southernmost stations affected by the OMZ along a longitude of 152° W (Table 4). The GP15 cross-section of the ETNP has a present dCo inventory

($I_{present}$) of 52 mol and is predicted to increase by 18 % to 26 % over the next 100 years, and the cross-section of the ETSP has an $I_{present}$ of 38 mol dCo and is predicted to increase by 25 % to 36 %.

This increase in the dCo inventory is similar to or higher than those predicted in the Atlantic, likely because the more pelagic regions of the OMZ captured by the GP15 transect are predicted to experience higher rates of deoxygenation than those closer to the coastal core of the equatorial OMZs. Similarly, the calculated $\Delta dCo/\Delta t$ of the ETSP on the GP15 expedition is greater than is predicted when we use the $dCo : O_2$ relationship from the GP16 expedition ($-0.34\ \mu M : mol\ kg^{-1}$), which estimates a $\Delta dCo/\Delta t$ of 0.044 to 0.064 $pM\ yr^{-1}$ using the same $\Delta O_2/\Delta t$ values. The GP16 expedition sampled closer to the South American coastline and the core of the ETSP than the GP15, and so a less dramatic dCo increase trend may be more representative of the near-shore equatorial OMZs. Estimating the open-ocean OMZ trend appears particularly important as the low dCo inventory of the more pelagic South Pacific is acutely sensitive to deoxygenation, and the ETSP expansion could increase the dCo inventory at 152° W by as much as 36 % over the next 100 years.

We recognize these are simple back-of-the-envelope calculations, but they nevertheless may be useful to inform the direction, if not the exact magnitude, of future changes in dCo inventory. The estimates presented here all have a high error associated with their calculation, which stems from the uncertainty in the original $\Delta O_2/\Delta t$ rates from Stramma et al. (2008). The rates of Pacific deoxygenation and ocean warming are relatively unconstrained, making it difficult to predict the effects of global climate change on the Pacific Co cycle. Furthermore, the assumption that the $dCo : O_2$ relationship will stay constant over the next 100 years of global change is not necessarily valid; excess dCo builds up in low-oxygen waters, and much of the observed $dCo : O_2$ correlation can be considered a mixing line between the OMZ source and oxic waters. The dCo source of the equatorial OMZs is primarily unscavenged dCo advected from continental shelf margins, which is driven by the surface area of the shelf sediments exposed to low-O_2 waters (Hawco et al., 2016). As the equatorial OMZs expand, the OMZ-shelf surface area will also expand, likely increasing the dCo source to the ETNP and ETSP. Thus, the $dCo : O_2$ slope presented here could become more negative over time if the OMZ (dCo source) end-member increased, but the oxic (low dCo) end-member stayed similar or constant, leading to greater increases in the dCo Pacific inventory than estimated here. We recommend future modeling,

experimental and observational work to better constrain the effect of deoxygenation on the oceanic Co inventories.

Although we did not observe a linear dCo : O_2 relationship in the North Pacific OMZ (see Sect. 2.5.4), Stramma et al. (2008) estimate that the North Pacific has had a higher rate of O_2 loss over the past 50 years than all other regions studied (−0.39 to −0.70 µmol kg^{-1} yr^{-1}). Strong North Pacific deoxygenation trends may drive relatively large increases in the dCo inventory over the next century as O_2 concentrations decrease, and the region becomes a source of dCo via Mn oxide reduction. Currently, the potential dCo trend in the North Pacific is difficult to estimate, but future deoxygenation could result in greater increases in the dCo inventory here than any other ocean basin. More research on the North Pacific OMZ and deoxygenation is required to determine the extent of future perturbation to the North Pacific Co cycle.

2.5.6 The presence of deep, stable dCo in the North Pacific

One of the most unexpected features in the GP15 dCo transect was the discovery of stable, ligand-bound dCo in the deep interior of the Pacific Ocean, particularly in the North Pacific basin. These higher dCo concentrations do not appear to be due to analytical error or blank correction error and instead appear to be robust evidence for the presence of complexed dCo below the mesopelagic that has been protected against scavenging. The discovery of elevated dCo in the North Pacific was unexpected since dCo has been shown to be scavenged along deep thermohaline circulation with deep-dCo concentrations decreasing with ^{14}C age (Hawco et al., 2018). When deep GP15 samples (>3000 m) were paired with their nearest radiocarbon age measurement from the GLODAP database and compared to data from previous GEOTRACES expeditions (Fig. 13a–b, Table 5), many GP15 samples from the North Pacific appeared to deviate from the expected trend of decreasing dCo with water mass age. Deep samples along this transect are estimated to have a conventional radiocarbon age of 918–1645 years, with the intermediate North Pacific containing the oldest waters (>1600 years). The low ventilation of these deep waters can also be seen in the average AOU value at each station below 1000 m depth (Fig. 13e), which displays a steady increase in oxygen utilization with latitude along the transect. Thus, intermediate and deep North Pacific waters were expected to have the lowest, most depleted concentrations of dCo as they are the some of the oldest, least ventilated ocean waters in the world and have had a relatively long time frame to scavenge their available dCo. While many of the deep GP15 samples,

particularly in the South and equatorial Pacific, fell along this predicted trend of slow but steady scavenging within aging water masses, many samples from the North Pacific were relatively high in dCo despite their age. This finding suggests a source of dCo to the deep North Pacific, superimposing a regional source process on top of a global circulation scavenging process.

Little excess pCo or pMn was observed in the North Pacific, suggesting that few Mn oxide particles were present in this region (Fig. 14). As noted in Sect. 2.5.2, pCo and dCo phases often exhibit mirror distributions; where there is high dCo, there tends to be low pCo and vice versa. This finding is consistent with a low rate of Mn and Co scavenging in the mesopelagic and deep North Pacific. Additionally, POC concentrations were elevated at depth in the North Pacific subpolar gyre, and the elevated ligand-bound dCo observed in this region partially overlaps with this deep POC signal, although the deep-dCo signal extends farther south than the deep POC signal. Therefore, the unexpected deep-dCo signal may be associated with regional POC export.

To better examine deep-ocean trends with latitude, the depth-weighted average deep-ocean (≥ 1500 m depth) concentrations of dCo and POC for each station were estimated using the equation

$$\text{Depth-weighted average} = \frac{\sum x_i w_i}{\sum w_i} \qquad (2)$$

$$w_i = \frac{|z_i - z_{i-1}| + |z_i - z_{i+1}|}{2} \qquad (3)$$

where x_i represents the concentration value of each sample, z_i represents the depth of each sample, and w_i represents the weight assigned to each point as defined by the sample's distance from adjacent points in the station profile. The deep-ocean averages show consistently elevated inventories of dCo in the North Pacific (Fig. 13c). In the same region, there was dramatically elevated POC inventories at some stations. Average deep concentrations of SPT POC spiked to 0.21 µM at Station 10 (42° N, 152° W), while the average deep concentrations of LPT POC had a similar maximum of 0.018 µM a little farther north at Station 8 (47° N, 152° W; Fig. 13d).

One compelling explanation for the complexed deep-dCo presence is the wide North Pacific OMZ. Unlike the shallower equatorial OMZs of the Atlantic and Pacific, this low-oxygen zone stretches across the majority of the North Pacific mesopelagic. Although the dCo : O_2 relationship is not as strong here as the equatorial OMZs, as described above, the low

oxygen would still suppress the rate of dCo scavenging in the mesopelagic, where the majority of Mn oxide scavenging typically occurs (Sect. 2.5.4). Additionally, this region contains the transition zone chlorophyll front (TZCF), a stark transition in surface chlorophyll concentrations between the low-macronutrient subtropical gyre to the south and the iron-limited subpolar gyre to the north (Polovina et al., 2001, 2017). The TZCF seasonally migrates between 30 and 45° N and is characterized by elevated biological activity, a net CO_2 uptake flux and a distinct CO_2 sink (Juranek et al., 2012). On the GP15 expedition, prominent upper-ocean and mesopelagic POC export (2000 m export depth) was also observed via ^{230}Th analysis in this region (Kenyon et al., 2022). High particulate export coupled with suppressed Mn oxide formation in the mesopelagic would carry biogenic particles and ligand-bound dCo associated with biomass, vitamin B_{12} and/or metalloproteins into the deep ocean, where the biogenic pCo is further remineralized by heterotrophs, releasing complexed dCo. The larger eukaryotes like diatoms and coccolithophores that are supported under nutrient-replete conditions in the TZCF (Juranek et al., 2012) are also prone to faster sinking velocities (Clegg and Whitfield, 1990), which would carry this regions' biogenic particles deeper into the water column.

The remineralization of vitamin B_{12} and its degradation products via eukaryotic cells could play an important role in this deep Co complexation process. Although eukaryotes cannot produce vitamin B_{12}, the organisms often have high vitamin B_{12} quotas (Bertrand et al., 2013). Eukaryotic cell remineralization in the mesopelagic could be supplying functionally inert Co(III) ligands in the form of these B_{12} molecules to the mesopelagic and deep ocean. This process would protect the biogenic ligand-bound dCo from further scavenging as complexed dCo is less likely to be scavenged (Saito et al., 2005), and Mn oxide precipitation rates in the deep ocean are relatively slow (Hawco et al., 2018; Johnson et al., 1996; Sunda and Huntsman, 1988). More research is needed on this deep, stable dCo fraction in the Pacific to confirm this proposed mechanism, but we believe the unique OMZ and particle export dynamics in this region contribute to its existence.

2.5.7 Comparison to a global biogeochemical Co model

The global biogeochemical model was able to well replicate the major cycling features of dCo in the Pacific Ocean in general, including the scavenging-induced “curl” in the dCo vs. dPO_4 relationship and the negative correlation between dCo and O_2 throughout the transect (Fig. 15). It was also able to capture the major remineralization, scavenging, surface uptake and

coastal source features observed along the GP15 transect (Fig. 16). The model was successful at replicating the major dCo surface features across the various Pacific oceanographic provinces, appropriately deepening the nutricline and predicting decreased dCo concentrations in the north and south subtropical gyres. The main differences between the observed and model dCo values can be attributed to both (1) differences in the O_2 and dPO_4 distributions that drive dCo distribution calculations and (2) the underestimation of some dCo flux intensities in the model.

The model was successful at capturing the broad, basin-wide trends across the Pacific but did not always capture more local processes. It did not predict that the ETNP and ETSP OMZs would be present as far west as 152° W, far from the continental coastlines, and so did not recreate the low-O_2 or elevated-dCo features observed in the GP15 transect. The model also never reached the lowest observed O_2 concentrations within the North Pacific OMZ; the lowest O_2 concentration it predicted in the North Pacific basin was 40 µM, while the lowest value observed within the North Pacific OMZ on the GP15 transect was 8 µM. Therefore, the biogeochemical model was able to replicate the $dCo : O_2$ correlation driven by suppressed scavenging in OMZs across the transect but did not capture the more intense O_2 minima observed and thus underestimates dCo concentrations within the ETNP, ETSP and North Pacific OMZs. Consistent with underestimating the extent of oxygen depletion, the remineralization flux supplying dPO_4 to subsurface waters was lower in the model, shown by the positive values of observed dPO_4 − model dPO_4, particularly in the mesopelagic ocean. This underestimated remineralization flux also affected the modeled dCo supply to the mesopelagic via remineralization, causing a similar underestimation of dCo values in the model.

Our data suggest that the dCo cycle is more robust and dynamic than the model predicts, with observations of higher dCo concentrations from sources and lower dCo concentrations from sinks than are predicted by the model. The deep ocean, for example, appears to be a larger sink of dCo via scavenging than is predicted in the model. Below 2000 m depth, the average observed dCo concentration was 27 ± 11 pM, but the average model concentration was consistently ~ 45 pM. This offset was driven by a parameterization of consistent ligand-bound dCo concentrations (Tagliabue et al., 2018), a pool of dCo that is known to be relatively inert. In the observed transect, we do not see these levels of ligand-bound dCo in the deep ocean, with the exception of the North Pacific as described above, which suggests that the complexed dCo pool in the Pacific interior is either smaller or not as inert as the model assumed. Additionally, the source of dCo from the

Alaskan coast was observed to result in greater regional dCo values, implying a larger dCo coastal source than the model predicted. This is not too surprising as coastal fluxes are often varying and unpredictable in time and location, and a global model is not expected to replicate fine-scale regional variations in the Co cycle. However, the model included a coastal dCo source primarily from intermediate waters along the continental shelf where sediment resuspension is likely to occur, while we observed a surface dCo source primarily from coastal freshwater inputs. It is possible that the model underestimated the coastal flux of dCo from freshwater sources (see also Bundy et al., 2020).

Recognizing inconsistencies between expected model dCo distributions and observed transect dCo distributions is an effective way to test and improve upon the biogeochemical model's parameters. The parameterization of ligand-bound cobalt in the deep Pacific, for example, could be improved by decreasing the assumed concentration of inert, organically bound dCo in deep water masses. It should be noted that the biogeochemical model was optimized for the global ocean Co cycle and not specifically for the Pacific Ocean, which likely contextualizes much of the offset between the observed and model transects, particularly for inconsistencies within the O_2 and PO_4 distributions. The model also did not incorporate a hydrothermal vent source to the Pacific, which we concur is an appropriate omission on a basin scale. Future iterations of the Co biogeochemical model will consider the successes and inconsistencies presented here and continue to improve upon our conceptualization and parameterization of the marine cobalt cycle.

2.6 Conclusions

The GP15 transect highlighted major differences in the Co biogeochemical cycle between the Pacific and Atlantic oceans. The processes of phytoplankton uptake, remineralization and scavenging drove much of the dCo distribution patterns in the Pacific. Biological uptake of dCo generated a dCo : dPO_4 stoichiometry of 82 ± 3 (μmol : mol) in the upper ocean. The Pacific Co cycle was heavily influenced by the poorly ventilated PDW that forms a wide OMZ across the North Pacific under a high-particle-export region. This aged water mass displayed a weaker dCo : O_2 correlation than equatorial OMZs in the Atlantic and Pacific (Hawco et al., 2016; Noble et al., 2017). However, the North Pacific OMZ still appeared to suppress dCo scavenging such that elevated ligand-bound dCo was observed well below the mesopelagic. The deep, bound Co fraction was protected from scavenging outside of the mesopelagic, where most Mn-oxidizing

bacteria are active. This finding represented a deviation from the expected thermohaline deep Co trend, which predicted that the North Pacific would exhibit the lowest concentration of deep dCo globally due to slow but steady Co scavenging over deep-ocean circulation (Hawco et al., 2018). Compared to a global ocean biogeochemical model, the observed dCo cycle (1) was more varied in distribution and (2) appeared more extreme in source and sink fluxes, indicating that the Pacific Co cycle is more dynamic than predicted by the model.

This study improves our understanding of dCo dynamics in the Pacific water column, but it should be mentioned that many are interested in Pacific Co biogeochemical cycling as it relates to Co scavenging and mineralization along the seafloor and the emerging deep-sea mining industry. When dCo is scavenged and removed from the water column in the form of pCo incorporated into Mn oxide particles, it sinks and forms vast regions of ferro-manganese oxide crusts and metal-rich nodules that accrete slowly along the seafloor (Aplin and Cronan, 1985). These nodules are formed from Mn oxide deposition over millennia and are rich in Co, Ni, Cd, Zn and rare earth elements (REEs) (Cameron et al., 1981; Hein et al., 2013). Such deposits are of interest to many because of the potential for deep-sea mining in the region, especially in the Clarion–Clipperton Zone of the central North Pacific basin. Here, international mining operations to extract Fe–Mn nodules along the seafloor could begin within the decade. The value of Co ore, which is currently only mined terrestrially, has been increasing in demand over the past 2 decades due to the metal's use in personal electronic devices and sustainable energy solutions like electric vehicle batteries, and many believe that mining the vast, concentrated deposits of Co on the Pacific seafloor could alleviate this demand (Hein et al., 2013). However, deep-sea mining and the potential heavy-metal rich sediment plumes it could create may have serious ramifications to the relatively fragile and unexplored benthic ecosystem in the region (Drazen et al., 2020; Fuchida et al., 2017; Sharma, 2011). Although the technology and facilities required to mine the deep sea have proven to be both complicated and expensive (Cameron et al., 1981), the potential new source of Co ore could, in theory, help support widespread adoption of electric vehicle fleets (Hein et al., 2013).

This work helps to establish a baseline for dCo distributions and features in the Pacific Ocean in light of future ocean warming and anthropogenic change expected to impact this region. Relative to other trace metals, the marine dCo inventory is among the smallest and is likely highly susceptible to regional mining and deoxygenation as anthropogenic sources of Co to the

mesopelagic and deep ocean. The full scope of the impacts that expanding oxygen minima could have on metal biogeochemical cycles is still an open question, and more sophisticated modeling of the effects of deoxygenation on redox-sensitive trace elements is required.

Data and Code availability

The GP15 expedition dCo dataset can be accessed online from the Biological and Chemical Oceanography Data Management Office (BCO-DMO) websites:
https://www.bco-dmo.org/dataset/818383 (Saito, 2021) (Leg 1),
https://www.bco-dmo.org/dataset/818610 (Saito, 2020) (Leg 2).
The nutrient and hydrographic dataset can be found at:
https://www.bco-dmo.org/dataset/777951 (Casciotti et al., 2021a) (Leg 1),
https://www.bco-dmo.org/dataset/824867 (Casciotti et al., 2021b) (Leg 2).
Relevant Python code used for this study can be found at:
https://github.com/rebecca-chmiel/GP15 (Chmiel, 2022).

Acknowledgments

The authors thank the crew and science party of the R/V *Roger Revelle* on the GP15 expedition, including David Murline and chief scientists Karen Casciotti and Grey Cutter. We also thank Laramie Jensen, Brent Summers, Vinicius Amaral, Yang Xiang and Janelle Steffen for at-sea sample collection; Sophie Rojas and Nicholas Carracino for POC sample processing; the Ocean Data Facility at Scripps Institution of Oceanography for nutrient sample analysis; Natalie Cohen for assistance in handling and transporting samples; Matthew Charette, Stephanie Dutkiewicz and Nicholas Hawco for science and writing insights; and Deepa Rao and Jaclyn Saunders for Python coding assistance.

References

Aplin, A. C. and Cronan, D. S.: Ferromanganese oxide deposits from the Central Pacific Ocean, I. Encrustations from the Line Islands Archipelago, Geochim. Cosmochim. Ac., 49, 427–436, https://doi.org/10.1016/0016-7037(85)90034-1, 1985.

Baars, O. and Croot, P. L.: Dissolved cobalt speciation and reactivity in the eastern tropical North Atlantic, Mar. Chem., 173, 310–319, https://doi.org/10.1016/j.marchem.2014.10.006, 2014.

Bertrand, E. M., Saito, M. A., Rose, J. M., Riesselman, C. R., Lohan, M. C., Noble, A. E., Lee, P. A., and DiTullio, G. R.: Vitamin B_{12} and iron colimitation of phytoplankton growth in the Ross Sea, Limnol. Oceanogr., 52, 1079–1093, https://doi.org/10.4319/lo.2007.52.3.1079, 2007.

Bertrand, E. M., Moran, D. M., McIlvin, M. R., Hoffman, J. M., Allen, A. E., and Saito, M. A.: Methionine synthase interreplacement in diatom cultures and communities: Implications for the persistence of B_{12} use by eukaryotic phytoplankton, Limnol. Oceanogr., 58, 1431–1450, https://doi.org/10.4319/lo.2013.58.4.1431, 2013.

Bishop, J. K. B. and Wood, T. J.: Year-round observations of carbon biomass and flux variability in the Southern Ocean, Global Biogeochem. Cy., 23, GB2019, https://doi.org/10.1029/2008GB003206, 2009.

Bonnet, S., Guieu, C., Bruyant, F., Prášil, O., Van Wambeke, F., Raimbault, P., Moutin, T., Grob, C., Gorbunov, M. Y., Zehr, J. P., Masquelier, S. M., Garczarek, L., and Claustre, H.: Nutrient limitation of primary productivity in the Southeast Pacific (BIOSOPE cruise), Biogeosciences, 5, 215–225, https://doi.org/10.5194/bg-5-215-2008, 2008.

Bown, J., Boye, M., Baker, A., Duvieilbourg, E., Lacan, F., Le Moigne, F., Planchon, F., Speich, S., and Nelson, D. M.: The biogeochemical cycle of dissolved cobalt in the Atlantic and the Southern Ocean south off the coast of South Africa, Mar. Chem., 126, 193–206, https://doi.org/10.1016/j.marchem.2011.03.008, 2011.

Bown, J., Boye, M., and Nelson, D. M.: New insights on the role of organic speciation in the biogeochemical cycle of dissolved cobalt in the southeastern Atlantic and the Southern Ocean, Biogeosciences, 9, 2719–2736, https://doi.org/10.5194/bg-9-2719-2012, 2012.

Boyd, P. W., Law, C. S., Wong, C. S., Nojiri, Y., Tsunda, A., Levasseur, M., Takeda, S., Rivkin, R., Harrison, P. J., Strzepek, R., Gower, J., McKay, R. M., Abraham, E., Arychuk, M., Barwell-Clarke, J., Crawford, W., Crawford, D., Hale, M., Harada, K., Johnson, K., Kiyosawa, H., Kudo, I., Marchetti, A., Miller, W., Needoba, J., Nishioka, J., Ogawa, H., Page, J., Robert, M., Saito, H., Sastri, A., Sherry, N., Soutar, T., Sutherland, N., Taira, Y., Whitney, F., Wong, S.-K. E., and Yoshimura, T.: The decline and fate of an iron-induced subarctic phytoplankton bloom, Lett. Nat., 428, 549–553, https://doi.org/10.1029/2001jb001129, 2004.

Browning, T. J., Achterberg, E. P., Rapp, I., Engel, A., Bertrand, E. M., Tagliabue, A., and Moore, C. M.: Nutrient co-limitation at the boundary of an oceanic gyre, Nature, 551, 242–246, https://doi.org/10.1038/nature24063, 2017.

Bruland, K. W. and Lohan, M. C.: Controls of trace metals in seawater, in: Treatise on Geochemistry, Vol. 6, edited by: Elderfield, H., Holland H. D., and Turekian, K. K., Elsevier, 23–47, https://doi.org/10.1016/B0-08-043751-6/06105-3, 2003.

Bundy, R. M., Tagliabue, A., Hawco, N. J., Morton, P. L., Twining, B. S., Hatta, M., Noble, A. E., Cape, M. R., John, S. G., Cullen, J. T., and Saito, M. A.: Elevated sources of cobalt in the Arctic Ocean, Biogeosciences, 17, 4745–4767, https://doi.org/10.5194/bg-17-4745-2020, 2020.

Cameron, H., Georghiou, L., Perry, J. G., and Wiley, P.: The economic feasibility of deep-sea mining, Eng. Costs Prod. Econ., 5, 279–287, https://doi.org/10.1016/0167-188X(81)90019-7, 1981.

Casciotti, K. L., Cutter, G. A., and Lam, P. J.: Bottle file from Leg 1 (Seattle, WA to Hilo, HI) of the US GEOTRACES Pacific Meridional Transect (PMT) cruise (GP15, RR1814) on R/V Roger Revelle from September to October 2018, Biological and Chemical Oceanography Data Management Office (BCO-DMO), (Version 6) Version Date 2021-05-05 [data set], https://doi.org/10.26008/1912/bco-dmo.777951.6, 2021a.

Casciotti, K. L., Cutter, G. A., and Lam, P. J.: Bottle file from Leg 2 (Hilo, HI to Papeete, French Polynesia) of the US GEOTRACES Pacific Meridional Transect (PMT) cruise (GP15, RR1815) on R/V Roger Revelle from October to November 2018, Biological and Chemical Oceanography Data Management Office (BCO-DMO), (Version 5) Version Date 2021-05-05 [data set], https://doi.org/10.26008/1912/bco-dmo.824867.5, 2021b.

Chmiel, R.: “GP15”, Version Date 2022-03-15, GitHub [code], https://github.com/rebecca-chmiel/GP15, last access: 3 May 2022.
Clague, D. A., Paduan, J. B., Caress, D. W., Moyer, C. L., Glazer, B. T., and Yoerger, D. R.: Structure of Lo`ihi Seamount, Hawai'i and lava flow morphology from high-resolution mapping, Front. Earth Sci., 7, 58, https://doi.org/10.3389/feart.2019.00058, 2019.
Clegg, S. L. and Whitfield, M.: A generalized model for the scavenging of trace metals in the open ocean – I. Particle cycling, Deep-Sea Res., 37, 809–832, https://doi.org/10.1016/0198-0149(90)90008-J, 1990.
Coale, K. H., Johnson, K. S., Fitzwater, S. E., Gordon, R. M., Tanner, S., Chavez, F. P., Ferioli, L., Sakamoto, C., Rogers, P., Millero, F., Steinberg, Pa., Nightingale, P., Cooper, D., Cochlan, W. P., Landry, M. R., Constantinou, J., Rollwagen, G., Trasvina, A., and Kudela, R.: A massive phytoplankton bloom induced by an ecosystem-scale iron fertilization experiment in the equatorial Pacific Ocean, Nature, 383, 495–501, https://doi.org/10.1038/383495a0, 1996.
Cox, A. D. and Saito, M. A.: Proteomic responses of oceanic *Synechococcus* WH8102 to phosphate and zinc scarcity and cadmium additions, Front. Microbiol., 4, 387, https://doi.org/10.3389/fmicb.2013.00387, 2013.
Crusius, J., Schroth, A. W., Gassó, S., Moy, C. M., Levy, R. C., and Gatica, M.: Glacial flour dust storms in the Gulf of Alaska: Hydrologic and meteorological controls and their importance as a source of bioavailable iron, Geophys. Res. Lett., 38, L06602, https://doi.org/10.1029/2010GL046573, 2011.
Cutter, G. A. and Bruland, K. W.: Rapid and noncontaminating sampling system for trace elements in global ocean surveys, Limnol. Oceanogr. Method., 10, 425–436, https://doi.org/10.4319/lom.2012.10.425, 2012.
Czeschel, R., Stramma, L., Schwarzkopf, F. U., Giese, B. S., Funk, A., and Karstensen, J.: Middepth circulation of the eastern tropical South Pacific and its link to the oxygen minimum zone, J. Geophys. Res., 116, C01015, https://doi.org/10.1029/2010JC006565, 2011.
de Carvalho, L. M., Hollister, A. P., Trindade, C., Gledhill, M., and Koschinsky, A.: Distribution and size fractionation of nickel and cobalt species along the Amazon estuary and mixing plume, Mar. Chem., 236, 104019, https://doi.org/10.1016/j.marchem.2021.104019, 2021.
de Lavergne, C., Madec, G., Roquet, F., Holmes, R. M., and McDougall, T. J.: Abyssal ocean overturning shaped by seafloor distribution, Nature, 551, 181–186, https://doi.org/10.1038/nature24472, 2017.
Drazen, J. C., Smith, C. R., Gjerde, K. M., Haddock, S. H. D., Carter, G. S., Choy, C. A., Clark, M. R., Dutrieux, P., Goetze, E., Hauton, C., Hatta, M., Koslow, J. A., Leitner, A. B., Pacini, A., Perelman, J. N., Peacock, T., Sutton, T. T., Watling, L., and Yamamoto, H.: Midwater ecosystems must be considered when evaluating environmental risks of deep-sea mining, P. Natl. Acad. Sci. USA, 117, 17455–17460, https://doi.org/10.1073/pnas.2011914117, 2020.
Dulaquais, G., Boye, M., Middag, R., Owens, S., Puigcorbe, V., Buesseler, K., Masqué, P., de Baar, H. J. W., and Carton, X.: Contrasting biogeochemical cycles of cobalt in the surface western Atlantic Ocean, Global Biogeochem. Cy., 28, 1387–1412, https://doi.org/10.1002/2014GB004903, 2014a.

Dulaquais, G., Boye, M., Rijkenberg, M. J. A., and Carton, X.: Physical and remineralization processes govern the cobalt distribution in the deep western Atlantic Ocean, Biogeosciences, 11, 1561–1580, https://doi.org/10.5194/bg-11-1561-2014, 2014b.

Dulaquais, G., Planquette, H., L'Helguen, S., Rijkenberg, M. J. A., and Boye, M.: The biogeochemistry of cobalt in the Mediterranean Sea, Global Biogeochem. Cy., 31, 377–399, https://doi.org/10.1002/2016GB005478, 2017.

Fuchida, S., Yokoyama, A., Fukuchi, R., Ishibashi, J. I., Kawagucci, S., Kawachi, M., and Koshikawa, H.: Leaching of metals and metalloids from hydrothermal ore particulates and their effects on marine phytoplankton, ACS Omega, 2, 3175–3182, https://doi.org/10.1021/acsomega.7b00081, 2017.

Gale, A., Dalton, C. A., Langmuir, C. H., Su, Y., and Schilling, J.-G.: The mean composition of ocean ridge basalts, Geochem. Geophy. Geosy., 14, 489–518, https://doi.org/10.1029/2012GC004334, 2013.

Glover, D., Jenkins, W., and Doney, S.: Modeling Methods for Marine Science, Cambridge University Press, New York, ISBN 978-0521867832, 2011.

Gobler, C. J., Norman, C., Panzeca, C., Taylor, G. T., and Sañudo-Wilhelmy, S. A.: Effect of B-vitamins (B_1, B_{12}) and inorganic nutrients on algal bloom dynamics in a coastal ecosystem, Aquat. Microb. Ecol., 49, 181–194, https://doi.org/10.3354/ame01132, 2007.

Hawco, N. J., Ohnemus, D. C., Resing, J. A., Twining, B. S., and Saito, M. A.: A dissolved cobalt plume in the oxygen minimum zone of the eastern tropical South Pacific, Biogeosciences, 13, 5697–5717, https://doi.org/10.5194/bg-13-5697-2016, 2016.

Hawco, N. J., Lam, P. J., Lee, J. M., Ohnemus, D. C., Noble, A. E., Wyatt, N. J., Lohan, M. C., and Saito, M. A.: Cobalt scavenging in the mesopelagic ocean and its influence on global mass balance: Synthesizing water column and sedimentary fluxes, Mar. Chem., 201, 151–166, https://doi.org/10.1016/j.marchem.2017.09.001, 2018.

Hawco, N. J., Yang, S., Foreman, R. K., Funkey, C. P., Dugenne, M., White, A. E., Wilson, S. T., Kelly, R. L., Bian, X., Huang, K., Karl, D. M., and John, S. G.: Metal isotope signatures from lava-seawater interaction during the 2018 eruption of Kīlauea, Geochim. Cosmochim. Ac., 282, 340–356, https://doi.org/10.1016/j.gca.2020.05.005, 2020.

Hein, J. R., Mizell, K., Koschinsky, A., and Conrad, T. A.: Deep-ocean mineral deposits as a source of critical metals for high- and green-technology applications: Comparison with land-based resources, Ore Geol. Rev., 51, 1–14, https://doi.org/10.1016/j.oregeorev.2012.12.001, 2013.

Hémond, C., Devey, C. W., and Chauvel, C.: Source compositions and melting processes in the Society and Austral plumes (South Pacific Ocean): Element and isotope (Sr, Nd, Pb, Th) geochemistry, Chem. Geol., 115, 7–45, https://doi.org/10.1016/0009-2541(94)90143-0, 1994.

Jenkins, W. J., Lott, D. E. III, and Cahill, K. L.: A determination of atmospheric helium, neon, argon, krypton, and xenon solubility concentrations in water and seawater, Mar. Chem., 211, 94–107, https://doi.org/10.1016/j.marchem.2019.03.007, 2019.

Jenkins, W. J., Hatta, M., Fitzsimmons, J. N., Schlitzer, R., Lanning, N. T., Shiller, A., Buckley, N. R., German, C. R., Lott, D. E. III, Weiss, G., Whitmore, L., Casciotti, K., Lam, P. J., Cutter, G. A., and Cahill, K. L.: An intermediate-depth source of hydrothermal ^{3}He and dissolved iron in the North Pacific, Earth Planet. Sci. Lett., 539, 116223, https://doi.org/10.1016/j.epsl.2020.116223, 2020.

Johnson, K. S., Coale, K. H., Berelson, W. M., and Gordon, R. M.: On the formation of the manganese maximum in the oxygen minimum zone, Geochim. Cosmochim. Ac., 60, 1291–1299, https://doi.org/10.1016/0016-7037(96)00005-1, 1996.

Juranek, L. W., Quay, P. D., Feely, R. A., Lockwood, D., Karl, D. M., and Church, M. J.: Biological production in the NE Pacific and its influence on air-sea CO_2 flux: Evidence from dissolved oxygen isotopes and O_2 Ar, J. Geophys. Res.-Ocean., 117, C05022, https://doi.org/10.1029/2011JC007450, 2012.

Karstensen, J., Stramma, L., and Visbeck, M.: Oxygen minimum zones in the eastern tropical Atlantic and Pacific oceans, Prog. Oceanogr., 77, 331–350, https://doi.org/10.1016/j.pocean.2007.05.009, 2008.

Kellogg, R. M., McIlvin, M. R., Vedamati, J., Twining, B. S., Moffett, J. W., Marchetti, A., Moran, D. M., and Saito, M. A.: Efficient zinc/cobalt interreplacement in northeast Pacific diatoms and relationship to high surface dissolved Co : Zn ratios, Limnol. Oceanogr., 65, 2557–2582, https://doi.org/10.1002/lno.11471, 2020.

Kenyon, J. A., Buesseler, K. O., Davidson, P., Pike, S. M., and Lam P. J.: ^{234}Th as a tracer of particulate export and remineralization along the GEOTRACES Pacific Meridional Transect, in preparation, 2022.

Key, R. M., Olsen, A., van Heuven, S., Lauvset, S. K., Velo, A., Lin, X., Schirnick, C., Kozyr, A., Tanhua, T., Hoppema, M., Jutterström, S., Steinfeldt, R., Jeansson, E., Ishii, M., Perez, F. F., and Suzuki, T.: Global Ocean Data Analysis Project, Version 2 (GLODAPv2), ORNL/CDIAC-162, ND-P093, Oak Ridge National Laboratory, U.S. Department of Energy or the Carbon Dioxide Information Analysis Center, Oak Ridge, Tennessee, https://doi.org/10.3334/CDIAC/OTG.NDP093_GLODAPv2, 2015.

Kleint, C., Bach, W., Diehl, A., Fröhberg, N., Garbe-Schönberg, D., Hartmann, J. F., de Ronde, C. E. J., Sander, S. G., Strauss, H., Stucker, V. K., Thal, J., Zitoun, R., and Koschinsky, A.: Geochemical characterization of highly diverse hydrothermal fluids from volcanic vent systems of the Kermadec intraoceanic arc, Chem. Geol., 528, 119289, https://doi.org/10.1016/j.chemgeo.2019.119289.

Lam, P. J. and Bishop, J. K. B.: The continental margin is a key source of iron to the HNLC North Pacific Ocean, Geophys. Reseach Lett., 35, L07608, https://doi.org/10.1029/2008GL033294, 2008.

Lam, P. J., Bishop, J. K. B., Henning, C. C., Marcus, M. A., Waychunas, G. A., and Fung, I. Y.: Wintertime phytoplankton bloom in the subarctic Pacific supported by continental margin iron, Global Biogeochem. Cy., 20, GB1006, https://doi.org/10.1029/2005GB002557, 2006.

Matear, R. J. and Hirst, A. C.: Long-term changes in dissolved oxygen concentrations in the ocean caused by protracted global warming, Global Biogeochem. Cy., 17, 1125, https://doi.org/10.1029/2002gb001997, 2003.

Matsumoto, K.: Radiocarbon-based circulation age of the world oceans, J. Geophys. Res.-Ocean., 112, C09004, https://doi.org/10.1029/2007JC004095, 2007.

McDougall, T. J. and Barker, P. M.: Getting started with TEOS-10 and the Gibbs Seawater (GSW) Oceanographic Toolbox, SCOR/IAPSO WG127, ISBN 978-0-646-55621-5, 2011.

Metz, S. and Trefry, J. H.: Chemical and mineralogical influences on concentrations of trace metals in hydrothermal fluids, Geochim. Cosmochim. Ac., 64, 2267–2279, https://doi.org/10.1016/S0016-7037(00)00354-9, 2000.

Moffett, J. W. and Ho, J.: Oxidation of cobalt and manganese in seawater via a common microbially catalyzed pathway, Geochim. Cosmochim. Ac., 60, 3415–3424, https://doi.org/10.1016/0016-7037(96)00176-7, 1996.

Moore, C. M., Mills, M. M., Arrigo, K. R., Berman-Frank, I., Bopp, L., Boyd, P. W., Galbraith, E. D., Geider, R. J., Guieu, C., Jaccard, S. L., Jickells, T. D., La Roche, J., Lenton, T. M., Mahowald, N. M., Marañón, E., Marinov, I., Moore, J. K., Nakatsuka, T., Oschlies, A., Saito, M. A., Thingstad, T. F., Tsuda, A., and Ulloa, O.: Processes and patterns of oceanic nutrient limitation, Nat. Geosci., 6, 701–710, https://doi.org/10.1038/ngeo1765, 2013.

Nishioka, J., Obata, H., Ogawa, H., Ono, K., Yamashita, Y., Lee, K., Takeda, S., and Yasuda, I.: Subpolar marginal seas fuel the North Pacific through the intermediate water at the termination of the global ocean circulation, P. Natl. Acad. Sci. USA, 117, 12665–12673, https://doi.org/10.1073/pnas.2000658117, 2020.

Noble, A. E., Saito, M. A., Maiti, K., and Benitez-Nelson, C. R.: Cobalt, manganese, and iron near the Hawaiian Islands: A potential concentrating mechanism for cobalt within a cyclonic eddy and implications for the hybrid-type trace metals, Deep-Sea Res. Pt. II, 55, 1473–1490, https://doi.org/10.1016/j.dsr2.2008.02.010, 2008.

Noble, A. E., Lamborg, C. H., Ohnemus, D. C., Lam, P. J., Goepfert, T. J., Measures, C. I., Frame, C. H., Casciotti, K. L., DiTullio, G. R., Jennings, J., and Saito, M. A.: Basin-scale inputs of cobalt, iron, and manganese from the Benguela-Angola front to the South Atlantic Ocean, Limnol. Oceanogr., 57, 989–1010, https://doi.org/10.4319/lo.2012.57.4.0989, 2012.

Noble, A. E., Moran, D. M., Allen, A. E., and Saito, M. A.: Dissolved and particulate trace metal micronutrients under the McMurdo Sound seasonal sea ice: basal sea ice communities as a capacitor for iron, Front. Chem., 1, 25, https://doi.org/10.3389/fchem.2013.00025, 2013.

Noble, A. E., Ohnemus, D. C., Hawco, N. J., Lam, P. J., and Saito, M. A.: Coastal sources, sinks and strong organic complexation of dissolved cobalt within the US North Atlantic GEOTRACES transect GA03, Biogeosciences, 14, 2715–2739, https://doi.org/10.5194/bg-14-2715-2017, 2017.

Ohnemus, D. C., Rauschenberg, S., Cutter, G. A., Fitzsimmons, J. N., and Sherrell, R. M.: Elevated trace metal content of prokaryotic communities associated with marine oxygen deficient zones, Limnol. Oceanogr., 62, 3–25, https://doi.org/10.1002/lno.10363, 2017.

Oldham, V. E., Chmiel, R., Hansel, C. M., DiTullio, G. R., Rao, D., and Saito, M.: Inhibited manganese oxide formation hinders cobalt scavenging in the Ross Sea, Global Biogeochem. Cy., 35, e2020GB006706, https://doi.org/10.1029/2020GB006706, 2021.

Olsen, A., Key, R. M., van Heuven, S., Lauvset, S. K., Velo, A., Lin, X., Schirnick, C., Kozyr, A., Tanhua, T., Hoppema, M., Jutterström, S., Steinfeldt, R., Jeansson, E., Ishii, M., Pérez, F. F., and Suzuki, T.: The Global Ocean Data Analysis Project version 2 (GLODAPv2) – an internally consistent data product for the world ocean, Earth Syst. Sci. Data, 8, 297–323, https://doi.org/10.5194/essd-8-297-2016, 2016.

Olsen, A., Lange, N., Key, R. M., Tanhua, T., Álvarez, M., Becker, S., Bittig, H. C., Carter, B. R., Cotrim da Cunha, L., Feely, R. A., van Heuven, S., Hoppema, M., Ishii, M., Jeansson, E., Jones, S. D., Jutterström, S., Karlsen, M. K., Kozyr, A., Lauvset, S. K., Lo Monaco, C., Murata, A., Pérez, F. F., Pfeil, B., Schirnick, C., Steinfeldt, R., Suzuki, T., Telszewski, M., Tilbrook, B., Velo, A., and Wanninkhof, R.: GLODAPv2.2019 – an

update of GLODAPv2, Earth Syst. Sci. Data, 11, 1437–1461, https://doi.org/10.5194/essd-11-1437-2019, 2019.
Polovina, J. J., Howell, E., Kobayashi, D. R., and Seki, M. P.: The transition zone chlorophyll front, a dynamic global feature defining migration and forage habitat for marine resources, Prog. Oceanogr., 49, 469–483, https://doi.org/10.1016/S0079-6611(01)00036-2, 2001.
Polovina, J. J., Howell, E. A., Kobayashi, D. R., and Seki, M. P.: The Transition Zone Chlorophyll Front updated: Advances from a decade of research, Prog. Oceanogr., 150, 79–85, https://doi.org/10.1016/j.pocean.2015.01.006, 2017.
Price, N. M. and Morel, F. M. M.: Cadmium and cobalt substitution for zinc in a marine diatom, Nature, 344, 658–660, https://doi.org/10.1038/344658a0, 1990.
Price, N. M., Harrison, G. I., Hering, J. G., Hudson, R. J., Nirel, P. M. V., Palenik, B., and Morel, F. M. M.: Preparation and chemistry of the artificial algal culture medium aquil preparation and chemistry of the artificial algal culture medium aquil, Biol. Oceanogr., 6, 443–461, https://doi.org/10.1080/01965581.1988.10749544, 1988/1989.
Quisel, J. D., Wykoff, D. D., and Grossman, A. R.: Biochemical characterization of the extracellular phosphatases produced by phosphorus-deprived *Chlamydomonas reinhardtii*, Plant Physiol., 111, 839–848, https://doi.org/10.1104/pp.111.3.839, 1996.
Reed, R. K.: Flow of the Alaskan Stream and its variations, Deep-Sea Res. Pt. A, 31, 369–386, https://doi.org/10.1016/0198-0149(84)90090-6, 1984.
Richon, C. and Tagliabue, A.: Biogeochemical feedbacks associated with the response of micronutrient recycling by zooplankton to climate change, Glob. Change Biol., 27, 4758–4770, https://doi.org/10.1111/gcb.15789, 2021.
Saito, M.: Dissolved Cobalt and Labile Cobalt from Leg 2 (Hilo, HI to Papeete, French Polynesia) of the US GEOTRACES Pacific Meridional Transect (PMT) cruise (GP15, RR1815) on R/V Roger Revelle from October to November 2018, Biological and Chemical Oceanography Data Management Office (BCO-DMO), (Version 1) Version Date 2020-07-15 [data set], https://doi.org/10.26008/1912/bco-dmo.818610.1, 2020.
Saito, M. A.: Dissolved Cobalt and Labile Cobalt from Leg 1 (Seattle, WA to Hilo, HI) of the US GEOTRACES Pacific Meridional Transect (PMT) cruise (GP15, RR1814) on R/V Roger Revelle from September to October 2018, Biological and Chemical Oceanography Data Management Office (BCO-DMO), (Version 2) Version Date 2021-05-05 [data set], https://doi.org/10.26008/1912/bco-dmo.818383.2, 2021.
Saito, M. A. and Moffett, J. W.: Complexation of cobalt by natural organic ligands in the Sargasso Sea as determined by a new high-sensitivity electrochemical cobalt speciation method suitable for open ocean work, Mar. Chem., 75, 49–68, https://doi.org/10.1016/S0304-4203(01)00025-1, 2001.
Saito, M. A. and Moffett, J. W.: Temporal and spatial variability of cobalt in the Atlantic Ocean, Geochim. Cosmochim. Ac., 66, 1943–1953, https://doi.org/10.1016/s0016-7037(02)00829-3, 2002.
Saito, M. A., Moffett, J. W., Chisholm, S. W., and Waterbury, J. B.: Cobalt limitation and uptake in *Prochlorococcus*, Limnol. Oceanogr., 47, 1629–1636, https://doi.org/10.4319/lo.2002.47.6.1629, 2002.
Saito, M. A., Rocap, G., and Moffett, J. W.: Production of cobalt binding ligands in a *Synechococcus* feature at the Costa Rica upwelling dome, Limnol. Oceanogr., 50, 279–290, 2005.

Saito, M. A., Goepfert, T. J., Noble, A. E., Bertrand, E. M., Sedwick, P. N., and DiTullio, G. R.: A seasonal study of dissolved cobalt in the Ross Sea, Antarctica: micronutrient behavior, absence of scavenging, and relationships with Zn, Cd, and P, Biogeosciences, 7, 4059–4082, https://doi.org/10.5194/bg-7-4059-2010, 2010.

Saito, M. A., McIlvin, M. R., Moran, D. M., Goepfert, T. J., DiTullio, G. R., Post, A. F., and Lamborg, C. H.: Multiple nutrient stresses at intersecting Pacific Ocean biomes detected by protein biomarkers, Science, 345, 1173–1177, https://doi.org/10.1126/science.1256450, 2014.

Saito, M. A., Noble, A. E., Hawco, N., Twining, B. S., Ohnemus, D. C., John, S. G., Lam, P., Conway, T. M., Johnson, R., Moran, D., and McIlvin, M.: The acceleration of dissolved cobalt's ecological stoichiometry due to biological uptake, remineralization, and scavenging in the Atlantic Ocean, Biogeosciences, 14, 4637–4662, https://doi.org/10.5194/bg-14-4637-2017, 2017.

Sañudo-Wilhelmy, S. A., Gobler, C. J., Okbamichael, M., and Taylor, G. T.: Regulation of phytoplankton dynamics by vitamin B_{12}, Geophys. Res. Lett., 33, L04604, https://doi.org/10.1029/2005GL025046, 2006.

Sarmiento, J. L., Gruber, N., Brzezinski, M. A., and Dunne, J. P.: High-latitude controls of thermocline nutrients and low latitude biological productivity, Lett. Nat., 427, 56–60, https://doi.org/10.1038/nature02127, 2004.

Schlitzer, R., Anderson, R. F., Dodas, E. M., et al.: The GEOTRACES Intermediate Data Product 2017, Chem. Geol., 493, 210–223, https://doi.org/10.1016/j.chemgeo.2018.05.040, 2018.

Schroth, A. W., Crusius, J., Hoyer, I., and Campbell, R.: Estuarine removal of glacial iron and implications for iron fluxes to the ocean, Geophys. Res. Lett., 41, 3951–3958, https://doi.org/10.1002/2014GL060199, 2014.

Sharma, R.: Deep-sea mining: Economic, technical, technological, and environmental considerations for sustainable development, Mar. Technol. Soc. J., 45, 28–41, https://doi.org/10.4031/MTSJ.45.5.2, 2011.

Stabeno, P. J., Reed, R. K., and Schumacher, J. D.: The Alaska Coastal Current: Continuity of transport and forcing, J. Geophys. Res., 100, 2477–2485, https://doi.org/10.1029/94JC02842, 1995.

Stramma, L., Johnson, G. C., Sprintall, J., and Mohrholz, V.: Expanding oxygen-minimum zones in the tropical oceans, Science, 320, 655–658, https://doi.org/10.1126/science.1153847, 2008.

Sunda, W. G. and Huntsman, S. A.: Effect of sunlight on redox cycles of manganese in the southwestern Sargasso Sea, Deep-Sea Res. Pt. A, 35, 1297–1317, https://doi.org/10.1016/0198-0149(88)90084-2, 1988.

Sunda, W. G. and Huntsman, S. A.: Cobalt and zinc interreplacement in marine phytoplankton: Biological and geochemical implications, Limnol. Oceanogr., 40, 1404–1417, https://doi.org/10.4319/lo.1995.40.8.1404, 1995.

Sundby, B., Anderson, L. G., Hall, P. O. J., Iverfeldt, Å., van der Loeff, M. M. R., and Westerlund, S. F. G.: The effect of oxygen on release and uptake of cobalt, manganese, iron and phosphate at the sediment-water interface, Geochim. Cosmochim. Ac., 50, 1281–1288, https://doi.org/10.1016/0016-7037(86)90411-4, 1986.

Swanner, E. D., Planavsky, N. J., Lalonde, S. V., Robbins, L. J., Bekker, A., Rouxel, O. J., Saito, M. A., Kappler, A., Mojzsis, S. J., and Konhauser, K. O.: Cobalt and marine redox

evolution, Earth Planet. Sc. Lett., 390, 253–263, https://doi.org/10.1016/j.epsl.2014.01.001, 2014.
Tagliabue, A., Hawco, N. J., Bundy, R. M., Landing, W. M., Milne, A., Morton, P. L., and Saito, M. A.: The role of external inputs and internal cycling in shaping the global ocean cobalt distribution: Insights from the first cobalt biogeochemical model, Global Biogeochem. Cy., 32, 594–616, https://doi.org/10.1002/2017GB005830, 2018.
Taylor, S. R. and McLennan, S. M.: The geochemical evolution of the continental crust, Rev. Geophys., 33, 241–265, https://doi.org/10.1029/95RG00262, 1995.
Tsuda, A., Kiyosawa, H., Kuwata, A., Mochizuki, M., Shiga, N., Saito, H., Chiba, S., Imai, K., Nishioka, J., and Ono, T.: Responses of diatoms to iron-enrichment (SEEDS) in the western subarctic Pacific, temporal and spatial comparisons, Prog. Oceanogr., 64, 189–205, https://doi.org/10.1016/j.pocean.2005.02.008, 2005.
Ustick, L. J., Larkin, A. A., Garcia, C. A., Garcia, N. S., Brock, M. L., Lee, J. A., Wiseman, N. A., Keith Moore, J., and Martiny, A. C.: Metagenomic analysis reveals global-scale patterns of ocean nutrient limitation, Science, 372, 287–291, https://doi.org/10.1126/science.abe6301, 2021.
Wojciechowski, C. L., Cardia, J. P., and Kantrowitz, E. R.: Alkaline phosphatase from the hyperthermophilic bacterium *T. maritima* requires cobalt for activity, Protein Sci., 11, 903–911, https://doi.org/10.1110/ps.4260102, 2002.
Wyatt, N. J., Milne, A., Achterberg, E. P., Browning, T. J., Bouman, H. A., Woodward, E. M. S., and Lohan, M. C.: Seasonal cycling of zinc and cobalt in the Southeast Atlantic along the GEOTRACES GA10 section, Biogeosciences, 18, 4265–4280, https://doi.org/10.5194/bg-18-4265-2021, 2021.
Xiang, Y. and Lam, P. J.: Size-fractionated compositions of marine suspended particles in the western Arctic Ocean: Lateral and vertical sources, J. Geophys. Res.-Ocean., 125, e2020JC016144, https://doi.org/10.1029/2020JC016144, 2020.
Zhang, H., van den Berg, C. M. G., and Wollast, R.: The determination of interactions of cobalt (II) with organic compounds in seawater using cathodic stripping voltammetry, Mar. Chem., 28, 285–300, https://doi.org/10.1016/0304-4203(90)90049-I, 1990.
Zheng, L., Minami, T., Konagaya, W., Chan, C. Y., Tsujisaka, M., Takano, S., Norisuye, K., and Sohrin, Y.: Distinct basin-scale-distributions of aluminum, manganese, cobalt, and lead in the North Pacific Ocean, Geochim. Cosmochim. Ac., 254, 102–121, https://doi.org/10.1016/j.gca.2019.03.038, 2019.

Tables

Table 1. Blanks, internal standard and GEOTRACES community intercalibration standards measured at sea during Co analysis.

	dCo [pM]	*n*	Consensus
Blanks[a]			
18 Sep 2018	9.44 ± 0.56	3	
6 Oct 2018	9.68 ± 0.41	2	
27 Oct 2018	0.035 ± 2.1	2	
9 Nov 2018	6.28 ± 0.84	2	
Internal standards			
26 Sep–9 Nov[b]	55.9 ± 3.9	18	
22 Oct–21 Nov[c]	15.5 ± 3.4	7	
Intercalibration standards			
GSC – shipboard	82.8 ± 2.9	4	77.7 ± 2.4[d]
GSC – laboratory[e]	80.2 ± 6.2	3	
SAFe D1	44.0 ± 0.0065	2	45.4 ± 4.7

[a] Pacific seawater, chelexed to remove metals and UV-irradiated. [b] Surface North Pacific seawater, collected 26 September 2018. [c] South Atlantic seawater, collected on the CoFeMUG expedition, 2007. [d] From Hawco et al. (2016). Not an official consensus. [e] Analyzed August 2019 to November 2019.

Table 2. Isopycnal analysis results. Samples were binned by potential density (σ_0), and as σ_0 increased, the $dCo : dPO_4$ relationship became more decoupled, as shown by the decreasing R^2 value of the correlation. Error is given as standard deviations.

Bin	σ_0 range [kg m^{-3}]	n	Average depth [m]	$dCo : dPO_4$ [µmol : mol]	R^2
a	$\sigma_0 < 26$	218	84 ± 67	82 ± 3	0.79
b	$26 \leq \sigma_0 < 26.25$	23	215 ± 86	86 ± 14	0.63
c	$26.25 \leq \sigma_0 < 26.5$	25	260 ± 100	86 ± 17	0.50
d	$26.5 \leq \sigma_0 < 26.75$	45	333 ± 104	125 ± 27	0.31
e	$26.75 \leq \sigma_0 < 27$	44	433 ± 132	79 ± 15	0.40
f	$27 \leq \sigma_0 < 27.25$	49	613 ± 147	123 ± 25	0.33
g	$27.25 \leq \sigma_0 < 27.5$	77	980 ± 154	409 ± 201	0.05
h	$27.5 \leq \sigma_0 < 27.75$	101	1933 ± 412	157 ± 35	0.16
i	$27.75 \leq \sigma_0 < 28$	116	4144 ± 845	1357 ± 1920	0.004

Table 3. Dissolved Co vs. O_2 correlation within OMZs in the Pacific GP15 transect (this study) and others.

Oceanographic location	Depth range [m]	n	$dCo : O_2$ [$\mu M : mol\,kg^{-1}$]	R^2	Reference
Tropical North Pacific (ETNP)	≥ 200	58	-0.72 ± 0.07	0.66	This study
Tropical South Pacific (ETSP)	≥ 200	54	-0.73 ± 0.06	0.72	This study
North Atlantic	300–800	73	-0.56	0.89	Noble et al. (2017)
South Atlantic Angola Dome	300–800	NA	-0.56	0.73	Noble et al. (2012)
Tropical North Atlantic	0–800	NA	-0.39	0.88	Baars and Croot (2015)
Tropical South Pacific (ETSP)	200–5500	NA	-0.34*	0.75	Hawco et al. (2016)

* The $dCo : O_2$ correlation was originally reported as $-0.33\ \mu M : M$ and was adapted to units of $\mu M : mol\,kg^{-1}$ using a conversion of $1.025\ kg\,L^{-1}$. NA: not available.

Table 4. Predicted effects of deoxygenation on the dCo inventories (I) of the upper 1000 m of the eastern tropical North Pacific (ETNP) and eastern tropical South Pacific (ETSP) oxygen minimum zones (OMZs) along the GP15 transect at 152 ºW. For comparison, ΔdCo/Δt was estimated using the $dCo : O_2$ relationship from the GP16 expedition (Hawco et al., 2016). $I_{present}$ represents the current dCo inventory integrated over the OMZ stations, and $I_{100\,yr}$ represents the estimated change in the dCo inventory in 100 years. $V_{section}$ represents the volume of each GP15 section sampled, with a width of 1 m and a depth of 1000 m.

OMZ	Stations included	Latitude range	$V_{section}$ [m^3]	$dCo : O_2$ [$\mu M : mol\,kg^{-1}$]	$\Delta O_2/\Delta t$* [$\mu mol\,kg^{-1}\,yr^{-1}$]	$\Delta dCo/\Delta t$ [$pM\,yr^{-1}$]	$I_{present}$ [mol]	$I_{100\,yr}$ [mol]	I % increase
ETNP	20, 21, 22, 23, 25	14.25 to 5° N	10×10^8	-0.72 ± 0.07	-0.13 ± 0.32 -0.19 ± 0.20	0.093 ± 0.23 0.14 ± 0.14	52	61 ± 23 65 ± 14	18 % 26 %
ETSP	29, 31, 33, 34	0° N to 7.5° S	8.3×10^8	-0.73 ± 0.06	-0.13 ± 0.32 -0.19 ± 0.20	0.094 ± 0.23 0.14 ± 0.15	38	47 ± 23 52 ± 15	25 % 36 %
GP16 ETSP	All			-0.34	-0.13 ± 0.32 -0.19 ± 0.20	0.044 ± 0.11 0.064 ± 0.068			

* Pacific deoxygenation trends ($\Delta O_2/\Delta t$) are from Stramma et al. (2008, Table 1 therein). $\Delta O_2/\Delta t$ rates were estimated within the core of the Pacific equatorial OMZs (-0.13 ± 0.32 μmol kg^{-1} yr^{-1}; 5 ºN to 5 ºS, 105 to 115 ºW) and along their western boundary (-0.19 ± 0.20 μmol kg^{-1} yr^{-1}; 5 ºN to 5 ºS, 165 to 175 ºW).

Table 5. Average conventional radiocarbon age, apparent oxygen utilization (AOU) and dCo of the deep Pacific Ocean (>3000 m depth). GP15 samples were matched with their nearest $\Delta^{14}C$ and AOU observations from the GLODAP database.

Region	n	Average radiocarbon age [Years]	Average AOU [$\mu mol\,kg^{-1}$]	Average dCo [pM]
North Pacific Subpolar Gyre	20	1342 ± 85	196 ± 10	24 ± 12
North Pacific Subtropical Gyre	29	1340 ± 98	187 ± 12	31 ± 11
Equatorial Pacific	32	1200 ± 130	174 ± 14	25 ± 13
South Pacific Subtropical Gyre	14	1110 ± 140	159 ± 11	23 ± 2

Figures

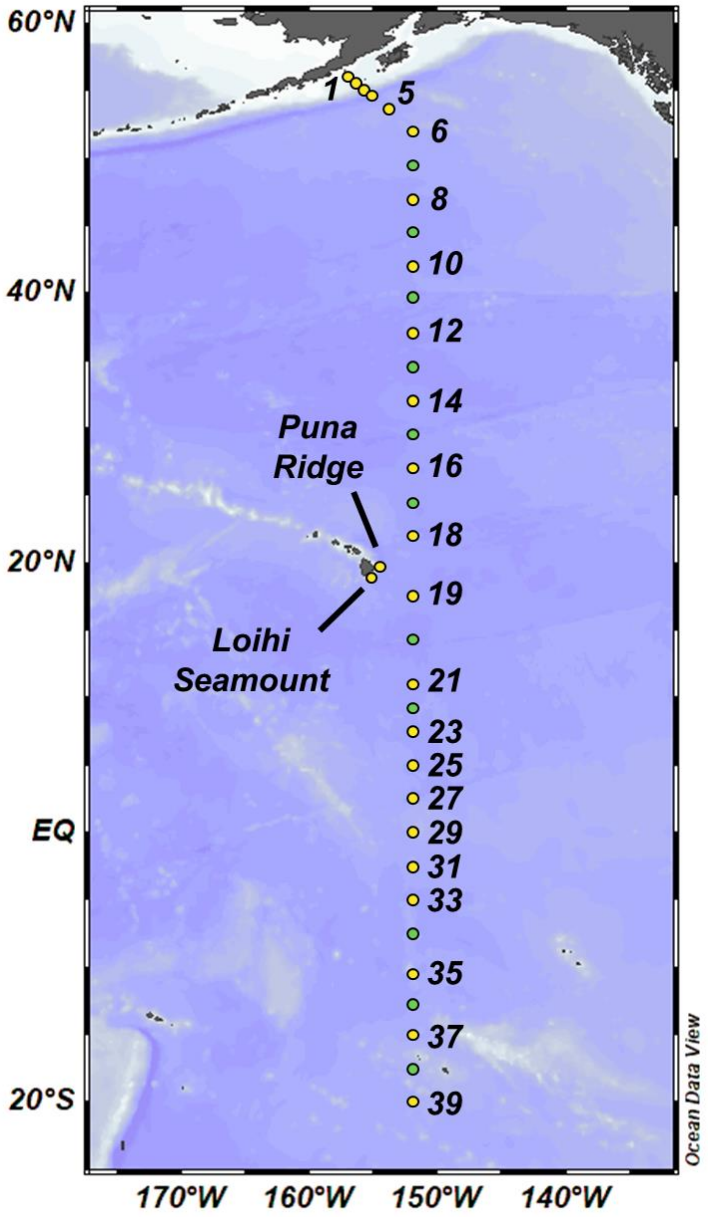

Figure 1. GEOTRACES GP15 expedition track. Leg 1 (RR1814, September–October 2018) spanned between the Alaskan coast and Hawaii, and Leg 2 (RR1815, October–November 2018) spanned between Hawaii and 20 ºS. Yellow points represent full-depth stations, and green points represent demi stations where only the upper 1000 m was sampled. At Station 11, only a surface towfish (~ 2 m) sample was collected.

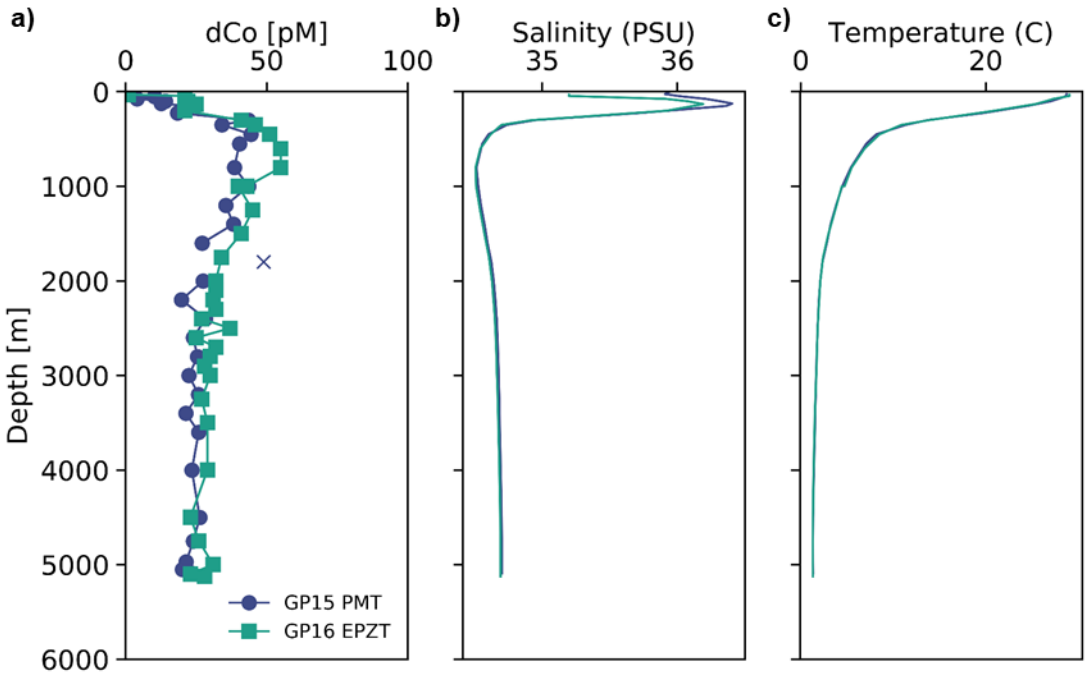

Figure 2. (a) Dissolved Co, (b) salinity and (c) temperature profiles from a crossover station between the GEOTRACES GP15 Pacific Meridional Transect (PMT; November 2018; navy) and the GEOTRACES GP16 East Pacific Zonal Transect (EPZT; December 2013; teal) at 10.5 ºS, 152 ºW. Outliers are marked with an X.

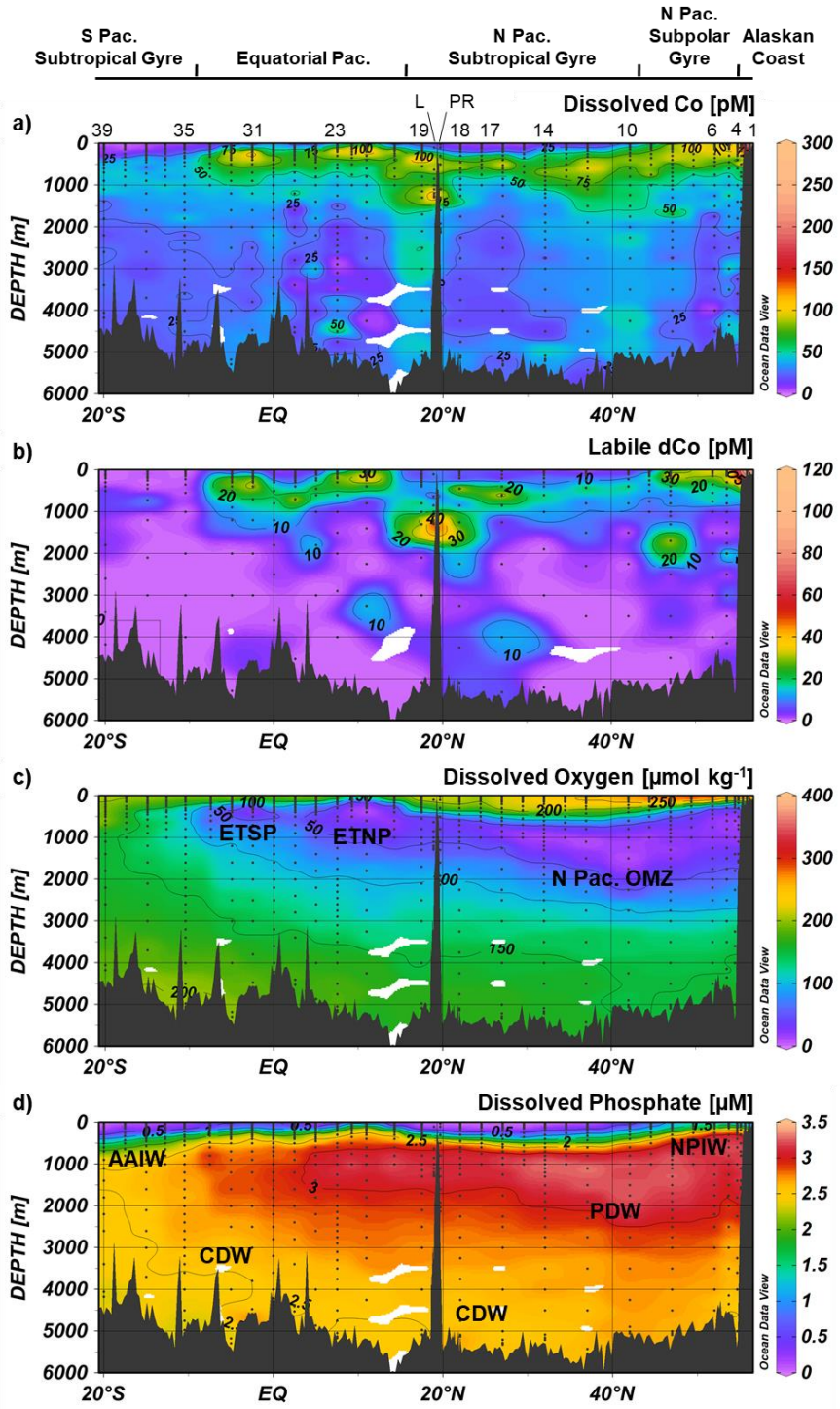

Figure 3. Dissolved Co (a), labile dissolved Co (b), dissolved oxygen (c) and dissolved phosphate (d) transects along the GP15 cruise track. Select stations numbers are shown in panel (a), with the Loihi Seamount station labeled as "L" and the Puna Ridge station labeled as "PR". The eastern tropical North Pacific (ETNP), eastern tropical South Pacific (ETSP) and North Pacific OMZs are labeled, as well as Antarctic Intermediate Water (AAIW), Circumpolar Deep Water (CDW), Pacific Deep Water (PDW) and North Pacific Intermediate Water (NPIW). Weighted-average gridding is used to interpolate between data points.

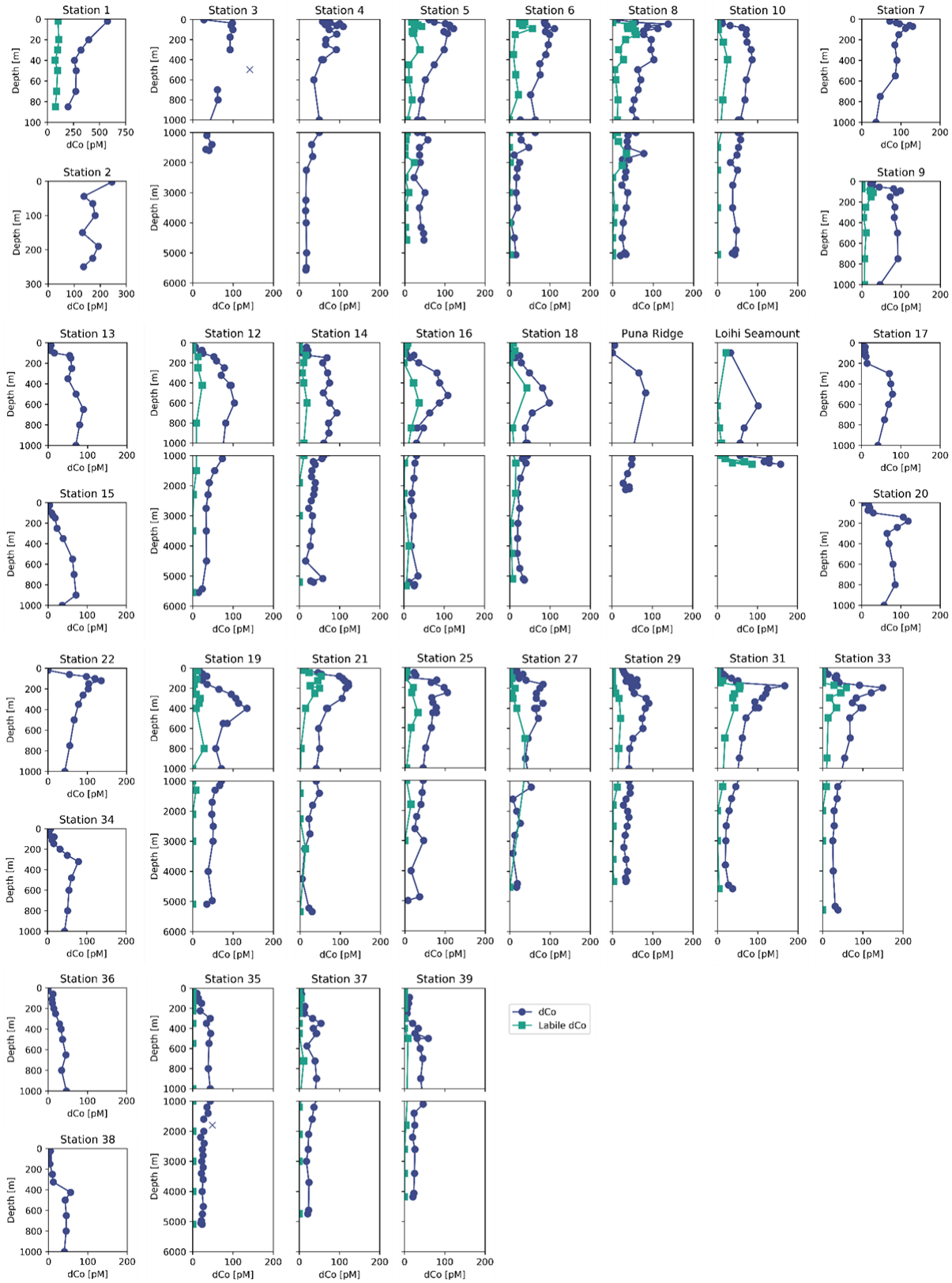

Figure 4. Depth profiles of dissolved Co (navy circles) and labile dissolved Co (teal squares) along the GP15 Pacific transect. Suspected outliers are marked as an X.

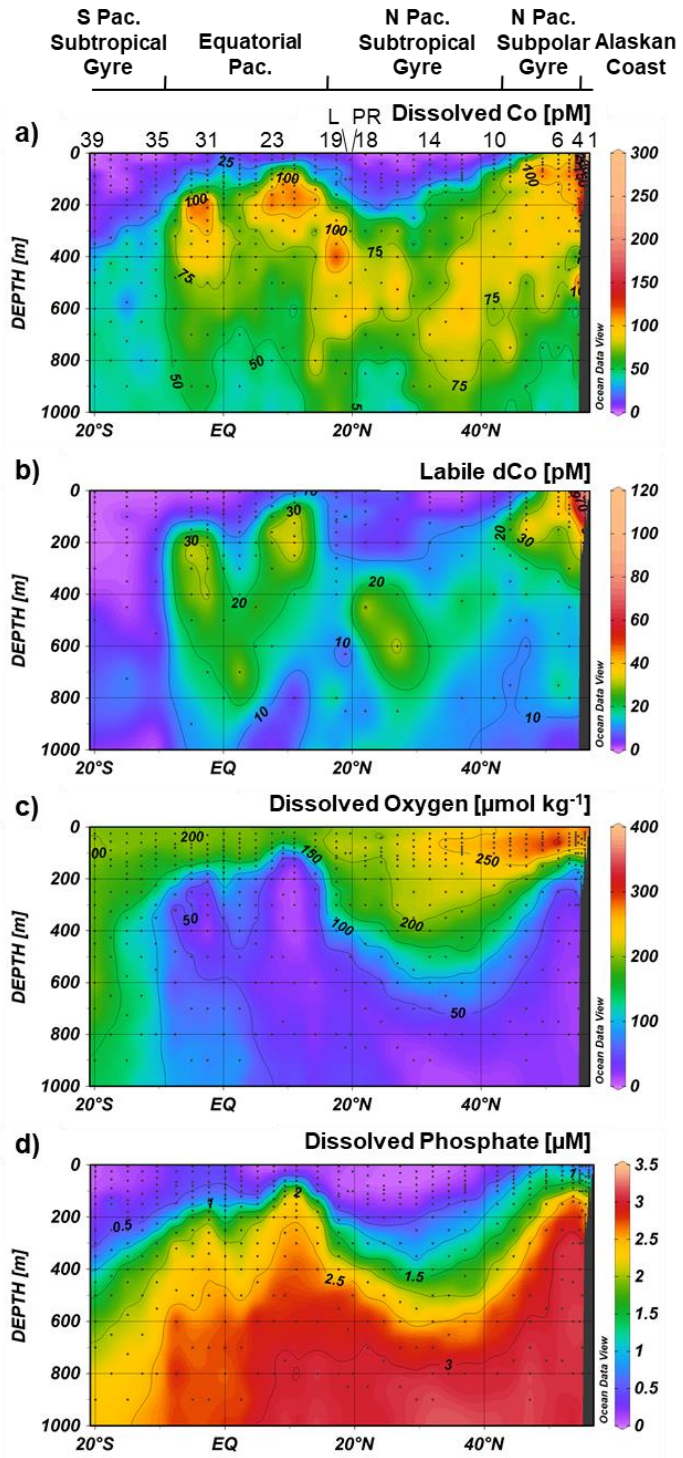

Figure 5. Upper-ocean transects of dissolved Co (a), labile dissolved Co (b), dissolved phosphate (c) and dissolved oxygen (d) along the GP15 cruise track. Weighted-average gridding is used to interpolate between data points. Select station numbers are shown in panel (a), with the Loihi Seamount station labeled as "L" and the Puna Ridge station labeled as "PR".

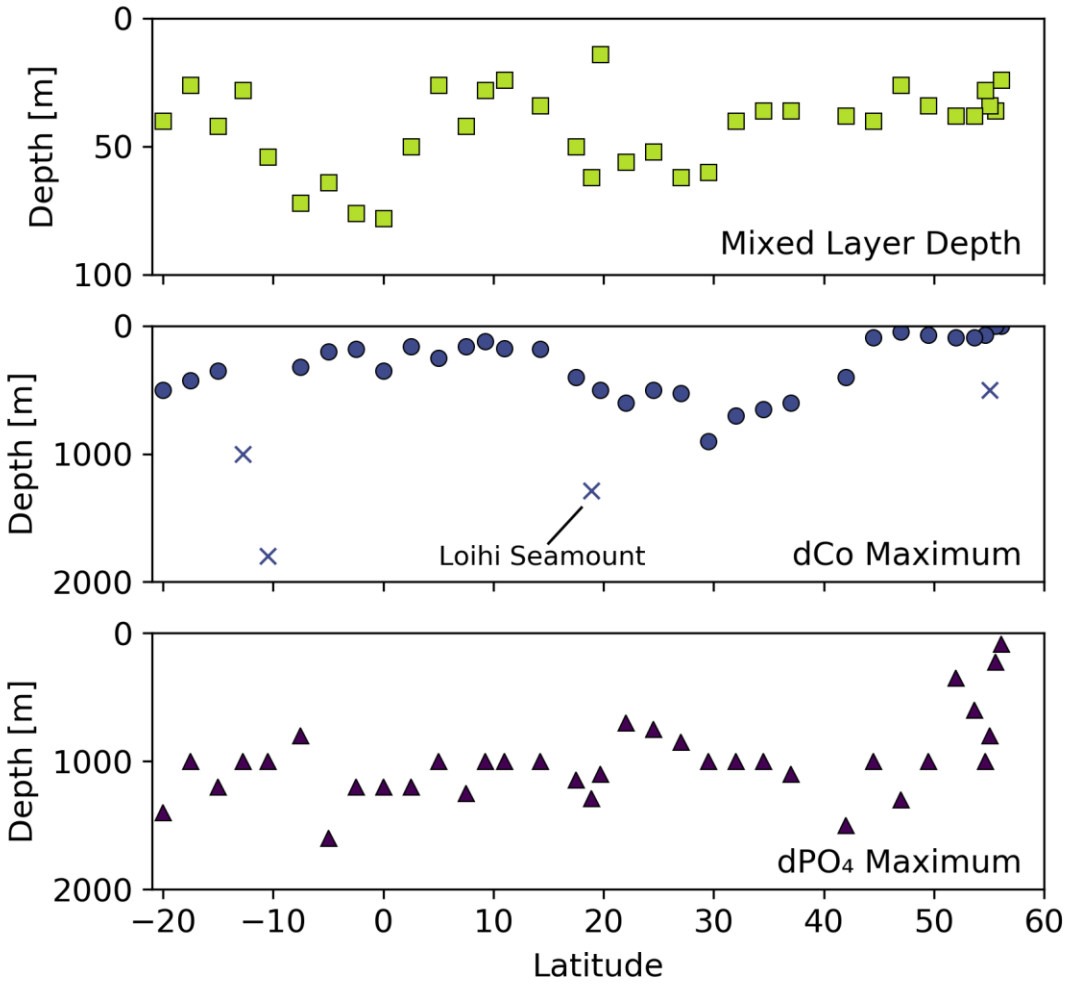

Figure 6. Mixed-layer depth, depth of the dCo maximum and depth of the dPO_4 maximum vs. latitude for the GP15 transect. Outlier dCo maxima depths are indicated with an X.

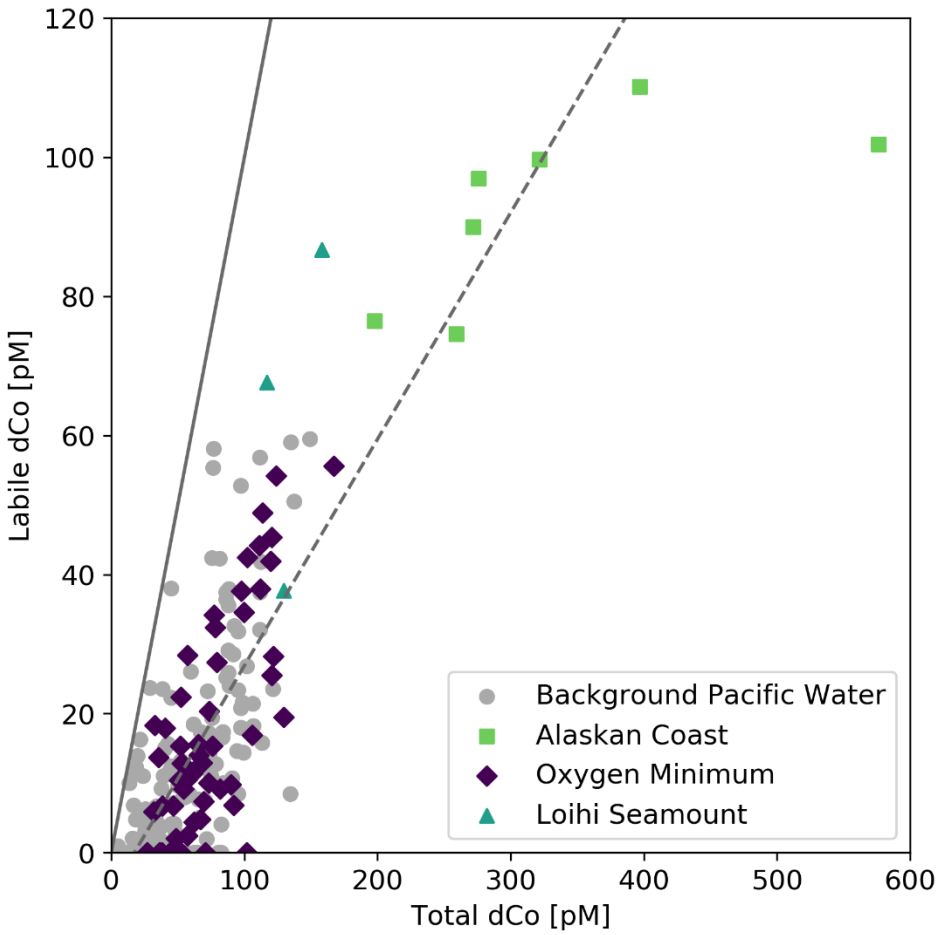

Figure 7. Labile dCo vs. total dCo, with notable sources of dCo plotted in color, including Station 1 along the Alaskan coast (green squares), oxygen minimum zones where O_2 concentrations are less than 50 µmol kg^{-1} (purple diamonds) and samples from within the Loihi Seamount vent plume (teal triangles). A theoretical 1:1 line (solid) and a linear regression of background Pacific seawater (dashed; slope = 0.33 ± 0.02, R^2 = 0.55, n = 237) are shown. Points to the right of the trend line represent greater dCo complexation compared to background seawater, and points to the left of the trend line represent more labile, un-complexed Co pools compared to background seawater.

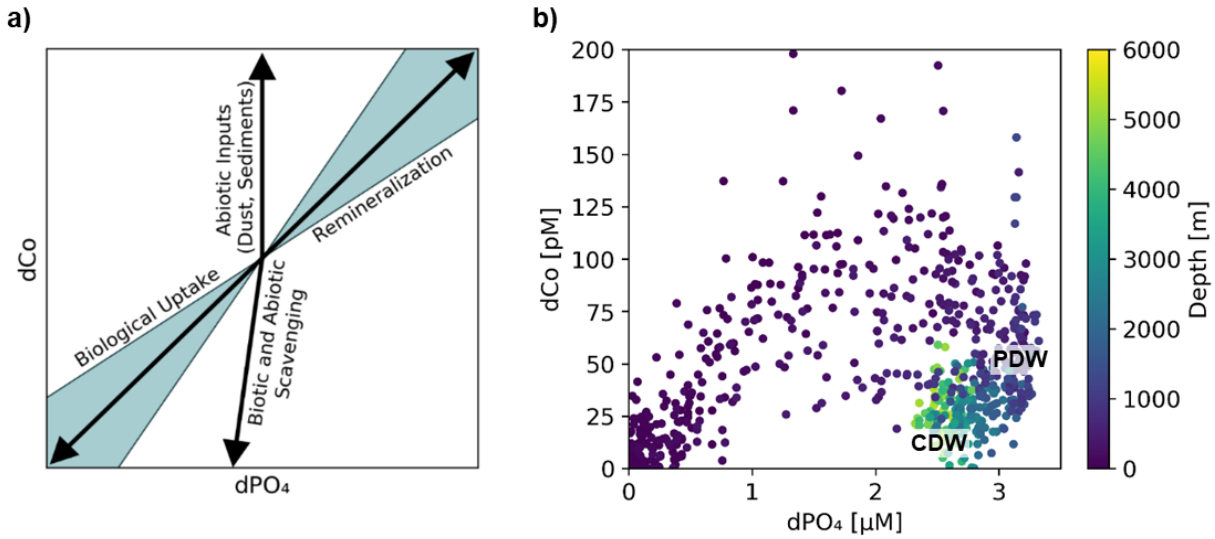

Figure 8. (a) A vector schematic showing the relationship between dCo and dPO_4 concentrations and the effects of major oceanic processes on nutrient distribution. Biological uptake and remineralization can exhibit a range of stoichiometric relationships, depicted here by the blue shaded region. Adapted from Noble et al. (2008). (b) Observed dCo vs. dPO_4 along the GP15 transect. Approximate positions of Circumpolar Deep Water (CDW) and Pacific Deep Water (PDW) are marked.

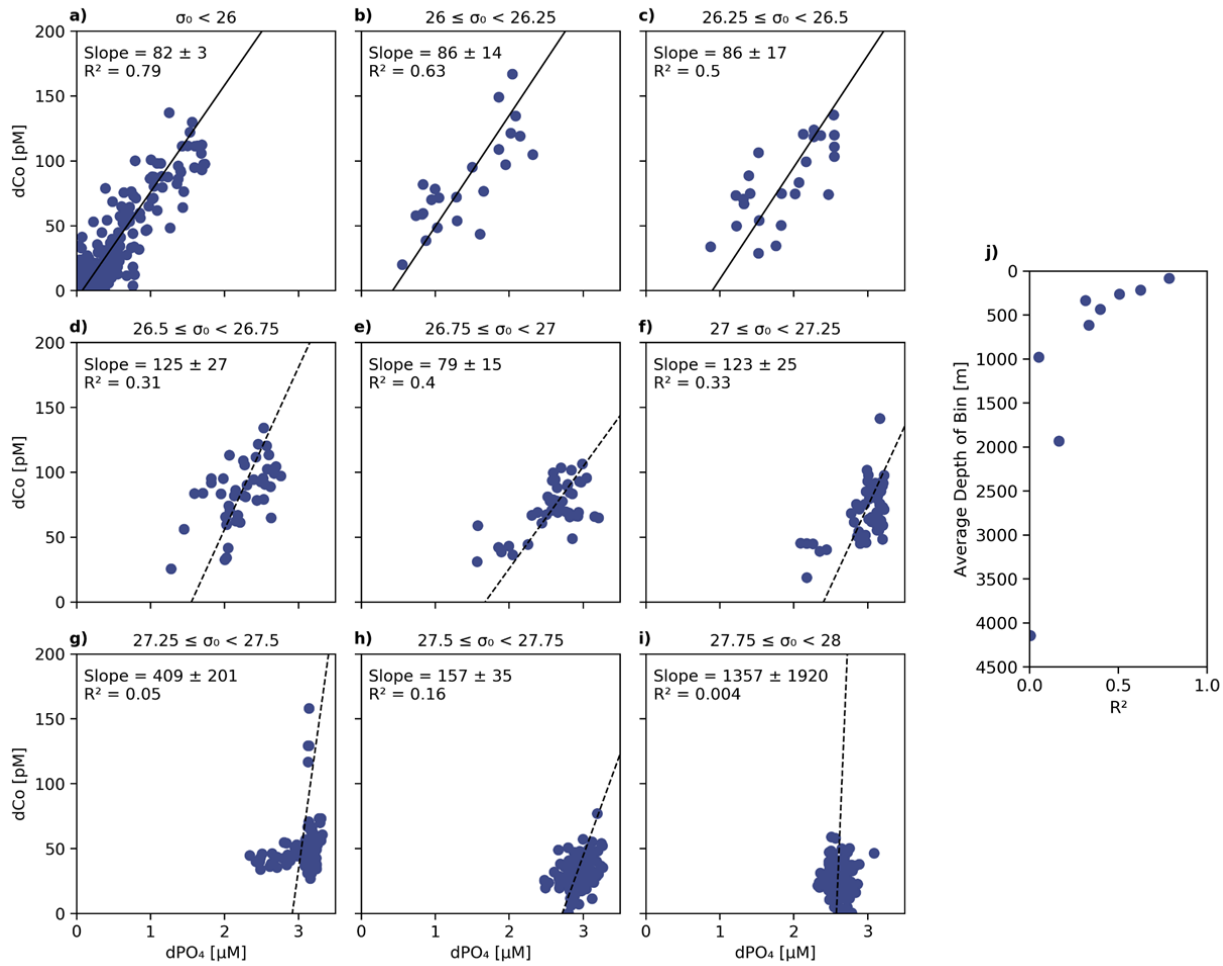

Figure 9. (a–i) The dCo vs. dPO_4 relationship sorted into nine isopycnal bins by potential density (σ_0) with a linear best-fit trend line. The least dense samples (a) represent the surface ocean and phytoplankton dCo : dPO_4 nutrient ratio (82 ± 3, µmol : mol; $n = 218$, $R^2 = 0.79$). The decreasing R^2 (j) in denser isopycnal bins represents the decoupling of dCo and dPO_4 at depth and increasing relevance of Co scavenging. Samples with [dCo] >200 pM and Stations 1 and 2 have been omitted from this analysis.

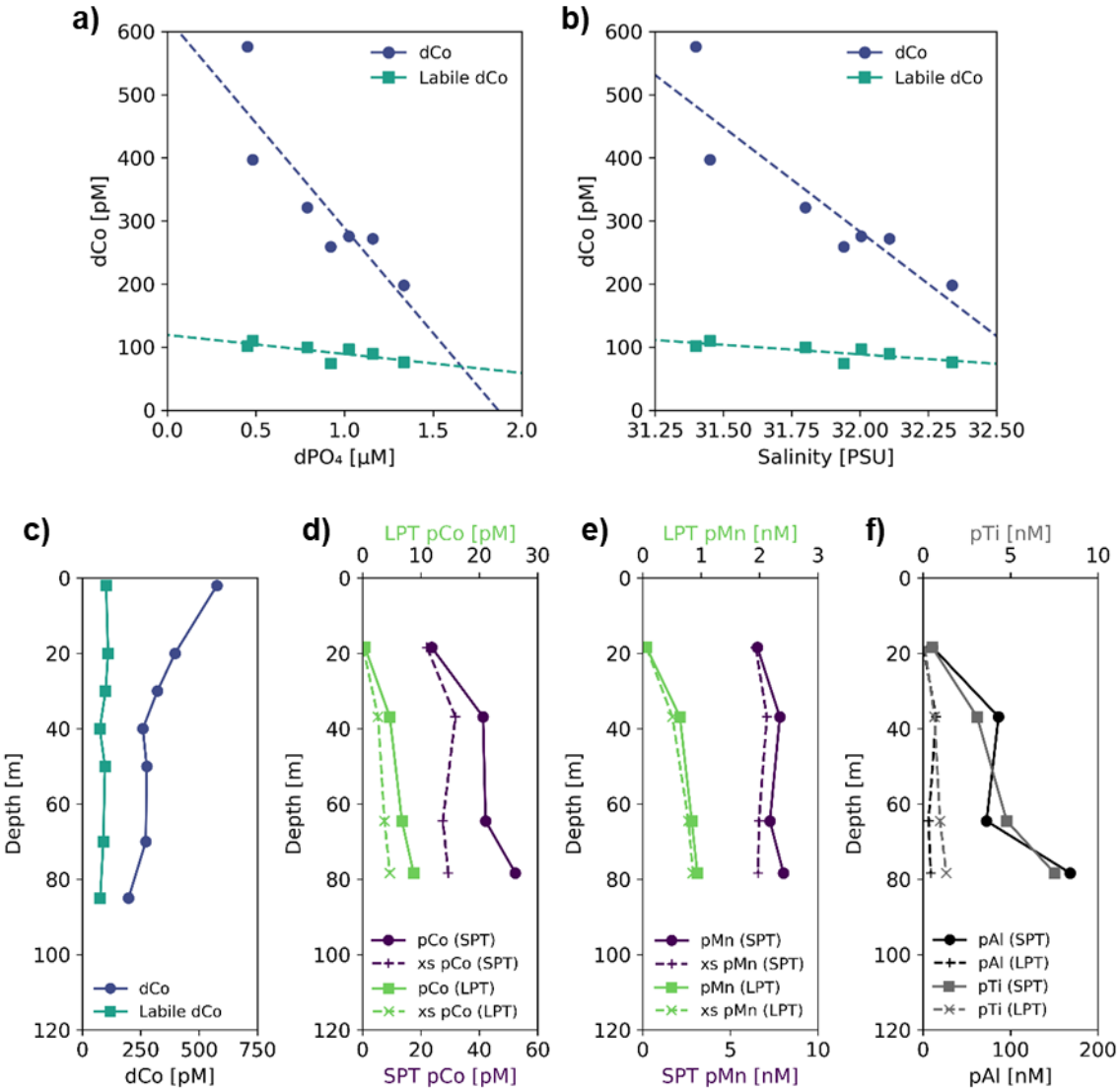

Figure 10. Sample data and profiles from Station 1, a coastal station in the Gulf of Alaska (56.06 ºN, 156.96 ºW); (a) dCo and labile dCo vs. dPO_4 show a significant negative correlation (slope = −430 ± 88, µmol : mol; R^2 = 0.77 and slope = −53 ± 18, µmol : mol; R^2 = 0.57, respectively); (b) dCo and labile dCo vs. salinity show a significant negative correlation (slope = −406 ± 73 pM PSU^{-1}, R^2 = 0.81 and slope = −50 ± 15 pM PSU^{-1}, R^2 = 0.60, respectively). Depth profiles of (c) dCo and labile dCo and of small particulate, total (SPT) and large particulate, total (LPT); (d) pCo and excess pCo (xs pCo); (e) pMn and excess pMn (xs pMn); and (f) pAl and pTi. Note the change in scale of the x axis between SPT and LPT (d, e) and between pAl and pTi (f).

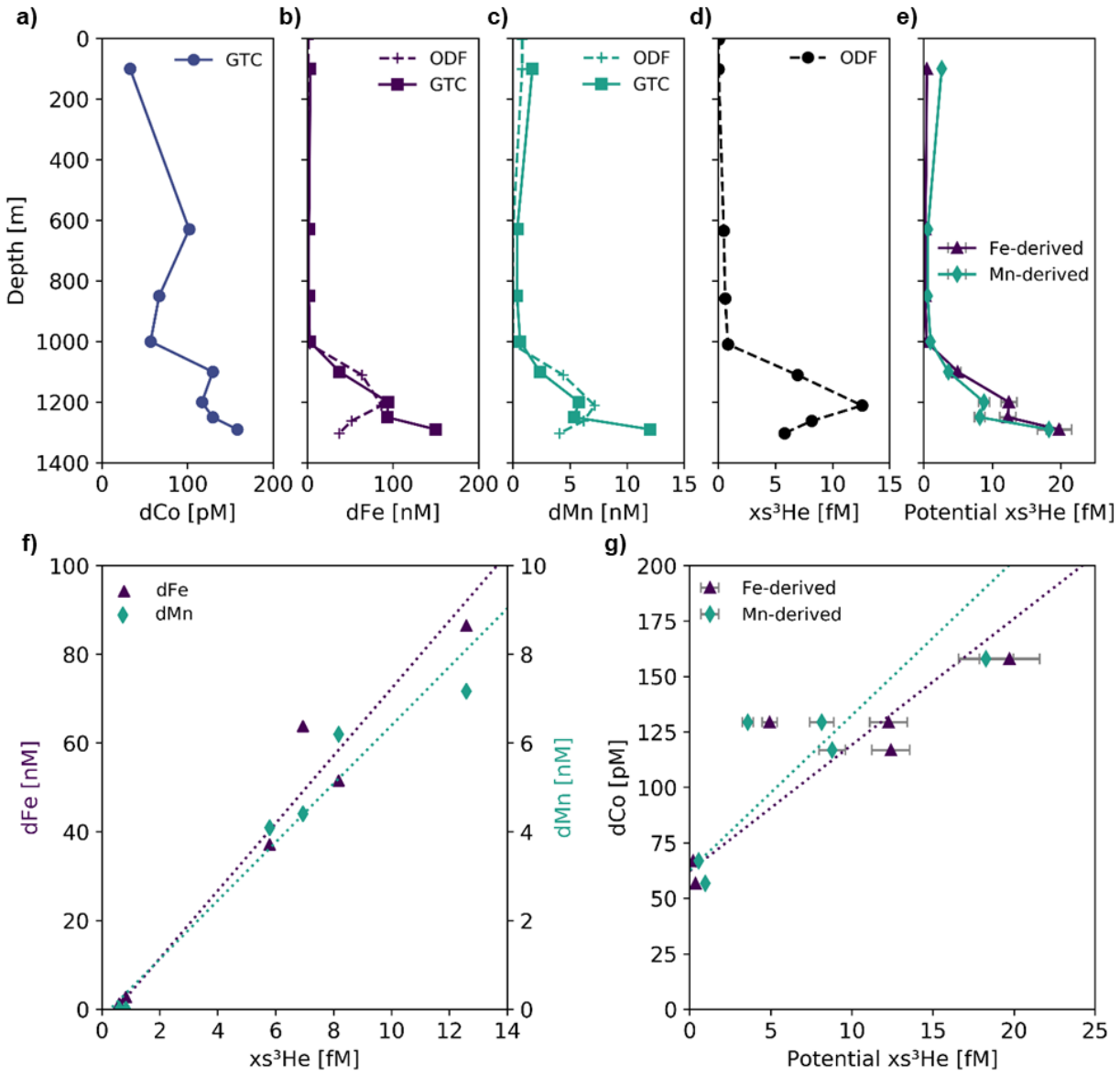

Figure 11. Profiles of (a) dCo, (b) dFe, (c) dMn and (d) excess ^{3}He (xs^3He) from the Loihi Seamount station (Station 18.6) from both the trace-metal-clean GEOTRACES CTD carousel (GTC; solid lines) and the general CTD from the Ocean Data Facility (ODF; dashed lines). To estimate xs^3He values for the GTC cast, (f) the ODF cast's dFe : xs^3He and dMn : xs^3He ratios (7.6 ± 0.7 mol : µmol, $R^2 = 0.95$ and 0.66 ± 0.06 mol : µmol, $R^2 = 0.95$, respectively) were used to predict (e) potential xs^3He values with respect to the GTC dFe and dMn values. (g) The GTC dCo : potential xs^3He ratios were 6 ± 1 mol : mmol (Fe-derived, $R^2 = 0.78$) and 7 ± 2 mol : mmol (Mn-derived, $R^2 = 0.71$). For the trace metal : xs^3He regressions, only samples below 750 m were used to isolate the hydrothermal signal from surface processes. Error bars for potential xs^3He (e, g) indicate the propagation of error from the regression slope in panel (f).

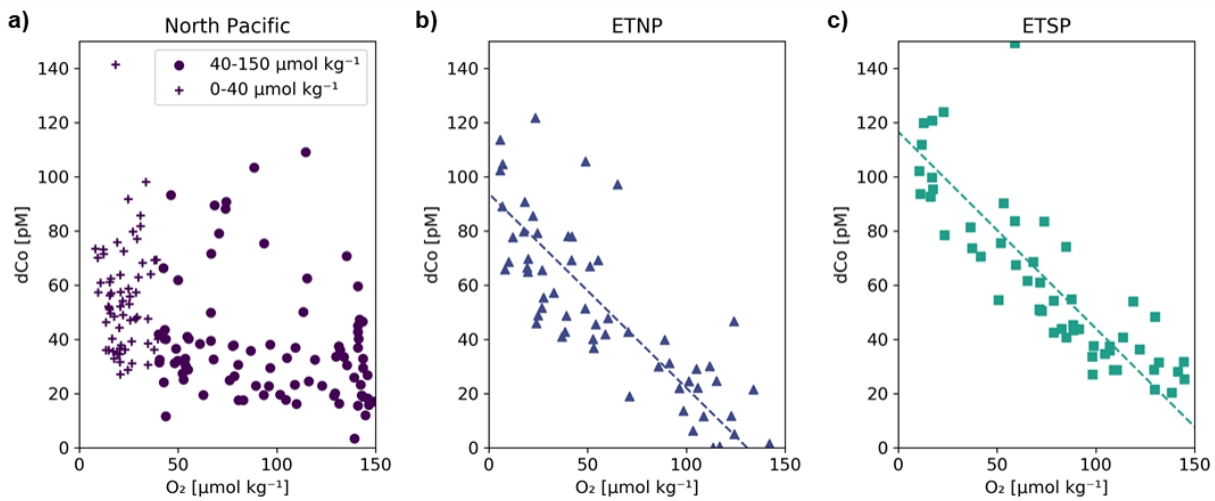

Figure 12. Dissolved dCo vs. O_2 relationships within the three Pacific OMZs. Data points from the North Pacific OMZ (a; Stations 3–18; ≥ 500 m depth) show a nonlinear trend where samples at O_2 < 40 µmol kg^{-1} display a wide range of dCo values, likely due to remineralization and scavenging at shallow depths in the OMZ, and samples between 40–150 µmol kg^{-1} O_2 displayed little correlation. Samples from the ETNP (b; Stations 20–25; ≥ 200 m depth) and ETSP (c; Stations 29–34; ≥ 200 m depth) show a linear relationship between dCo and O_2 associated with advection from the eastern core of the OMZ. The ETNP displayed a dCo : O_2 slope of −0.72 ± 0.07 µM : mol kg^{-1} (R^2 = 0.66, n = 58), and the ETSP displayed a dCo : O_2 slope of −0.73 ± 0.06 µM : mol kg^{-1} (R^2 = 0.72, n = 54). See Appendix A for additional dCo : O_2 analysis.

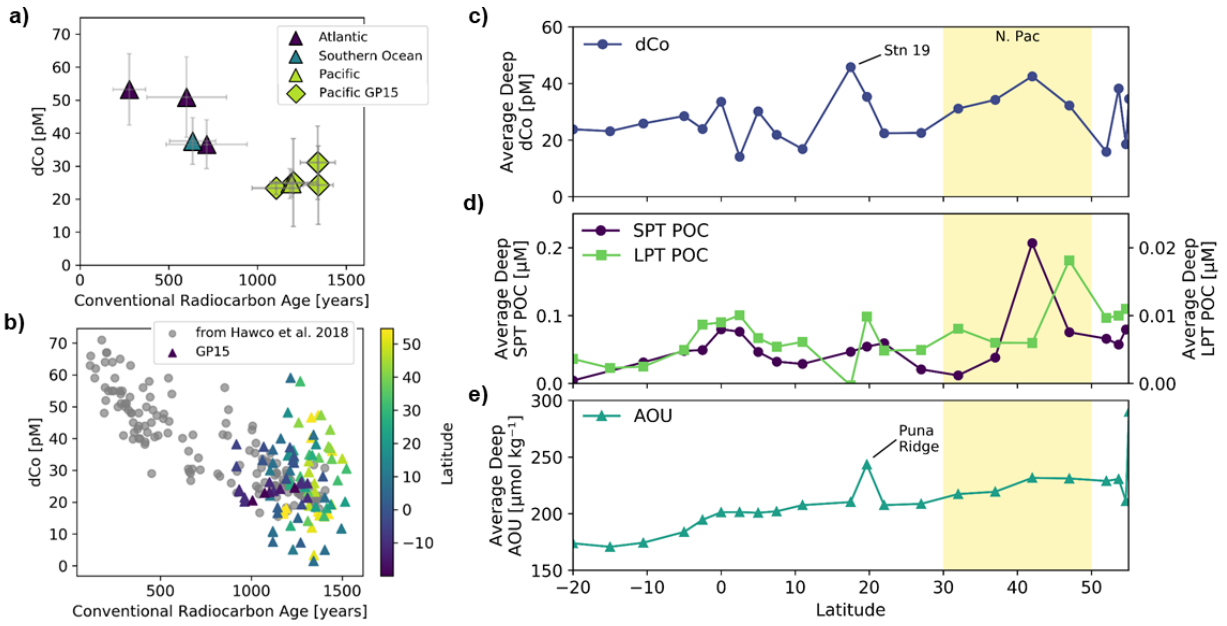

Figure 13. (a) Average dCo concentrations vs. radiocarbon age of the deep ocean (≥ 3000 m) by oceanographic basin with error bars of standard deviation. Data from GEOTRACES expeditions other than GP15 (triangles) are from Hawco et al. (2018; Table 2 therein); (b) dCo vs. radiocarbon age of individual GEOTRACES dCo samples matched with their nearest GLODAP radiocarbon measurement. (c–e) Deep-ocean (≥ 1500 m), depth-weighted averages of dCo, small particulate, total (SPT) particulate organic carbon (POC), large particulate, total (LPT) POC and apparent oxygen utilization (AOU) for each deep-station profile. The yellow boxes highlight the region in the North Pacific where average deep dCo and POC are elevated. Note the order-of-magnitude difference between the scales of the POC y axes (d).

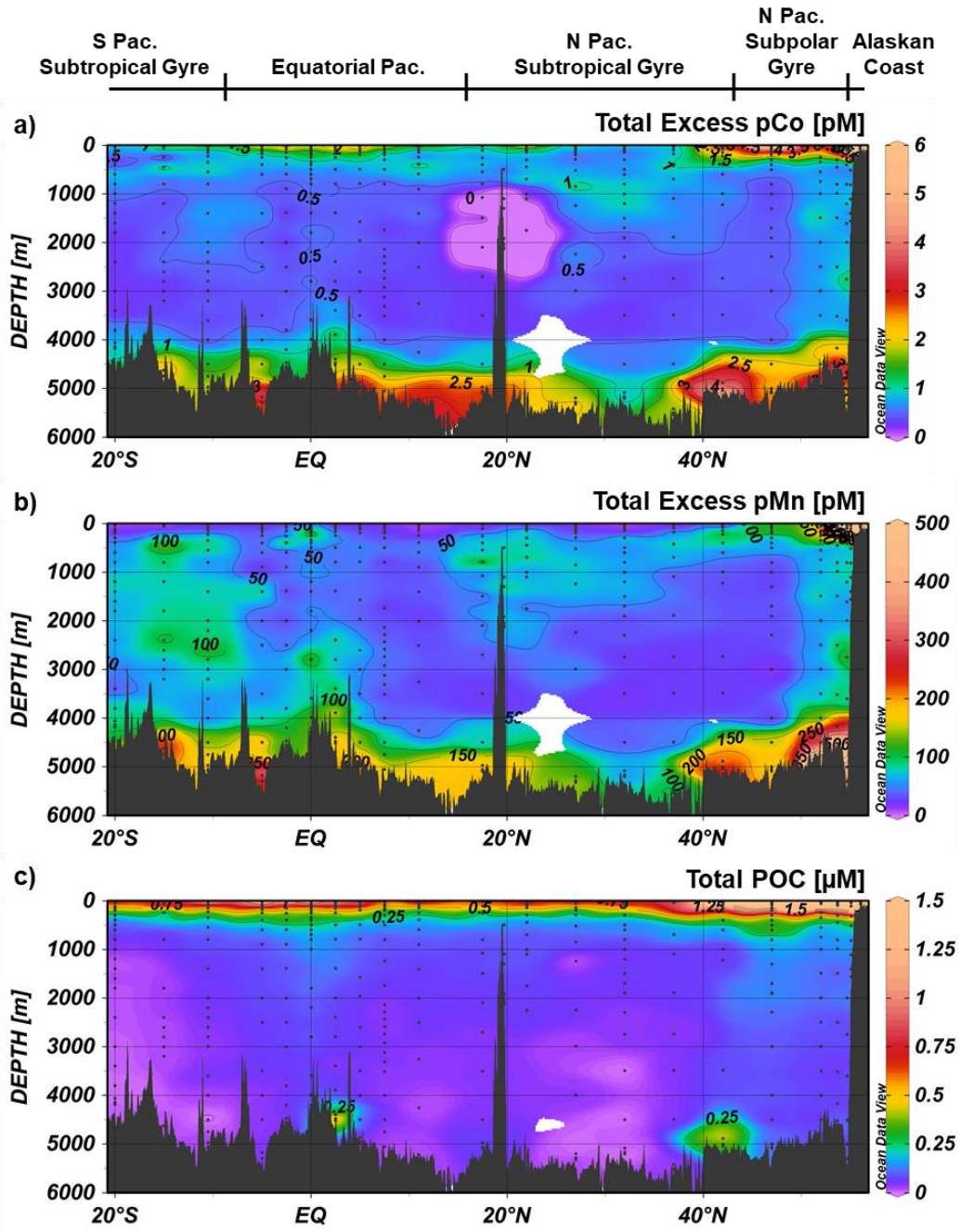

Figure 14. Total excess (lithogenically corrected) pCo (a), total excess (lithogenically corrected) pMn, (b) and total POC (c) transects along the GP15 cruise track. Total particulate values are summations of the small particulate, total (SPT) and large particulate, total (LPT) size fractions. Weighted-average gridding is used to interpolate between data points.

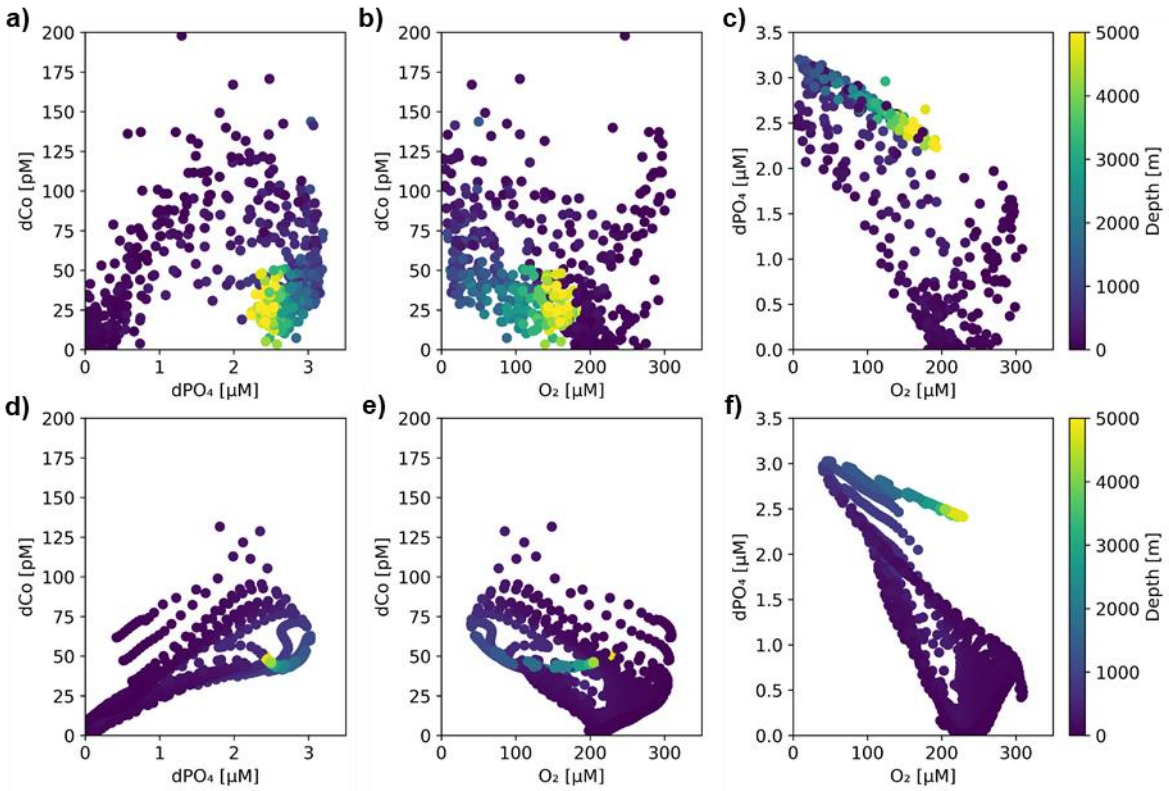

Figure 15. Nutrient relationships between dCo, dPO_4 and O_2 in (a)–(c) binned observed values and (d)–(f) model output values. Observed values have been binned and averaged by 1º latitude and 31 depth divisions to ensure comparability between the model and sample values. Note that O_2 values are reported here in units of micromolar.

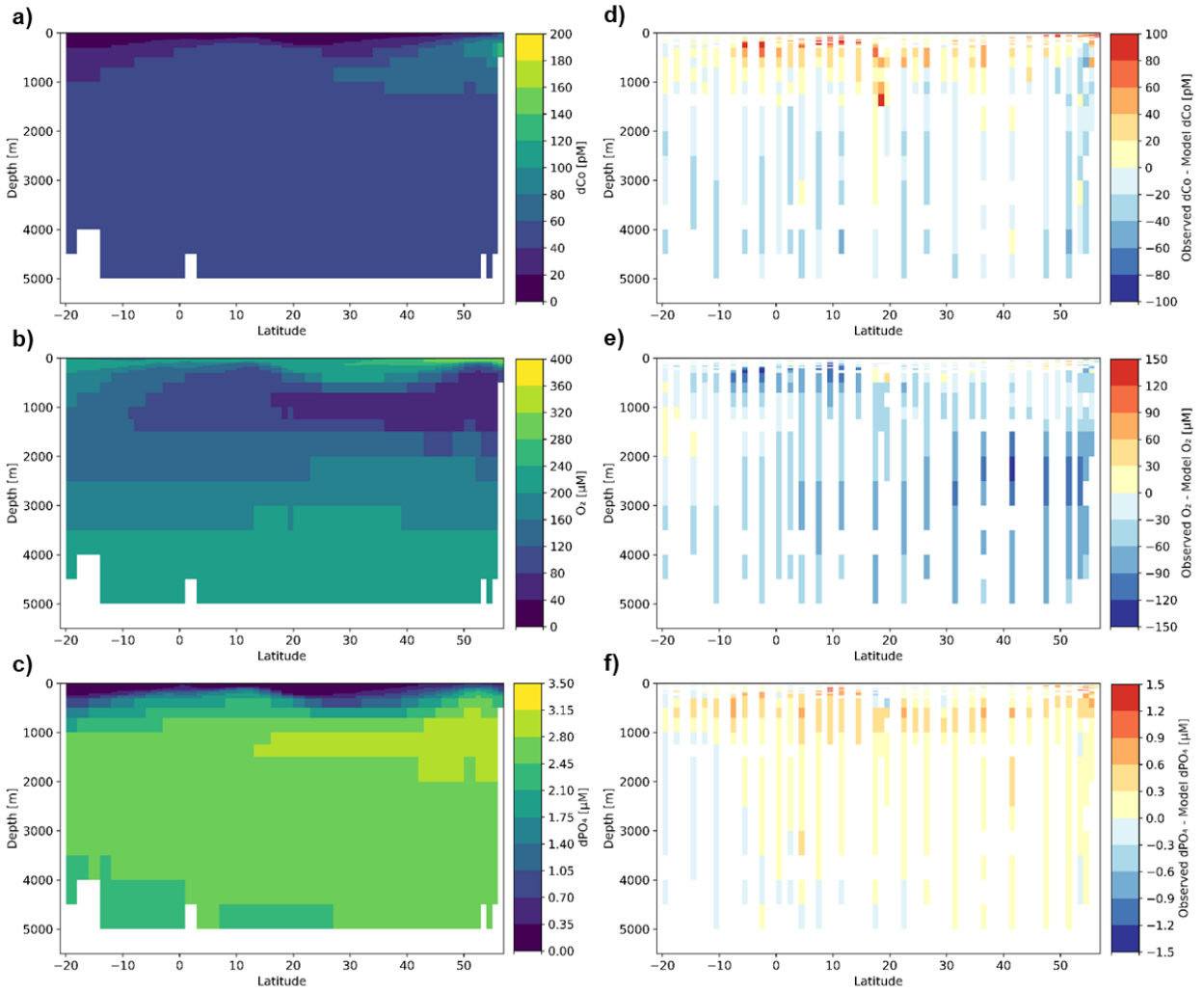

Figure 16. (a–c) Model output of dCo, O_2 and dPO_4 distributions along the GP15 transect. (d–f) Differences between observed values and model outputs of dCo, O_2 and dPO_4 concentrations along the GP15 transect. Observed values have been binned and averaged by 1º latitude and 31 depth divisions to ensure comparability between the model and sample values. Note that O_2 values are reported here in units of micromolar.

Chapter 3.

Elevated cobalt ecological stoichiometry at biogeochemical transitions in the Pacific Ocean as defined by protein nutrient biomarkers

Rebecca Chmiel[a,b], Nathan Lanning[c], Allison Laubach[d], Jong-Mi Lee[d], Christopher L. Dupont[e], Joshua Espinoza[e], Jessica Fitzsimmons[c], Tyler J. Goepfert[f], Nicholas Hawco[g], Phoebe J. Lam[d], Matthew McIlvin[b], Dawn Moran[b], Jaclyn K. Saunders[h], Reiner Schlitzer[i] and Mak Saito[b]

[a] MIT/WHOI Joint Program in Oceanography/Applied Ocean Science and Engineering, Woods Hole, MA, USA
[b] Department of Marine Chemistry and Geochemistry, Woods Hole Oceanographic Institution, Woods Hole, MA, USA
[c] Department of Oceanography, Texas A&M University, College Station, TX, USA
[d] Department of Ocean Sciences, University of California Santa Cruz, Santa Cruz, CA, USA
[e] Microbial & Environmental Genomics, J. Craig Venter Institute, La Jolla, CA, USA
[f] School of Earth and Space Exploration, Arizona State University, Tempe, AZ, USA
[g] Department of Oceanography, University of Hawai‘i at Manoa, Honolulu, HI, USA
[h] Department of Marine Sciences, University of Georgia, Athens, GA, USA
[i] Alfred Wegener Institute, Helmholtz Centre for Polar and Marine Research, Bremerhaven, Am Handelshafen 12, Bremerhaven 27570, Germany

3.1 Abstract

Quantifying the ecological stoichiometry of the surface ocean is of interest to the study of global phytoplankton nutrient limitations and productivity. Among trace metal nutrients, cobalt (Co) stoichiometry exhibits exceptionally high regional variability due to its malleable use in plankton metabolisms. Here, we synthesize dissolved Co (dCo) and particulate Co (pCo) data from four Pacific expeditions – ProteOMZ, GEOTRACES GP15 and GP16, and METZYME – including novel dCo and pCo datasets from the ProteOMZ and METZYME expeditions, respectively. Together, these four expeditions extend from the North Pacific subpolar gyre to the South Pacific oligotrophic gyre and allow for the investigation of Co ecological stoichiometry through the lens of 3 stoichiometry metrics: Redfieldian dCo : dPO_4^{3-} slopes, dCo : dPO_4^{3-} ratios and pCo : pP ratios. Additionally, we present a surface transect of bacterial protein biomarkers from the GP15 expedition that reveal overlapping transitions between nutrient stress regimes and bacterial metabolic responses across biogeochemical provinces in the Pacific Ocean, including a novel observation of a P-stress biomarker signal in the subtropical North Pacific. An evaluation of Co stoichiometry across distinct nutrient biomes reveals that dCo uptake and incorporation into a biological pCo was high in the North and equatorial Pacific, displaying dCo : dPO_4^{3-} slopes consistently above 80 µmol : mol in the North Pacific and as high as 279 ± 12 µmol : mol in the equatorial Pacific (5º S). Elevated dCo : dPO_4^{3-} slopes were found in regions of nutrient transition between oceanographic provinces, creating overlapping macro- and micronutrient stress, while

discrete dCo : dPO_4^{3-} surface ratios followed trends within oceanographic provinces. Trends in Co uptake stoichiometry appear related to the bioavailability of Zn, which often shares an uptake transporter system with Co; dCo : dZn ratios in the surface ocean were elevated in the North Pacific subpolar gyre and equatorial Pacific, and reached extraordinarily high values along the Alaskan coast, where dCo concentrations exceeded those of dZn (dCo : dZn = 2.46). The dCo : dPO_4^{3-} slope, dCo : dPO_4^{3-} ratio and pCo : pP ratio are distinct metrics that can be used in tandem to evaluate the processes that govern Co cycling between dissolved and particulate phases in the upper ocean. This multi-expedition, interdisciplinary study provides insights into Co biogeochemistry and the dynamic nature of ecological stoichiometry in microorganisms.

3.2 Introduction

Cobalt (Co) is a scarce but necessary micronutrient for many marine phytoplankton (Saito et al., 2002; Sunda and Huntsman, 1995). Co is used as the cofactor in vitamin B_{12} and some forms of the metalloprotein carbonic anhydrase (Bertrand et al., 2013; Lane and Morel, 2000; Morel et al., 2020). Some cyanobacteria like *Prochlorococcus* have a small but essential requirement for Co (Hawco et al., 2020; Saito et al., 2002), while many eukaryotic plankton are able to substitute Co for Zn at the active site of the carbonic anhydrase enzyme, allowing for flexibility in their metal micronutrient metabolism in regions of Zn scarcity (Kellogg et al., 2020; Price and Morel, 1990; Sunda and Huntsman, 1995). Culture studies have also shown a higher Co metal use efficiency in *Prochlorococcus* than can be explained by known Co metabolic uses, suggesting Co plays additional roles in marine microbial metabolisms than are currently unknown (Hawco et al., 2020). One possible but unconfirmed metabolic use of Co could be as a metallic cofactor in alkaline phosphatase, an extracellular enzyme that facilitates the acquisition of phosphate (dPO_4^{3-}) from organic phosphorous molecules when dPO_4^{3-} is low (Cox and Saito, 2013; Quisel et al., 1996). Alkaline phosphatases typically use a Zn metallic cofactor, but a Co cofactor has been observed in the hyperthromophile *Thermotoga maritima* (Wojciechowski et al., 2002) and is consistent with observations of high Co demand in regions of P limitation (Saito et al., 2017).

Dissolved Co concentrations are typically in the picomolar range in the pelagic ocean, resulting in a small marine dCo inventory compared to other bioactive trace metal nutrients like dissolved zinc (dZn) and iron (dFe), which leaves the dCo inventory more vulnerable to perturbations by biogeochemical processes. The low dCo inventory and metabolic flexibility in Co use by plankton results in wide variations in Co stoichiometry throughout the oceans (Saito et al., 2017).

Here, we will examine the basin-scale biogeochemistry of Co in the surface ocean through the lens of ecological stoichiometry, which considers the ratios of the biological uptake of nutrients into aquatic microorganism communities, encompassing both the balance of elements incorporated into biomass as well as the balance of elements remaining in the external environment (Sterner and Elser, 2002). Notably, Redfield (1958) concluded that concentrations of macronutrients in the marine environment are influenced by marine microbial communities, whose biochemical nutrient requirements have in turn been determined by the availability of chemicals in their environment (Redfield, 1958). In this way, marine ecological stoichiometry is dictated by the coupling of the dissolved and particulate phases of elemental nutrients. Redfield's study of the ecological ratios of carbon (C), nitrogen (N) and phosphorous (P) in the oceans has been expanded to include studies of extended Redfield ratios that include trace metal nutrient stoichiometry, which have to be more variable and circumstantial than macronutrient stoichiometry (Ho et al., 2003; Moore et al., 2013a; Sunda and Huntsman, 1995; Twining and Baines, 2013). In natural ocean environments, the ratio of pCo : pP in phytoplankton biomass varies significantly by species (Twining et al., 2015; Twining and Baines, 2013), and yet that variability is often distilled to a coherent ecosystem stoichiometry. Examining Co ecological stoichiometry, which exhibits one of the most malleable nutrient stoichiometries within marine organisms and the seawater environment, can give insight into both Co biogeochemistry and the dynamic nature of ecological stoichiometry in microorganisms.

The relationship between dCo and dPO_4^{3-} can provide insight into the biogeochemical and ecological processes impacting the marine Co cycle (Chmiel et al., 2022; Noble et al., 2008; Saito et al., 2017). The dCo vs. dPO_4^{3-} relationship considered in vector space (Fig. 1) depicts the directionality of major dCo processes, including microbial biological uptake, which depletes both dCo and dPO_4^{3}, and organic matter remineralization, which regenerates dCo and dPO_4^{3-}. Together, biological uptake and remineralization create a positive linear relationship in the upper and intermediate ocean with a slope that is reflected within the aggregate Co : P stoichiometry of the coupled dissolved and particulate phases. In the upper ocean, the slopes of dCo : dPO_4^{3-} relationship can differ by orders of magnitude; in the Atlantic Ocean, for example, the slope of the dCo vs. dPO_4^{3-} relationship was observed to vary greatly by depth in the surface ocean, with stoichiometric slopes "accelerating" towards the surface due to high Co demand in P-limiting waters (Saito et al., 2017).

The dCo vs. dPO_4^{3-} relationship becomes decoupled when an additional process adds or removes dCo with little change to dPO_4^{3-} concentrations, such as an abiotic source of dCo from a continental shelf or dCo scavenging to Mn-oxide particles. In intermediate waters, the removal of dCo by particle scavenging is primarily mediated by Mn-oxidizing bacteria (Moffett and Ho, 1996; Tebo et al., 1984) and is the primary sink for dCo in the marine environment, diminishing the dCo inventory throughout deep and intermediate dCo waters (Hawco et al., 2017). The influence of both surface uptake and deep Mn-oxide scavenging give the marine dCo profile a typical "hybrid-type" shape, indicating that its distribution is influenced by both nutrient drawdown in the surface ocean and scavenging drawdown at intermediate and deep depths (Bruland and Lohan, 2003). In intermediate waters, the combination of both remineralization and scavenging processes to a net vector towards the lower right, representing low dCo, high dPO_4^{3-} waters (Fig. 1).

The drivers of spatial Co : P stoichiometric variation in the upper ocean is not well understood, particularly in the central Pacific Ocean, which has only recently been surveyed on the basin-scale for high-resolution trace metal distributions by the international GEOTRACES program and wider biogeochemical community (Chmiel et al., 2022; Hawco et al., 2016, 2020; Zheng et al., 2019). Co demand from plankton is highly elastic and can be influenced by the availability of other macro- and micronutrients, including Zn and P. The high variability of Co and other trace metal ecological stoichiometry is a challenge for the creation of global marine biogeochemical models, which often rely on fixed trace metal stoichiometries to estimate community plankton uptake (Tagliabue et al., 2018).

This study aims to evaluate spatial trends in Co ecological stoichiometry in the Pacific Ocean and their potential biogeochemical drivers. We have integrated the results of four recent Pacific expeditions that utilized trace-metal-clean techniques to determine large-scale transects of micronutrients in the North, equatorial and South Pacific Ocean. Three metrics of Co stoichiometry were evaluated across the transects: the slopes of the aggregate dCo : dPO_4^{3-} relationship in the surface ocean, the dCo : dPO_4^{3-} ratios of individual depths, and the pCo : pP ratios of bulk particles at individual depths. We also present a novel surface protein dataset focused on the bacterial size fraction data from the GP15 expedition that allowed for the evaluation of protein biomarkers for P, N and Fe stress across the wide range of oceanographic biomes in the North and equatorial Pacific. A comparison of Co ecological stoichiometry to bacterial protein biomarkers synthesized

the observed patterns of Co ecological stoichiometry with phytoplankton metabolic function across Pacific nutrient regimes.

3.3 Methods

3.3.1 Study area and data availability

Trace metal dCo and dPO_4^{3-} concentrations from 4 Pacific Ocean expeditions are synthesized here, including datasets from the METZYME GPc03 expedition (KM1128; October 2011), the U.S. GEOTRACES GP16 expedition (TN303; October–December 2013), the ProteOMZ expedition (FK160115; January–February 2016), and the U.S. GEOTRACES GP15 expedition (RR1814 and RR1815; September–November 2018) (Fig. 2). Dissolved Co and PO_4^{3-} datasets for the METZYME, GP16 and GP15 expeditions have previously been published (Chmiel et al., 2022; Hawco et al., 2016, 2020) and are publicly available in the GEOTRACES Intermediate Data Product (IDP2021; https://www.geotraces.org/geotraces-intermediate-data-product-2021/) (GEOTRACES Intermediate Data Product Group, 2021), and expedition datasets can be accessed individually on the Biological and Chemical Oceanography Data Management Office (BCO-DMO) website (METZYME: https://www.bco-dmo.org/project/2236; GP16: https://www.bco-dmo.org/project/499723; ProteOMZ: https://www.bco-dmo.org/project/685696; GP15: https://www.bco-dmo.org/project/695926).

3.3.2 Dissolved Co and PO_4^{3-} concentrations from the ProteOMZ expedition

Dissolved Co and dPO_4^{3-} concentration data from the ProteOMZ expedition represent novel datasets reported by this study and are available on the BCO-DMO website (https://www.bco-dmo.org/project/685696). Dissolved Co and PO_4^{3-} samples were collected using a trace metal rosette equipped with 8 L X-Niskin bottles (Ocean Test Equipment) as described in (Cutter and Bruland, 2012), subsampled in a trace metal clean plastic "bubble" equipped with HEPA filters providing positive air pressure, and filtered using a 142 mm, polycarbonate plastic sandwich filter rig (Geotech Environmental Equipment) equipped with a 0.2 µm Supor membrane filter (Pall Corporation). Oxygen concentration data was acquired from a calibrated dissolved oxygen sensor (Sea-Bird Electroncs) deployed with the trace metal rosette.

Dissolved Co samples were collected in acid-washed 60 mL low-density polyethylene (LDPE) bottles (Nalgene) and stored until analysis at 4 ºC with one oxygen-absorbing satchel per

sample bottle (Mitsubishi Gas Chemical, model RP-3K). Dissolved Co samples were analyzed in Nov-Dec 2017 by cathodic stripping voltammetry (CSV) as originally described by (Saito and Moffett 2001) and modified by (Saito et al. 2010; Hawco et al. 2016), the same electrochemical procedure used on the METZYME, GP16 and GP15 expeditions. One portion of the samples (Stations 1–10) were analyzed in the Saito laboratory in Woods Hole, MA, and the remaining samples (stations 11–14) were analyzed at sea on the CICLOPS NBP-1801 cruise in the trace metal plastic "bubble". This was done so that all of the samples could be run synchronously using the same batch of DMG and EPPS reagents. The analytical dCo blank associated with this sample batch of reagents was determined to be 2.3 pM (n = 3).

Dissolved PO_4^{3-} samples from the ProteOMZ expedition were stored frozen in acid-washed 60 mL high-density polyethylene (HDPE) bottles until analysis via the molybdenum blue method on a Technicon AutoAnalyzer IITM (Bernhardt and Wilhelms, 1967).

3.3.3 Particulate Co and P concentrations on the GP15, GP16 and METZYME expeditions

Particulate Co and P samples from the GP15 expedition were collected using in situ pumps (McLane Research; WTS-LV) equipped with polyester prefilters (> 51 µm) and Supor filters (0.8–51 µm). Small particulate, total (SPT) pCo and pP samples were subsampled from the Supor filter, while large particulate, total (LPT) samples were subsampled from the prefilter. Particulate samples were digested via hot refluxing with nitric and hydrofluoric acid, and were measured via high-resolution ICP-MS following methods previously described (Lam et al., 2015, 2018). The pCo and pP dataset from the GP16 expedition used comparable methods and have been published and described in (Lam et al., 2018). The dataset is available on the BCO-DMO website (https://www.bco-dmo.org/project/499723). Particulate Co and P samples from the METZYME expedition were collected from a trace metal clean CTD rosette and filtered onto 47 mm, 0.2 µm Supor filters (size fraction ≥ 0.2 µm). Note that this size fraction is smaller than the size fraction from the GP15 and GP16 expeditions, and as such METZYME likely capture additional microbial populations. Samples were digested for 3 hours in 50% nitric acid at 90º C and analyzed via ICP-MS by T. Goepfert, as described in (Goepfert, 2013). Since pCo tends to have a small lithogenic component, particularly in this geographic region, and the biogenic component is acid labile, the variability in digestion approaches between the GEOTRACES expeditions and METZYME likely had a minor impact on results.

3.3.4 Two-way (type-II) linear regressions

Two-way linear regressions allow for error in both the x and y parameters and do not assume dependence between the two axes; this makes two-way regressions ideal for stoichiometric analyses where both axes represent a concentration value. This study used an algorithm for two-way linear regressions that was originally written for MATLAB (lsqfitma.m) by Ed Peltzer circa 1995 (Glover et al., 2011) and was re-written in Python 3 in 2021 (Chmiel et al., 2022). The Python code is available at https://github.com/rebecca-chmiel/GP15.

3.3.5 Determination of dZn concentrations

Upper ocean dZn samples from the GP15 expedition were analyzed following the procedures presented in (Jensen et al., 2020; Lagerström et al., 2013). Briefly, samples were collected in LDPE bottles, acidified to 24 mM HCl, and spiked with an isotope standard that included ^{68}Zn. Samples were then pre-concentrated using a seaFAST system onto a Nobias Chelate PA-1 resin, eluted off of the column with HNO_3, and quantified by ICP-MS using isotope dilution.

3.3.6 GP15 surface protein transect

Filtered particulate samples for proteomic analysis were collected from 24 stations on both legs of the GP15 expedition via the underway seawater system (Table C1). Particulate samples were first filtered through 51 µm Nitex filters (not collected), then sequentially filtered through 3 µm Versapore filters and 0.2 µm Supor filters. The volume of seawater filtered varied between 15 L and 58 L, depending on the oligotrophy of the seawater. Both size fractions of filter were sub-sampled into proteomics samples and DNA samples (not included in this dataset), with 7/8 of the filter collected for proteomic analysis. Samples were stored at -80ºC. The dataset presented here includes only the 0.2 µm filter samples, representing the bacterial 0.2–3 µm particulate fraction.

Protein samples were extracted and analyzed using methods previously described in (Cohen et al., 2021; Saito et al., 2014). Briefly, proteins were extracted, purified and digested with trypsin via the polyacrylamide gel electrophoresis tube gel method (Lu and Zhu, 2005), then quantified with a BSA assay (Bio-Rad Laboratories). Protein extracts were then separated by online nanoflow 2D active modulation liquid chromatography and run on a Thermo Fusion quadrupole-Orbitrap mass spectrometer (Thermo Scientific) to detect peptide amino acid sequences (McIlvin and Saito, 2021). Mass spectra were searched against the METZYME

transcriptome using Proteome Discoverer's SEQUEST HT algorithm (Thermo, Proteome Discoverer 2.2) with a fragment tolerance of 0.6 Da and parent tolerance of 10 ppm. Identification criteria consisted of a peptide threshold of 95% and protein threshold of 99% (1 peptide minimum), corresponding to a protein false discovery rate (FDR) of less than 1% when analyzed with Scaffold version 5.1.2 (Proteome Software, Inc.). Peptide sequences were matched to annotations in the National Center for Biotechnology Information (NCBI) non-redundant database by J. Espinoza and C. Dupont using the DIAMOND protein aligner.

3.4 Results

3.4.1 Dissolved Co distributions across the Pacific basin

3.4.1.1 The ProteOMZ dCo transect

The ProteOMZ expedition surveyed trace metal biogeochemistry of the pelagic equatorial Pacific, including the Eastern Tropical North Pacific (ETNP) oxygen minimum zone (OMZ), and a region of equatorial upwelling at and around the equator (Fig. 3a). The expedition first transited south from Hawaii 17º N–8º N (Stations 1-5), bisecting the ETNP OMZ and recording an oxygen minimum of 3 µmol kg^{-1} (300 m) at 10º N (Station 4), then traveled east along 10º N through the center of the ETNP feature. At 140º W, the transect turned south again towards Tahiti, bisecting the equator and less intense oxygen minimum in the ETSP at 4.2º S (17.89 µmol kg^{-1} O_2 at 400 m; Station 13). Within the equatorial Pacific, regional upwelling sustained shallow mixed layer depths throughout the majority of the ProteOMZ expedition, observable from the nutricline of the dPO_4^{3-} transect (Fig. 3d). At the north and south boundaries of the expedition (Stations 1 and 14), the mixed layer depth deepened, indicating the beginning of the downwelling, oligotrophic North and South Pacific subtropical gyres.

The ETNP OMZ forms along the coast of North America and extends westward into the pelagic Pacific basin. It is mirrored by the Eastern Tropical South Pacific (ETSP) OMZ to the south of the equator, which extends westward off the coast of South America but does not reach as far west into the central Pacific basin as the ETNP (Stramma et al., 2008). Both OMZ features are formed from high productivity fueled by the coastal upwelling of macronutrients and the corresponding consumption of O_2 via the remineralization of organic carbon. The poor ventilation of the intermediate water mass isolates the water and forms "shadow zones" that propagate the oxygen minima feature westward (Karstensen et al., 2008). The resulting low-oxygen

environments in the equatorial Pacific Ocean alter the biogeochemistry of redox-sensitive trace metals like Co within their waters (Chmiel et al., 2022; Hawco et al., 2016).

Dissolved Co concentrations along the ProteOMZ transect are novel data presented by this study (Fig. 3b). In the surface ocean (20 m), dCo was depleted by biological uptake to an average concentration of 13 ± 11 pM (n = 11), and this depletion signal becomes deeper and more extreme towards the oligotrophic gyres to the north and south of the transect, following the dPO_4^{3-} nutricline. Dissolved Co accumulated in intermediate waters due to the remineralization of biomass and regeneration of inorganic nutrients. Within the low-O_2 environments of the ETNP and ETSP, hotspots of elevated dCo within intermediate waters were observed, particularly along the shallower regions of the OMZs. Elevated dCo concentrations within OMZs have been observed in the North Atlantic and South Atlantic, as well as previously in the ETNP and ETSP (Ahlgren et al., 2014; Baars and Croot, 2014; Chmiel et al., 2022; Hawco et al., 2016; Noble et al., 2012, 2017; Saito et al., 2004) due to the converging processes of a terrestrial dCo source from the continental margins, organic matter remineralization and a suppression of dCo scavenging rates to Mn-oxide particles in the low-O_2 environment (Chmiel et al., 2022; Hawco et al., 2016). Above 1500 m, the entire ProteOMZ section displayed a negative linear trend between dCo and O_2, with a dCo : O_2 ratio of -0.32 ± 0.02 µM : mol kg^{-1} (R^2 = 0.58; n = 155; Fig. 3e). The dCo : O_2 ratio observed on the ProteOMZ expedition was similar to those observed within the ETSP on the GP16 expedition (-0.34 µM : mol kg^{-1}; Hawco et al., 2016) and within the Tropical North Atlantic (-0.39 µM : mol kg^{-1}; Baars and Croot, 2014), but lower than those observed within the ETNP and ETSP along the GP15 expedition (-0.72 and -0.73 µM : mol kg^{-1}, respectively; Chmiel et al., 2020), possibly because, like the GP16 ratio, the value was derived as an aggregate signal across the entire ProteOMZ transect and the multiple water mass regions covered by it.

3.4.1.2 Comparison of dCo along ProteOMZ, GP15, GP16 and METZYME

The GP15, GP16 and METZYME dCo sections have been previously characterized elsewhere (Chmiel et al., 2022; Hawco et al., 2016, 2020). Similar to the ProteOMZ section, dCo was depleted in the surface ocean in these three datasets, particularly within the North Pacific subtropical gyre (~18º–40º N) and the South Pacific subtropical gyre (> 5º S and > 100º W), and accumulated in intermediate waters (Fig. 4; Fig. D1). The GP15 and METZYME transects crossed both the ETNP and ETSP, and cross sections of both OMZs were observable in the dCo transect

in the subsurface ocean at ~10º N and ~5º S where elevated dCo levels depict the geochemical influence of OMZs on dCo cycling, even far removed from the continental margins where the OMZs are strongest. The GP16 transect began within the core of the ETSP OMZ along the Peruvian coast and followed the OMZ westward into the pelagic Pacific. The resulting dataset captured a dCo hotspot associated with low-O_2 concentrations where substantial dCo sources from phytoplankton biomass remineralization and continental margin sediments coincided with a suppressed dCo sink from low oxide scavenging rates within the OMZ (Hawco et al., 2016), forming the advected ETSP dCo signal observed in the GP15, METZYME and ProteOMZ transects. Both the GP15 and GP16 transects depicted coastal sources of dCo from the Alaskan and Peruvian coast, respectively, and hydrothermally-associated dCo was observed directly above the Loihi Seamount (1290 m) at GP15's Station 18.6 (18.9º N) (Chmiel et al., 2022; Hawco et al., 2016).

3.4.2 The METZYME pCo transect and comparison to prior pCo datasets

Particulate Co and P concentrations from the METZYME represent novel data presented by this study. The resulting particulate transect extended southwest from Hawaii towards the Samoan Islands, spanning ~35º of latitude (Fig. 5). South of the Samoan Islands, the transect turned west, traveling between 170º - 173º W. Particulate Co and P were collected on 0.2 μm filters, primarily characterizing the bacterial biomass fraction. The resulting pCo transect displayed elevated concentrations in the surface ocean above ~100 m depth, including a maximum of 2.6 pM at 40 m depth (Station 6). Particulate Co distributions followed similar trends as the pP transect, which also exhibited a subsurface maximum at Station 6 (19.6 nM; 40 m depth), indicating that the majority of pCo along the METZYME transect was associated with particulate biomass in a surface phytoplankton bloom. The hotspot of pCo south of the equator sat directly above the ETSP OMZ, which began ~150 m depth; there, the distribution of pCo was generally opposite the depth trends of dCo, which showed a deeper hotspot at 199 m depth and surface dCo concentrations under 10 pM (Fig. D1). These mirrored distributions reflect the coupling of Co's dissolved and particulate phases as mediated by biological uptake of dCo into the particulate phase by phytoplankton in the surface ocean and remineralization of particulate biomass back into the dissolved phase in intermediate waters.

The previously reported GP15 and GP16 pCo datasets (Chmiel et al., 2022; Hawco et al., 2016; Lam et al., 2018) were collected on quartz filters with a prefilter that have an effective size fraction of 0.8–51 µm, which is a slightly larger fraction than METZYME (> 0.2 µm) and may miss some of the smaller prokaryotic fraction. Both the GP15 and GP16 transects displayed surface pCo maximums associated with particulate biomass (Fig. D2). GP15 exhibited elevated pCo concentrations in the surface North Pacific subpolar gyre and the equator, two upwelling regions associated with high phytoplankton productivity, and displayed relatively lower surface pCo concentrations in the oligotrophic North and South Pacific subtropical gyres. Along GP16, surface pCo was highest along the coast above the core of the ETSP OMZ (77º–100º W), where abundant phytoplankton were fueled by upwelling macronutrients along the Peruvian coast (Hawco et al., 2016; Lam et al., 2018). The elevated surface pCo signature continued between 100º–140º W as upwelled macronutrients were advected westward, and declined towards the western extreme of the transect (152º W). Like the METZYME transect, the surface pCo hotspots were offset from intermediate dCo hotspots around 200 m depth (Fig. D1), illustrating the coupling of dCo and pCo during biological uptake and remineralization processes. In the GP16 transect, an intermediate (~350 m) pCo hotspot west of the oxic-anoxic boundary of the ETSP OMZ core (~100º W) suggests a high Co scavenging rate to Mn-oxides due to the build-up of dCo within the OMZ and resulting loss of dCo to pCo once advected westward to oxic waters (Hawco et al., 2016).

3.4.3 Bacterial protein biomarkers along the GP15 surface transect

The bacterial fraction (0.2–3 µm) metaproteome of the surface ocean (~2 m depth) was analyzed at 24 stations along the GP15 expedition, providing insight into the dynamic bacterial communities and expression of protein biomarkers across several nutrient limitation regimes in the Pacific Ocean. Across the 24 stations, 28,701 proteins were identified from 52,531 unique tryptic peptides and 896,751 identified mass spectra of bacterial and archaeal proteins. Select protein biomarkers were chosen to identify locations of P, N and Fe stress across multiple bacterial genera, including proteins associated with PO_4^{3-}, urea and Fe transport, as well as the Fe-stress biomarker flavodoxin. As nutrient availability decreases, organisms tend to produce more proteins associated with nutrient transport systems as a strategy to maximize uptake of the nutrient in demand (Cohen et al., 2018; Cox and Saito, 2013). Additionally, flavodoxin is a biomarker of Fe-stress due to its ability to substitute for the Fe-containing ferredoxin protein when Fe is less

available (La Roche et al., 1996; Thompson et al., 2011). Along the GP15 surface transect, 56 PO_4^{3-} ABC transporters, 56 urea ABC transporters, 92 proteins associated with Fe transporters, and 21 flavodoxins were identified in the metaproteome (Fig. 6), reflecting the diversity of metagenomic sequences among the bacterial and archaeal community. 99 of the proteins were annotated as being from *Prochlorococcus* and 25 were annotated as being from *Synechococcus*, the two genera that appeared most frequently in the GP15 protein transect. The data for all proteins are in the process of being incorporated into the Ocean Protein Portal (www.oceanproteinportal.org) (Saito et al., 2021).

The GP15 surface protein transect displayed 3 distinct regions of P, N and Fe nutrient stress. Between ~20º–40º N, phosphate ABC transporters were abundant (Fig. 6a), suggesting regional P-stress within the North Pacific subtropical gyre. This observation was surprising since only diazotrophs are predicted by modeling studies to experience P-limitation in this region (Moore et al., 2013b), while plankton who do not fix N_2 like *Prochlorococcus* are not predicted by observational or modeling studies to be growth limited by PO_4^{3-} in this region (Moore et al., 2013a, 2013b). However, *Prochlorococcus* and some Alphaproteobacteria exhibited a robust, regional signal of metabolic P-stress. Further south between ~5º–20º N, urea ABC transporters rose in the northern equatorial Pacific, suggesting N-stress in the region. Then, at the equator between ~5º S–15º N, flavodoxins and iron transport proteins were abundant, suggesting Fe-stress. Flavodoxins were more abundant on the equator as well as slightly to the north (~5º–11º N), while iron transport proteins were abundant primarily at the equator. This second peak of flavodoxin north of the equator is suggestive of an intermediate response (increased flavodoxin without increased iron transporter) to scarce dFe, similar to that observed in coastal *Synechococcus* (Mackey et al., 2015). Alternatively, it is possible (albeit less likely) that the matagenomic database used for mapping protein identifications lacked a gyre homologue for *Prochlorococcus* transporters.

The stations at which biomarker spectral counts were at their maximums did not tend to overlap with biomarker peaks for stressors of different nutrient regimes (i.e. the phosphate ABC transporter peak began ~22º N, exactly where the urea ABC transporter peak trended downward). However, the biomarker proteins were often still present at lower abundances in regions where another nutrient stress biomarker was abundant, indicating regions of co-stress and possibly nutrient co-limitation. Such regions of overlapping nutrients included N- and P-stress throughout

most of the North Pacific basin between ~0º–40º N, and especially the north equatorial Pacific between ~0º–20º N, where biomarkers for N-, P- and Fe-stress were all abundant, suggesting a complex nutrient limitation regime among the equatorial bacterial community. It is notable, however, that *Prochlorococcus* urea transporter spectra were detected in the transect's metaproteome at an abundance at least an order of magnitude higher than those of other stress biomarkers in the subtropical North Pacific, suggesting that while P-stress and Fe-stress displayed regional trends among the bacterial community, N-stress appeared widespread throughout the region.

The low spectral counts of cyanobacterial nutrient stress-related proteins in the subpolar North Pacific above ~40º N was caused by a decrease in abundance of *Prochlorococcus*, whose proteins were extremely abundant throughout the rest of the surface protein transect as larger eukaryotic phytoplankton like diatoms, which are not reflected in this dataset due to the genomic database used, increasingly contributed to primary productivity. Future analysis will explore this eukaryotic community on this transect. Within the subpolar gyre, *Prochlorococcus* was mostly absent from the phytoplankton community, as its growth rate is strongly limited at low temperatures (Moore et al., 1995; Zinser et al., 2007) and "shared predation" while in competition with heterotrophic bacteria (Follett et al., 2022). Interestingly, flavodoxin and iron transport biomarkers from the diminished *Prochlorococcus* population and *Synechococcus* did exhibit local maximums above 40º N, consistent the North Pacific being an Fe-limited region (Boyd et al., 2004; Tsuda et al., 2005).

3.5 Discussion

3.5.1 Pacific Co : P stoichiometry

3.5.1.1 Overview of metrics

To explore trends in cobalt ecological stoichiometry, we used three conventional definitions of stoichiometry: (1) dissolved Co : PO_4^{3-} slopes, (2) dissolved Co : PO_4^{3-} ratios and (3) particulate Co : P ratios. The dCo : dPO_4^{3-} slope is a metric derived from classic Redfieldian stoichiometry (Redfield, 1958), which observed the consistency of dissolved nutrient ratios like N : P across a range of depths, while the dCo : dPO_4^{3-} and pCo : pP ratios of discrete sample depths can inform upon the distributions of nutrients available for uptake and particle composition,

respectively. Comparing and interpreting the results of all three stoichiometry metrics allowed for an in-depth analysis of Pacific Co uptake stoichiometry and biogeochemical cycling processes.

The dCo : dPO_4^{3-} slope was determined from two-way linear regressions of dCo and dPO_4^{3-} concentrations from each expedition, as well as from each station. The dCo vs. dPO_4^{3-} relationship tends to be linear throughout the photic zone and upper ocean as concentrations are driven by the aggregate influence of biological uptake and remineralization processes (Fig. 1; southwest and northeast vectors, respectively), and decouples deeper in the water column as scavenging processes preferentially remove dCo with little effect on dPO_4^{3-} concentrations (south vector). In intermediate waters, the overlap of remineralization and scavenging processes (net southeast vector) creates a "curl" in the dCo vs. dPO_4^{3-} relationship due to the hybrid nature of dCo distributions. This curl was observed in all four Pacific cruises analyzed (Fig. 7a-d), which exhibited a fairly homogenous dCo : dPO_4^{3-} relationship in the deep Pacific ocean (Fig. 7i). To evaluate the dCo : dPO_4^{3-} slope in the upper ocean, it is best to include the sample depths that represent the more linear dCo vs. dPO_4^{3-} relationship as driven by uptake and remineralization, and to omit deeper sample depths where dCo scavenging increasingly becomes a dominant process. Because the depth at which the scavenging process overwhelms the remineralization signal varies by oceanographic province, a consistent method for choosing the depth threshold was used that included upper water column depths that maximized the R^2 value of the dCo : dPO_4^{3-} linear regression. This depth threshold selection allows for the best characterization of the linear relationship between dCo and dPO_4^{3-} in the upper ocean, and best captures the uptake stoichiometry in the photic zone and the remineralization stoichiometry in the mesopelagic prior to losing those signals when scavenging takes over as a dominant process.

The dCo : dPO_4^{3-} ratios from discrete sample depths are interesting stoichiometric trends to consider because they illustrate where dCo is more or less available with respect to the macronutrient dPO_4^{3-}. However, unlike the dCo : dPO_4^{3-} slope, discrete dissolved nutrient ratios can be more ephemeral in their response to biogeochemical processes of Co uptake and remineralization since they can be influenced by short-term or localized biological processes (bloom events), as well as sources of dCo and dPO_4 from aerosol deposition, continental margin sources and advection. The dCo : dPO_4^{3-} ratios have been included here as a way to analyze the availability of dCo compared to other nutrients and to compare the discrete stoichiometry of dCo : dPO_4^{3-} to the stoichiometry of the vertical profile as determined by the dCo : dPO_4^{3-} slopes, but

the Redfield-style slopes are likely a more meaningful value when considering the influence of aggregate plankton stoichiometry on the dissolved nutrient inventory.

The pCo : pP stoichiometric ratio in many ways reflects the inverse of the dissolved stoichiometry and is a direct measure of the aggregate particle stoichiometry as influenced by inputs from biological uptake and losses during remineralization. However, below a certain depth, the signal of phytoplankton Co stoichiometry becomes mixed with a distinctly different signal from mineral phases due to pCo's association with Mn-oxide particles. In the North Atlantic Ocean, pCo vs. pP displayed a linear relationship above 400 m where pCo was primarily associated with phytoplankton biomass, while pCo vs. pMn displayed a linear relationship below 400 m where pCo was primarily associated with Mn-oxides (Saito et al., 2017).

3.5.1.2 dCo : dPO_4^{3-} slope stoichiometry

Dissolved Co : PO_4^{3-} slopes were calculated for each expedition, as well as an aggregate dCo : dPO_4^{3-} slope of 70 ± 2 µmol : mol across the entire Pacific basin (Fig. 7e-h,j; Table 1). The ProteOMZ and METZYME datasets displayed the lowest dCo : dPO_4^{3-} slopes (41 ± 2 and 53 ± 2 µmol : mol, respectively), and the deepest depth thresholds (155 and 225 m, respectively). The GP15 and GP16 expeditions demonstrated higher dCo : dPO_4^{3-} slopes (78 ± 3 and 64 ± 1 µmol : mol, respectively) and shallower depth thresholds (95 and 110 m). These differences span an almost two-fold difference in Co stoichiometry, far greater than that typically observed for other macro- and micronutrients and which could be induced by a variety of biogeochemical influences. Because all four expeditions included here span multiple oceanographic provinces with unique Co biogeochemistry, we also employed an analysis of the dCo : dPO_4^{3-} slope on a station-by-station basis to further evaluate trends in Co stoichiometry.

The results of the dCo : dPO_4^{3-} slopes calculated for each station are presented in Fig. 8 and Tables G1-G4. Of the station regressions that displayed a linear correlation ($R^2 \geq 0.7$), the average slope was 48 ± 71 µmol : mol and the average depth threshold was 360 ± 460 m (n = 87). Several stations displayed a linear relationship between dCo and dPO_4^{3-} deep into the water column (up to 1502 m at GP16 Station 26), which indicates that dCo remineralization in intermediate waters was a dominant process compared to Co scavenging in those locations. However, when the depth threshold was deeper than 750 m, the average dCo : dPO_4^{3-} slope was lower than the average slope of all stations (22 ± 10 µmol : mol compared to 48 ± 71 µmol : mol), likely because dCo

scavenging was still depressing the dCo : dPO_4^{3-} stoichiometry despite the lack of a strong dCo and dPO_4^{3-} decoupling signal and/or the preferential loss of Co relative to P during remineralization. The dCo : dPO_4^{3-} slopes were consistently low along the ProteOMZ and METZYME transects, which is consistent our observations of lower aggregate dCo : dPO_4^{3-} slopes for the expeditions (Fig. 7f,h).

The dCo : dPO_4^{3-} slopes displayed several regions of high stoichiometry, particularly around the equator and in the North Pacific (Fig. 9). In the equatorial Pacific between 0º–5º S, the GP15, ProteOMZ and METZYME expeditions all contained local maximum in slopes compared to the surrounding stations (GP16 did not cross these latitudes). GP15 Stations 29 (0º) and 33 (5º S) both showed extraordinarily high slopes of 209 ± 14 (R^2 = 0.97) and 279 ± 12 (R^2 = 0.99), respectively. Similarly, in the North Pacific, the dCo : dPO_4^{3-} slope was elevated above 80 µmol : mol consistently along the GP15 transect between 49.5º–32º N (Stations 7 – 14), reaching as high as 173 ± 47 µmol : mol (R^2 = 0.73) at Station 8 (47º N). This region of consistently high dCo : dPO_4^{3-} stoichiometry across depth was not contained to one oceanographic province; instead, it spanned from the highly productive North Pacific subpolar gyre into the oligotrophic North Pacific subtropical gyre, implying a trend towards higher dCo stoichiometry in regions of nutrient province transition. The GP16 transect also displayed some regions of high dCo : dPO_4^{3-} slope, reaching as high as 175 ± 12 µmol : mol (R^2 = 0.97) at Station 15 (104º W). This location is notably just west of the approximate oxic-anoxic boundary of the core of the ETSP OMZ (100º W) (Hawco et al., 2016), representing another location of high dCo stoichiometry within regions of biogeochemical transition. The high Co stoichiometry signals in the equator and the North Pacific are examined in more detail in Sect. 3.5.3 and 3.5.4, respectively.

3.5.1.3 dCo : dPO_4^{3-} ratio stoichiometry

In the upper ocean (≤ 500 m depth), the dCo : dPO_4 ratios ranged between 4 – 1650 µmol : mol, spanning 4 orders of magnitude (Fig. 9; Tables F1-F4). Intermediate depths below ~200 m exhibited lower and more consistent dCo : dPO_4^{3-} ratios (average = 28 ± 12 µmol : mol at depths of 300–500, n = 232), while higher dissolved ratios tended to occur in the surface and subsurface ocean. The highest dCo : dPO_4 ratios occurred along the northern component of the GP15 transect; at the surface of Station 1, the most coastal station along the Alaskan coast, the dCo : dPO_4^{3-} ratio was 1279 µmol : mol (~2 m depth), driven by high coastal sources of dCo associated with fresh

riverine inputs. Moderately elevated dCo : dPO_4^{3-} ratios along the subsurface GP16 transect followed the dCo plume within the ETSP (see Sect. 3.4.1.2), illustrating how dCo accumulation – due to remineralization and lack of Mn-oxide bacterial scavenging – and advection within OMZs can act as an internal dCo source.

The GP15 transect displayed high dCo : dPO_4^{3-} ratios in the surface and sub-surface of the ultra-oligotrophic North Pacific subtropical gyre (35.5º–17.5º N). The maximum dCo : dPO_4^{3-} ratio in this region was observed to be 1127 µmol : mol (80 m depth), but in some cases the dissolved ratio may have been even higher since dPO_4^{3-} was present at undetectable levels (reported to 2 decimal places) and the ratio could not be calculated. This elevated dCo : dPO_4^{3-} signal in the North Pacific subtropics was also visible to a lesser extent at the north end of the METZYME transect (maximum of 115 µmol : mol at 17º N, 150 m depth) and perhaps in the ProteOMZ transect between 10º–20º N (maximum of 302 µmol : mol at 10º N, 60 m depth). The high dCo : dPO_4^{3-} values within the surface and subsurface of the oligotrophic gyre notably overlapped with the peak in spectral counts for PO_4^{3-} ABC transporters, biomarkers for P-stress along GP15 (Fig. 6a). This elevation in the discrete dissolved ratio was likely influenced by high PO_4^{3-} depletion to undetectable values (< 0.01 µM) in this oligotrophic region, while dCo concentrations were depleted (< 10 pM) to a lesser extent). It is interesting to note that the dCo : dPO_4^{3-} discrete ratios appeared to follow trends within oceanographic provinces, while the dCo : dPO_4^{3-} slope values were elevated within regions of transition across oceanographic provinces.

3.5.1.4 Particulate Co : P stoichiometry

The pCo : pP ratio tended to be highest in deeper intermediate waters (563 ± 519 µmol : mol between 300 and 500 m depth; n = 84), and lower in shallower waters (186 ± 302 µmol : mol ≤ 100 m depth; n = 158; Fig. 10; Tables G1-G3). Like in the Atlantic, pCo and pP distributions were linearly correlated across the GP15, GP16 and METZYME expeditions (≤ 300 m depth) (Fig. 10b,e,h; Table 2). In intermediate waters (300–500 m), pCo and pMn were linearly correlated along GP16 (R^2 = 0.86), loosely correlated along METZYME (R^2 = 0.55), and uncorrelated along GP15 (R^2 = 0.18). This regression analysis suggests that pCo was consistently associated with phytoplankton biomass throughout the upper Pacific Ocean, but that pCo association with Mn-oxide particles in intermediate waters was regionally dependent. The GP16 expedition displayed a strong pCo scavenging signal to the west of the anoxic OMZ core (~100º W), while there was

evidence of suppressed scavenging at low O_2 levels within the ETSP OMZ (Hawco et al., 2016). In comparison, the North Pacific exhibited a weaker scavenging signal, likely related to the broad, deep oxygen minima the stretches across the intermediate North Pacific basin, and corresponding lower Mn-oxide particles and higher concentrations of strong ligand-bound dCo, as characterized by Chmiel et al., 2022. This weak scavenging signal, in addition to the wide range of oceanographic provinces sampled, likely contributed to the lack of pCo : pMn correlation along GP15.

A study by Ohnemus et al. 2017 corrected for the lithogenic and ferruginous phases of particles sampled on GP16, allowing for the analysis of biological-associated particles. The study concluded that there were higher ratios of bioactive trace metals associated with biomass within the ETSP OMZ compared to the surrounding oxic ocean (Ohnemus et al., 2017). The pCo : pP ratio associated with biomass along GP16 was found to be elevated within the western "heterotrophic" OMZ (430 ± 160 μmol : mol compared to 270 ± 60 μmol : mol in the mixed layer; from Ohnemus et al., 2017; Table 3), which refers to the western tail of the ETSP OMZ between 91.5º and 101.5º W where heterotrophic respiration of the ETSP upwelling bloom is a dominant process. This is also a region where we observed slightly higher total particle pCo : pP ratios in the depths associated with the OMZ (~150–300 m) along the GP16 transect, supporting the conclusion that pCo : pP stoichiometry was elevated in the heterotrophic OMZ where the plankton community was transitioning between an oxygen deficient and oxic mesopelagic.

3.5.2 dZn : dCo stoichiometry in the surface ocean of the GP15 transect

The distribution of dZn in the upper ocean must also be examined when considering Co stoichiometry and metabolic use by phytoplankton. Dissolved Zn concentrations are typically at least an order of magnitude more abundant that dCo concentrations throughout the ocean due to dZn's deep inventory and lack of significant loss via particle scavenging, but recent data showing high dCo : dZn ratios in the coastal surface ocean reveals that this is not always the case (Kellogg et al., 2020). The Zn uptake transporters of many phytoplankton have difficulty distinguishing between Zn and Co because they share the same divalent charge and similar atomic radii, and thus the uptake rate of the two metals influenced by their relative concentrations within the surrounding seawater and their binding affinities to the ligands within their membrane transport systems (Irving and Williams, 1953; Sunda and Huntsman, 1995). Additionally, many but not all phytoplankton

are able to substitute Co for Zn as the cofactor in the carbonic anhydrase metalloenzyme (Kellogg et al., 2020, 2022; Price and Morel, 1990; Sunda and Huntsman, 1995), which contributes to the flexibility of Co metabolic use and thus Co stoichiometry among phytoplankton (Saito et al., 2017).

Along the pelagic GP15 expedition (excluding coastal stations 1-3), surface ocean (~2 m) dZn concentrations ranged from 26–622 pM, ~1 of magnitude higher than the dCo surface concentration range of 0 (undetectable)–88 pM. However, at Stations 1 and 2, the two most coastal stations along the Alaskan coast, surface dCo concentrations (576 and 244 pM, respectively) actually exceeded dZn concentrations (234 pM and 201 pM, respectively), for a dCo : dZn ratio of 2.46 and 1.22, respectively. Surface dCo : dZn ratios as high as 3.52 have previously been observed along Line P within the coastal Northeastern Pacific Ocean, and have been linked to efficient Zn/Co substitution metabolisms within diatom strains isolated from the region (Kellogg et al., 2020). In both the GP15 and Line P coastal stations, the excess dCo concentrations were likely the result of local riverine sedimentary sources that themselves contained a high Co : Zn ratio.

In the more pelagic regions of the GP15 transect, the dCo : dZn tended to be highest in the subsurface ocean between ~50–300 m (Fig. 11). In the equatorial Pacific, high dCo : dZn values (maximum of 0.74) appeared associated with the elevated dCo concentrations within the ETNP and ETSP at ~10º N and ~5º S (see Sect. 3.4.1.2), which is consistent with the understanding the dCo is elevated within OMZs due to a suppressed rate of scavenging to Mn-oxides, a process that has little effect on dZn concentrations. In the surface of the equatorial Pacific (~2.5º N–2.5º S) and North Pacific subpolar gyre (~55–44º N), the dCo : dZn ratios were also elevated to maximums of 0.52 and 0.50, respectively, suggesting that in regions of macronutrient upwelling and the subsequent development of Fe-limitation, dZn may become depleted with respect to dCo due to high eukaryotic requirements for Zn. In contrast, the dCo : dZn ratios were particularly low throughout the surface of the North and South Pacific subtropical gyres, indicating that dCo was depleted with respect to dZn and was less available for uptake by phytoplankton. Additionally, Co bound to strong organic ligands would not be available for uptake through the shared labile Zn/Co transport system, and so would likely be protected from uptake even under low dZn conditions. The observation of notably high dCo : dZn ratios in several regions of the Pacific basin have implications for the micronutrient availability and metabolic strategies of the microorganisms

living there. Organisms with flexible metal requirements – that can substitute Co for Zn in carbonic anhydrase, for example – are more likely to succeed in this environment (Kellogg et al., 2020).

3.5.3 High dCo stoichiometry in regions of oceanographic province transition

The dCo : dPO_4 slope was consistently elevated above 80 μmol : mol between 49.5º–32º N (GP15 Stations 7–14) in the North Pacific Ocean (Fig. 9a). This region spans the transition zone chlorophyll front (TZCF), which separates the low-chlorophyll subtropical gyre to the south, dominated by pico-cyanobacteria like *Prochlorococcus*, from the higher-productivity subpolar gyre to the north, dominated by eukaryotes like diatoms and haptophytes (Polovina et al., 2001, 2017). The transition between biomes was clearly reflected in the bacterial protein biomarkers, which illustrate a shift from low bacterial peptide abundances and a local maximum of flavodoxin north of 40º N, to a P- and N-stressed bacterial community south of 40º N (Fig. 12). The region also showed a transition between higher dCo : dZn ratios to the north to lower dCo : dZn ratios to the south (Fig. 11), indicating a shift in the relative availability of micronutrients to phytoplankton communities in the region.

Below the TZCF, a broad oxygen minimum region is caused by overturning old, deep Pacific water, high surface productivity and subsequent drawdown of oxygen via subsurface remineralization. TZCF has previously been observed to contain a unique dCo cycle, with low rates of mesopelagic ventilation and Co scavenging in and below the oxygen minima, high particulate organic carbon (POC) export, and a higher intermediate and deep dCo inventory than predicted by thermohaline circulation and advection (Chmiel et al., 2022). It is likely that eukaryotic phytoplankton communities like diatoms and haptophytes, at the transition between macronutrient-replete and Fe-replete oceanographic provinces, displayed increased productivity and increased uptake and use of dZn (and by proxy, dCo) due to the high metabolic demand required from living in a transitional biome. Zn is required for a wide range of metabolic processes including the uptake of organic PO_4^{3-} via alkaline phosphatase, an enzyme that reduces P-stress by cleaving dPO_4^{3-} functional groups from dissolved organic phosphorous molecules (Duhamel et al., 2010; Quisel et al., 1996). It is also speculated that Co can also substitute for Zn within some alkaline phosphatases, although this has not been proven among marine phytoplankton (Saito et al., 2017). High surface uptake of dZn and dCo through their shared metal transport system, coupled with strong mesopelagic remineralization and low rates of Co scavenging, likely explain

the elevated dCo : dPO_4^{3-} slopes and illustrate strong biological coupling between dCo and pCo processes.

3.5.4 Elevated dCo stoichiometry in the Equatorial Pacific

The pelagic equatorial Pacific is characterized by equatorial upwelling of deep water that transports nutrients like PO_4^{3-} and nitrate (NO_3^-) into the upper ocean, as well as the ETNP and ETSP OMZs in intermediate waters to the north and south of the equator. The upwelling of macronutrients from the deep ocean alleviates the N and P limitation characteristic of the surrounding subtropical gyres and allows for the development of Fe limitation due to low supply of available Fe from the deep ocean or from aerosol particle loading in the region (Behrenfeld et al., 1996; Kolber et al., 1994). Fe limitation in this region is supported by the surface cyanobacterial biomarkers, which show maximums in the spectral counts of both flavodoxin and Fe transport proteins (Fig. 12), a trend that has been previously observed at the equator within the METZYME metaproteome dataset (Saito et al., 2014). To the north and south of the equator, N and P biomarkers are also abundant, suggesting a surface ocean biome that experiences simultaneous micro- and macronutrient stress.

Within the equatorial Pacific, Co stoichiometry displayed instances of elevated dCo : dPO_4^{3-} slopes across 3 expeditions (Fig. 9; Fig. 12). The surface and subsurface pCo : pP ratio was also elevated in this region compared to the surrounding subtropical gyres (Fig. 10a,j), indicating that Co is being incorporated into biomass at a relatively higher stoichiometry. Both of these elevated Co stoichiometry metrics can be explained by the high dCo : dZn ratio in the surface ocean (Fig. 11); high eukaryotic productivity at the equator driven by the upwelling of macronutrients likely depleted the dZn concentrations in surface waters in addition to dFe concentrations. Eukaryotic phytoplankton like diatoms are more abundant in the macronutrient-rich equatorial upwelling biome compared to the surrounding oligotrophic gyre (Chavez et al., 1990), and they often require a high metabolic requirement of Zn and contain efficient Zn transport systems (John et al., 2007; Kellogg et al., 2020, 2022; Sunda and Huntsman, 1992). In contrast, Pacific *Prochlorococcus* exhibit a low requirement for Zn and no evidence of upregulating Zn transport systems under low Zn conditions (Hawco et al., 2020), which could explain the low dCo : dZn signal in the *Prochlorococcs*-dominated oligotrophic gyres. The dCo inventory, unlike the dZn inventory, had an additional source from internal cycling within the ETNP and ETSP OMZs,

allowing dCo to have been relatively more available throughout the upper equatorial Pacific Ocean. The low dZn concentrations likely led to the increase of both Zn and Co uptake via their shared transporters, and eukaryotes with flexible metabolisms that can utilize Co as a replacement for Zn would also have been environmentally favored, providing two possible mechanisms for the observed increase in the Co stoichiometry associated with phytoplankton biomass.

3.6 Conclusion: interpreting Co ecological stoichiometry metrics

The three stoichiometric values – Redfieldian dCo : dPO_4^{3-} slopes, discrete dCo : dPO_4^{3-} ratios and discrete pCo : pP ratios – are distinct metrics that can be used to illuminate spatial patterns of marine Co ecological stoichiometry. Of the three metrics, the Redfieldian slope analysis appeared to best account for the coupling between the dCo and pCo fractions within phytoplankton uptake and remineralization processes (Fig. 13). The dCo : dPO_4^{3-} slope stoichiometry was inherently highest when dCo was depleted in the surface ocean and elevated in intermediate waters, and thus was a measurement of the coupling between the dissolved and particulate phases of the marine Co cycle via biological uptake and remineralization. The dCo : dPO_4^{3-} and pCo : pP ratios tended to capture a wider range of Co cycling processes and timescales, and were affected by additional source and sink processes like external abiotic inputs and Mn-oxide scavenging. An analysis of all three metrics has allowed this study to illustrate trends in Co ecological stoichiometry that were dependent on the processes of biological uptake, remineralization, scavenging and terrestrial sources across a range of nutrient regimes.

This study evaluated the relationship between Co stoichiometry metrics and the biogeochemical processes their values were responding to. Surface protein biomarkers illuminated basin-scale patterns of nutrient stress across oceanographic provinces, including identifying a region of P-stress not previously predicted by nutrient limitation models (Moore et al., 2013b) in the subtropical North Pacific. The wide variation and flexibility that Co stoichiometry exhibits in the ocean displayed some trends with latitude and oceanographic region, and could be attributed to variations in nutrient limitation regime, internal (OMZ) and external sources of abiotic Co, relative Zn availability, and phytoplankton community requirements. One key explanation for Co's high stoichiometric variability throughout the upper ocean is its tendency to be cycled with Zn via a shared uptake transporter, allowing Zn stress and Zn uptake requirements to influence Co uptake and thus Co stoichiometry. Co stoichiometry tended to be high in regions of oceanographic

province transition, suggesting that the biological cycling and possibly the metabolic use of Co by phytoplankton increased in regions of multi-nutrient relief. Improving our understanding of Co stoichiometry and its variability throughout the surface ocean can help to develop biogeochemical models of Co and other micronutrients in the global ocean. Co uptake stoichiometry should be expected to vary by Co availability, Zn availability and community structure, and this work helps to establish the special patterns and underlying biogeochemical processes that create the flexible Co metabolisms observed across the Pacific Ocean.

Acknowledgments

The authors thank the crews and science parties of: the R/V Roger Revelle on the GP15 expedition, the R/V Falkor on the ProteOMZ expedition, the R/V Thomas G. Thompson on the GP16 expedition, and the R/V Kilo Moana on the METZYME expedition. We also thank Matthew Charette, Stephanie Dutkiewicz, and Alessandro Tagliabue for writing insights.

References

Ahlgren, N. A., Noble, A., Patton, A. P., Roache-Johnson, K., Jackson, L., Robinson, D., McKay, C., Moore, L. R., Saito, M. A. and Rocap, G.: The unique trace metal and mixed layer conditions of the costa rica upwelling dome support a distinct and dense community of Synechococcus, Limnol. Oceanogr., 59(6), 2166–2184, doi:10.4319/lo.2014.59.6.2166, 2014.

Baars, O. and Croot, P. L.: Dissolved cobalt speciation and reactivity in the eastern tropical North Atlantic, Mar. Chem., 173, 310–319, doi:10.1016/j.marchem.2014.10.006, 2014.

Behrenfeld, M. J., Bale, A. J., Kolber, Z. S., Aiken, J. and Falkowski, P. G.: Confirmation of iron limitation of phytoplankton photosynthesis in the equatorial Pacific Ocean, Lett. to Nat., 383, 508–511, 1996.

Bernhardt, H. and Wilhelms, A.: The continuous determination of low level iron, soluble phosphate and total phosphate with the AutoAnalyzer(TM), in Technicon Symposium, vol. 1, p. 386., 1967.

Bertrand, E. M., Moran, D. M., McIlvin, M. R., Hoffman, J. M., Allen, A. E. and Saito, M. A.: Methionine synthase interreplacement in diatom cultures and communities: Implications for the persistence of B12 use by eukaryotic phytoplankton, Limnol. Oceanogr., 58(4), 1431–1450, doi:10.4319/lo.2013.58.4.1431, 2013.

Boyd, P. W., Law, C. S., Wong, C. S., Nojiri, Y., Tsunda, A., Levasseur, M., Takeda, S., Rivkin, R., Harrison, P. J., Strzepek, R., Gower, J., McKay, R. M., Abraham, E., Arychuk, M., Barwell-Clarke, J., Crawford, W., Crawford, D., Hale, M., Harada, K., Johnson, K., Kiyosawa, H., Kudo, I., Marchetti, A., Miller, W., Needoba, J., Nishioka, J., Ogawa, H., Page, J., Robert, M., Saito, H., Sastri, A., Sherry, N., Soutar, T., Sutherland, N., Taira, Y., Whitney, F., Wong, S.-K. E. and Yoshimura, T.: The decline and fate of an iron-induced subarctic phytoplankton bloom, Lett. to Nat., 428, 549–553, doi:10.1029/2001jb001129, 2004.

Bruland, K. W. and Lohan, M. C.: Controls of trace metals in seawater, in Treatise on geochemistry, edited by H. D. Holland and K. K. Turekian, pp. 23–47, Elsevier., 2003.
Chavez, F. P., Buck, K. R. and Barber, R. T.: Phytoplankton taxa in relation to primary production in the equatorial Pacific, Deep Sea Res., 37(11), 1733–1752, doi:10.1016/0198-0149(90)90074-6, 1990.
Chmiel, R., Lanning, N., Laubach, A., Lee, J.-M., Fitzsimmons, J., Hatta, M., Jenkins, W. J., Lam, P. J., Mcilvin, M., Tagliabue, A. and Saito, M. A.: Major processes of the dissolved cobalt cycle in the North and equatorial Pacific Ocean, Biogeosciences, 19, 2365–2395 [online] Available from: https://doi.org/10.5194/bg-19-2365-2022, 2022.
Cohen, N. R., Gong, W., Moran, D. M., McIlvin, M. R., Saito, M. A. and Marchetti, A.: Transcriptomic and proteomic responses of the oceanic diatom Pseudo-nitzschia granii to iron limitation, Environ. Microbiol., 20(8), 3109–3126, doi:10.1111/1462-2920.14386, 2018.
Cohen, N. R., McIlvin, M. R., Moran, D. M., Held, N. A., Saunders, J. K., Hawco, N. J., Brosnahan, M., DiTullio, G. R., Lamborg, C., McCrow, J. P., Dupont, C. L., Allen, A. E. and Saito, M. A.: Dinoflagellates alter their carbon and nutrient metabolic strategies across environmental gradients in the central Pacific Ocean, Nat. Microbiol., 6, 173–186, doi:10.1038/s41564-020-00814-7, 2021.
Cox, A. D. and Saito, M. A.: Proteomic responses of oceanic Synechococcus WH8102 to phosphate and zinc scarcity and cadmium additions, Front. Microbiol., 4(DEC), 1–17, doi:10.3389/fmicb.2013.00387, 2013.
Cutter, G. A. and Bruland, K. W.: Rapid and noncontaminating sampling system for trace elements in global ocean surveys, Limnol. Oceanogr. Methods, 10, 425–436, doi:10.4319/lom.2012.10.425, 2012.
Duhamel, S., Dyhrman, S. T. and Karl, D. M.: Alkaline phosphatase activity and regulation in the North Pacific Subtropical Gyre, Limnol. Oceanogr., 55(3), 1414–1425, doi:10.4319/lo.2010.55.3.1414, 2010.
Follett, C. L., Dutkiewicz, S., Ribalet, F., Zakem, E., Caron, D., Armbrust, V. E. and Follows, M. J.: Trophic interactions with heterotrophic bacteria limit the range of Prochlorococcus, Proc. Natl. Acad. Sci., 119(2), e2110993118, doi:10.1073/pnas.2110993118, 2022.
GEOTRACES Intermediate Data Product Group: The GEOTRACES Intermediate Data Product 2021 (IDP2021)., 2021.
Glover, D., Jenkins, W. and Doney, S.: Modeling Methods for Marine Science, Cambridge University Press, New York., 2011.
Goepfert, T. J.: Urea and nickel utilization in marine cyanobacteria as evaluated by incubation, proteomic, and uptake techniques, Massachusetts Institute of Technology and Woods Hole Oceanographic Institution. [online] Available from: http://dspace.mit.edu/handle/1721.1/7582, 2013.
Hawco, N. J., Ohnemus, D. C., Resing, J. A., Twining, B. S. and Saito, M. A.: A dissolved cobalt plume in the oxygen minimum zone of the eastern tropical South Pacific, Biogeosciences, 13(20), 5697–5717, doi:10.5194/bg-13-5697-2016, 2016.
Hawco, N. J., Lam, P. J., Lee, J., Ohnemus, D. C., Noble, A. E., Wyatt, N. J., Lohan, M. C. and Saito, M. A.: Cobalt scavenging in the mesopelagic ocean and its influence on global mass balance: Synthesizing water column and sedimentary fluxes, Mar. Chem., (August), doi:10.1016/j.marchem.2017.09.001, 2017.
Hawco, N. J., McIlvin, M. M., Bundy, R. M., Tagliabue, A., Goepfert, T. J., Moran, D. M.,

Valentin-Alvarado, L., DiTullio, G. R. and Saito, M. A.: Minimal cobalt metabolism in the marine cyanobacterium prochlorococcus, Proc. Natl. Acad. Sci., 117(27), 15740–15747, doi:10.1073/pnas.2001393117, 2020.

Ho, T., Quigg, A., Finkel, Z. V, Milligan, A. J., Wyman, K., Falkowski, P. G. and Morel, M. M.: The elemental composition of some marine phytoplankton, J. Phycol., 39, 1145–1159, 2003.

Irving, H. and Williams, R. J. P.: The Stability of Transition-metal Complexes, J. Chem. Soc., 3192–3210, 1953.

Jensen, L. T., Wyatt, N. J., Landing, W. M. and Fitzsimmons, J. N.: Assessment of the stability, sorption, and exchangeability of marine dissolved and colloidal metals, Mar. Chem., 220, 103754, doi:10.1016/j.marchem.2020.103754, 2020.

John, S. G., Geis, R. W., Saito, M. A. and Boyle, E. A.: Zinc isotope fractionation during high-affinity and low-affinity zinc transport by the marine diatom Thalassiosira oceanica, Limnol. Oceanogr., 52(6), 2710–2714, doi:10.4319/lo.2007.52.6.2710, 2007.

Karstensen, J., Stramma, L. and Visbeck, M.: Oxygen minimum zones in the eastern tropical Atlantic and Pacific oceans, Prog. Oceanogr., 77, 331–350, doi:10.1016/j.pocean.2007.05.009, 2008.

Kellogg, R. M., McIlvin, M. R., Vedamati, J., Twining, B. S., Moffett, J. W., Marchetti, A., Moran, D. M. and Saito, M. A.: Efficient zinc/cobalt interreplacement in northeast Pacific diatoms and relationship to high surface dissolved Co : Zn ratios, Limnol. Oceanogr., 65(11), 2557–2582, doi:10.1002/lno.11471, 2020.

Kellogg, R. M., Moosburner, M. A., Cohen, N. R., Hawco, N. J., McIlvin, M. R., Moran, D. M., DiTullio, G. R., Subhas, A. V., Allen, A. E. and Saito, M. A.: Adaptive responses of marine diatoms to zinc scarcity and ecological implications, Nat. Commun., 13, doi:10.1038/s41467-022-29603-y, 2022.

Kolber, Z. S., Barber, R. T., Coale, K. H., Fitzwater, S. E., Greene, R. M., Johnson, K. S., Lindley, S. and Falkowski, P. G.: Iron limitation of phytoplankton photosynthesis in the equatorial Pacific Ocean, Lett. to Nat., 371, 145–149, 1994.

Lagerström, M. E., Field, M. P., Séguret, M., Fischer, L., Hann, S. and Sherrell, R. M.: Automated on-line flow-injection ICP-MS determination of trace metals (Mn, Fe, Co, Ni, Cu and Zn) in open ocean seawater: Application to the GEOTRACES program, Mar. Chem., 155, 71–80, doi:10.1016/j.marchem.2013.06.001, 2013.

Lam, P. J., Ohnemus, D. C. and Auro, M. E.: Size-fractionated major particle composition and concentrations from the US GEOTRACES North Atlantic Zonal Transect, Deep. Res. Part II, 116, 303–320, doi:10.1016/j.dsr2.2014.11.020, 2015.

Lam, P. J., Lee, J. M., Heller, M. I., Mehic, S., Xiang, Y. and Bates, N. R.: Size-fractionated distributions of suspended particle concentration and major phase composition from the U.S. GEOTRACES Eastern Pacific Zonal Transect (GP16), Mar. Chem., 201, 90–107, doi:10.1016/j.marchem.2017.08.013, 2018.

Lane, T. W. and Morel, F. M. M.: Regulation of carbonic anhydrase expression by zinc, cobalt, and carbon dioxide in the marine diatom Thalassiosira weissflogii, Plant Physiol., 123(1), 345–352, doi:10.1104/pp.123.1.345, 2000.

Lu, X. and Zhu, H.: Tube-gel digestion: a novel proteomic approach for high throughput analysis of membrane proteins, Mol. Cell. Proteomics, 4(12), 1948–1958, 2005.

Mackey, K. R. M., Post, A. F., McIlvin, M. R., Cutter, G. A., John, S. G. and Saito, M. A.: Divergent responses of Atlantic coastal and oceanic *Synechococcus* to iron limitation,

Proc. Natl. Acad. Sci., 112(32), 9944–9949, doi:10.1073/pnas.1509448112, 2015.
McIlvin, M. R. and Saito, M. A.: Online Nano flow Two-Dimension Comprehensive Active Modulation Reversed Phase − Reversed Phase Liquid Chromatography High-Resolution Mass Spectrometry for Metaproteomics of Environmental and Microbiome Samples, J. Proteome Res., 20, 4589–4597, doi:10.1021/acs.jproteome.1c00588, 2021.
Moffett, J. W. and Ho, J.: Oxidation of cobalt and manganese in seawater via a common microbially catalyzed pathway, Geochim. Cosmochim. Acta, 60(18), 3415–3424, doi:10.1016/0016-7037(96)00176-7, 1996.
Moore, C. M., Mills, M. M., Arrigo, K. R., Berman-Frank, I., Bopp, L., Boyd, P. W., Galbraith, E. D., Geider, R. J., Guieu, C., Jaccard, S. L., Jickells, T. D., La Roche, J., Lenton, T. M., Mahowald, N. M., Marañón, E., Marinov, I., Moore, J. K., Nakatsuka, T., Oschlies, A., Saito, M. A., Thingstad, T. F., Tsuda, A. and Ulloa, O.: Processes and patterns of oceanic nutrient limitation, Nat. Geosci., 6, 701–710, doi:10.1038/ngeo1765, 2013a.
Moore, J. K., Lindsay, K., Doney, S. C., Long, M. C. and Misumi, K.: Marine ecosystem dynamics and biogeochemical cycling in the community earth system model [CESM1(BGC)]: Comparison of the 1990s with the 2090s under the RCP4.5 and RCP8.5 scenarios, J. Clim., 26, 9291–9312, doi:10.1175/JCLI-D-12-00566.1, 2013b.
Moore, L. R., Goericke, R. and Chisholm, S. W.: Comparative physiology of Synechococcus and Prochlorococcus: Influence of light and temperature on growth, pigments, fluorescence and absorptive properties, Mar. Ecol. Prog. Ser., 116(1), 259–276, doi:10.3354/meps116259, 1995.
Morel, F. M. M., Lam, P. J. and Saito, M. A.: Trace Metal Substitution in Marine Phytoplankton, Annu. Rev. Earth Planet. Sci., 48, 491–517, doi:10.1146/annurev-earth-053018-060108, 2020.
Noble, A. E., Saito, M. A., Maiti, K. and Benitez-Nelson, C. R.: Cobalt, manganese, and iron near the Hawaiian Islands: A potential concentrating mechanism for cobalt within a cyclonic eddy and implications for the hybrid-type trace metals, Deep. Res. Part II Top. Stud. Oceanogr., 55(10–13), 1473–1490, doi:10.1016/j.dsr2.2008.02.010, 2008.
Noble, A. E., Lamborg, C. H., Ohnemus, D. C., Lam, P. J., Goepfert, T. J., Measures, C. I., Frame, C. H., Casciotti, K. L., DiTullio, G. R., Jennings, J. and Saito, M. A.: Basin-scale inputs of cobalt, iron, and manganese from the Benguela-Angola front to the South Atlantic Ocean, Limnol. Oceanogr., 57(4), 989–1010, doi:10.4319/lo.2012.57.4.0989, 2012.
Noble, A. E., Ohnemus, D. C., Hawco, N. J., Lam, P. J. and Saito, M. A.: Coastal sources, sinks and strong organic complexation of dissolved cobalt within the US North Atlantic GEOTRACES transect GA03, Biogeosciences, 14(11), 2715–2739, doi:10.5194/bg-14-2715-2017, 2017.
Ohnemus, D. C., Rauschenberg, S., Cutter, G. A., Fitzsimmons, J. N., Sherrell, R. M. and Twining, B. S.: Elevated Trace Metal Content of Prokaryotic Communities Associated with Marine Oxygen Deficient Zones, Limnol. Oceanogr., 62, 3–25, doi:10.1002/lno.10363, 2017.
Polovina, J. J., Howell, E., Kobayashi, D. R. and Seki, M. P.: The transition zone chlorophyll front, a dynamic global feature defining migration and forage habitat for marine resources, Prog. Oceanogr., 49, 469–483, doi:10.1016/S0079-6611(01)00036-2, 2001.
Polovina, J. J., Howell, E. A., Kobayashi, D. R. and Seki, M. P.: The Transition Zone Chlorophyll Front updated: Advances from a decade of research, Prog. Oceanogr., 150,

79–85, doi:10.1016/j.pocean.2015.01.006, 2017.
Price, N. M. and Morel, F. M. M.: Cadmium and cobalt substitution for zinc in a marine diatom, Nature, 344(6267), 658–660, doi:10.1038/344658a0, 1990.
Quisel, J. D., Wykoff, D. D. and Grossman, A. R.: Biochemical Characterization of the Extracellular Phosphatases Produced by Phosphorus-Deprived Chlamydomonas reinhardtii, Plant Physiol., 111(3), 839–848, doi:10.1104/pp.111.3.839, 1996.
Redfield, A. C.: The biological control of chemical factors in the environment, Am. Sci., 46(3), 205–221, 1958.
La Roche, J., Boyd, P. W., McKay, R. M. L. and Geider, R. J.: Flavodoxin as an in situ marker for iron stress in phytoplankton, Nature, 382, 802–805, doi:10.1038/382802a0, 1996.
Saito, M. A., Moffett, J. W., Chisholm, S. W. and Waterbury, J. B.: Cobalt limitation and uptake in Prochlorococcus, Limnol. Oceanogr., 47(6), 1629–1636, doi:10.4319/lo.2002.47.6.1629, 2002.
Saito, M. A., Moffett, J. W. and DiTullio, G. R.: Cobalt and nickel in the Peru upwelling region: A major flux of labile cobalt utilized as a micronutrient, Global Biogeochem. Cycles, 18(4), 1–14, doi:10.1029/2003GB002216, 2004.
Saito, M. A., McIlvin, M. R., Moran, D. M., Goepfert, T. J., DiTullio, G. R., Post, A. F. and Lamborg, C. H.: Multiple nutrient stresses at intersecting Pacific Ocean biomes detected by protein biomarkers, Science (80-.)., 345(6201), 1173–1177, doi:10.1126/science.1256450, 2014.
Saito, M. A., Noble, A. E., Hawco, N., Twining, B. S., Ohnemus, D. C., John, S. G., Lam, P., Conway, T. M., Johnson, R., Moran, D. and McIlvin, M.: The acceleration of dissolved cobalt's ecological stoichiometry due to biological uptake, remineralization, and scavenging in the Atlantic Ocean, Biogeosciences, 14(20), 4637–4662, doi:10.5194/bg-14-4637-2017, 2017.
Saito, M. A., Saunders, J. K., Chagnon, M., Gaylord, D. A., Shepherd, A., Held, N. A., Dupont, C., Symmonds, N., York, A., Charron, M. and Kinkade, D. B.: Development of an Ocean Protein Portal for Interactive Discovery and Education, J. Proteome Res., 20, 326–336, doi:10.1021/acs.jproteome.0c00382, 2021.
Sterner, R. W. and Elser, J. J.: Ecological stoichiometry: the biology of elements from molecules to the biosphere, Princeton University Press, Princeton, NJ., 2002.
Stramma, L., Johnson, G. C., Sprintall, J. and Mohrholz, V.: Expanding Oxygen-Minimum Zones in the Tropical Oceans, Science (80-.)., 320(May), 655–658, 2008.
Sunda, W. G. and Huntsman, S. A.: Feedback interactions between zinc and phytoplankton in seawater, Limnol. Oceanogr., 37(1), 25–40, doi:10.4319/lo.1992.37.1.0025, 1992.
Sunda, W. G. and Huntsman, S. A.: Cobalt and zinc interreplacement in marine phytoplankton: Biological and geochemical implications, Limnol. Oceanogr., 40(8), 1404–1417, doi:10.4319/lo.1995.40.8.1404, 1995.
Tagliabue, A., Hawco, N. J., Bundy, R. M., Landing, W. M., Milne, A., Morton, P. L. and Saito, M. A.: The Role of External Inputs and Internal Cycling in Shaping the Global Ocean Cobalt Distribution: Insights From the First Cobalt Biogeochemical Model, Global Biogeochem. Cycles, 32, 594–616, doi:10.1002/2017GB005830, 2018.
Tebo, B. M., Nealson, K. H., Emerson, S. and Jacobs, L.: Microbial Mediation of Mn (II) and Co (II) Precipitation at the O2/H2S Interfaces in Two Anoxic Fjords, Limnol. Oceanogr., 29(6), 1247–1258, 1984.
Thompson, A. W., Huang, K., Saito, M. A. and Chisholm, S. W.: Transcriptome response of

high- and low-light-adapted Prochlorococcus strains to changing iron availability, ISME J., 5, 1580–1594, doi:10.1038/ismej.2011.49, 2011.
Tsuda, A., Kiyosawa, H., Kuwata, A., Mochizuki, M., Shiga, N., Saito, H., Chiba, S., Imai, K., Nishioka, J. and Ono, T.: Responses of diatoms to iron-enrichment (SEEDS) in the western subarctic Pacific, temporal and spatial comparisons, Prog. Oceanogr., 64(2–4), 189–205, doi:10.1016/j.pocean.2005.02.008, 2005.
Twining, B. S. and Baines, S. B.: The Trace Metal Composition of Marine Phytoplankton, Ann. Rev. Mar. Sci., 5(1), 191–215, doi:10.1146/annurev-marine-121211-172322, 2013.
Twining, B. S., Rauschenberg, S., Morton, P. L., Ohnemus, D. C. and Lam, P. J.: Comparison of particulate trace element concentrations in the North Atlantic Ocean as determined with discrete bottle sampling and in situ pumping, Deep. Res. Part II, 116, 273–282, doi:10.1016/j.dsr2.2014.11.005, 2015.
Wojciechowski, C. L., Cardia, J. P. and Kantrowitz, E. R.: Alkaline phosphatase from the hyperthermophilic bacterium T . maritima requires cobalt for activity, Protein Sci., 11(4), 903–911, doi:10.1110/ps.4260102.characterized, 2002.
Zheng, L., Minami, T., Konagaya, W., Chan, C. Y., Tsujisaka, M., Takano, S., Norisuye, K. and Sohrin, Y.: Distinct basin-scale-distributions of aluminum, manganese, cobalt, and lead in the North Pacific Ocean, Geochim. Cosmochim. Acta, 254, 102–121, doi:10.1016/j.gca.2019.03.038, 2019.
Zinser, E. R., Johnson, Z. I., Coe, A., Karaca, E., Veneziano, D. and Chisholm, S. W.: Influence of light and temperature on Prochlorococcus ecotype distributions in the Atlantic Ocean, Limnol. Oceanogr., 52(5), 2205–2220, doi:10.4319/lo.2007.52.5.2205, 2007.

Tables

Table 1. Aggregate upper ocean dCo : dPO_4^{3-} ratios from 4 expeditions, as show in Fig. 7. The depth threshold of the upper ocean was calculated as the threshold that maximized the linearity (R^2) of the dCo vs. dPO_4^{3-} linear regression.

Expedition	**dCo : dPO_4^{3-} [µmol : mol]**	**Depth Threshold [m]**	**R^2**	**n**
GP15	78 ± 3	95	0.86	138
ProteOMZ	41 ± 2	155	0.86	55
GP16	64 ± 1	109.7	0.93	162
METZYME	53 ± 2	225	0.86	87
All	**70 ± 2**	**95.2**	**0.85**	**366**

Table 2. Aggregate upper ocean (0–300 m) pCo : pP ratios and intermediate (300–500 m) pCo : pMn ratios from the GP15, GP16 and METZYME expeditions, as shown in Fig. 10. No slope value is given when $R^2 < 0.5$.

Expedition	pCo : pP (0-300 m) [µmol : mol]	R^2	n	pCo : pMn (300-500 m) [mol : mol]	R^2	n
GP15	136 ± 6	0.85	93	--	0.18	93
GP16	180 ± 15	0.58	106	0.0120 ± 0.0009	0.86	106
METZYME	121 ± 4	0.92	90	0.007 ± 0.001	0.55	90

Figures

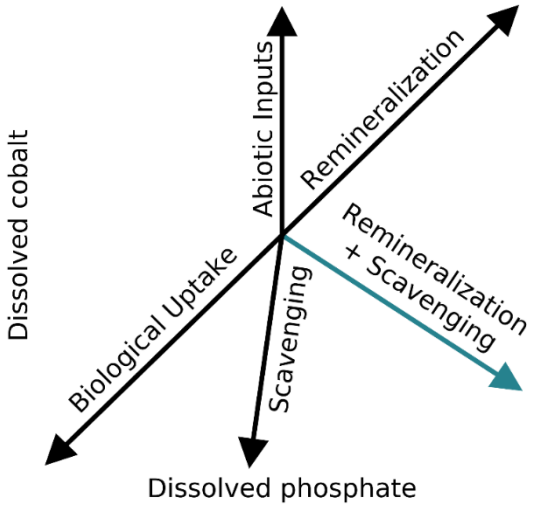

Figure 1. Vector schematic of the dCo vs. dPO_4^{3-} relationship, depicting the impact of major dCo biogeochemical processes in the oceans on dCo and dPO_4^{3-} concentrations. Adapted from Noble et al. (2008). The blue line depicts the sum of the scavenging and remineralization vectors; both processes tend to dominate the dCo cycle below the mixed layer, resulting in intermediate and deep waters characterized by high dPO_4^{3-}, low dCo distributions.

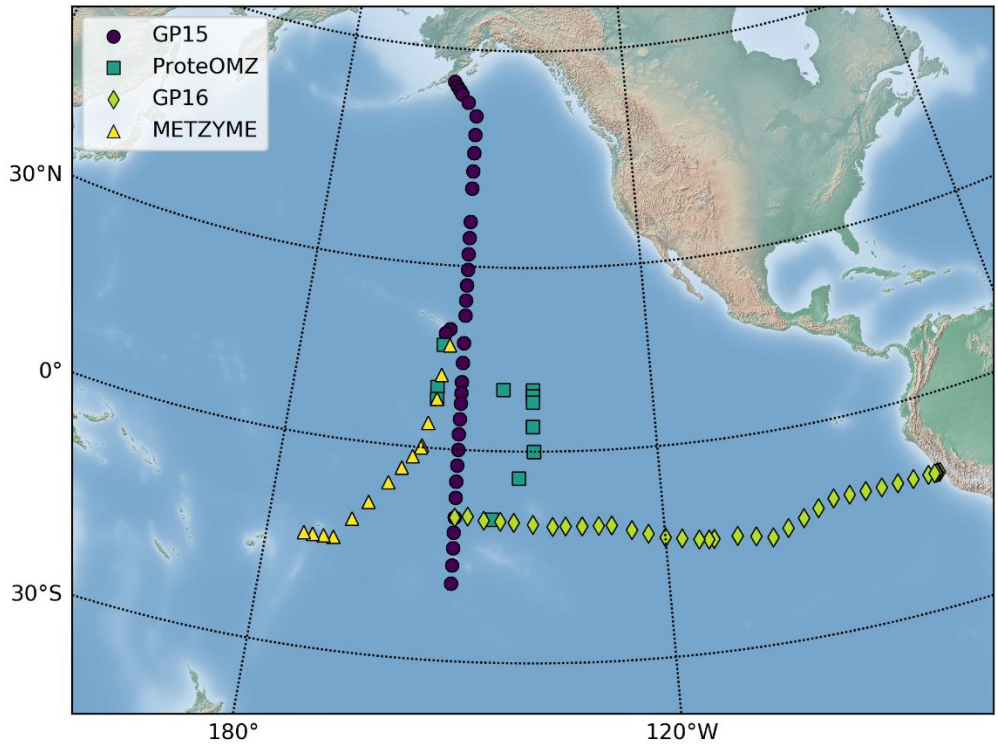

Figure 2. Map of stations for 4 Pacific expeditions: U.S. GEOTRACES GP15 (September–November 2018), ProteOMZ (January–February 2016), U.S. GEOTRACES GP16 (October–December 2013), and METZYME (October 2011).

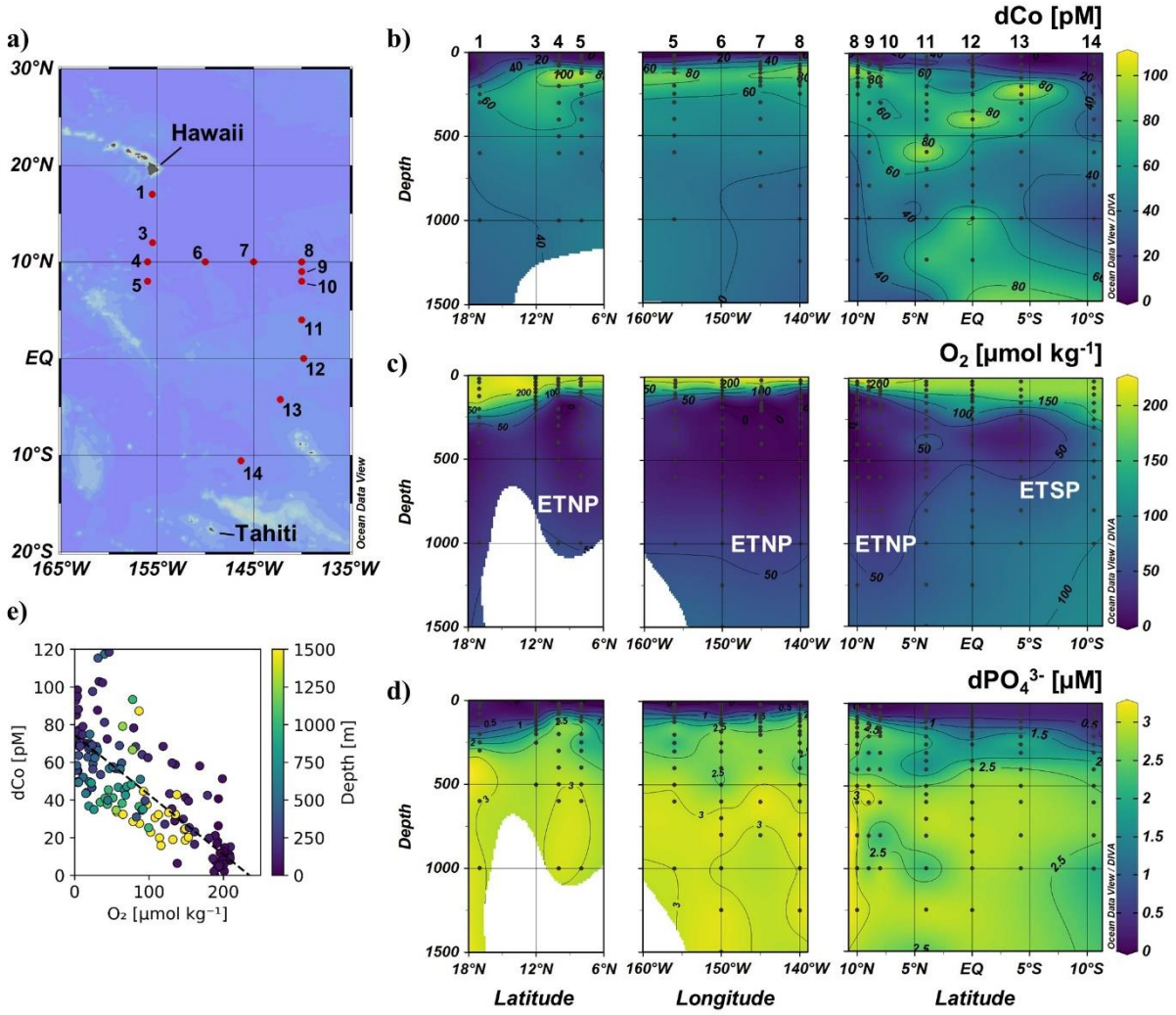

Figure 3. (a) Map of the ProteOMZ expedition from Hawaii to Tahiti. Upper and intermediate ocean (≤ 1500 m) transects of (b) dissolved Co, (c) dissolved oxygen and (d) dissolved phosphate concentrations are shown by latitude between stations 1–5, by longitude between stations 5-8, and by latitude again between stations 8-14 to best represent the expedition track. The low O_2 concentrations in intermediate waters are evidence of the Eastern Tropical North Pacific (ETNP) OMZ (~5–18º N) and Eastern Tropical South Pacific (ETSP) OMZ (~2–10º S). DIVA gridding was used to interpolate between data points. (e) The dCo vs. dO_2 relationship (0–1500 m) within the ProteOMZ dataset, displaying a negative linear dCo : O_2 trend of -0.32 ± 0.02 µM : mol kg^{-1} (R^2 = 0.58; n = 155; dashed line).

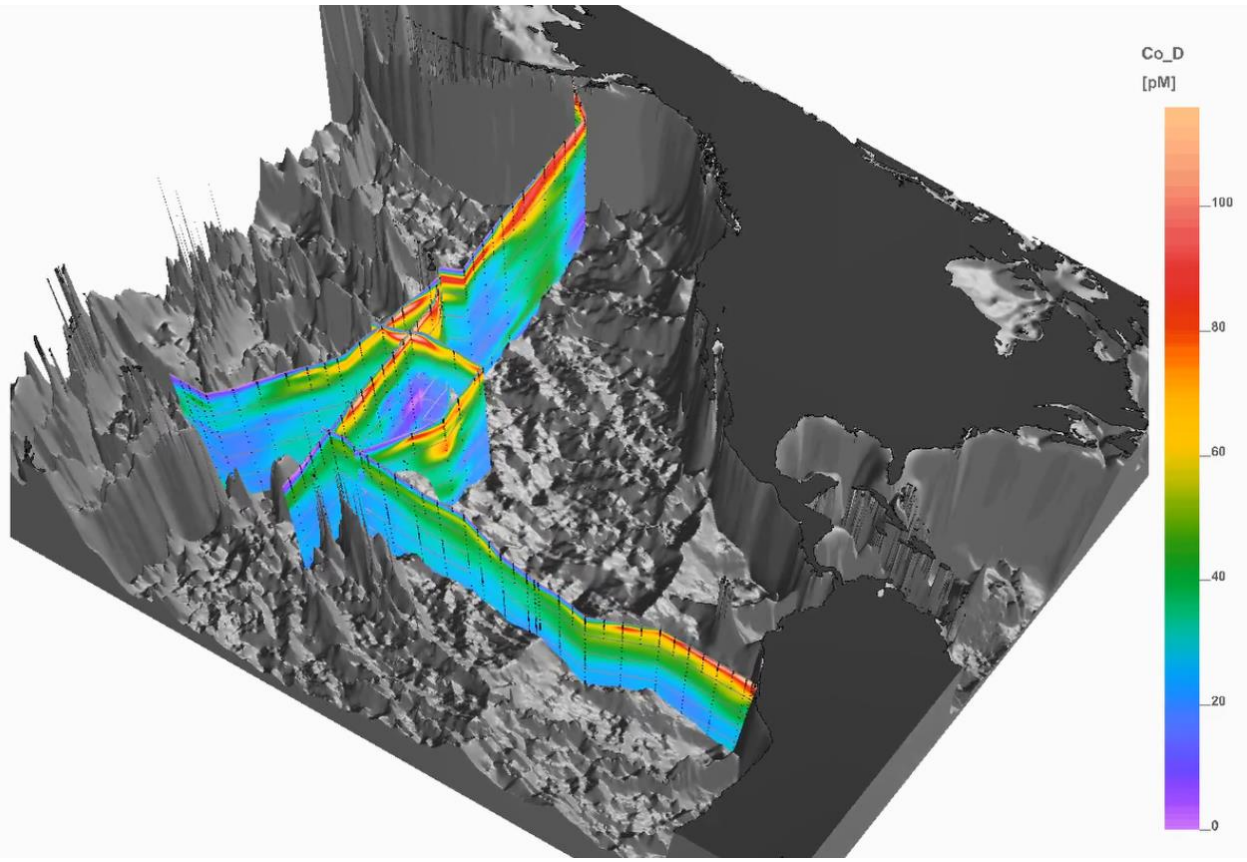

Figure 4. 3-dimensional distribution of dCo throughout the Pacific basin from synthesized datasets from the GP15, ProteOMZ, GP16 and METZYME expeditions. Produced by Reiner Schlitzerand.

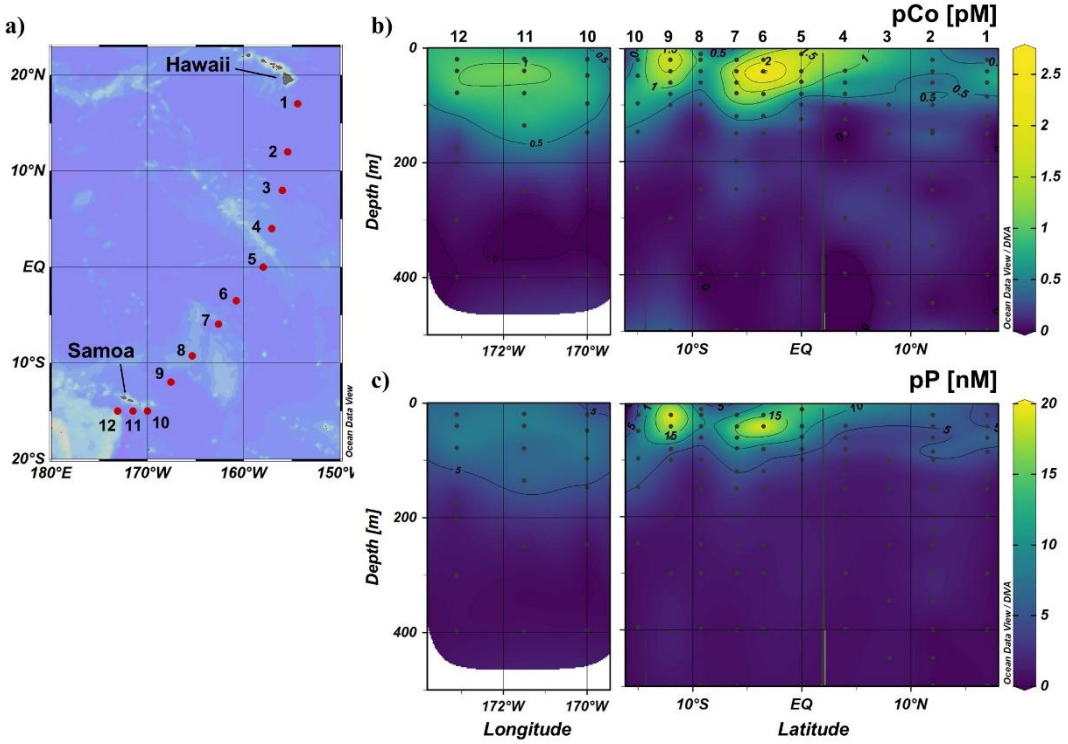

Figure 5. (a) Map of the Metzyme expedition from Hawaii to American Samoa. Upper ocean (≤ 500 m) transects of (b) particulate Co and (c) particulate phosphorous concentrations are shown by latitude between stations 1–10 and by longitude between stations 10–12 to best represent the expedition track. DIVA gridding was used to interpolate between data points.

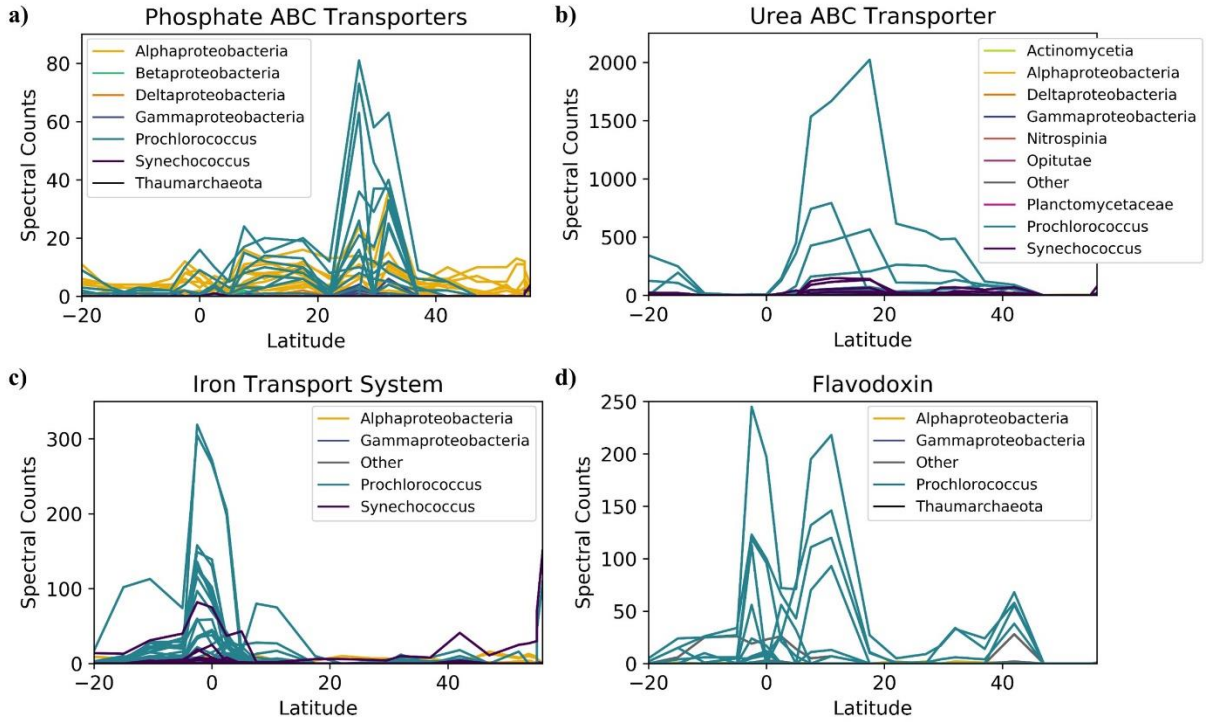

Figure 6. Select nutrient stress biomarkers from the bacterial fraction (0.2–3 µm) metaproteome along a surface transect (~2 m depth) of the GP15 expedition. The data is presented as non-exclusive spectral counts where peptides are allowed to map to more than one metagenomics sequence, and hence the peaks reflect the potential diversity of each biomarker.

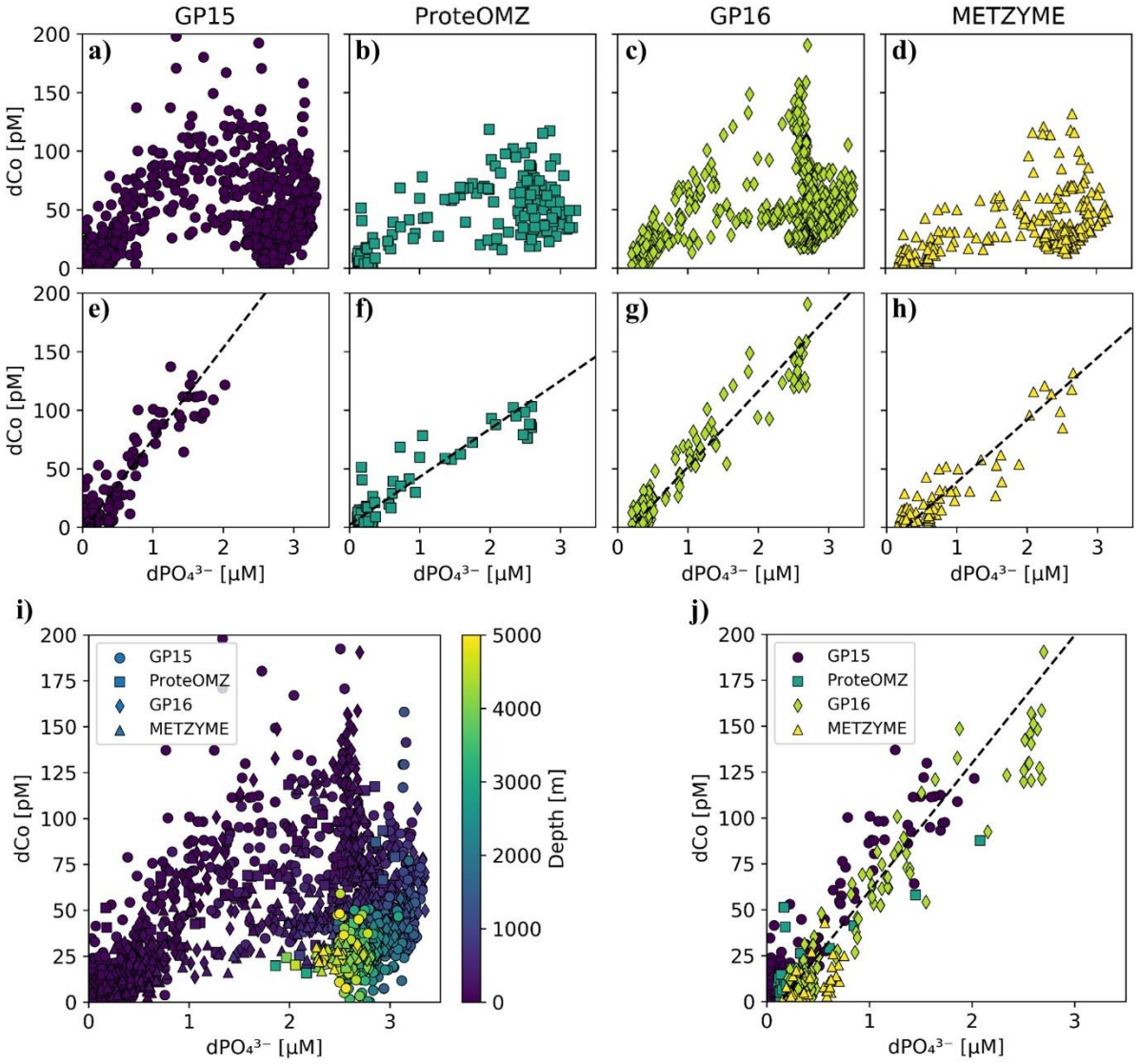

Figure 7. The observed dCo vs. dPO_4^{3-} relationship from each expedition (a-d), demonstrating a linear relationship in the surface ocean and a "curl" towards low dCo, high dPO_4^{3-} concentrations from Co scavenging that decouples dCo and dPO_4^{3-} in the mesopelagic and deep ocean. (e-f) The positive linear dCo vs. dPO_4^{3-} relationship in the upper ocean; the depth threshold of the datapoints included in the upper ocean was calculated as the threshold that maximized the linearity (R^2) of the dCo vs. dPO_4^{3-} regression. (i) The dCo vs. dPO_4^{3-} relationship colored by depth from all 4 expeditions. (j) The linear upper ocean dCo vs. dPO_4^{3-} relationship from all 4 expeditions, with a uniform depth threshold of 95.2 m to maximize linearity. The GP15 coastal stations 1 and 2 display a negative relationship between dCo and dPO_4^{3-} due to riverine influences (Chmiel et al., 2022) and have been omitted. dCo : dPO_4^{3-} slope statistics are given in Table 1.

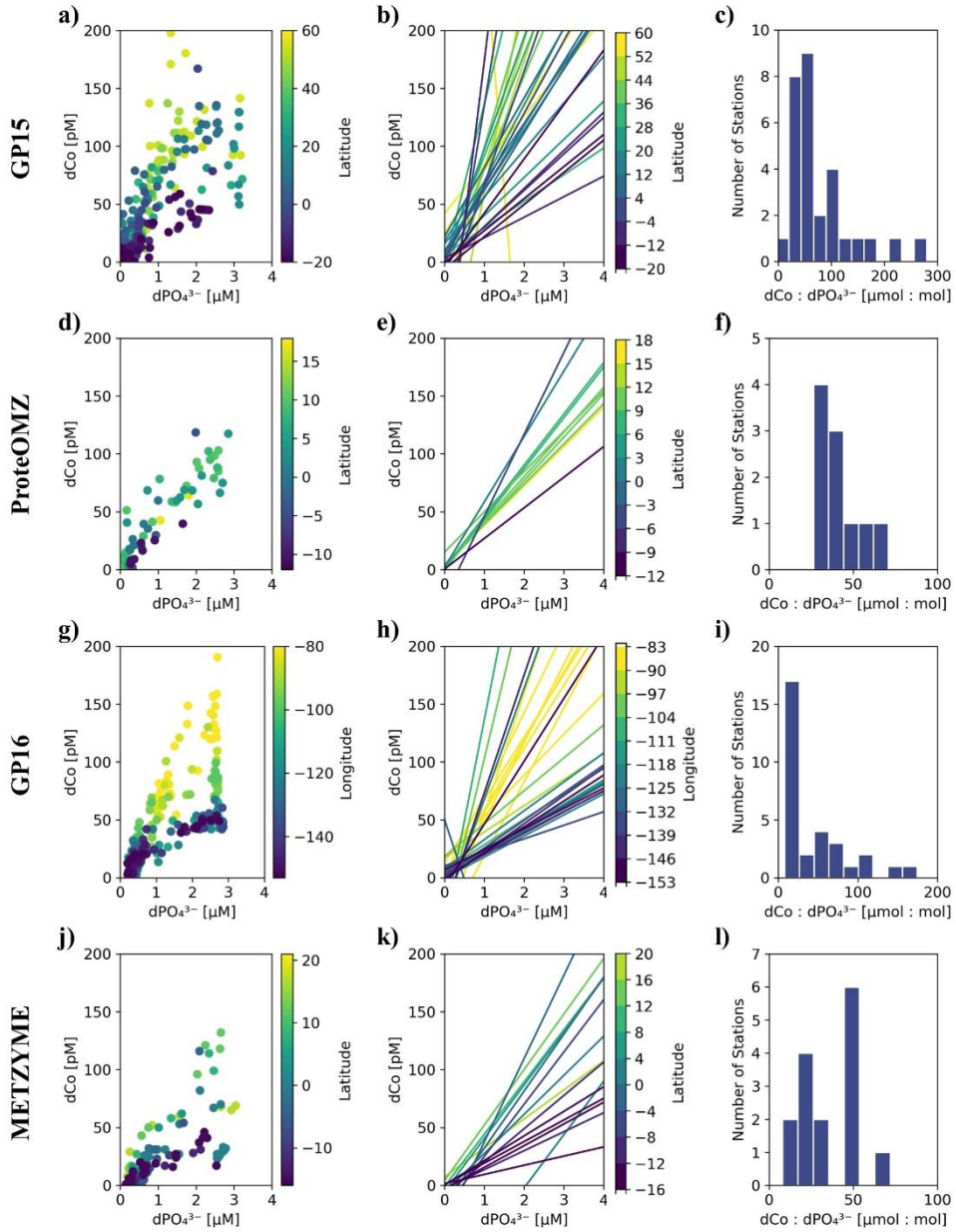

Figure 8. Determination of the dCo : dPO_4^{3-} slope from each station for each expedition. Panels a, d, g and j depict dCo vs. dPO_4^{3-} from depths that maximized the R^2 value of each two-way linear regression from each station, colored by latitude. Panels b, e, h and k depict dCo : dPO_4^{3-} slopes with the depth range that produced the highest R^2 value at each station, colored by latitude. Panels c, g, i, and l are histograms of the dCo : dPO_4^{3-} slopes with the highest R^2 value at each station; note that negative slopes, which typically occur near the coast, have been omitted. All slopes shown have an R^2 value equal to or higher than a threshold of 0.7 ($R^2 \geq 0.7$).

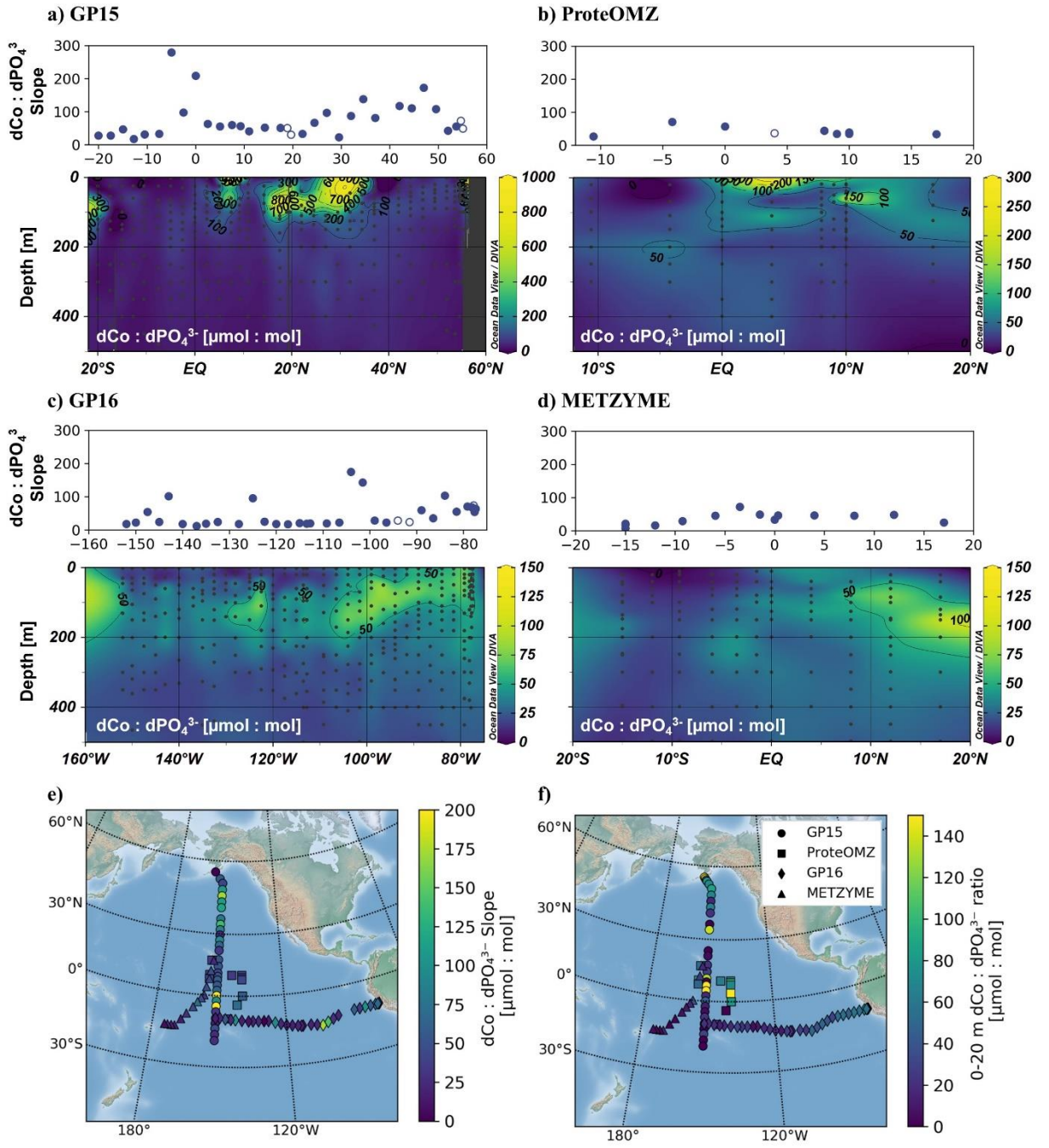

Figure 9. Dissolved Co : PO_4^{-3} stoichiometry by latitude for the (a) GP15, (b) ProteOMZ and (d) METZYME expeditions and by longitude for the (d) GP16 expedition. Top panels for each expedition depict the dCo : dPO_4^{3-} slope determined for each station in units of µmol : mol. Slopes whose R^2 value is less than a 0.7 threshold are shown as empty circles. Bottom section panels depict the dCo : dPO_4^{3-} ratios from discrete samples in the upper ocean (≤ 500 m depth). Note the variation in the y-axis. Maps displaying the (e) surface (≤ 20 m) dCo : dPO_4^{3-} ratios and (f) dCo : dPO_4^{3-} slopes; regressions where $R^2 < 0.7$ have been omitted from panel e. DIVA gridding was used to interpolate between data points.

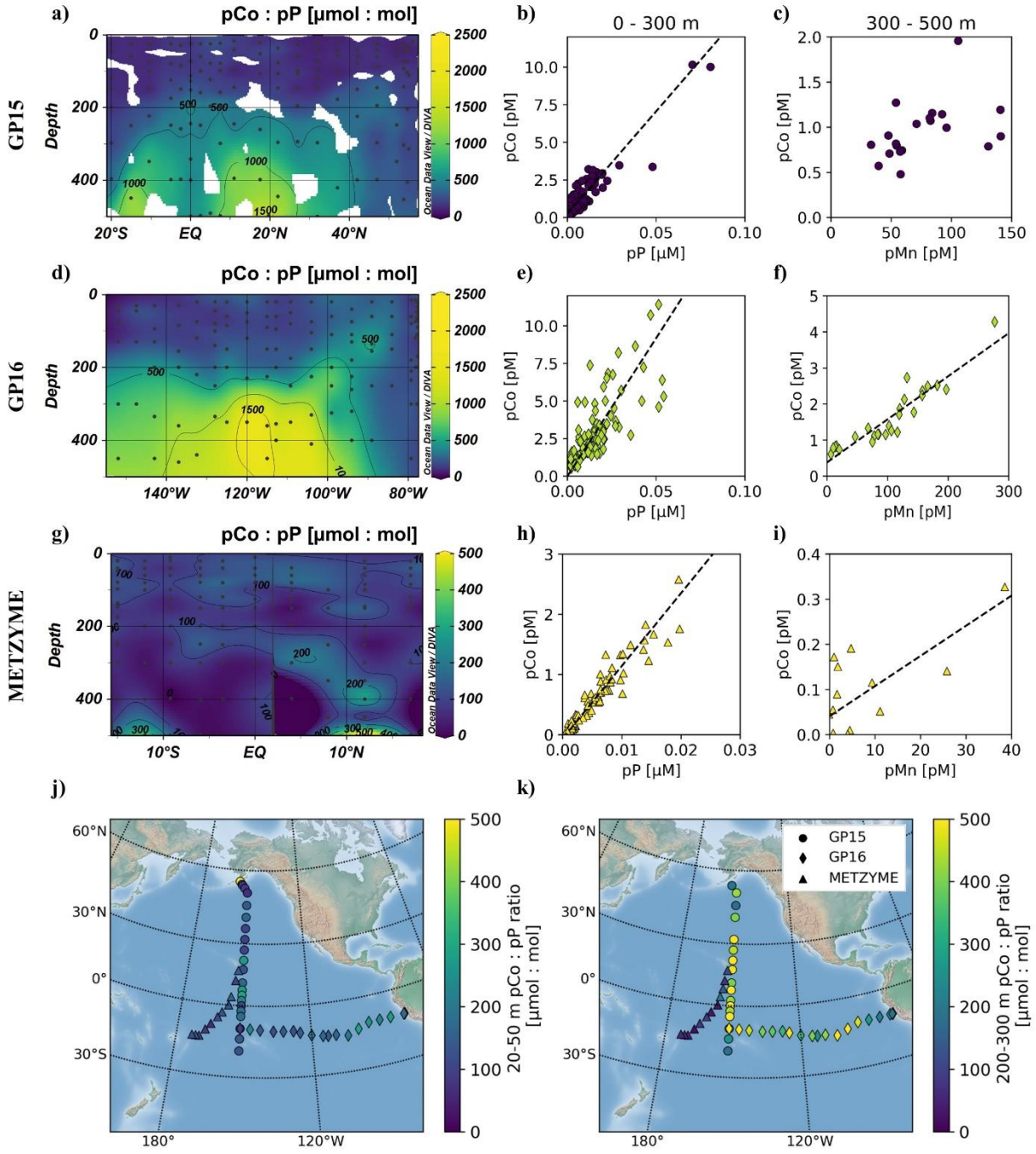

Figure 10. Particulate Co : P section plots by latitude for the (a) GP15 and (g) METZYME expeditions and by longitude for the (d) GP16 expedition. DIVA gridding was used to interpolate between data points. Panels b, e and h depict the pCo vs. pP relationship in the upper ocean (0–300 m), and panels c, f and i depict the pCo vs. pMn relationship between 300–500 m depth. Linear regressions are shown where $R^2 \geq 0.5$. GP15 stations 1 and 2, which contained high pCo concentrations from riverine sources (Chmiel et al., 2022), were omitted from the regression analysis. Maps displaying the (j) surface (20-50 m) and (k) intermediate (200-300 m) pCo : pP ratios.

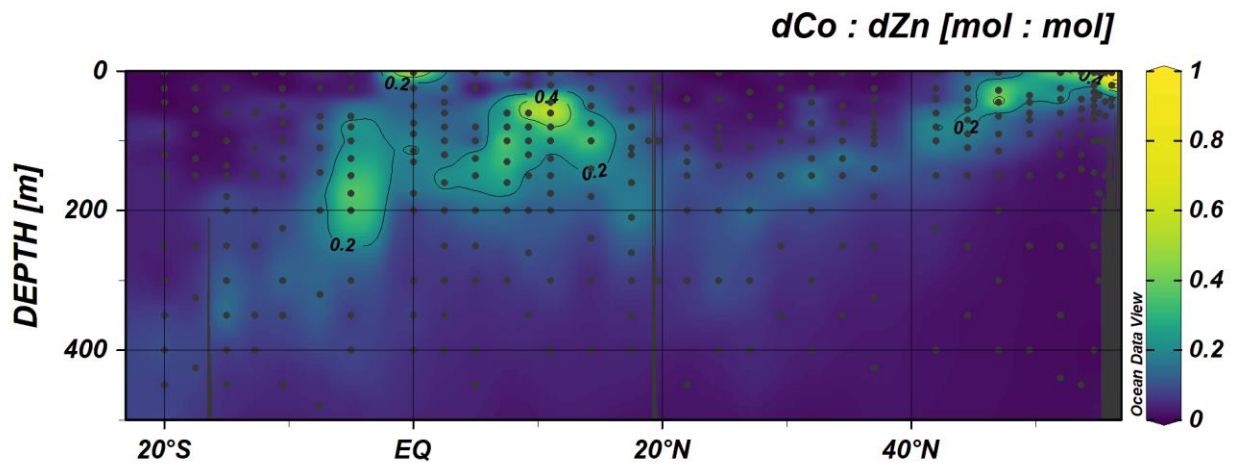

Figure 11. Upper ocean transect of dCo : dZn ratios along the GP15 expedition transect. DIVA gridding was used to interpolate between data points.

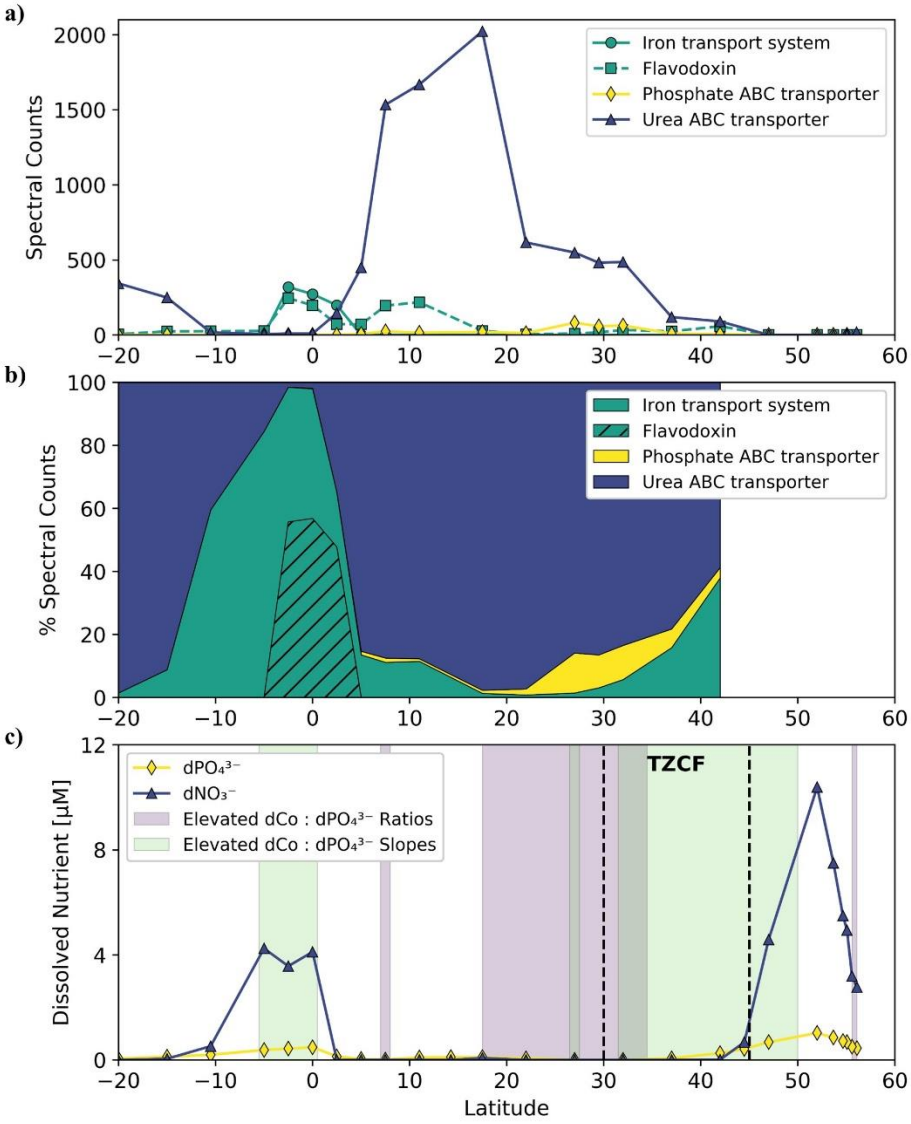

Figure 12. (a) The most abundant *Prochlorococcus* protein detected in the surface ocean for each nutrient stress biomarker class (iron transport system proteins, flavodoxin, phosphate ABC transporters and urea ABC transporters) by latitude. Proteins are quantified by their non-exclusive spectral counts. (b) The percent spectral counts of each of the four *Prochlorococcus* biomarkers studied by latitude, displaying the relative nutrient stress experienced by *Prochlorococcus* over the surface transect. No percentages were calculated from stations North of 42º N (Station 10) because the abundance of *Prochlorococcus* substantially decreased and *Prochlorococcus* proteins were often undetected. (c) The concentration of macronutrients phosphate (dPO_4^{3-}) and nitrate (dNO_3^-) in the surface ocean transect. Marked in purple are regions where the dCo : dPO_4^{3-} surface (~2 m depth) ratio was elevated (≥ 100 µmol : mol), and marked in green are regions where the dCo : dPO_3^{3-} slope was elevated ((≥ 80 µmol : mol). Dotted lines mark the boundaries of the transition zone chlorophyll front (TZCF), which migrates seasonally between 30 and 45◦ N.

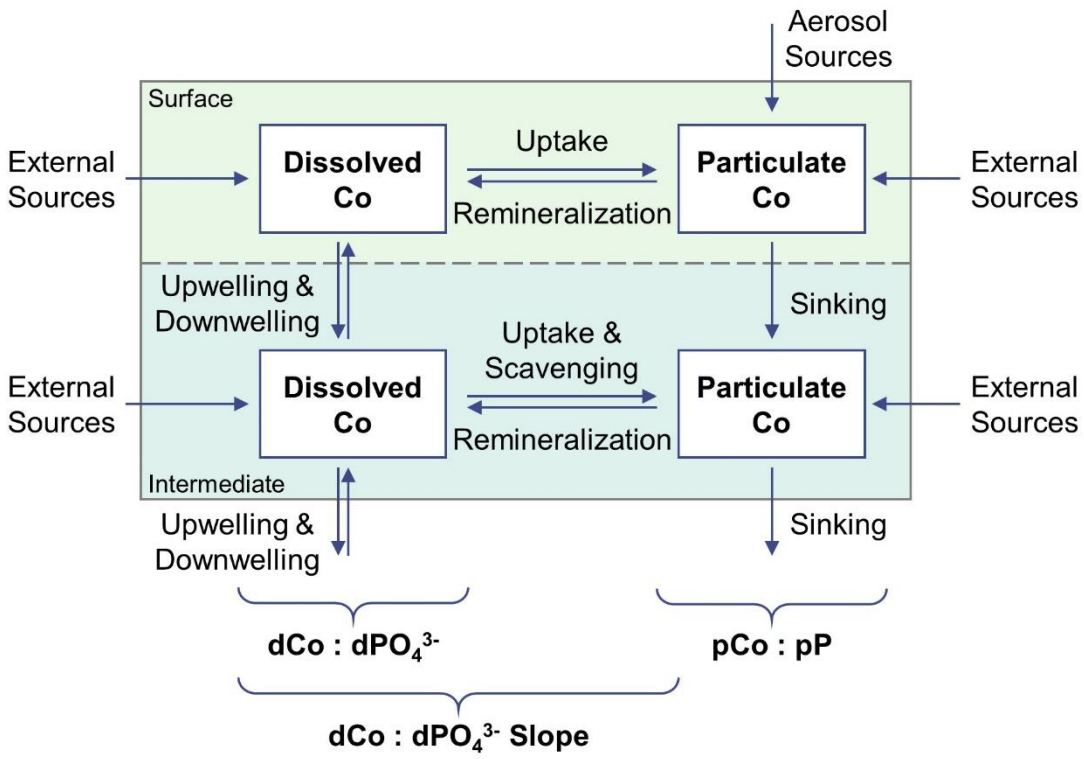

Figure 13. Schematic of the coupled dissolved and particulate Co cycle in the upper and intermediate ocean. The stoichiometry metrics of dCo : dPO_4^{3-} and pCo : pP can provide insight into the dCo and pCo fractions, and the Redfieldian dCo : dPO_4^{3-} slope is able to account for the interchange between the dCo and pCo fractions, characterizing the effects of uptake and remineralization on dCo concentrations.

Chapter 4.

Low cobalt inventories in the Amundsen and Ross Seas driven by high demand for labile cobalt uptake among bloom communities

Rebecca Chmiel[a,b], Deepa Rao[a], Riss Kellogg[a], Dawn Moran[b], Giacomo DiTullio[c], and Mak A. Saito[b]

[a] MIT/WHOI Joint Program in Oceanography/Applied Ocean Science and Engineering, Woods Hole, MA, USA
[b] Department of Marine Chemistry and Geochemistry, Woods Hole Oceanographic Institution, Woods Hole, MA, USA
[c] Hollings Marine Laboratory, 331 Fort Johnson, Charleston SC 29412

4.1 Abstract

Cobalt (Co) is often a scarce but essential micronutrient for marine plankton in the Southern Ocean and coastal Antarctic seas where dissolved cobalt (dCo) concentrations can be extremely low. This study presents total dCo and labile dCo distributions measured via shipboard voltammetry in the Amundsen Sea, Ross Sea and Terra Nova Bay during the CICLOPS (Cobalamin and Iron Co-Limitation of Phytoplankton Species) expedition. The resulting profiles indicate that a significantly smaller dCo inventory was observed during the 2017/2018 CICLOPS expedition compared to two 2005/2006 expeditions to the Ross Sea over a decade earlier. The dCo inventory loss (~10–20 pM) was present in both the surface and deep ocean and can be attributed to the loss of labile dCo, resulting in the near-100% strong ligand-bound complexation of dCo in the photic zone. A changing dCo inventory in Antarctic coastal seas could be driven by the alleviation of iron (Fe) limitation in coastal areas where the flux of Fe-rich sediments from melting Antarctic ice shelves and deep sediment resuspension may have shifted the region towards vitamin B_{12} and/or zinc (Zn) limitation, both of which are likely to increase the demand for Co among marine plankton. High demand for Zn by phytoplankton can result in increased Co and cadmium (Cd) uptake because the metals often share the same metal uptake transporters. This study compared the magnitudes and ratios of Zn, Cd and Co uptake (ρ) across upper ocean profiles and observed order of magnitude uptake trends (ρZn > ρCd > ρCo) that paralleled the trace metal concentrations in seawater. High rates of Co and Zn uptake were observed throughout the region, and the speciation of available Co and Zn appeared to influence trends in dissolved metal : phosphate stoichiometry and uptake rates over depth. Multi-year loss of the dCo inventory throughout the water column may be explained by an increase in Co uptake into particulate organic matter (POM) and subsequent increased flux of Co into sediments via sinking and burial. This perturbation of the Southern Ocean Co biogeochemical cycle could signal changes in the nutrient limitation regimes, phytoplankton bloom composition, and carbon sequestration sink of the Southern Ocean.

4.2 Introduction

Coastal Antarctic seas are highly productive environments for phytoplankton blooms and are characterized by high nutrient, low chlorophyll (HNLC) surface waters that tend to be growth limited by iron (Fe) and other trace metal micronutrients (Martin et al. 1990; Arrigo et al. 2008, 2012). During the spring and summer months, katabatic winds and fragmenting sea ice forms open coastal polynyas in the Amundsen and Ross Seas that represent regions of high phytoplankton productivity and significant global carbon sinks (Arrigo et al. 2012). In the winter, ice cover supports the turnover of deep waters that allow trace metals like Fe to be redistributed to the upper ocean (Sedwick and Ditullio 1997; Sedwick et al. 2011). Phytoplankton blooms in coastal Antarctic polynyas are dominated by eukaryotes such as diatoms and the haptophyte *Phaeocystis antarctica* (Arrigo et al. 1999; DiTullio et al. 2003), while cyanobacteria like *Prochlorococcus* and *Synechococcus* that are highly abundant in the adjacent South Pacific and South Atlantic gyres are near-absent from the phytoplankton community in the Southern Ocean (DiTullio et al. 2003; Bertrand et al. 2011; Chandler et al. 2016).

Cobalt (Co) is an essential trace metal nutrient for many marine plankton and is relatively scarce in the marine environment, often present in the dissolved phase (dCo) in picomolar concentrations (10^{-12} mol L^{-1}). Co acts as a cofactor for metalloenzymes like carbonic anhydrase, a crucial enzyme in the carbon concentrating mechanism of photosynthesis (Sunda and Huntsman 1995; Roberts et al. 1997; Kellogg et al. 2020) and vitamin B_{12} (cobalamin), which can be used for the biosynthesis of methionine but is only produced by some bacteria and archaea (Warren et al. 2002; Bertrand et al. 2013). In the Ross Sea, vitamin B_{12} availability has been observed to co-limit phytoplankton growth with iron (Fe) when the bacterial community is low (Bertrand et al. 2007). Some phytoplankton exhibit flexible vitamin B_{12} metabolisms and can express a vitamin B_{12}-independent methionine synthase pathway (MetE gene) instead of the vitamin B_{12}-dependent pathway (MetH gene), allowing the organism to thrive in vitamin-depleted environments (Rodionov et al. 2003; Bertrand et al. 2013; Helliwell 2017). Recently, *P. antarctica* was discovered to contain both MetH and a punitive MetE gene, displaying a metabolism that is flexible to vitamin B_{12} availability (Rao et al. [In review]). Additionally, recent observations of Zn co-limitation with Fe have been observed in the Ross Sea (Kellogg et al. [Submitted]), suggesting a complex landscape of trace metal and vitamin stress in the otherwise macronutrient-rich waters of coastal Antarctica.

Dissolved Co is present as two primary species in the marine environment: a "free" labile Co(II) species with weakly bound ligands and a Co(III) species that is strongly bound to organic ligands ($K_s > 10^{16.8}$) (Saito et al. 2005). Labile dCo is considered to be more bioavailable to marine microbes than strongly-bound dCo, although there is evidence that phytoplankton communities can access Co in strongly-bound organic ligand complexes (Saito and Moffett 2001) and that microbial communities may produce extracellular Co ligands that stabilize dCo and prevent its loss via scavenging to manganese (Mn)-oxide particles (Saito et al. 2005; Bown et al. 2012). Previous dCo sampling expeditions to the Ross Sea, including two 2005/2006 Controls of Ross Sea Algal Community Structure (CORSACS) expeditions (Saito et al. 2010) and fieldwork in 2009 that sampled the water column below early spring sea ice in the McMurdo Sound (Noble et al. 2013), reported relatively high concentrations of labile dCo in the surface Ross Sea when compared to the tropical and subtropical global oceans, suggesting that labile dCo was fairly replete and bioavailable to phytoplankton at the time (Saito et al. 2010).

This study examines the biogeochemical cycle of Co in the Amundsen and Ross Seas during the 2017/2018 austral summer as part of the Cobalamin and Iron Co-Limitation of Phytoplankton Species (CICLOPS) expedition. Here, we present profiles of dCo speciation that reveal a lower dCo inventory during the 2017/2018 summer bloom compared to that observed during the 2005/2006 CORSACS expeditions, as well as mostly undetectable concentrations of labile dCo in the surface ocean. Additional datasets of dissolved zinc (dZn) and cadmium (dCd), as well as profiles of Co, Zn and Cd uptake rates measured by isotope tracer incubation experiments suggest that regions of vitamin B_{12} and Zn stress within phytoplankton blooms could be driving high demand for bioavailable Co in the surface ocean. The results presented by this study reveal a substantial perturbation of the Co cycle and a shift towards vitamin B_{12} and/or Zn limitation in coastal Antarctic waters impacted by high rates of glacial ice melt and a warming climate.

4.3 Methods

4.3.1 Study area and trace metal sampling

Samples were collected along the coastal Antarctic Shelf from the Amundsen Sea, Ross Sea, and Terra Nova Bay (Fig. 1) during the CICLOPS expedition on the RVIB Nathanial B. Palmer (NBP-1801; December 11, 2017 – March 3, 2018). Dissolved seawater was collected from

full-depth station profiles using a trace metal clean sampling rosette deployed on a conducting synthetic line, both supplied by the U.S. Antarctic Program (USAP), and equipped with twelve 8 L X-Niskin bottles (Ocean Test Equipment), supplied by the Saito Laboratory. Real-time trace metal rosette operations allowed for the careful collection of seawater from 10 and 20 m above the ocean floor to study sediment-water interactions within a potential nepheloid layer. After deployment, the X-Niskin bottles were transported to a trace metal clean van and pressurized with high-purity N_2 gas. Seawater samples for nutrients, dCo and trace metal analysis were then filtered through acid-washed 0.2 µM Supor polyethersulfone membrane filters (Pall Corporation, 142 mm diameter) within 3 hours of rosette recovery.

To minimize metal contamination of samples, all sample bottles were prepared using trace metal clean procedures prior to the expedition. The cleaning procedure for dCo sample bottles entailed soaking sample bottles for ~1 week in Citranox, an acidic detergent, rinsing with Milli-Q water (Millipore), soaking sample bottles for ~2 weeks in 10% trace metal grade HCl (Optima, Fisher Scientific), and rinsing with lightly acidic Milli-Q water (> 0.1% HCl). Macronutrient sample bottles were rinsed with Milli-Q water and soaked overnight in 10% HCl. The procedure for total dissolved metal sample bottles (dZn and dCd) was identical to that used for dCo bottles except the Citranox soak step was omitted.

Samples for dCo analysis were collected in 60 mL low-density polyethylene (LDPE) bottles and stored at 4ºC until analysis. Duplicate dCo samples were collected: one for at-sea analysis of labile dCo and total dCo, and another for preservation and total dCo analysis in the laboratory after the expedition. Preserved total dCo samples were stored with oxygen-absorbing satchels (Mitsubishi Gas Chemical, model RP-3K), which preserve the sample for long-term storage and future analysis (Noble et al. 2017; Bundy et al. 2020). Preserved dCo samples were stored in groups of 6 within an open (unsealed) plastic bag, which was then placed into a gas-impermeable plastic bag (Ampac) with one oxygen-absorbing satchel per 60 mL dCo sample. The outer bag was then heat-sealed and stored at 4ºC until analysis.

Samples for total dissolved metal analysis (dZn and dCd) were collected in 250 mL LDPE bottles and stored double-bagged at room temperature. After ~7 months, the total dissolved metals samples were acidified to a pH of 1.7 with trace metal grade HCl (Optima, Fisher Scientific), and were stored acidified for more than one year before instrumental analysis.

4.3.2 Dissolved Co and labile dCo analysis

Total dCo – the combined fractions of labile and ligand-bound dCo, hereafter simply dCo – and labile dCo concentrations were analyzed via cathodic stripping voltammetry (CSV) as described by Saito and Moffett (2001) and modified by Saito et al. (2010) and Hawco et al. (2016). CSV analysis was conducted using a Metrohm 663 VA and μAutolabIII systems equipped with a hanging mercury drop working electrode. All reagents were prepared as described in Chmiel et al. (2022). Most samples were analyzed at sea within 3 weeks of sample collection, and stations 57 and 60 were analyzed for labile dCo at sea and their duplicate preserved samples were analyzed for total dCo in November 2019 in the laboratory.

To measure total dCo concentrations, filtered seawater samples were first UV-irradiated in quartz tubes for one hour in a Metrohm 705 UV Digester to destroy natural ligand-bound Co complexes. 11 mL of sample was then added to a 15 mL trace metal clean polypropylene vial, and 100 μL of 0.1 M dimethyglyoxime (DMG; Sigma Aldrich) ligand and 130 μL of 0.5 M N-(2-hydroxyethyl)piperazine-N-(3-propanesulfonic acid) (EPPS, Sigma Aldrich) buffer was added to each sample vial. A Metrohm 858 Sample Processor then loaded 8.5 mL of each sample into the electrode's Teflon cup and added 1.5 mL of 1.5 M $NaNO_2$ reagent (Merck). The mercury electrode performed a fast linear sweep from -1.4 V to -0.6 V at a rate of 5 V s^{-1} and produced a cobalt reduction peak at -1.15 V, the voltage at which the $Co(DMG)_2$ complex is reduced from Co(II) to Co(0) (Saito and Moffett 2001). The height of the Co reduction peak is linearly proportional to the amount of total dCo present in the sample. Peak heights were determined by NOVA 1.10 software. A standard curve was created with 4 additions of 25 pM dCo to each sample, and a type-I linear regression of the addition standard curve performed by the LINEST function in Microsoft Excel allowed for the calculation of the initial amount of Co present in the sample.

When analyzing labile dCo concentrations, samples were not UV-irradiated so as to only quantify the free or weakly bound dCo not bound to strong organic ligands. 11 mL of labile samples were instead allowed to equilibrate with the DMG ligand and EPPS reagent overnight (~8 hours) before analysis so as to allow time for the labile dCo present in the sample to bind to the DMG ligand via competitive ligand exchange ($K > 10^{16.8}$). Labile dCo samples were then loaded onto the Sample Processor and analyzed electrochemically using identical methods as described above for total dCo samples.

4.3.3 Dissolved Co standards and blanks

During the CICLOPS expedition, an internal standard consisting of filtered, UV-irradiated seawater was analyzed for dCo every few days while samples were being analyzed (39 ± 4 pM, n = 9). While additional preserved dCo samples were analyzed in the laboratory in November 2019, triplicate GSC2 GEOTRACES community intercalibration standards were carefully neutralized to a pH of ~8 using negligible volumes of ammonium hydroxide (NH_4OH) and analyzed for dCo. This is the same intercalibration batch originally reported in Table 1 of Chmiel et al. (2022), as analysis for both expeditions overlapped temporally. The GSC2 standard was determined to have a dCo concentration of 80.2 ± 6.2 (n = 3), a value that is very similar to the one reported in Hawco et al. (2016) (77.7 ± 2.4). Currently, no official community consensus for dCo in the GSC2 intercalibration standard exists.

Analytical blank measurements for each reagent batch (a unique combination of DMG, EPPS, and $NaNO_2$ reagent batches) were measured to determine any Co contamination due to reagent impurities. Blanks were prepared in triplicate with UV-irradiated surface seawater passed through a column with Chelex 100 resin beads (Bio-Rad) to remove metal contaminants, then UV-irradiated again. Chelex beads were prepared as described in Price et al. (2013) to remove organic impurities from leaching into the eluent. For the 5 batches of reagents used on this expedition, the analytical blanks were found to be 2.3 pM, 4.0 pM, 10.1 pM, 15.6 pM, and 8.6 pM dCo, with an average of 8.1 pM Co. The analytical blank detected for the laboratory-run total dCo samples was 1.0 pM. It should be noted that blank values above 10 pM are considered high for this method. Analytical blank values were subtracted from the measured Co values determined with the respective reagent batch. The average standard deviation within each triplicate batch of blanks (1.3 pM) was used to estimate the analytical limit of detection (3 * blank standard deviation) of 4 pM. When detectable dCo concentrations were found below the 4 pM detection limit, their values were preserved in the dataset and flagged as below the detection limit (>DL). In cases where no dCo or labile dCo were detected (i.e. when no peak was measurable and/or the dCo value predicted was > 0 pM), values of 0 pM were assigned for the purposes of plotting and select statistical analysis and were flagged as not detected (n.d.) as well as >DL in the dataset; although these concentrations are not detectable with our methodology, we believe the incredibly low concentrations of dCo and labile dCo observed on this expedition were meaningful, and that removing these values from our analysis misrepresents the data and would skew the results to appear higher than was observed.

4.3.4 Dissolved Zn and Cd analyzed by ICP-MS

Total dissolved trace metal samples were analyzed for dZn and dCd using isotope dilution and inductively coupled plasma mass spectrometry (ICP-MS) as described in Kellogg et al. (In prep) based on methodology described in Cohen et al. (2021). Briefly, 15 mL of acidified filtered seawater samples were spiked with an acidified mixture of stable isotopes including ^{67}Zn, and ^{110}Cd, among other metal stable isotopes, and pre-concentrated via a solid phase extraction system seaFAST-pico (Elemental Scientific) to an elution volume of 500 µL. The samples were then analyzed using a iCAP-Q ICP-MS (Thermo Scientific) and concentrations were determined using a standard curve of a multi-elemental standard (SPEX CertiPrep).

4.3.5 Co, Zn and Cd uptake rates via isotope incubations

Co, Zn and Cd uptake rates were quantified using incubations of collected marine microbial communities spiked with stable or radioisotopes to trace the conversion of dissolved trace metal into the particulate phase. Briefly, unfiltered seawater used for the incubation uptake experiments was collected from the trace metal rosette, and the Co, Zn and Cd uptake incubations were spiked with 0.1 pM $^{57}CoCl_2$, 2 nM ^{67}ZnO and 300 pM ^{110}CdO, respectively. All incubation bottles were then sealed and placed in a flow-through deck-board incubator shielded by black screens for 24 hours. Incubation biomass was collected by vacuum filtration onto acid-rinsed 3 µm filters. The ^{57}Co incubation filters were stored at room temperature in petri dishes prior to radiochemical gamma ray counting both at sea and in the laboratory, and the ^{67}Zn and ^{110}Cd incubation filters were stored at -80 ºC in acid-rinsed cryovials until ICP-MS analysis in the laboratory. See Kellogg et al. (In prep), Rao 2020 and Kellogg (2022) for full methodology and instrumental analysis.

4.3.6 Pigment and phosphate analysis

Phytoplankton pigment samples were collected via filtration and analyzed for select pigments by high performance liquid chromatography (HPLC) as described in DiTullio and Geesey (2003). Macronutrient samples were collected from the trace metal rosette alongside dCo samples and were filtered using the same methodology as dCo and total metal samples (see above). Samples were collected in 60 mL high-density polyethylene (HDPE) bottles and were stored frozen until analysis. Dissolved PO_4 concentrations were determined by Joe Jennings at Oregon

State University via the molybdenum blue method (Bernhardt and Wilhelms 1967) using a Technicon AutoAnalyzer II attached to an Alpkem autosampler.

4.3.7 Historical dCo and pigment data

In this study, dCo profiles from the CICLOPS expedition are compared to those from previous fieldwork in the Ross Sea, including the Controls of Ross Sea Algal Community Structure (CORSACS) expeditions: CORSACS-1 (NBP-0601; December 27, 2005 – January 23, 2006) and CORSACS-2 (NBP-0608; November 8, 2006 – December 3, 2006), reported in Saito et al. (2010), and fieldwork sampling the water column under the sea ice of the McMurdo Sound (November 9 – 23, 2009), reported in Noble et al. (2013). Dissolved cobalt and pigment data from these three fieldwork expeditions were sampled and analyzed with comparable methodologies as those used on the CICLOPS expedition, and the CORSACS data are accessible online at https://www.bco-dmo.org/dataset/3367.

4.3.8 Type-II regressions

The linear regressions presented in this study are two-way (type-II) linear regressions, with the exception of the standard addition curves used to calculate dCo concentrations (Sect. 4.3.2). Two-way regressions are ideal for stoichiometric ratios because they allow for error in both the x and y parameters and do not assume dependence between the x and y axes. The two-way regression function used in this study was rewritten to Python from a MATLAB file (lsqfitma.m) originally written by Ed Pelzer circa 1995 (Chmiel et al. 2022) and is available at https://github.com/rebecca-chmiel/GP15.

4.4 Results

4.4.1 Dissolved Co distribution and speciation

During the CICLOPS expedition, full-depth profiles of dCo and labile dCo samples were analyzed from 13 stations in the Amundsen Sea (Stations 4, 10, 11, 15), the Ross Sea (Stations 20, 29, 32, 35) and Terra Nova Bay (Stations 22, 27, 41, 57, 60; Fig. 1). The resulting dCo profiles (Fig. 2) show depletion in the surface ocean consistent with a nutrient-type profile; at 10 m depth, dCo concentrations were found to be 28 ± 7 pM in the Amundsen Sea (n = 4), 28 ± 12 pM in the Ross Sea (n = 4), and only 11 ± 7 pM in Terra Nova Bay (n = 5; Table 1). Labile dCo distributions

generally followed those of dCo, and also showed strong depletion in the surface ocean. In the Amundsen and Ross Seas, surface (~10 m) labile dCo concentrations ranged between 12 pM at station 10 and undetected (n.d.) concentrations at stations 15, 20, 32 and 35. In Terra Nova Bay, no surface labile dCo concentrations were detected at any of the 5 stations sampled, indicating that the dCo inventory was dominated by the strongly ligand-bound dCo fraction.

In the deep ocean (≥ 100 m depth), dCo distributions were relatively consistent throughout the water column, with the exception of elevated concentrations of dCo at near-bottom depths. The Amundsen Sea, Ross Sea, and Terra Nova Bay all displayed similar deep (≥ 100 m depth) dCo concentrations of 41 ± 5 pM (n = 30), 46 ± 8 pM (n = 32), and 39 ± 18 pM (n = 34), respectively (Table 1). The high standard deviation of deep dCo in Terra Nova Bay is partially driven by the elevated near-seafloor signal at Station 41; when the two deepest points at Station 41 are omitted (770 m and 780 m), the average deep dCo in Terra Nova Bay was 36 ± 10 pM. The CICLOPS expedition included regular near-bottom sampling as allowed by the altimeter aboard the trace metal rosette. As a result, many of the deepest profile samples contained elevated concentrations of dCo and labile dCo along the seafloor, including stations 20, 22, 27, 29, 32, 41 and 57. This deep dCo signal was particularly observable in stations where two near-seafloor samples were taken: one ~10 m above the seafloor and a second ~20 m above the seafloor. At stations 41 and 57, the elevated near-seafloor dCo signal was pronounced (Fig. 2); the samples ~10 m above the seafloor contained 111 pM and 50 pM dCo, respectively, which represents a 31 pM and 18 pM increase, respectively, from the samples collected ~20 m above the seafloor. This finding indicates that dCo was elevated in a narrow band close to the seafloor, and it is likely that dCo concentrations continued to increase in the 10 m between the deepest samples and the seafloor.

4.4.2 Phytoplankton communities in the Amundsen Sea, Ross Sea and Terra Nova Bay

Stations 11, 15, 22 and 27 exhibited high surface fluorescence (17–42 mg m^{-3} at 10 m), characteristic of phytoplankton blooms. The Amundsen Sea stations displayed high concentrations of 19-hexanolyoxyfucoxanthin (19-Hex), a pigment commonly used as a proxy for haptophyte biomass. In the coastal Southern Ocean, 19-Hex is often correlated with *Phaeocystis antarctica* (DiTullio and Smith 1996; DiTullio et al. 2003), and it is typical to find concentrated blooms of *P. antarctica* in these regions, particularly during the highly productive spring blooms of the Antarctic polynyas (Arrigo et al. 1999; Ditullio et al. 2000). The pigment fucoxanthin (Fuco) is

commonly used as a proxy for diatom biomass, although it can also be produced by haptophytes like *P. antarctica* (DiTullio et al. 2003); Fuco was observed at stations throughout the expedition and tended to be relatively consistent throughout the CICLOPS stations, particularly in comparison to 19-Hex, which displayed very high concentrations at some stations and much lower concentrations at others. In general, higher concentrations of Fuco were observed within Terra Nova Bay as well as at stations sampled later in the summer season. This is consistent with past observations of summer diatom blooms, which tend to occur after the annual spring bloom where and when dFe is available (Sedwick et al. 2000; Peloquin and Smith 2007; Saito et al. 2010).

The upper ocean inventories of three pigments, 19-Hex, Fuco and Chlorophyll-a (Chl-a), a proxy for general phytoplankton biomass, were estimated via trapezoidal integration of their profiles between 5 and 50 m depth and compared to the 2005/2006 summer bloom observed on the CORSACS-1 expedition (Fig. 3). In the Ross Sea and Terra Nova Bay, CICLOPS stations contained lower inventories of Chl-a and 19-Hex compared to the Amundsen Sea, which likely reflects the end of the spring bloom and transition to a summer phytoplankton assemblage in these regions. One noticeable difference between the overlapping 2006 and 2018 January seasons is the larger Fuco inventory in 2006 in both the Ross Sea and Terra Nova Bay compared to the 2018 season, indicating a higher presence of diatom biomass during the CORSACS-1 expedition than the CICLOPS expedition, despite relatively similar magnitudes of the Chl-a inventory.

4.4.3 dZn, dCd and trace metal uptake rates

Dissolved Cd and Zn profiles, as well as trace metal uptake rate (ρM) profiles for Co, Zn and Cd from the CICLOPS expedition are originally presented in Rao (2020) and Kellogg (2022). This study presents a comparison between Co distribution and the distribution and uptake of Zn and Cd, two metals whose uptake and use by marine phytoplankton may be linked with Co biogeochemical cycling since the three metals can use similar uptake transporter pathways and often can be substituted as cofactors for metalloenzymes like carbonic anhydrase (Sunda and Huntsman 1995, 2000; Saito and Goepfert 2008; Kellogg et al. 2020, 2022).

The dZn and dCd profiles observed on the CICLOPS expedition displayed a nutrient-like structure, with depleted concentrations near the surface (Fig. 4). In the deep ocean (≥100 m), dZn and dCd concentrations were relatively uniform, displaying average deep concentrations of 4.6 ± 1.1 pM (n = 182) and 700 ± 90 pM, respectively (Table 2). Average dissolved metal concentrations

in the surface ocean (10 m depth) were higher in the Amundsen Sea (2.5 ± 1.2 nM dZn; 450 ± 170 pM Cd) compared to the Ross Sea (1.1 ± 1.2 nM dZn; 250 ± 170 pM dCd) and Terra Nova Bay (0.87 ± 0.42 nM dZn; 130 ± 170 pM dCd). This trend of decreasing surface dissolved metals from the Amundsen to Terra Nova Bay is mirrored in the dCo distributions, and could be explained by the seasonal drawdown of metal nutrients in the mixed layer over time, differences in the metal uptake of phytoplankton in the different regions, or both phenomenon occurring simultaneously.

At Stations 4, 11, 20, 22 and 57, uptake rates of Co, Zn and Cd were determined via spiked-isotope incubations from upper ocean seawater (0–200 m) (Rao 2020; Kellogg 2022). The relative ratios of the resulting uptake profiles from biomass collected onto 3 µm filters provide insight into the demand for Co, Zn and Cd of eukaryotic phytoplankton in coastal Antarctica (Fig. 5). Note that Co uptake within the bacterial size fraction (0.2–3 µm) was also analyzed and the results are presented in Rao (2020), but here we present the results of the eukaryotic size fraction (> 3 µm) to best represent the eukaryotic phytoplankton community present and compare to the Zn and Cd uptake experiments. It should be noted that uptake rates measured via tracer addition and deck-board incubation represent potential uptake and may be overestimations of the environmental nutrient uptake rates because the isotope tracer addition was labile – not at equilibrium with the natural seawater ligands – and could have perturbated the natural micronutrient inventories. The $^{57}CoCl_2$ addition (0.1 pM) was likely a small enough addition that the inventory was not significantly disturbed, but the ^{67}ZnO (2 nM) and ^{110}CdO (300 pM) were not tracer-level additions and may have perturbated the existing trace metal inventories, possibly increase the observed uptake rates (Rao 2020; Kellogg 2022).

Of the five stations with uptake rate data from all three trace metals of interest, four (Stations 4, 11, 20 and 22) are from a transect conducted from the Amundsen Sea to Terra Nova Bay, and were sampled within a span of 10 days from December 31, 2017 to January 9, 2018, while the last station, (Station 57) was sampled later in the summer on February 6, 2018; this range of stations allows us to assess the uptake stoichiometry along both spatial (location) and time (bloom progression) dimensions. The ρTM profiles displayed an increase in metal uptake of Co, Zn and Cd towards the surface, a shape which is mirrored in the lower dissolved trace metal concentrations of the surface ocean, suggesting the influence of phytoplankton uptake on the drawdown of micronutrients in the photic zone. The stoichiometry of ρTM among Co, Zn and Cd tended to directly follow the metals' availability as dissolved species: Co, which is present at the

lowest concentrations of ~10^{-11} M, was taken up at rates ranging between 10^{-13} and 10^{-12} M d^{-1}; Cd, at concentrations of ~10^{-10} M, was taken up at rates of 10^{-12} to 10^{-11} M d^{-1}; and Zn, present in the highest concentration of ~10^{-9} M, was taken up at rates of 10^{-12} to 10^{-10} M d^{-1}. This observation reveals order-of-magnitude differences in biological uptake between the three metals, matching patterns of metal availability in the water column.

4.5 Discussion

4.5.1 Biogeochemical Co cycle processes observed via dCo profiles and dCo : dPO_4^{3-} stoichiometry

Low surface ocean dCo and labile dCo concentrations are attributable to uptake by phytoplankton and bacteria in the Southern Ocean, giving the dCo and labile dCo profiles a distinct nutrient-like shape (Fig. 2). The labile dCo fraction was extremely low or below the limit of detection in surface waters, particularly within Terra Nova Bay, indicating strong drawdown of the labile fraction and near 100% complexation of dCo in the water column. Labile dCo is considered to be more bioavailable than strongly-bound dCo and thus is likely preferentially taken up by microbes when available. This labile dCo may then be rapidly cycled by phytoplankton in the mixed layer and any labile dCo released via remineralization, cell lysis, or grazing would be promptly taken up by other algae and microbes. A rapid turnover of labile dCo suggests a high demand for bioavailable Co from the surface phytoplankton community.

Dissolved Co and PO_4 displayed a generally positive relationship in the upper ocean, which is indicative of the co-cycling of both nutrients via phytoplankton uptake and remineralization (Fig. 6a). The processes of biological uptake and remineralization, when observed along dCo vs. dPO_4^{3-} axes, can be represented by vectors with positive slopes and opposite directionality. Abiotic dCo inputs and Co scavenging processes can be represented by vertical or near-vertical vectors because they decouple the cycling of dCo and dPO_4^{3-}. The positive dCo vs. dPO_4^{3-} linear relationship that is often observed within the ocean's mixed layer can exhibit a variety of slopes that are dictated by the nutrient uptake and remineralization stoichiometry of the microbial community (Saito et al. 2017). On CICLOPS, the dCo vs. dPO_4^{3-} relationship displayed a drawdown of both dCo and dPO_4^{3-} in the upper ocean, and the labile dCo vs. dPO_4^{3-} relationship revealed the stark lack of labile dCo throughout the upper ocean (Fig. 6b,d). The dCo vs. dPO_4^{3-} slope in the upper ocean (0–100 m depth) was found to be distinct for each of the three regions

sampled on the expedition; the Ross Sea displayed the highest slope (74 ± 18 µmol : mol), followed by the Amundsen Sea (47 ± 9 µmol : mol) and Terra Nova Bay, which displayed the lowest dCo vs. dPO_4^{3-} slope (26 ± 4 µmol : mol; Fig. 7; Table 3). These slopes reflect a relatively wide range of dCo stoichiometries that vary by a factor of 2.8 between the lowest and highest slopes observed. For comparison, the 2005/2006 CORSACS-1 and CORSACS-2 Ross Sea data points were pooled and the dCo vs. dPO_4 slope was recalculated (originally reported as 37.6 µmol : mol between 5–500 m depth; Saito et al., 2010) to fall within the same depth window (0–100 m). The resulting slope fell within the range of slopes observed on CICLOPS (49 ± 4 µmol : mol; $R^2 = 0.57$; n = 106).

The range of dCo vs. dPO_4^{3-} slopes reflects the elasticity of cobalt uptake stoichiometry in the upper ocean, which varies by microbial community, dCo availability, and the availability of other nutrients. Due to the number of factors that can affect the environmental stoichiometry of trace metal nutrients, the dCo vs. dPO_4^{3-} slope must be interpreted alongside other information about the marine environment, such as the available dCo inventory and the local nutrient limitation regime, making global comparisons of dCo : dPO_4^{3-} stoichiometry complex. The lower stoichiometric slope observed in Terra Nova Bay compared to the Ross and Amundsen Seas likely indicates not a lack of demand for Co by phytoplankton, but the low availability of Co in the surface ocean despite high demand for the metal. Terra Nova Bay was found to have the lowest average surface dCo, dZn and dCd concentrations of the three regions studied, and both Terra Nova Bay stations where ρCo was measured (Stations 22 and 57) displayed higher surface Co uptake rates (0.71 and 0.51 pM d^{-1}, respectively, at 25 m depth) than Station 20 in the Ross Sea (0.09 pM d^{-1} at 30 m depth). It is likely that the lower dCo stoichiometry in Terra Nova Bay is driven by nutrient draw down and low availability of labile dCo in the region resulting from productive phytoplankton blooms. Remineralization would also have played a role in setting the dCo vs. dPO_4 slope below the photic zone; a remineralization vector with a relatively low slope indicates that there is a lower dCo source from particulate Co biomass and a rapid turnover of recycled dCo back into biomass, suggesting a tight coupling of the dissolved and particulate phases.

Deviations from the linear uptake-remineralization line in the dCo vs. dPO_4^{3-} relationship occur when dCo distributions become decoupled from dPO_4^{3-} or vice versa, as with Co scavenging onto particles and lithogenic dCo sources. In other ocean regions, the dCo vs. dPO_4^{3-} relationship

displays a characteristic "curl" towards the high- dPO_4^{3-}, low-dCo in deeper waters, resulting from the net vector sum of both remineralization, which increases both dPO_4^{3-} and dCo, and scavenging to Mn-oxides, which removes dCo in excess of dPO_4^{3-} from the water column (Noble et al. 2008; Hawco et al. 2017; Saito et al. 2017). The dCo vs. dPO_4^{3-} relationship observed on CICLOPS, however, displayed no such scavenging curl, indicating no clear signal of dCo loss due to scavenging, at least within timescales relevant to water column mixing. This finding is consistent with previous studies of the Ross Sea that have also observed little evidence of dCo loss via scavenging in the mesopelagic (Saito et al. 2010; Noble et al. 2013). The lack of a visible scavenging signal may be attributable to the deep winter mixed layers of coastal Antarctic seas that reach depths of up to 600 m and can extend to the seafloor (Smith and Jones 2015). This deep vertical mixing allows the dCo : dPO_4^{3-} ratio in the deep ocean to reset on an annual timescale, potentially erasing any signals of dCo scavenging, which would be expected to occur on a timescale of decades to centuries (Hawco et al. 2017). Additionally, Oldham et al. (2021) concluded that a suppressed Co scavenging flux might be the result of a unique Mn cycle in the Ross Sea, characterize by low to undetectable concentrations of Mn-oxide particles, slow rates of Mn-oxide formation, and the stabilization of organic dMn via Mn(III) ligands (Oldham et al. 2021).

The elevated dCo signal observed from several depths within 20 m of the seafloor were sourced from a benthic nepheloid layer: a near-seafloor region of the water column characterized by high particle abundance, turbulence, and isopycnal movement of both dissolved and particulate material along the seafloor (Gardner et al. 2018). The Ross Sea has been observed to display strong nepheloid layers as cold, dense water flows northward along the Ross Sea shelf until it reaches the shelf break, carrying suspended sediments with it along the seafloor (Budillon et al. 2006). Nepheloid layers tend to be enriched in dissolved trace metals like dFe, and can act as a source of micronutrients if upwelled to the surface ocean (Marsay et al. 2014; Noble et al. 2017). Elevated dCo concentrations within the Ross Sea nepheloid layer is a novel finding, as previous expeditions analyzing dCo concentrations in the Ross Sea did not sample as close to the seafloor as the CICLOPS trace metal rosette was able to (Fitzwater et al. 2000; Saito et al. 2010; Noble et al. 2013). This finding is evidence of a dCo source to the deep ocean that may be upwelled to intermediate and upper ocean waters via vertical mixing.

4.5.2 Decreased Ross Sea dCo and labile dCo inventories

The dCo and labile dCo profiles observed along the 2017/2018 CICLOPS expedition displayed similar vertical structure as those observed along the 2005/2006 CORSACS expeditions; however, the CICLOPS dCo and labile dCo concentrations were notably lower throughout the water column compared to the CORSACS datasets (Fig. 8). This trend was particularly clear in the Ross Sea, where the stations from both expeditions contained the greatest regional overlap and labile dCo distributions from the prior 2006 CORSACS-2 expedition exceeded those observed on the 2017/2018 CICLOPS expedition (Fig. 9a-c; Table 4). The CORSACS-1 and CORSACS-2 expeditions displayed average deep (≥ 100 m) dCo concentrations of 55 ± 4 pM and 56 ± 6 pM, respectively, and CORSACS-2 displayed average deep labile dCo concentrations of 21 ± 7 pM; on CICLOPS, in contrast, the Ross Sea displayed average deep dCo and labile dCo concentrations of 46 ± 8 pM and 9 ± 7 pM, respectively. Independent t-tests determined that CORSACS-1 and CORSACS-2 deep Ross Sea dCo samples were statistically similar (p = 0.27) while deep CICLOPS samples were statistically different from CORSACS-1 and CORSACS-2 deep dCo (p < 0.0001; Table 4). This offset represents a mean dCo inventory loss of 8 – 10 pM dCo in the deep ocean, and approximately all of the difference can be accounted for by the loss of deep labile dCo (12 pM dCo; Fig. 9d-g), the more bioavailable form for dCo for biological uptake.

In the near-surface (10 m), labile dCo was undetectable at 3 of the 4 stations in the Ross Sea on CICLOPS, and the near-surface labile : total ratio in the one station where labile dCo was detectable (station 29; 3.5 pM labile dCo) was only 0.09. In contrast, the 2006 CORSACS-2 expedition reported the presence of labile dCo at five stations with concentrations of 17 ± 7 pM at 6 m depth and 14 ± 9 pM at 16 m depth, and reported labile : total ratios at 6 m and 16 m depth of 0.37 ± 0.13 and 0.28 ± 0.17, respectively. This trend can be at least partially explained by the seasonality differences between the spring CORSACS-2 expedition and the summer CICLOPS expedition; as the phytoplankton bloom progresses in the photic zone of the Ross Sea, labile dCo concentrations would be drawn down by community uptake and would exhibit lower concentrations later in the summer season. This seasonal trend was evident in the surface dCo inventory differences between the summer CORSACS-1 and spring CORSACS-2 expeditions (Fig. 9a,d,e). However, the low, often undetectable, labile dCo concentrations observed in the surface Ross Sea on the CICLOPS expedition illustrate the intensity of bloom-driven labile dCo depletion in the region, leaving 91–100% strong ligand-bound dCo in the surface Ross Sea. These

observations are consistent with the Co uptake rate measurements, which were found to be higher on CICLOPS (0.84 pM d^{-1}, n = 38) than on either CORSACS-1 or CORSACS-2 (0.67 pM d^{-1} and 0.25 pM d^{-1}, respectively) (Saito et al. 2010; Rao 2020).

Dissolved Co and labile dCo was also analyzed in the Ross Sea in 2009 by sampling the water column below the McMurdo Sound seasonal sea ice in the early spring (November 9–23) (Noble et al. 2013). Under the ice, the water column was well-mixed, and the dCo and labile dCo profiles showed relatively uniformity at all three stations measured (Fig. 2 of Noble et al., 2013). In the deep ocean (≥ 100 m), the mean dCo and labile dCo concentrations were 51 ± 4 and 15 ± 2 pM, respectively, which is lower than those observed on the 2005/2006 CORSACS expeditions and higher than those observed on the 2017/2018 CICLOPS expedition (Table 4). The mean deep labile dCo concentrations from the McMurdo Sound fieldwork were also significantly different from the mean deep labile dCo observed on CICLOPS (p = 0.0006), displaying an average deep labile dCo difference of 6 pM. This dataset supports the possibility of a long-term trend towards a decreasing deep dCo inventory in the Ross Sea, although the more coastal location and difference in sea ice cover should be considered when comparing the McMurdo Sound dataset to the CORSACS and CICLOPS observations. Notably, the methodology and instrumentation used to measure both dCo and labile dCo on both CORSACS expeditions, the McMurdo Sound fieldwork and the CICLOPS expedition were functionally identical, with the exception of an autosampler (Metrohm 858 Sample Processor) used on the 2017/2018 CICLOPS expedition.

The low labile dCo inventory in the Ross Sea was a surprising discovery during CICLOPS since relatively high concentrations of labile dCo were previously noted to be a distinctive feature of the Ross Sea and Southern Ocean when compared to the tropical and subtropical global oceans (Saito et al. 2010). In prior studies in this region, high labile : total dCo ratios were hypothesized to be due to the absence of ligand-producing – and vitamin B_{12}-producing – marine cyanobacteria like *Synechococcus* in the Ross Sea (Caron et al. 2000; DiTullio et al. 2003; Bertrand et al. 2007), since *Synechococcus*-dominated communities have been known to produce a substantial amount of Co ligands (Saito et al. 2005). However, high Co ligand concentrations and low labile dCo concentrations have previously been observed at a more pelagic location in the Southern Ocean near New Zealand, where it was hypothesized that the decay of a eukaryotic phytoplankton bloom generated higher abundances of co-binding ligands in the surface ocean (Ellwood et al. 2005).

The decrease in the dCo and labile dCo inventories is clearly apparent when the CICLOPS and CORSACS dCo vs. dPO_4^{3-} relationships across all expedition regions are compared (Fig. 6c,e). Over similar dPO_4^{3-} ranges, the CICLOPS dCo concentrations are generally lower than those observed on CORSACS, and the CICLOPS labile dCo concentrations are considerably lower, with labile dCo essentially absent from upper ocean samples with a dPO_4^{3-} concentration < 1.75 µM. Despite the lack of observable scavenging, the CICLOPS dCo vs. dPO_4^{3-} relationship appeared to be noticeably nonlinear throughout the water column (R^2 = 0.42), while CORSACS samples displayed a more linear trend (R^2 = 0.57). The CICLOPS dCo vs. dPO_4^{3-} relationship creates a concave, "scooped" shape where dCo was depleted relative to dPO_4^{3-}, displaying a lower slope in the upper ocean than was observed on the CORSACS expeditions (Fig. 6c). This scooped shape was particularly evident in Terra Nova Bay where the upper ocean dCo : dPO_4^{3-} stoichiometric slope was the lowest (26 ± 4 µmol : mol; R^2 = 0.65). The depletion of dCo relative to dPO_4^{3-} observed on CICLOPS appears driven by the shift in Co speciation as a result of near-total uptake of the upper ocean labile dCo fraction and subsequent dominance of the remaining strong ligand-bound dCo fraction in the upper ocean. Similar to the deep dCo loss described above, the difference between the CORSACS and CICLOPS dCo vs. dPO_4^{3-} relationship can be accounted for by the depletion of the labile dCo inventory. In the deep ocean where both dCo and dPO_4^{3-} are more abundant, the large range in dCo concentrations relative to dPO_4^{3-} concentrations may be evidence of deep inputs of dCo and labile dCo from the nepheloid layer, which was more attentively sampled on CICLOPS than either CORSACS expedition (Sect. 4.5.1).

4.5.3 dZn and dCd stoichiometry

Dissolved Zn concentrations observed on CICLOPS were low in the surface ocean, particularly in Terra Nova Bay, where dZn concentrations in the sub-nanomolar ranges were observed (average dZn = 0.87 ± 0.42 at 10 m depth, n = 11). Marine microbes require Zn for a wide range of metabolic uses; for example, eukaryotic phytoplankton use Zn as a cofactor in carbonic anhydrase (Roberts et al. 1997; Morel et al. 2020) and bacteria such as *Pseudoalteromonas* use Zn in a range of proteases (Mazzotta et al. 2021). Prior culture studies have found that Zn scarcity can lead to co-limitation of both Zn and carbon in several eukaryotic phytoplankton strains (Morel et al. 1994; Sunda and Huntsman 2000), and field incubation experiments have shown evidence for Zn co-limitation with Fe (Jakuba et al. 2012) and silicate

(Chappell et al. 2016) in the Pacific Ocean. During the CICLOPS expedition, an incubation experiment performed at Station 27 in Terra Nova Bay found compelling evidence for Zn and Fe co-limitation, which constrained Chl-a production and DIC draw-down by phytoplankton in the region (Kellogg et al. [Submitted]).

Many but not all phytoplankton are able to substitute Co and Cd for Zn as their carbonic anhydrase metallic cofactor (Lee and Morel 1995; Sunda and Huntsman 1995; Lane et al. 2005; Kellogg et al. 2022), which provides metabolic flexibility and a competitive edge in low-dZn environments (Kellogg et al. 2020). The Cd-containing carbonic anhydrase CDCA is currently the only known metabolic use of Cd by phytoplankton, and the uptake of dCd and dCo in the photic zone, both metals which are typically less abundant than dZn in the oceans, often increases under low dZn conditions (Sunda and Huntsman 1995, 1996; Jakuba et al. 2008; Kellogg et al. 2020; Morel et al. 2020). Cations like Zn, Cd and Co that possess similar charge and atomic radii often share the same transporter uptake systems, and the relative availability of different metal cofactors for use in an organism's metalloproteome is partially determined by the environmental metal concentrations and the affinity of the metals for ligands associated with a cell's metal transport proteins (Irving and Williams 1948; Sunda and Huntsman 1992, 1995). When dZn concentrations are low, more Cd and Co are able to bind to the transporter ligands despite the relative stability of their ligand-bound complexes, which tend to be lower for Co than for Zn. Through this mechanism, dZn concentrations and cycling can influence the distribution and uptake of Co and Cd, particularly in low dZn environments like the Ross Sea and Terra Nova Bay.

The dZn vs. dPO_4^{3-} and dCd vs. dPO_4^{3-} relationships observed in the Amundsen Sea, Ross Sea and Terra Nova Bay were compared relative to dCo vs. dPO_4^{3-} (Fig. 7; Table 3). The resulting shapes of these relationships were similar to that of dCo vs. dPO_4^{3-}, exhibiting distinct differences in slope between surface and deep waters. The stark difference in trace metal stoichiometry slopes between the upper and deep ocean are likely driven by differences in metal speciation over depth. In the surface ocean, a shallower trace metal : dPO_4^{3-} slope suggests a trace metal fraction that is largely bound to strong organic ligands, with a smaller excess labile fraction. The more bioavailable labile fraction of metals would have been drawn down by phytoplankton, whose uptake transport systems preferentially bind to labile metals. At deeper depths, the presence of labile metals in excess of strong organic ligands result in a higher metal : dPO_4^{3-} slope. For this analysis, the depth threshold that separates the upper ocean from the deep ocean was selected

manually in order to optimize the linear fit of the upper and deep ocean trends and to best capture the depth dependence of the observed trace metal stoichiometries. This depth threshold can best be conceptualized as an inflection point that represents the largest change in trace metal concentrations with respect to depth or, in this case, dPO_4^{3-} concentration. The depth threshold used for dCo in both the Ross Sea and Terra Nova Bay (100 m) is deeper than those used for dZn and dCd, (range of 25 – 50 m). Thus, the inflection points of the "scoops" in the trace metal stoichiometries are driven by the uptake stoichiometry of the region's phytoplankton community rather than the mixed layer depth of the upper ocean.

A shallow dCo : dPO_4^{3-} slope that extends below the photic zone could suggest Co uptake by heterotrophic bacteria, archaea and possibly sinking phytoplankton below the photic zone. Heterotrophic prokaryotic uptake of labile Co is largely driven by the bacteria and archaea that contain a vitamin B_{12} synthesis pathway that is absent in all eukaryotes (Warren et al. 2002; Osman et al. 2021); unlike carbonic anhydrase, the use of Co as a co-factor in the vitamin B_{12} corrin ring structure cannot be substituted for by other divalent cations like Zn and Cd. Many vitamin B_{12}-synthesizing bacteria possess genes for Co(II)-specific transporters in addition to more general metal ion transporters, and the Co-specific transporters are regulated by cellular concentrations of vitamin B_{12}, illustrating the importance of vitamin B_{12} synthesis in driving bacterial Co uptake (Osman et al. 2021); however, this mechanism has not been observed within marine bacterial communities. Additionally, vitamin B_{12} uptake by both prokaryotes and eukaryotes has been found to be common in Antarctic coastal communities (Taylor and Sullivan 2008; Rao 2020), and likely contributes to the depletion of ligand-bound dCo in both the surface and mesopelagic ocean.

The shallower Zn apparent nutricline could also be explained by the higher stability of Zn metal-ligand complexes compared to Co complexes within phytoplankton metabolisms, allowing for higher uptake rates of dZn when available (Irving and Williams 1948; Sunda and Huntsman 1995). The vertical dimension of trace metal loss captured by a comparison of these apparent nutriclines could be conceptualized as a time-dependent process driven by the phytoplankton community's preference for each trace metal, with preferred nutrients like Zn exhibiting a shallower stoichiometric inflection point from the metal being depleted quickly within the photic zone, and nutrients like dCo, which is often taken up by eukaryotes when dZn is scarce (Sunda and Huntsman 1995; Kellogg et al. 2020), exhibiting a deeper stoichiometric inflection point below the photic zone. This analysis suggests that substitution at the interface of the uptake mechanism

for trace metal transporters at least partially controlled the stoichiometry of Zn/Cd/Co distributions and uptake in the upper ocean.

4.5.4 Zn/Cd/Co uptake using a shared trace metal membrane transport system

This study synthesized dissolved concentration and uptake datasets for Co, Zn and Cd (Table 5), three trace metal nutrients whose use by phytoplankton is collectively integral to surface ocean productivity and the biogeochemical cycling of Fe, vitamin B_{12} and carbon in the Southern Ocean. This combined dataset is ideal for interrogating questions of environmental competitive inhibition of Zn, Cd and Co transport in low-dZn environments. The observation of order of magnitude trends in trace metal uptake rates over depth profiles (ρZn > ρCd > ρCo) was novel, and paralleled the order of magnitude trends of trace metal concentrations in seawater ([Zn] > [Cd] > [Co]; Fig 5). This environmental observation reflected the findings of numerous culture experiments that quantify the uptake of trace metals as a function of the concentration of available labile metals and the affinity of the metal for a cell transporter's binding ligand (Irving and Williams 1948; Sunda and Huntsman 1992, 1995, 2000; Kellogg et al. 2020).

Evidence for elevated Co uptake in the low-dZn environments of the surface ocean was supported by the trace metal uptake rates. When ρZn and ρCd was normalized to ρCo (ρTM : ρCo; Fig. 5), deviations from these order-of-magnitude trends can be observed; in particular, at Stations 4 and 11 in the Amundsen Sea and Station 22 in Terra Nova Bay, ρZn and ρCd stoichiometry relative to ρCo tended to decrease towards the surface in the upper 50 m, while the opposite trend appeared to occur at Station 57 in the late summer. The surface-most trends of stations 20 and 57 were undetermined due to a lack of a 10 m ρCo value. This increasing surface Co uptake stoichiometry relative to Zn and Cd at Stations 4, 11 and 22 – stations that also displayed significant phytoplankton blooms – suggests that Co uptake increased in low-Zn environments, while later in the summer at Station 57, ρCo lessened relative to ρZn, possibly due to the deepening of the mixed layer in February, bringing additional dZn to the upper ocean via vertical mixing (Fig. 4). The increase in the observed ρCo rate was likely due to the upregulation of the shared Zn and Co uptake transporter system.

From laboratory culture experiments aimed at examining the microbial uptake of Zn and other trace metals, it is apparent that many diatoms and coccolithophores contain two distinct Zn uptake systems: a low-affinity system that operates at higher concentrations of dZn and a high-

affinity system that functions at lower concentrations of dZn (Sunda and Huntsman 1992; John et al. 2007). Both transport mechanisms are relatively unspecific as to the divalent metals transported into the cell; the low-affinity system is known to transport Zn, Cd and Mn, while the high-affinity system transports Zn, Cd and Co. (Sunda and Huntsman 1995, 1996); thus, Co uptake is often inhibited at high dZn concentrations when the low-affinity system is active (Sunda and Huntsman 1995; Sunda 2012). In culture, diatoms have been observed to switch from the low-affinity to the high-affinity transport system between $10^{-10.5}$ and $10^{-9.5}$ M dZn^{2+} (Sunda and Huntsman 1992; John et al. 2007), a relevant range for the lowest values of total dZn observed in the surface ocean on CICLOPS (dZn minimum = 1 x 10^{-10} M at Station 46, 10 m depth), and the dZn^{2+} pool would have been even smaller due to organic complexation.

To investigate the influence of transporter competitive inhibition on trace metal uptake via the high-affinity uptake system, we can estimate the predicted ρCo, ρCd and ρZn values given the observed trace metal concentrations with an equation adapted from Michaelis-Menten enzyme-substrate kinetics (Sunda and Huntsman 1996, 2000):

$$\text{Predicted } \rho M = \frac{V_{max}[M^{2+}]K_M}{[Co^{2+}]K_{Co} + [Cd^{2+}]K_{Cd} + [Zn^{2+}]K_{Zn}}$$

where M is the trace metal (Co, Cd, Zn) whose uptake is being calculated, V_{max} is the saturation uptake rate of the transporter system, and K_{Co}, K_{Cd} and K_{Zn} are steady state affinity constants for the metal-ligand complex associated with the membrane transporter. For this system, we assumed $K_{Zn} = K_{Cd} = K_{Co} = 10^{9.6}$, where $10^{9.6}$ is the value of K_{Zn} for the high-affinity uptake system determined by Sunda et al. (1992), and that 99% of the dCo, dCd and dZn inventory was bound to strong organic ligands, leaving 1% of the total metal concentration labile. Note that the assumption that K and the percent labile multipliers are equal for all metals results in their value being nullified by their presence in both the numerator and denominator of the predicted uptake equation, and so their assumed values have no numerical impact on the predicted uptake values. It was also assumed that the V_{max} for each trace metal were equal, which is likely a good assumption for metals that share an uptake system, although V_{max} is known to vary with trace metal concentration, a function that we have assumed here to be negligible (Sunda and Huntsman 1985, 1996; Sunda 1989). V_{max} is in units of μmol (mol C)$^{-1}$ d^{-1}, and the predicted trace metal uptake rates were converted to units

of M d^{-1} using a C : Chl-a ratio of 130 w/w, derived from the Ross Sea phytoplankton community (DiTullio and Smith 1996).

When the predicted metal uptake rates were calculated using a V_{max} value of 262 µmol (mol C)$^{-1}$ d^{-1} from previous Zn culturing experiments (Sunda and Huntsman 1992), the resulting values recreated the trend of the observed trace metal uptake profiles, with higher uptake rates in the surface ocean and lower rates below the photic zone, but the predicted values were over an order of magnitude greater than the measured uptake rates (Fig. H1). This offset may be due to several factors: (1) the assumed C : Chl-a ratio to scale predicted uptake with observed biomass may be high, (2) the V_{max} value calculated from laboratory experiments may be high, or (3) the assumptions that the speciation of the dissolved trace metals are 99% strongly-bound at all depths, for all metals is incorrect. The final explanation may play a role in the offset between the predicted and observed uptake rates, and illustrates the complexities of translating lab-based culture work to environmental measurements and in-situ analyses. The V_{max} value is also relatively unconstrained, and it is reasonable to assume it may be lower in the Ross Sea than observed in culture if the phytoplankton exhibit suppressed metal quotas to survive in a metal-deplete environment. With this in mind, the V_{max} value was tuned to 4 µmol (mol C)$^{-1}$ d^{-1} to fit the observed uptake rates, which is lower than any Co, Cd or Zn V_{max} reported in the literature from culture studies (Fig. 10). Using the tuned V_{max} value, the high-affinity uptake system equation properly predicts the order of magnitude trends inherent in the observed Co/Cd/Zn uptake rates. This analysis demonstrates the measured uptake rates from the Ross Sea were likely driven by the concentration ratios of available metals throughout the water column, following a high-affinity transporter model of Co, Cd and Zn uptake.

The maximum diffusive limit, a calculation of the phytoplankton community's maximum diffusion rate for the uptake of trace metal nutrients through their cell membranes, was also estimated and compared to the observed and predicted uptake rate profiles. The physical limits of uptake via diffusion was determined as a function of the surface area of phytoplankton membranes (Sunda and Huntsman 1992):

$$\text{Maximum diffusive limit} = 4\pi r D[M^{2+}]$$

where *r* is the equivalent spherical radius of a phytoplankton cell, assumed to be 3 µm, a reasonable value for diatom species, and *D* is a diffusion rate constant of 2 x 10^{-6} cm^2 s^{-1}, calculated for Zn^{2+} at 20ºC (Sunda and Huntsman 1992). The diffusive limit was converted to units of M d^{-1} using a C : cell volume ratio of 12.5 mol C L^{-1}, which is the average of two diatom ratios reported in Sunda and Huntsman (1995) (11 and 14 mol C L^{-1}), and the same C : Chl-a ratio of 130 w/w used for the predicted uptake rate estimate above (DiTullio and Smith 1996). The resulting diffusive limit profiles are highly dependent on the assumed speciation of each trace metal; when the dCo, dCd and dZn inventories were assumed to be 99% bound (Fig. 10), the maximum diffusive limit was slightly greater than the predicted and observed uptake rates, but when the inventories were assumed to be 100% labile (Fig. H1), the diffusive limit greatly exceeded the uptake rates by several orders of magnitude. Since the metal inventories almost certainly vary in their speciation of dZn and dCd over depth, as was observed in the dCo inventory, an accurate maximum diffusive limit would exist between the two extremes of 0% bound and 99% bound, and might be expected to be greater at deeper depths, where a higher fraction of the dissolved metal inventory is labile. For additional analysis of the predicted metal uptake ratios and the maximum diffusive limit, see Appendix H.

4.5.5 Vitamin B_{12} and Zn stress, and their implications for increasing biological dCo demand

The near-absence of labile dCo and low concentration of ligand-bound dCo in coastal Antarctic seas may indicate a larger shift in the region towards vitamin B_{12} limitation. Vitamin B_{12} has been shown to be co-limiting with Fe in the Ross Sea and elsewhere (Sañudo-Wilhelmy et al. 2006; Bertrand et al. 2007), and increased vitamin B_{12} uptake by both bacterioplankton and eukaryotic phytoplankton has been observed in incubation experiments following the alleviation of surface ocean Fe limitation (Bertrand et al. 2011). Two primary sources of Fe to the Antarctic seas are a flux of lithogenic Fe from melting ice shelves along the continent and sediment resuspension along the seafloor, both of which have been observed to be meaningful Fe sources to the Amundsen Sea (Planquette et al. 2013; St-Laurent et al. 2017). The source of particulate Fe from glacial meltwater to coastal Antarctic seas has been increasing over the past several decades and is expected to continue to increase as Antarctic ice shelves and glaciers melt and retreat due to global climate change (Monien et al. 2017). The source of particulate Co from glacial meltwater would also be expected to increase since Co, like Fe, has been observed to be transported from the

Antarctic continent via ice melt (Westerlund and Öhman, 1991), and it is yet unclear what role this presumably increasing source of Co to the surface ocean plays in the reduced inventories of dCo in the surface ocean.

Although it is difficult to definitively conclude that the low dCo inventory observed on CICLOPS is representative of a decadal trend towards vitamin B_{12} limitation and not simply variation in micronutrient availability and community structure, the inventory and stoichiometric uptake trends documented in this study are compelling evidence for a changing biogeochemical Co cycle in the coastal Southern Ocean. Paired with the recent discovery of Zn/Fe co-limitation in Terra Nova Bay (Kellogg et al. [Submitted]), these results suggest a complex landscape of micronutrient scarcity and limitation in coastal Antarctic seas where plankton community structures and Fe additions from melting ice sheets can generate patches of vitamin B_{12} and Zn limitation within a broadly Fe-scarce HNLC region.

The bacterial community is essential to the development and alleviation of vitamin B_{12} limitation within a eukaryotic phytoplankton bloom since only prokaryotes possess the metabolic pathway to synthesize the vitamin (Warren et al. 2002; Croft et al. 2005). In the Southern Ocean, near-zero counts of photosynthetic bacteria indicate that the heterotrophic bacterial communities are primarily responsible for vitamin B_{12} production in the region (Bertrand et al. 2011). Vitamin B_{12} can become limiting when the bacterial community is low in abundance and/or growth limited by a different nutrient such as dissolved organic matter (DOM). In the Ross Sea, bacterioplankton have been found to be growth limited by an inadequate supply of DOM (Church et al. 2000; Bertrand et al. 2011), and there can be up to a one-month lag between the onset of the spring phytoplankton bloom and an associated bacterial bloom stimulated by phytoplankton DOM production (Ducklow et al. 2001). This offset suggests that vitamin B_{12} limitation among eukaryotes is most probable earlier in the season within the spring bloom. Additionally, low abundances of mezozooplankton in the Ross Sea create phytoplankton blooms with low grazing rates (Caron et al. 2000; Ducklow et al. 2001), which may allow low DOM conditions to persist later into a bloom and exacerbate vitamin B_{12} stress among eukaryotes.

A shift towards vitamin B_{12} limitation would likely favor phytoplankton with flexible metabolisms that are able to reduce their demand for Co and vitamin B_{12} when necessary. Organisms that can express the vitamin B_{12}-independent MetE gene may out-compete those expressing the vitamin B_{12}-dependent MetH gene (Rao et al. [In review]; Rodionov et al. 2003;

Bertrand et al. 2013; Helliwell 2017). *P. antarctica*, for example, may be well suited to periods of vitamin B_{12} limitation due to the symbiotic bacterial microbiomes that form within its colonies and produce B vitamins that allow the colonies to grow when B vitamins are otherwise unavailable (Brisbin et al. 2022). *P. antacrica* has also been found to express a novel MetE-fusion gene when vitamin B_{12} limited and MetH while vitamin-replete, suggesting a highly flexible vitamin B_{12} metabolism (Rao et al. [In review]).

There is compelling evidence for high rates of biological Co uptake in the Ross Sea during the 2017/2018 summer compared to the 2005/2006 summer driven by the uptake of dCo from vitamin B_{12} and Zn scarcity. Together, these two stressors increase the rate of Co uptake as well as the Co : C stoichiometry of phytoplankton biomass. The stoichiometry of Co uptake has been observed to be highly plastic in this study and others, responding to the availability of other micronutrients and the requirements of the microbial community (Sunda and Huntsman 1995; Saito et al. 2017). An increase in ρCo could then result in a decrease of the Co inventory in coastal Antarctic seas, following the mechanism detailed below.

Biological uptake alone would not permanently remove Co from the water column; uptake only shifts Co from the dissolved phase to the particulate phase, where POM remineralization restores Co back to the dissolved phase. The net removal pathways of Co include (1) burial as POM, (2) particle scavenging and (3) depletion of dCo into Circumpolar Deep Water (CDW). We have already noted that Co scavenging to Mn-oxides is particularly low in the Southern Ocean (Oldham et al. 2021), and we would expect the advection of dCo into CDW to be at steady state. Therefore, an increase in the burial flux of Co in POM is the most likely pathway for sustained loss of the Co inventory. When the ρCo rate increases, the stoichiometry of Co incorporation into biomass relative to P would also increase. Over years, a strengthened demand for Co via vitamin B_{12} and Zn stress could result in a steady loss of Co if the Co : C and Co : PO_4^{3-} stoichiometry of POM increases but the remineralization of POM is unchanged, increasing the flux of particulate Co into the deep ocean and sediments. In the winter, sea ice covers the Antarctic seas and the water column mixes, a process that would propagate the low dCo concentrations from the photic zone into the deep ocean and result in a steady loss of the dCo inventory throughout the water column.

Additionally, warming surface ocean temperatures likely play a role in phytoplankton productivity and nutrient uptake. Increasing both dFe availability and temperature have been shown to significantly increase phytoplankton growth and phytoplankton abundance in the Ross

Sea, and impact community structure (Rose et al., 2009; Spackeen et al., 2018; Zhu et al., 2016). From a kinetic perspective, higher surface temperatures would be expected to increase the uptake rates of nutrients, including micronutrients like Fe, Co and Zn, by increasing the value of K_M. However, the effects of temperature on productivity and community composition are more complex since increasing ocean temperatures would also decrease the solubility of CO_2, change the seasonality of ice cover and thus sunlight availability, and effect water column turnover and mixing regimes (Rose et al., 2009). The effects of warming temperatures on the intricate landscape of nutrient availability and limitation regimes described here is an open question in this study.

4.5.6 A two-box model that describes a mechanism for deep dCo inventory loss

To test the proposed mechanism that higher Co uptake rates and winter mixing can lead to a deep inventory loss of ~10 pM Co over 12 years, a time step two-box model of a 1 m^2 water column was created in Microsoft Excel to simulate the Ross Sea dCo cycle. A schematic of the modeled dCo cycle is presented in Fig. 11, flux equations to describe the biogeochemical cycling of Co are presented in Appendix I, and the parameters used to simulate dCo loss over 12 years and a hypothetical steady state condition are given in Table 6.

The change in dCo concentration over time (d[dCo]/dt) for a surface ocean (0–100 m) and deep ocean (100–500 m) was calculated as the sum of the dCo source fluxes minus the sum of the sink fluxes:

$$\left(\frac{d[dCo]}{dt}\right)_{Surface} = \frac{F_{Over} + F_{Remin} - F_{Up}}{V_{Surface}}$$

$$\left(\frac{d[dCo]}{dt}\right)_{Deep} = \frac{F_{Remin} + F_{Neph} - F_{Up} - F_{Over}}{V_{Deep}}$$

where F_{Over} is the overturning flux between the two boxes, F_{Remin} is the remineralization flux, F_{Up} is the biological uptake flux, and F_{Neph} is the flux of dCo from the nepheloid layer into the deep ocean (Table I1). F_{Up} was calculated using the measured ρCo uptake rates observed on the CORSACS and CICLOPS expeditions, and F_{Remin} was calculated using an assumed surface and deep remineralization factor (RF) of 0.9, indicating that 90% of the POM generated in the surface ocean is remineralized back to its inorganic dissolved components. In the Southern Ocean, the

fluxes of scavenging and aerosol deposition would be relatively negligible, and so these fluxes have been omitted from the model. The magnitude of F_{Neph} in the Ross Sea remains unconstrained, and in this model, the deep nepheloid dCo source was used as an adjustable parameter to tune the magnitude of deep dCo loss to be 10 pM over 12 years, which represents the approximate observed differences between the CORSACS and CICLOPS expeditions detailed in Sect. 4.5.2. An F_{Neph} was calculated to be 3550 pmol m^{-2} d^{-1} to the deep ocean, but this should not be considered a meaningful calculation of the observed nepheloid layer flux.

In the Ross Sea, the deep winter mixed layer can extend 600 m to the seafloor and turn over the whole water column in some locations (Smith and Jones 2015), mixing the surface and deep ocean under the winter sea ice and resulting in near-vertical profiles of dCo in the early spring (Noble et al. 2013). Here, the winter mixing process was modeled by combining the surface and deep ocean boxes into one homogenized box during the winter season (151 days, ~5 months). The dCo concentrations of the winter box were calculated using a volume-weighted average (see Appendix I).

This model provides a reasonable mechanism by which increases in ρCo such as those observed along the CICLOPS expedition might increase the burial flux of particulate Co, resulting in a net loss to the deep dCo inventory. The uptake rate of Co both within and below the photic zone, as well as the fraction of POM that is remineralized, dictated the flux of particulate Co into the sediments via burial. The initial dCo concentration was set at 56 pM, which approximates the mean deep dCo concentrations observed on both CORSACS-1 and CORSACS-2. When the model was run for 12 years, the time period between the first CORSACS expedition and the CICLOPS expedition, it generated a sawtooth pattern; the surface and deep boxes diverged over the course of the summer bloom season as biological uptake removed dCo from the surface box and remineralization replenished dCo in the deep box (Fig. 12). Winter mixing then unified and reset the water column, replenishing the surface dCo inventory. The model was run at steady state using the average surface ρCo rate observed on CORSACS-1 (0.27 pmol L^{-1} d^{-1}; Table 6) (Saito et al. 2010) and deep ρCo values that were tuned to allow no change in the deep dCo inventory every winter. When the model was run using representative surface and deep ρCo values observed on the CICLOPS expedition (0.87 and 0.1 pmol Co L^{-1} d^{-1}, respectively), the surface depletion of dCo was more pronounced by the end of the bloom season compared to the steady state model, and winter mixing resulted in a steady annual decrease of the deep dCo inventory. The mechanism of

dCo loss was driven by increasing ρCo, particularly in the surface ocean, and the propagation of dCo loss into the deep ocean via vertical mixing. The resulting burial flux when the model exhibited a deep dCo loss mechanism was higher than when the model was run at steady state (Table 6), demonstrating how higher Co uptake rates among plankton paired with a deep winter mixed layer can result in a diminishing dCo inventory on a decadal timescale.

The purpose of this model was to illustrate a possible mechanism for a dCo inventory loss over the 12-year period between the CORSACS and CICLOPS expeditions using reasonable estimates of Co uptake and other Co cycle fluxes to achieve the observed 10 pM deep inventory loss. This box model successfully shows the directionality of the changes to the deep ocean dCo inventory and deep burial flux when the ρCo values increase, but the magnitude of the estimated Co burial or the nepheloid Co source should not be considered meaningful flux values. The model represented a greatly simplified version of the carbon pump in the Southern Ocean, and it is likely that at least some of the unquantified Co cycle fluxes were not negligible, including horizontal advection, overturning water during the summer season, Co scavenging, and a surface aerosol source. Additionally, it is a simplifying assumption that ρCo values would be consistent throughout a surface or deep depth region, as well as consistent over an entire summer season. Despite its simplicity, the box model presented a concise and reasonable mechanism for this study's observation of a shrinking dCo inventory in the Ross Sea.

4.6 Conclusion

The Ross Sea, Amundsen Sea and Terra Nova Bay displayed lower dCo and labile dCo inventories during the 2017/2018 austral summer relative to prior observations in the region, which is consistent with observations of higher rates of Co use and uptake by phytoplankton and heterotrophic bacteria. The near-100% complexation of the dCo inventory reveals that the dCo loss is primarily due to the uptake of labile dCo, the most bioavailable form of dCo to marine microbes. The decrease in dCo throughout the water column compared to prior observations is indicative of a multi-year mechanism, whereby the removal of dCo from the surface mixed layer via uptake over the summer has been propagated into the deep ocean via winter mixing, resulting in a decrease in dCo concentration throughout the water column. This change may be due to the alleviation of Fe limitation through inputs from increased glacial melting and subsequent

development of intermittent vitamin B_{12} and/or Zn limitation, both of which would be expected to increase the demand for Co among plankton communities.

In coastal Antarctica and other regions impacted by global climate change, Co is a noteworthy trace nutrient to investigate because its small inventory and flexible phytoplankton stoichiometry make its biogeochemical cycle particularly vulnerable to perturbation. In the Arctic Ocean, for example, the dCo and labile dCo inventories have increased as melting ice and permafrost have increased the flux of Co-enriched riverine waters and sediments to the upper ocean (Bundy et al. 2020). Like many other trace nutrients, the Co cycle is integrally connected to that of other elements like Zn, Cd, Fe and carbon, and observations of perturbed Co inventories and changing nutrient limitation regimes would affect their biogeochemical cycles as well. In highly productive coastal Antarctic seas, shifts in micronutrient inventories and growth limitation could have implications for the composition of regional phytoplankton blooms and the magnitude of the Southern Ocean carbon sink.

Since the late 1980s, it has been hypothesized that the primary productivity and net carbon sequestration flux of the Southern Ocean is controlled by the supply of Fe to surface waters (Martin 1990; Martin et al. 1990). This theory, called the "iron hypothesis", posits that the addition of bioavailable Fe to an Fe-limited surface ocean stimulates productivity and, in turn, increases the regional and possibly global carbon sequestration flux from the atmosphere into deep ocean sediments. When applied to potential carbon dioxide removal (CDR) geoengineering projects, the iron hypothesis provides a theoretical framework for ocean iron fertilization (OIF), where significant quantities of Fe are introduced to the surface Southern Ocean to enhance the net sequestration of CO_2 and reduce global atmosphere CO_2 concentrations (Emerson 2019). Over the past three decades, several mesoscale Fe fertilization experiments have shown that large phytoplankton blooms can be stimulated by the addition of Fe to the surface Southern Ocean, and that the impact on the CO_2 sink is variable, modest and often difficult to assess (Coale et al. 1996; Boyd et al. 2000; de Baar et al. 2005; Smetacek et al. 2012). This study provides additional insights into the potential of OIF, suggesting that the alleviation of Fe limitation might shift the region towards the limitation of another trace nutrient such as vitamin B_{12}, Zn, and potentially Co. The nutrient limitation regimes of the Southern Ocean are complex, heterogeneous and possibly shifting on decadal timescales, and these intricacies must be examined when considering future OIF projects.

Acknowledgments

The authors thank the captain, crew and science party of the RVIB Nathanial B. Palmer for their support during the CICLOPS expedition. We also thank Joe Jennings (OSU) for dissolved macronutrient analysis, Véronique Oldham for sampling assistance, and Matthew Charette, Stephanie Dutkiewicz, and Alessandro Tagliabue for writing insights. This work was funded by grants from the National Science Foundation's Office of Polar Programs (OPP-1643684, OPP-1644073 and OPP-1643845).

References

Arrigo, K. R., Robinson, D. H., Worthen, D. L., Dunbar, R. B., Ditullio, G. R., Vanwoert, M. and Lizotte, M. P.: Phytoplankton community structure and the drawdown of nutrients and CO2 in the Southern Ocean, Science., 283, 365–367, 1999.

Arrigo, K. R., van Dijken, G. L. and Bushinsky, S.: Primary production in the Southern Ocean, 1997-2006, J. Geophys. Res., 113, C08004, doi:10.1029/2007JC004551, 2008.

Arrigo, K. R., Lowry, K. E. and van Dijken, G. L.: Annual changes in sea ice and phytoplankton in polynyas of the Amundsen Sea, Antarctica, Deep. Res. Part II Top. Stud. Oceanogr., 71–76, 5–15, doi:10.1016/j.dsr2.2012.03.006, 2012.

de Baar, H. J. W., Boyd, P. W., Coale, K. H., Landry, M. R., Tsuda, A., Assmy, P., Bakker, D. C. E., Bozec, Y., Barber, R. T., Brzezinski, M. A., Buesseler, K. O., Boyé, M., Croot, P. L., Gervais, F., Gorbunov, M. Y., Harrison, P. J., Hiscock, W. T., Laan, P., Lancelot, C., Law, C. S., Levasseur, M., Marchetti, A., Millero, F. J., Nishioka, J., Nojiri, Y., van Oijen, T., Riebesell, U., Rijkenberg, M. J. A., Saito, H., Takeda, S., Timmermans, K. R., Veldhuis, M. J. W., Waite, A. M. and Wong, C. S.: Synthesis of iron fertilization experiments: From the iron age in the age of enlightenment, J. Geophys. Res. C Ocean., 110(9), 1–24, doi:10.1029/2004JC002601, 2005.

Bernhardt, H. and Wilhelms, A.: The continuous determination of low level iron, soluble phosphate and total phosphate with the AutoAnalyzer(TM), in Technicon Symposium, vol. 1, p. 386., 1967.

Bertrand, E. M., Saito, M. A., Rose, J. M., Riesselman, C. R., Lohan, M. C., Noble, A. E., Lee, P. A. and DiTullio, G. R.: Vitamin B12 and iron colimitation of phytoplankton growth in the Ross Sea, Limnol. Oceanogr., 52(3), 1079–1093, doi:10.4319/lo.2007.52.3.1079, 2007.

Bertrand, E. M., Saito, M. A., Lee, P. A., Dunbar, R. B., Sedwick, P. N. and DiTullio, G. R.: Iron limitation of a springtime bacterial and phytoplankton community in the Ross Sea: implications for vitamin B12 nutrition, Front. Microbiol., 2, 160, doi:10.3389/fmicb.2011.00160, 2011.

Bertrand, E. M., Moran, D. M., McIlvin, M. R., Hoffman, J. M., Allen, A. E. and Saito, M. A.: Methionine synthase interreplacement in diatom cultures and communities: Implications for the persistence of B12 use by eukaryotic phytoplankton, Limnol. Oceanogr., 58(4), 1431–1450, doi:10.4319/lo.2013.58.4.1431, 2013.

Bown, J., Boye, M. and Nelson, D. M.: New insights on the role of organic speciation in the biogeochemical cycle of dissolved cobalt in the southeastern Atlantic and the Southern Ocean, Biogeosciences, 9, 2719–2736, doi:10.5194/bg-9-2719-2012, 2012.

Boyd, P. W., Watson, A. J., Law, C. S., Abraham, E. R., Trull, T., Murdoch, R., Bakker, D. C. E., Bowie, A. R., Buesseler, K. O., Chang, H., Charette, M., Croot, P., Downing, K., Frew, R., Gall, M., Hadfield, M., Hall, J., Harvey, M., Jameson, G., LaRoche, J., Liddicoat, M., Ling, R., Maldonado, M. T., McKay, R. M., Nodder, S., Pickmere, S., Pridmore, R., Rintoul, S., Safi, K., Sutton, P., Strzepek, R., Tanneberger, K., Turner, S., Waite, A. and Zeldis, J.: A mesoscale phytoplankton bloom in the polar Southern Ocean stimulated by iron fertilization, Nature, 407(6805), 695–702, doi:10.1038/35037500, 2000.

Brisbin, M. M., Mitarai, S., Saito, M. A. and Alexander, H.: Microbiomes of bloom-forming Phaeocystis algae are stable and consistently recruited, with both symbiotic and opportunistic modes, ISME J, doi:10.1038/s41396-022-01263-2, 2022.

Budillon, G., Salusti, E. and Tucci, S.: The evolution of density currents and nepheloid bottom layers in the Ross Sea (Antarctica), J. Mar. Res., 64(4), 517–540, doi:10.1357/002224006778715739, 2006.

Bundy, R. M., Tagliabue, A., Hawco, N. J., Morton, P. L., Twining, B. S., Hatta, M., Noble, A., Cape, M. R., John, S. G., Cullen, J. T. and Saito, M. A.: Elevated sources of cobalt in the Arctic Ocean, Biogeosciences, 17, 4745–4767, doi:https://doi.org/10.5194/bg-2020-84, 2020.

Caron, D. A., Dennett, M. R., Lonsdale, D. J., Moran, D. M. and Shalapyonok, L.: Microzooplankton herbivory in the Ross Sea, Antarctica, Deep Sea Res. II, 47, 3249–3272, 2000.

Chandler, J. W., Lin, Y., Gainer, P. J., Post, A. F., Johnson, Z. I. and Zinser, E. R.: Variable but persistent coexistence of Prochlorococcus ecotypes along temperature gradients in the ocean's surface mixed layer, Environ. Microbiol. Rep., 8(2), 272–284, doi:10.1111/1758-2229.12378, 2016.

Chappell, P. D., Vedmati, J., Selph, K. E., Cyr, H. A., Jenkins, B. D., Landry, M. R. and Moffett, J. W.: Preferential depletion of zinc within Costa Rica upwelling dome creates conditions for zinc co-limitation of primary production, J. Plankton Res., 38(2), 244–255, doi:10.1093/plankt/fbw018, 2016.

Chmiel, R., Lanning, N., Laubach, A., Lee, J.-M., Fitzsimmons, J., Hatta, M., Jenkins, W. J., Lam, P. J., Mcilvin, M., Tagliabue, A. and Saito, M. A.: Major processes of the dissolved cobalt cycle in the North and equatorial Pacific Ocean, Biogeosciences, 19, 2365–2395 [online] Available from: https://doi.org/10.5194/bg-19-2365-2022, 2022.

Church, M. J., Hutchins, D. A. and Ducklow, H. W.: Limitation of bacterial growth by dissolved organic matter and iron in the Southern Ocean, Appl. Environ. Microbiol., 66(2), 455–466, doi:10.1128/AEM.66.2.455-466.2000, 2000.

Coale, K. H., Johnson, K. S., Fitzwater, S. E., Gordon, R. M., Tanner, S., Chavez, F. P., Ferioli, L., Sakamoto, C., Rogers, P., Millero, F., Steinberg, Pa., Nightingale, P., Cooper, D., Cochlan, W. P., Landry, M. R., Constantinou, J., Rollwagen, G., Trasvina, A. and Kudela, R.: A massive phytoplankton bloom induced by an ecosystem-scale iron fertilization experiment in the equatorial Pacific Ocean, Nature, 383(334), 495–501, 1996.

Cohen, N. R., McIlvin, M. R., Moran, D. M., Held, N. A., Saunders, J. K., Hawco, N. J., Brosnahan, M., DiTullio, G. R., Lamborg, C., McCrow, J. P., Dupont, C. L., Allen, A. E. and Saito, M. A.: Dinoflagellates alter their carbon and nutrient metabolic strategies

across environmental gradients in the central Pacific Ocean, Nat. Microbiol., 6, 173–186, doi:10.1038/s41564-020-00814-7, 2021.
Croft, M. T., Lawrence, A. D., Raux-deery, E., Warren, M. J. and Smith, A. G.: Algae acquire vitamin B12 through a symbiotic relationship with bacteria, Nature, 438, 90–93, doi:10.1038/nature04056, 2005.
DiTullio, G. and Geesey, M. E.: Photosynthetic Pigments in Marine Algae and Bacteria, in Encyclopedia of Environmental Microbiology, edited by G. Bitton, pp. 2453–2470, John Wiley & Sons, Inc., New York, NY., 2003.
Ditullio, G. R., Grebmeier, J. M., Arrigo, K. R. and Lizotte, M. P.: Rapid and early export of Phaeocystis antarctica blooms in the Ross Sea , Antarctica, Nature, 404, 595–598, 2000.
DiTullio, G. R. and Smith, W. O. J.: Spatial patterns in phytoplankton biomass and pigment distributions in the Ross Sea, J. Geophys. Res., 101, 18467–18477, 1996.
DiTullio, G. R., Geesey, M. E., Jones, D. R., Daly, K. L., Campbell, L. and Smith, W. O. J.: Phytoplankton assemblage structure and primary productivity along 170° W in the South Pacific Ocean, Mar. Ecol. Prog. Ser., 255, 55–80, 2003.
Ducklow, H., Carlson, C., Church, M., Kirchman, D., Smith, D. and Steward, G.: The seasonal development of the bacterioplankton bloom in the Ross Sea, Antarctica, 1994-1997, Deep. Res. Part II, 48, 4199–4221, 2001.
Ellwood, M. J., Van Den Berg, C. M. G., Boye, M., Veldhuis, M., de Jong, J. T. M., de Baar, H. J. W., Croot, P. L. and Kattner, G.: Organic complexation of cobalt across the Antarctic Polar Front in the Southern Ocean, Mar. Freshw. Res., 56, 1069–1075, doi:10.1071/MF05097, 2005.
Emerson, D.: Biogenic iron dust: A novel approach to ocean iron fertilization as a means of large scale removal of carbon dioxide from the atmosphere, Front. Mar. Sci., 6, 22, doi:10.3389/fmars.2019.00022, 2019.
Fitzwater, S. E., Johnson, K. S., Gordon, R. M., Coale, K. H. and Smith, W. O.: Trace metal concentrations in the Ross Sea and their relationship with nutrients and phytoplankton growth, Deep. Res. Part II, 47, 3159–3179, 2000.
Gardner, W. D., Richardson, M. J. and Mishonov, A. V.: Global assessment of benthic nepheloid layers and linkage with upper ocean dynamics, Earth Planet. Sci. Lett., 482, 126–134, doi:10.1016/j.epsl.2017.11.008, 2018.
Glover, D., Jenkins, W. and Doney, S.: Modeling Methods for Marine Science, Cambridge University Press, New York., 2011.
Hawco, N. J., Ohnemus, D. C., Resing, J. A., Twining, B. S. and Saito, M. A.: A dissolved cobalt plume in the oxygen minimum zone of the eastern tropical South Pacific, Biogeosciences, 13(20), 5697–5717, doi:10.5194/bg-13-5697-2016, 2016.
Hawco, N. J., Lam, P. J., Lee, J., Ohnemus, D. C., Noble, A. E., Wyatt, N. J., Lohan, M. C. and Saito, M. A.: Cobalt scavenging in the mesopelagic ocean and its influence on global mass balance: Synthesizing water column and sedimentary fluxes, Mar. Chem., (August), doi:10.1016/j.marchem.2017.09.001, 2017.
Helliwell, K. E.: The roles of B vitamins in phytoplankton nutrition: new perspectives and prospects, New Phytol., 216, 62–68, doi:10.1111/nph.14669, 2017.
Irving, H. and Williams, R. J. P.: Order of stability of metal complexes, Nature, 162, 746–747, 1948.

Jakuba, R. W., Moffett, J. W. and Dyhrman, S. T.: Evidence for the linked biogeochemical cycling of zinc, cobalt, and phosphorus in the western North Atltic Ocean, Global Biogeochem. Cycles, 22(4), GB4012, doi:10.1029/2007GB003119, 2008.

Jakuba, R. W., Saito, M. A., Moffett, J. W. and Xu, Y.: Dissolved zinc in the subarctic North Pacific and Bering Sea: Its distribution, speciation, and importance to primary producers, Global Biogeochem. Cycles, 26, GB2015, doi:10.1029/2010GB004004, 2012.

John, S. G., Geis, R. W., Saito, M. A. and Boyle, E. A.: Zinc isotope fractionation during high-affinity and low-affinity zinc transport by the marine diatom Thalassiosira oceanica, Limnol. Oceanogr., 52(6), 2710–2714, doi:10.4319/lo.2007.52.6.2710, 2007.

Kellogg, R. M.: Assessing the potential for Zn limitation of marine primary production: proteomic characterization of the low Zn stress response in marine diatoms, Massachusetts Institute of Technology; the Woods Hole Oceanographic Institution., 2022.

Kellogg, R. M., McIlvin, M. R., Vedamati, J., Twining, B. S., Moffett, J. W., Marchetti, A., Moran, D. M. and Saito, M. A.: Efficient zinc/cobalt interreplacement in northeast Pacific diatoms and relationship to high surface dissolved Co : Zn ratios, Limnol. Oceanogr., 65(11), 2557–2582, doi:10.1002/lno.11471, 2020.

Kellogg, R. M., Moosburner, M. A., Cohen, N. R., Hawco, N. J., McIlvin, M. R., Moran, D. M., DiTullio, G. R., Subhas, A. V., Allen, A. E. and Saito, M. A.: Adaptive responses of marine diatoms to zinc scarcity and ecological implications, Nat. Commun., 13, doi:10.1038/s41467-022-29603-y, 2022.

Kellogg, R. M., Schanke, N. L., Lees, L. E., Chmiel, R. J., Rao, D., Brisbin, M. M., Moran, D. M., McIlvin, M. R., Bolinesi, F., Casotti, R., Balestra, C., Horner, T. J., Subhas, A. V., Dunbar, R. B., Allen, A. E., DiTullio, G. R. and Saito, M. A.: Zinc co-limitation of natural marine phytoplankton assemblages in coastal Antarctica [Submitted].

Lane, T. W., Saito, M. A., George, G. N., Pickering, I. J., Prince, R. C. and Morel, F. M. M.: A cadmium enzyme from a marine diatom, Nature, 435, 42–42, doi:https://doi.org/10.1038/435042a, 2005.

Lee, J. G. and Morel, F. M. M.: Replacement of zinc by cadmium in marine phytoplankton, Mar. Ecol. Prog. Ser., 127, 305–309, doi:10.3354/meps127305, 1995.

Marsay, C. M., Sedwick, P. N., Dinniman, M. S., Barrett, P. M., Mack, S. L. and McGillicuddy, D. J.: Estimating the benthic efflux of dissolved iron on the Ross Sea continental shelf, Geophys. Res. Lett., 41(21), 7576–7583, doi:10.1002/2014GL061684, 2014.

Martin, J. H.: Glacial-interglacial CO2 change: the iron hypothesis, Paleoceanography, 5(1), 1–13, doi:https://doi.org/10.1029/PA005i001p00001, 1990.

Martin, J. H., Fitzwater, S. E. and Gordon, R. M.: Iron deficiency limits phytoplankton growth in Antarctic waters, Global Biogeochem. Cycles, 4(1), 5–12, 1990.

Mazzotta, M. G., McIlvin, M. R., Moran, D. M., Wang, D. T., Bidle, K. D., Lamborg, C. H. and Saito, M. A.: Characterization of the metalloproteome of Pseudoalteromonas (BB2-AT2): biogeochemical underpinnings for zinc, manganese, cobalt, and nickel cycling in a ubiquitous marine heterotroph, Metallomics, 13, mfab060, doi:https://doi.org/10.1093/mtomcs/mfab060, 2021.

Monien, D., Monien, P., Brünjes, R., Widmer, T., Kappenberg, A., Silva Busso, A. A., Schnetger, B. and Brumsack, H.-J.: Meltwater as a source of potentially bioavailable iron to Antarctica waters, Antarct. Sci., 29(03), 277–291, doi:10.1017/S095410201600064X, 2017.

Morel, F. M. M., Reinfelder, J. R., Roberts, S. B., Chamberlain, C. P., Lee, J. G. and Yee, D.: Zinc and carbon co-limitation of marine phytoplankton, Nature, 369(6483), 740–742, doi:10.1038/369740a0, 1994.

Morel, F. M. M., Lam, P. J. and Saito, M. A.: Trace Metal Substitution in Marine Phytoplankton, Annu. Rev. Earth Planet. Sci., 48, 491–517, doi:10.1146/annurev-earth-053018-060108, 2020.

Noble, A. E., Saito, M. A., Maiti, K. and Benitez-Nelson, C. R.: Cobalt, manganese, and iron near the Hawaiian Islands: A potential concentrating mechanism for cobalt within a cyclonic eddy and implications for the hybrid-type trace metals, Deep. Res. Part II Top. Stud. Oceanogr., 55(10–13), 1473–1490, doi:10.1016/j.dsr2.2008.02.010, 2008.

Noble, A. E., Moran, D. M., Allen, A. E. and Saito, M. A.: Dissolved and particulate trace metal micronutrients under the McMurdo Sound seasonal sea ice: basal sea ice communities as a capacitor for iron, Front. Chem., 1, 25, doi:10.3389/fchem.2013.00025, 2013.

Noble, A. E., Ohnemus, D. C., Hawco, N. J., Lam, P. J. and Saito, M. A.: Coastal sources, sinks and strong organic complexation of dissolved cobalt within the US North Atlantic GEOTRACES transect GA03, Biogeosciences, 14(11), 2715–2739, doi:10.5194/bg-14-2715-2017, 2017.

Oldham, V. E., Chmiel, R., Hansel, C. M., DiTullio, G. R., Rao, D. and Saito, M.: Inhibited manganese oxide formation hinders cobalt scavenging in the Ross Sea, Global Biogeochem. Cycles, 35, e2020GB006706, doi:10.1029/2020GB006706, 2021.

Osman, D., Cooke, A., Young, T. R., Deery, E., Robinson, N. J. and Warren, M. J.: The requirement for cobalt in vitamin B12: A paradigm for protein metalation, Biochim. Biophys. Acta - Mol. Cell Res., 1868, 118896, doi:10.1016/j.bbamcr.2020.118896, 2021.

Peloquin, J. A. and Smith, W. O. J.: Phytoplankton blooms in the Ross Sea, Antarctica: Interannual variability in magnitude, temporal patterns, and composition, J. Geophys. Res., 112, C08013, doi:10.1029/2006JC003816, 2007.

Planquette, H., Sherrell, R. M., Stammerjohn, S. and Field, M. P.: Particulate iron delivery to the water column of the Amundsen Sea, Antarctica, Mar. Chem., 153, 15–30, doi:10.1016/j.marchem.2013.04.006, 2013.

Price, N. M., Harrison, G. I., Hering, J. G., Hudson, R. J., Pascale, M., Nirel, V., Palenik, B. and Morel, F. M. M.: Preparation and Chemistry of the Artificial Algal Culture Medium Aquil, Biol. Oceanogr., 6, 443–461, 2013.

Rao, D.: Characterizing cobalamin cycling by Antarctic marine microbes across multiple scales, Massachusetts Institute of Technology; the Woods Hole Oceanographic Institution., 2020.

Rao, D., Fussy, Z., Moran, D. M., McIlvin, M. R., Allen, A. E., Follows, M. J. and Saito, M. A.: Flexible B12 ecophysiology of Phaeocystis antarctica to a fusion B12-independent methionine synthase with widespread homologues [In review]., PNAS [online] Available from: http://arxiv.org/abs/1712.09707.

Roberts, S. B., Lane, T. W. and Morel, F. M. M.: Carbonic Anhydrase in the Marine Diatom Thalassiosira Weissflogii (Bacillariophyceae), J. Phycol., 33(5), 845–850, doi:10.1111/j.0022-3646.1997.00845.x, 1997.

Rodionov, D. A., Vitreschak, A. G., Mironov, A. A. and Gelfand, M. S.: Comparative genomics of the vitamin B12 metabolism and regulation in prokaryotes, J. Biol. Chem., 278(42), 41148–41159, doi:10.1074/jbc.M305837200, 2003.

Rose, J. M., Feng, Y., Ditullio, G. R., Dunbar, R. B., Hare, C. E., Lee, P. A., Lohan, M., Long,

M., Smith, W. O., Sohst, B., Tozzi, S., Zhang, Y. and Hutchins, D. A.: Synergistic effects of iron and temperature on Antarctic phytoplankton and microzooplankton assemblages, Biogeosciences, 6, 3131–3147, doi:10.5194/bg-6-3131-2009, 2009.

Saito, M. A. and Goepfert, T. J.: Zinc-cobalt colimitation of Phaeocystis antarctica, Limnol. Oceanogr., 53(1), 266–275, 2008.

Saito, M. A. and Moffett, J. W.: Complexation of cobalt by natural organic ligands in the Sargasso Sea as determined by a new high-sensitivity electrochemical cobalt speciation method suitable for open ocean work, Mar. Chem., 75(1–2), 49–68, doi:10.1016/S0304-4203(01)00025-1, 2001.

Saito, M. A., Rocap, G. and Moffett, J. W.: Production of cobalt binding ligands in a Synechococcus feature at the Costa Rica upwelling dome, Limnol. Oceanogr., 50(1), 279–290, 2005.

Saito, M. A., Goepfert, T. J., Noble, A. E., Bertrand, E. M., Sedwick, P. N. and DiTullio, G. R.: A seasonal study of dissolved cobalt in the Ross Sea, Antarctica: micronutrient behavior, absence of scavenging, and relationships with Zn, Cd, and P, Biogeosciences, 7, 4059–4082, doi:10.5194/bg-7-4059-2010, 2010.

Saito, M. A., Noble, A. E., Hawco, N., Twining, B. S., Ohnemus, D. C., John, S. G., Lam, P., Conway, T. M., Johnson, R., Moran, D. and McIlvin, M.: The acceleration of dissolved cobalt's ecological stoichiometry due to biological uptake, remineralization, and scavenging in the Atlantic Ocean, Biogeosciences, 14(20), 4637–4662, doi:10.5194/bg-14-4637-2017, 2017.

Sañudo-Wilhelmy, S. A., Gobler, C. J., Okbamichael, M. and Taylor, G. T.: Regulation of phytoplankton dynamics by vitamin B12, Geophys. Res. Lett., 33(4), 10–13, doi:10.1029/2005GL025046, 2006.

Sedwick, P. N. and Ditullio, G. R.: Regulation of algal blooms in Antarctic shelf waters by the release of iron from melting sea ice, Geophys. Reseach Lett., 24(20), 2515–2518, 1997.

Sedwick, P. N., Ditullio, G. R. and Mackey, D. J.: Iron and manganese in the Ross Sea, Antarctica: Seasonal iron limitation in Antarctic shelf waters, J. Geophys. Res., 105(C5), 11321–11336, 2000.

Sedwick, P. N., Marsay, C. M., Sohst, B. M., Aguilar-Islas, A. M., Lohan, M. C., Long, M. C., Arrigo, K. R., Dunbar, R. B., Saito, M. A., Smith, W. O. and Ditullio, G. R.: Early season depletion of dissolved iron in the Ross Sea polynya: Implications for iron dynamics on the Antarctic continental shelf, J. Geophys. Res., 116, C12019, doi:10.1029/2010JC006553, 2011.

Smetacek, V., Klaas, C., Strass, V. H., Assmy, P., Montresor, M., Cisewski, B., Savoye, N., Webb, A., D'Ovidio, F., Arrieta, J. M., Bathmann, U., Bellerby, R., Berg, G. M., Croot, P., Gonzalez, S., Henjes, J., Herndl, G. J., Hoffmann, L. J., Leach, H., Losch, M., Mills, M. M., Neill, C., Peeken, I., Röttgers, R., Sachs, O., Sauter, E., Schmidt, M. M., Schwarz, J., Terbrüggen, A. and Wolf-Gladrow, D.: Deep carbon export from a Southern Ocean iron-fertilized diatom bloom, Nature, 487, 313–319, doi:10.1038/nature11229, 2012.

Smith, W. O. J. and Jones, R. M.: Vertical mixing, critical depths, and phytoplankton growth in the Ross Sea, ICES J. Mar. Sci., 72(6), 1952–1960, 2015.

Spackeen, J. L., Sipler, R. E., Bertrand, E. M., Xu, K., McQuaid, J. B., Walworth, N. G., Hutchins, D. A., Allen, A. E. and Bronk, D. A.: Impact of temperature, CO2, and iron on nutrient uptake by a late-season microbial community from the Ross Sea, Antarctica, Aquat. Microb. Ecol., 82, 145–159, doi:10.3354/ame01886, 2018.

St-Laurent, P., Yager, P. L., Sherrell, R. M., Stammerjohn, S. E. and Dinniman, M. S.: Pathways and supply of dissolved iron in the Amundsen Sea (Antarctica), J. Geophys. Res. Ocean., 122(9), 7135–7162, doi:10.1002/2017JC013162.Received, 2017.

Sunda, W. G.: Trace metal interactions with marine phytoplankton, Biol. Oceanogr., 6(5–6), 411–442, doi:10.1080/01965581.1988.10749543, 1989.

Sunda, W. G.: Feedback interactions between trace metal nutrients and phytoplankton in the ocean, Front. Microbiol., 3, 204, doi:10.3389/fmicb.2012.00204, 2012.

Sunda, W. G. and Huntsman, S. A.: Regulation of cellular manganese and manganese transport in the unicellular rates alga Chlamydomonas, Limnol. Oceanogr., 30(1), 71–80, doi:10.4319/lo.1985.30.1.0071, 1985.

Sunda, W. G. and Huntsman, S. A.: Feedback interactions between zinc and phytoplankton in seawater, Limnol. Oceanogr., 37(1), 25–40, doi:10.4319/lo.1992.37.1.0025, 1992.

Sunda, W. G. and Huntsman, S. A.: Cobalt and zinc interreplacement in marine phytoplankton: Biological and geochemical implications, Limnol. Oceanogr., 40(8), 1404–1417, doi:10.4319/lo.1995.40.8.1404, 1995.

Sunda, W. G. and Huntsman, S. A.: Antagonisms between cadmium and zinc toxicity and manganese limitation in a coastal diatom, Limnol. Oceanogr., 41(3), 373–387, 1996.

Sunda, W. G. and Huntsman, S. A.: Effect of Zn, Mn, and Fe on Cd accumulation in phytoplankton: Implications for oceanic Cd cycling, Limnol. Oceanogr., 45(7), 1501–1516, 2000.

Taylor, G. T. and Sullivan, C. W.: Vitamin B12 and cobalt cycling among diatoms and bacteria in Antarctic sea ice microbial communities, Limnol. Oceanogr., 53(5), 1862–1877, 2008.

Warren, M. J., Raux, E., Schubert, H. L. and Escalante-Semerena, J. C.: The biosynthesis of adenosylcobalamin (vitamin B12), Nat. Prod. Rep., 19, 390–412, doi:10.1039/B108967F, 2002.

Westerlund, S. and Öhman, P.: Cadmium, copper, cobalt, nickel, lead, and zinc in the water column of the Weddell Sea, Antarctica, Geochim. Cosmochim. Acta, 55(8), 2127–2146, doi:10.1016/0016-7037(91)90092-J, 1991.

Zhu, Z., Xu, K., Fu, F., Spackeen, J. L., Bronk, D. A. and Hutchins, D. A.: A comparative study of iron and temperature interactive effects on diatoms and Phaeocystis antarctica from the Ross Sea, Antarctica, Mar. Ecol. Prog. Ser., 550, 39–51, doi:10.3354/meps11732, 2016.

Tables

Table 1. Mean dCo and labile dCo values measured in the surface ocean (10 m) and the deep ocean (> 100 m) in the three regions sampled. One dCo sample and numerous labile dCo samples analyzed were determined to be below the analytical detection limit (<DL) of 4 pM. Only using the values measured above the detection limit would artificially inflate the calculation of the mean value; instead, samples measured between 0 and the DL were left unaltered as their originally measured value and samples with no detected concentrations of dCo or labile dCo (n.d.) were adjusted to 0 pM. The number of samples included in the mean calculation that are <DL is indicated by $n_{<DL}$.

Surface (10 m)					
Region	**n**	**dCo_{mean} [pM]**	**$n_{<DL}$ for dCo**	**Labile dCo_{mean} [pM]**	**$n_{<DL}$ for labile dCo**
Amundsen Sea	4	28 ± 7	0	5 ± 6	2
Ross Sea	4	28 ± 12	0	1 ± 2[a]	4
Terra Nova Bay	5	11 ± 7	1	n.d.[b]	5
Deep (> 100 m)					
Region	**n**	**dCo_{mean} [pM]**	**dCo $n_{<DL}$**	**Labile dCo_{mean} [pM]**	**Labile dCo $n_{<DL}$**
Amundsen Sea	30	41 ± 5	0	4 ± 4	14
Ross Sea	32	46 ± 8	0	9 ± 7	9
Terra Nova Bay	34	39 ± 18	0	6 ± 8	18

[a] Of the 4 surface samples analyzed for labile dCo in the Ross Sea, 3 were n.d. and the fourth contained 3.5 pM labile dCo.

[b] All surface samples in Terra Nova Bay were n.d. for labile dCo.

Table 2. Mean dZn and dCd values from the surface ocean (10 m) and the deep ocean (> 100 m) in the three regions sampled.

Surface (10 m)				
Region	**dZn_{mean} [nM]**	**n_{dZn}**	**dCd_{mean} [pM]**	**n_{dCd}**
Amundsen Sea	2.6 ± 1.2	4	450 ± 170	4
Ross Sea	1.1 ± 1.2	6	250 ± 170	7
Terra Nova Bay	0.87 ± 0.42	11	130 ± 60	11
All	1.3 ± 1.0	21	230 ± 170	22
Deep (> 100 m)				
Region	**dZn_{mean} [nM]**	**n_{dZn}**	**dCd_{mean} [pM]**	**n_{dCd}**
Amundsen Sea	5.4 ± 0.6	30	730 ± 40	30
Ross Sea	4.7 ± 0.6	65	740 ± 80	65
Terra Nova Bay	4.3 ± 1.4	87	670 ± 100	90
All	4.6 ± 1.1	182	700 ± 90	185

Table 3. Trace metal : dPO_4^{3-} stoichiometric regressions for dCo, dZn and dCd in both the surface and deep ocean of the Amundsen Sea, Ross Sea and Terra Nova Bay, as shown in Fig. 7. Linear regression slopes with a $R^2 < 0.50$ are not show as the slope values should not be considered meaningful stoichiometric values.

Region	dCo:dPO_4^{3-} [µmol:mol]				dZn:dPO_4^{3-} [mmol:mol]				dCd:dPO_4^{3-} [mmol:mol]			
	Depths [m]	**n**	**Slope**	**R^2**	**Depths [m]**	**n**	**Slope**	**R^2**	**Depths [m]**	**n**	**Slope**	**R^2**
Amundsen Sea												
Surface	0-100	16	47 ± 9	0.64	0-30	9	4.6 ± 0.9	0.72	0-25	6	0.47 ± 0.08	0.86
Deep	>100	20	--	0.02	>30	35	--	0.37	>25	38	0.59 ± 0.06	0.72
Ross Sea												
Surface	0-100	15	74 ± 18	0.53	0-30	11	--	0.07	0-25	11	0.19 ± 0.05	0.56
Deep	>100	24	--	0.21	>30	77	9.8 ± 1.0	0.54	>25	79	--	0.26
Terra Nova Bay												
Surf	0-100	20	26 ± 4	0.65	0-50	24	1.9 ± 0.3	0.65	0-30	21	0.15 ± 0.03	0.59
Deep	>100	26	--	0.05	>50	95	--	0.30	>30	104	0.64 ± 0.03	0.80

Table 4. The mean dCo and labile dCo observed in the deep (≥ 100 m) Ross Sea, and the average deep dCo loss between 3 previous sampling expeditions (CORSACS-1 in summer 2005/2006; CORSACS-2 in spring 2006; under-ice sampling in McMurdo Sound in spring 2009) and the CICLOPS expedition (2017/2018). Dissolved Co and labile dCo loss values were calculated as the difference between mean deep concentrations observed on previous expeditions and those observed on the CICLOPS expedition. No labile dCo data (n.d.) is presented from the CORSACS-1 expedition. Independent t-test were performed to determine the significance of difference between the deep mean concentrations from previous expeditions compared to the CICLOPS expedition; * indicates a result that shows significant difference between CICLOPS and a previous expedition ($p < 0.005$). The mean deep dCo concentrations from the CORSACS expeditions were not significantly different from each other ($p = 0.27$).

	dCo_{mean} [pM]	**n**	**Labile dCo_{mean} [pM]**	**n**	**dCo Loss [pM]**	***p*-value**	**Labile dCo Loss [pM]**	***p*-value**
CORSACS-1[a]	55 ± 4	26	n.d.		8 ± 9	< 0.0001*	--	--
CORSACS-2[a]	56 ± 6	19	21 ± 7	20	10 ± 10	< 0.0001*	12 ± 10	< 0.0001*
McMurdo Sound[b]	51 ± 4	19	15 ± 2	19	4 ± 8	0.02	6 ± 7	0.0006*
CICLOPS	46 ± 8	32	9 ± 7	32	--	--	--	--

[a] Data originally published in Saito et al., 2010.
[b] Data originally published in Noble et al., 2013.

Table 5. Dissolved stoichiometric ratios and uptake stoichiometric ratios of five station profiles for Co, Cd and Zn. The dCo : dCd : dZn : dPO_4^{3-} ratio is the dissolved stoichiometry of metals present in the water column normalized to dPO_4^{3-}, and the ρCo : ρCd : ρZn ratio is the uptake stoichiometry of microbial communities normalized to ρCo.

Region	Station	Depth [m]	dCo : dCd : dZn : dPO_4^{3-}	ρCo : ρCd : ρZn
Amundsen Sea	4	10	19 : 314 : 1,716 : 1,000,000	1 : 8 : 56
		30	23 : 295 : 1,889 : 1,000,000	1 : 16 : 88
		50	24 : 293 : 2,096 : 1,000,000	1 : 15 : 108
	11	10	13 : 204 : 1,018 : 1,000,000	1 : 10 : 77
		20	15 : 212 : 970 : 1,000,000	1 : 13 : 89
		30	17 : 231 : 1,290 : 1,000,000	1 : 29 : 294
		50	19 : 280 : 1,835 : 1,000,000	1 : 0*: 229
		75	21 : 301 : 2,009 : 1,000,000	1 : 0* : 532
		100	23 : 358 : 2,727 : 1,000,000	1 : 11 : 708
		150	17 : 313 : 1,974 : 1,000,000	1 : 0* : 797
		200	17 : 325 : 2,137 : 1,000,000	1 : 3 : 885
Ross Sea	20	30	17 : 323 : 1,846 : 1,000,000	1 : 13 : 349
		50	13 : 305 : 2,020 : 1,000,000	1 : 11 : 163
		100	17 : 333 : 2,400 : 1,000,000	1 : 0* : 376
		150	16 : 330 : 2,321 : 1,000,000	1 : 0* : 507
		200	14 : 336 : 2,358 : 1,000,000	1 : 0* : 913
Terra Nova Bay	22	10	15 : 136 : 617 : 1,000,000	1 : 12 : 81
		25	10 : 158 : 546 : 1,000,000	1 : 11 : 75
		40	11 : 254 : 1,127 : 1,000,000	1 : 29 : 166
		75	13 : 301 : 1,965 : 1,000,000	1 : 7 : 228
		100	11 : 304 : 1,938 : 1,000,000	1 : 56 : 705
		150	16 : 310 : 2,212 : 1,000,000	1 : 122 : 584
	57	50	13 : 179 : 894 : 1,000,000	1 : 17 : 37
		75	13 : 297 : 1,644 : 1,000,000	1 : 3 : 18
		100	15 : 320 : 1,798 : 1,000,000	1 : 8 : 40

*Denotes depths at which ρCd was under the methodological detection limit.

Table 6. Parameters of the Co cycle two-box model, run as both a steady state model with lower Co uptake rates (ρCo) and as a mechanism for deep dCo inventory loss driven by higher ρCo values. The calculated burial flux of particulate Co within each model variation is also given, but note that the burial flux values should be interpreted a comparison of the Co sink via the biological pump when ρCo is varied, and not as observed or meaningful Co flux magnitudes.

Model Parameters	**Value**	**Units**
Bloom season length	214	days
Surface box height	100	m
Deep box height	500	m
Remineralization Factor (RF)	0.9	
Deep Nephloid Flux	3550	pmol Co m^{-2} d^{-1}
Overturning Water Flux	0	m^3 d^{-1}
Steady State Parameters		
Surface ρCo	0.27	pmol Co L^{-1} d^{-1}
Deep ρCo	0.66	pmol Co L^{-1} d^{-1}
Burial Flux	3550	pmol Co m^{-2} d^{-1}
dCo Loss Parameters		
Surface ρCo	0.87	pmol Co L^{-1} d^{-1}
Deep ρCo	0.1	pmol Co L^{-1} d^{-1}
Burial Flux	5870	pmol Co m^{-2} d^{-1}

Figures

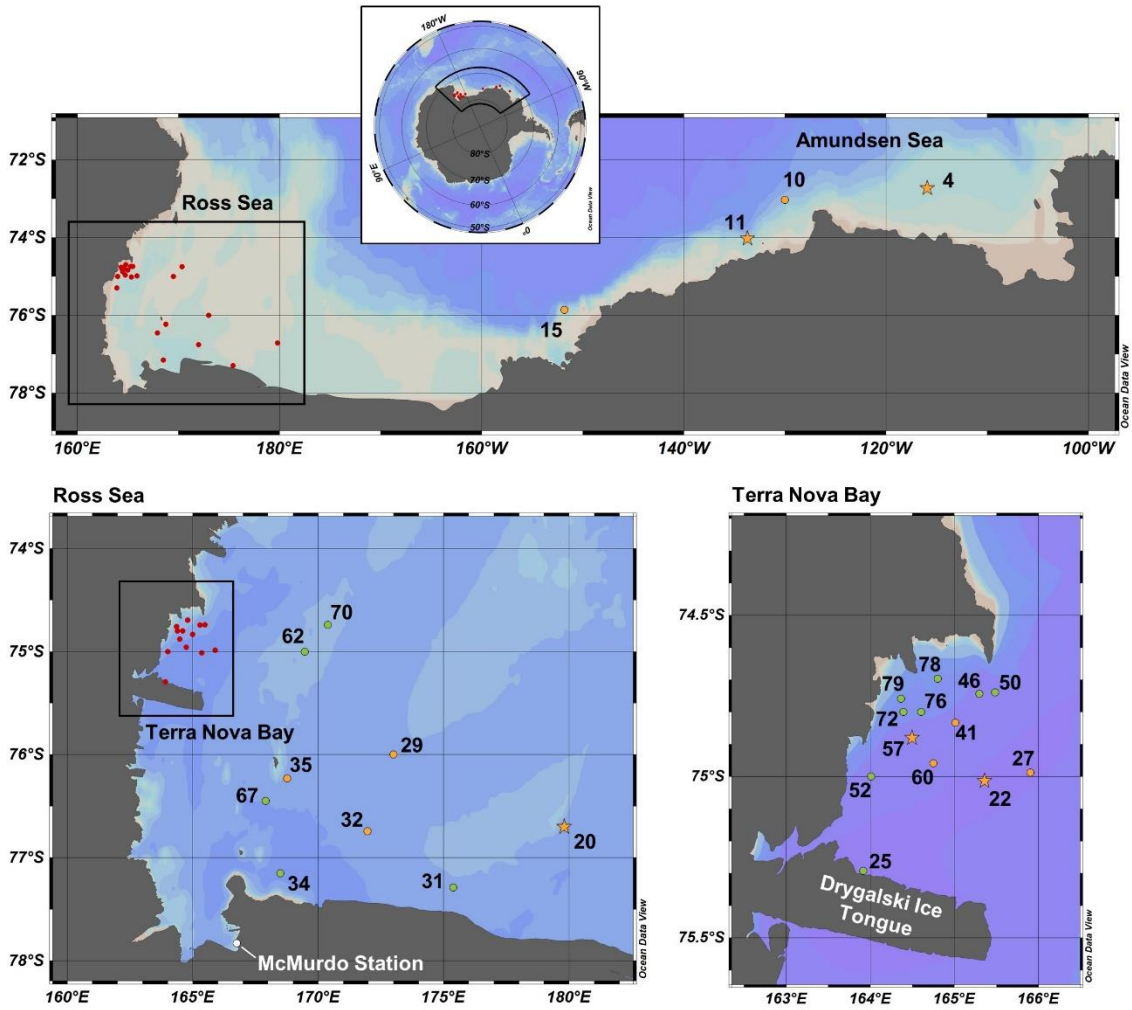

Figure 1. Map of CICLOPS stations in coastal Antarctic waters, including insets of stations within the Ross Sea and Terra Nova Bay. Dissolved Co, dZn and dCd were analyzed at stations marked in yellow, and stations marked in green were analyzed for dZn and dCd, but electrochemical dCo measurements were not conducted. At stations marked with a star, Co, Zn and Cd uptake profiles are presented in this study. Stations marked in red are shown in more detail in an inset. Note that the grey coastline marks both terrestrial coastline and areas of consistent ice, including ice shelves and glaciers; this includes the Drygalski Ice Tongue, a glacier to the south of Terra Nova Bay.

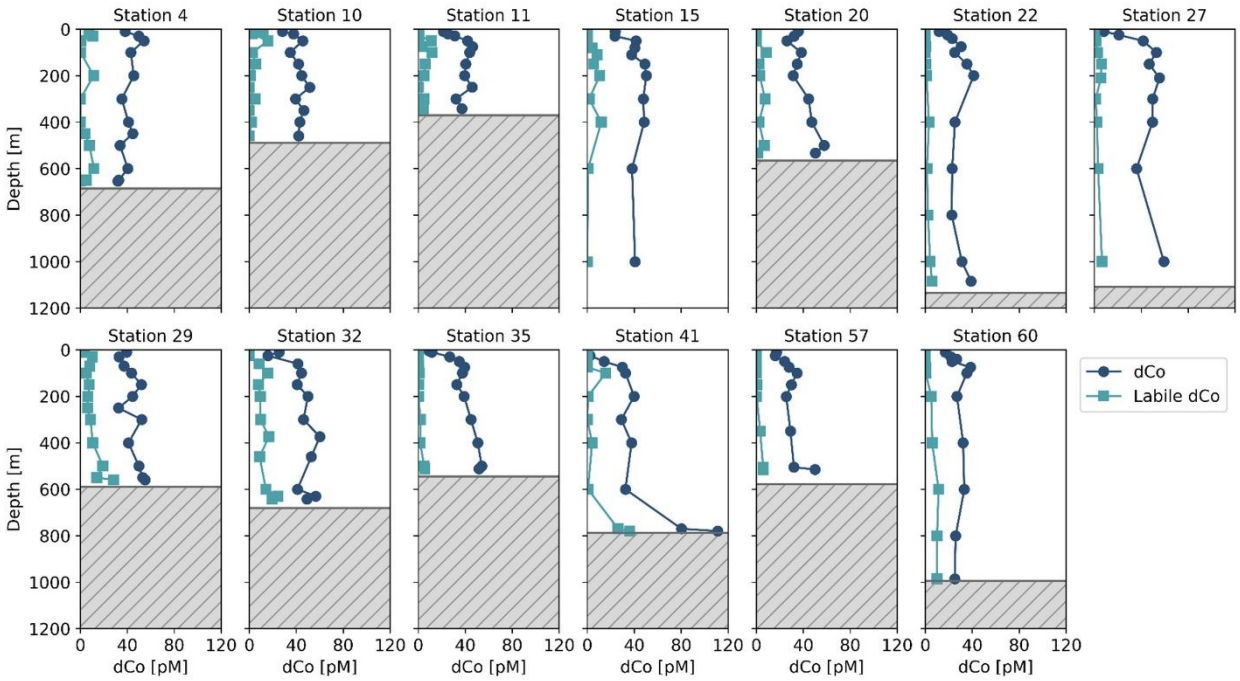

Figure 2. Dissolved Co and labile dCo full-depth profiles from the CICLOPS expedition to the Amundsen Sea (Stations 4, 10, 11, 15), Ross Sea (Stations 20, 29, 32, 35) and Terra Nova Bay (Stations 22, 27, 41, 57, 60). The top of the grey box marks the location of the seafloor.

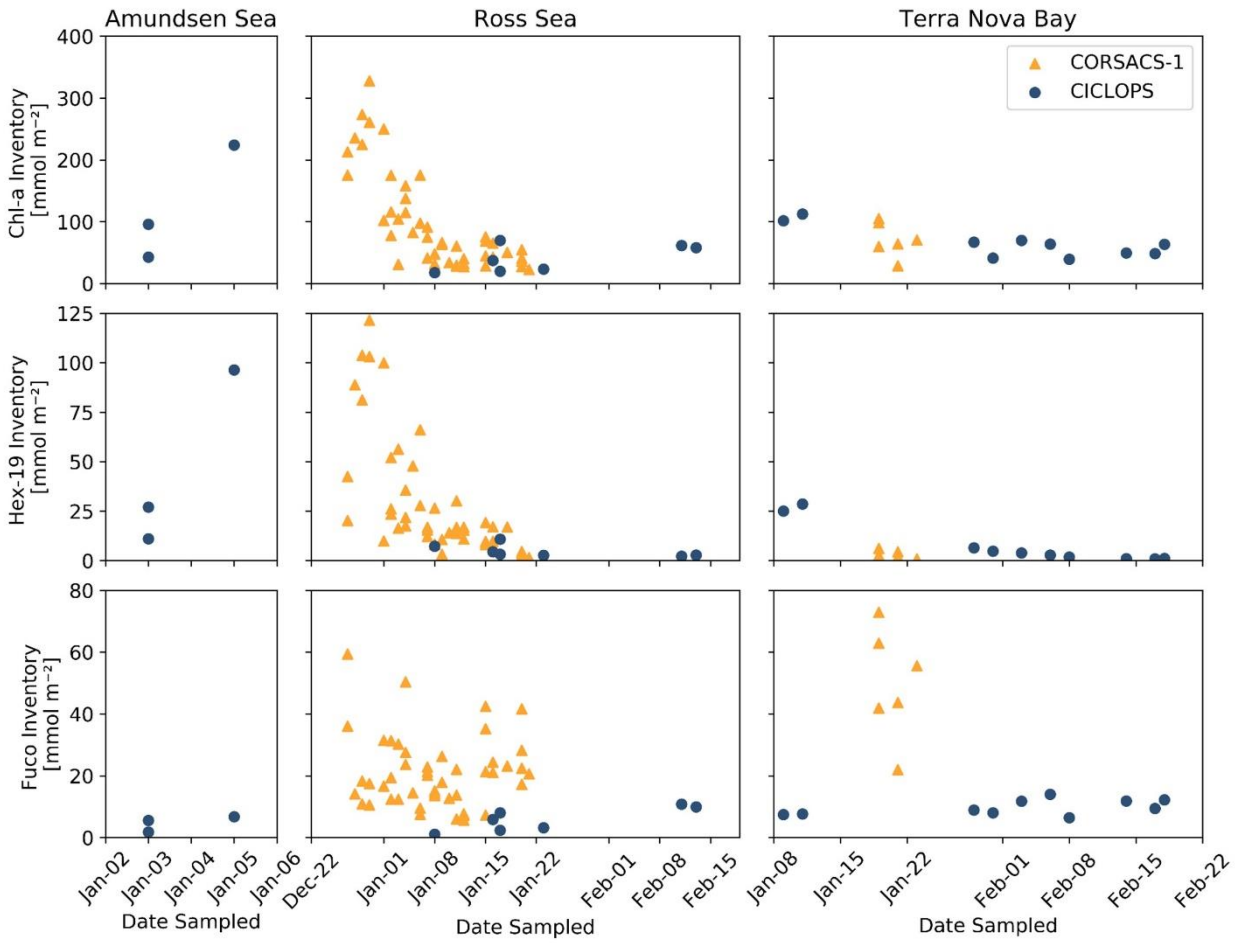

Figure 3. Upper ocean inventories of Chlorophyll-a (Chl-a), 19-hexanolyoxyfucoxanthin (19-Hex) and fucoxanthin (Fuco) plotted over the austral summer season for both the 2005/2006 CORSACS-1 and 2017/2018 CICLOPS expeditions. Inventories were estimated via trapezoidal integration of the pigment depth profiles between 5 and 50 m depth. Note that the dates along the x-axis are not continuous between plots of each region.

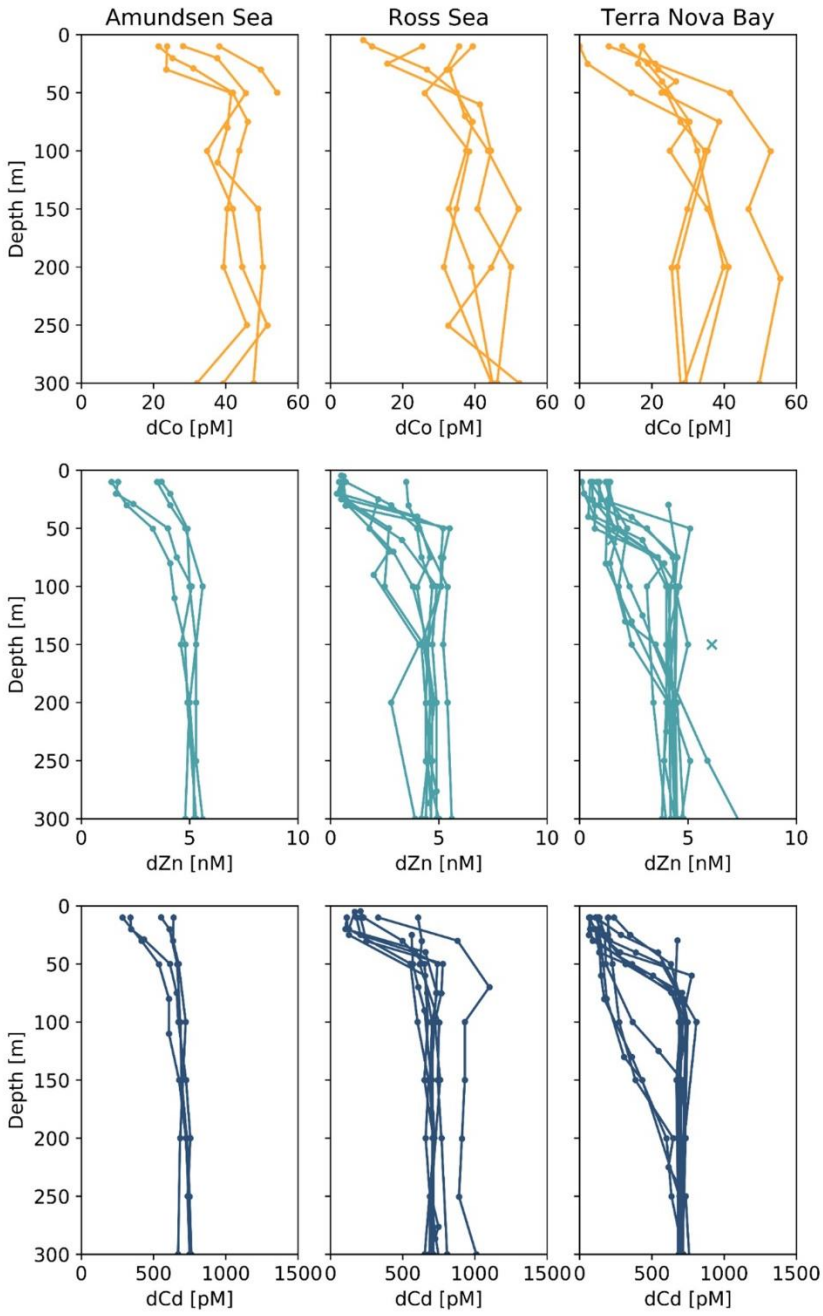

Figure 4. Upper ocean trace metal depth profiles of dCo, dZn and dCd, by region (left panels, Amundsen Sea; middle panels, Ross Sea; right panels, Terra Nova Bay). Outliers are marked with an 'x'. Dissolved Zn and Cd profile data are further described in Kellogg (2022).

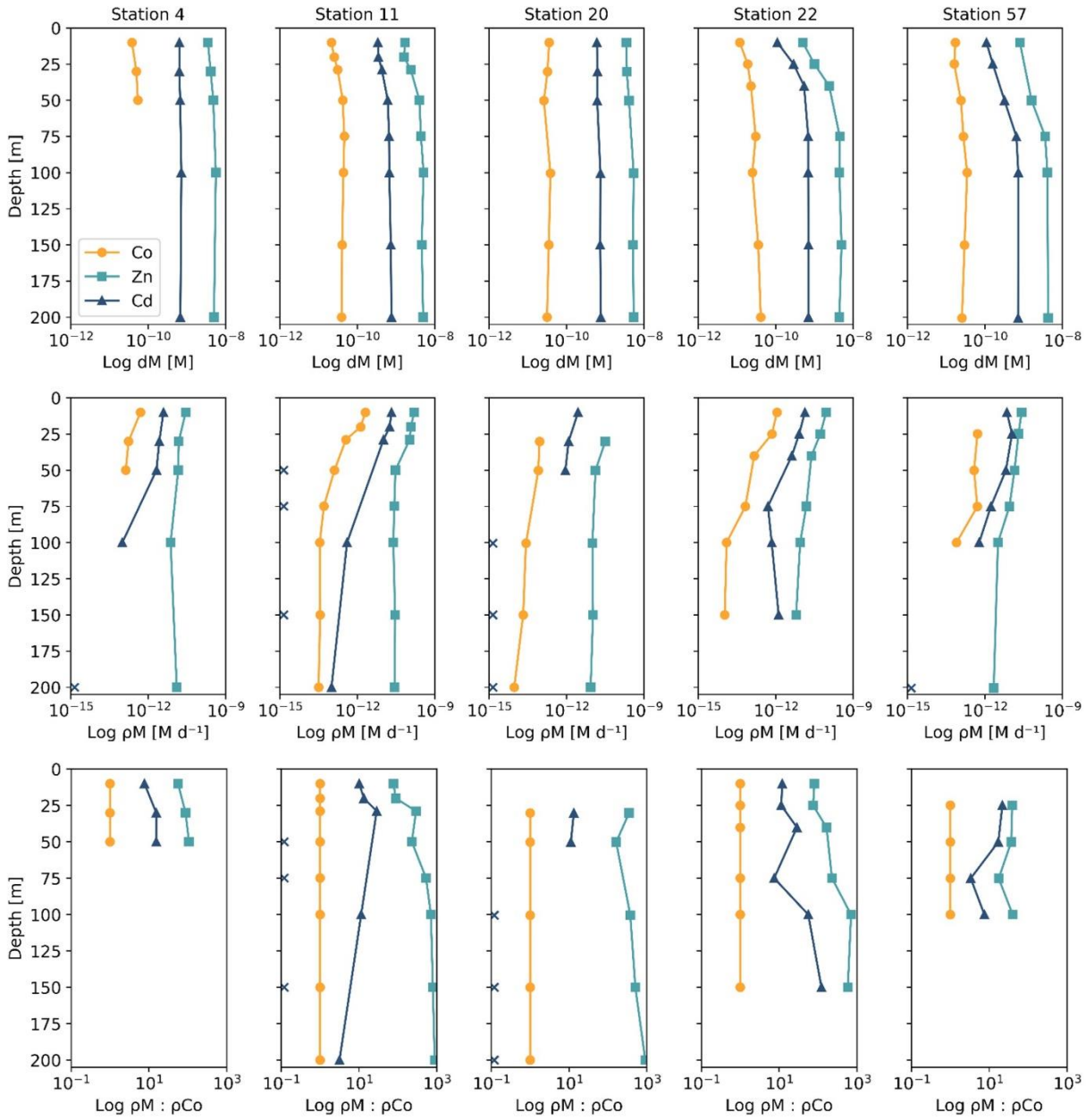

Figure 5. Depth profiles of dissolved metals (dM; top), trace metal uptake rates (ρM; middle), and trace metal uptake rates normalized to the uptake rate of dCo (ρM : ρCo), plotted along a log scale. Stations 4 and 11 are from the Amundsen Sea, Station 20 is from the Ross Sea, and Stations 22 and 57 are from Terra Nova Bay. Depths at which an uptake rate below detection (specifically for *ρ*Cd) are marked with an 'x' along the y-axis. Co trace metal uptake data are further described in Rao (2020) and Zn and Cd uptake data are further described in Kellogg (2022).

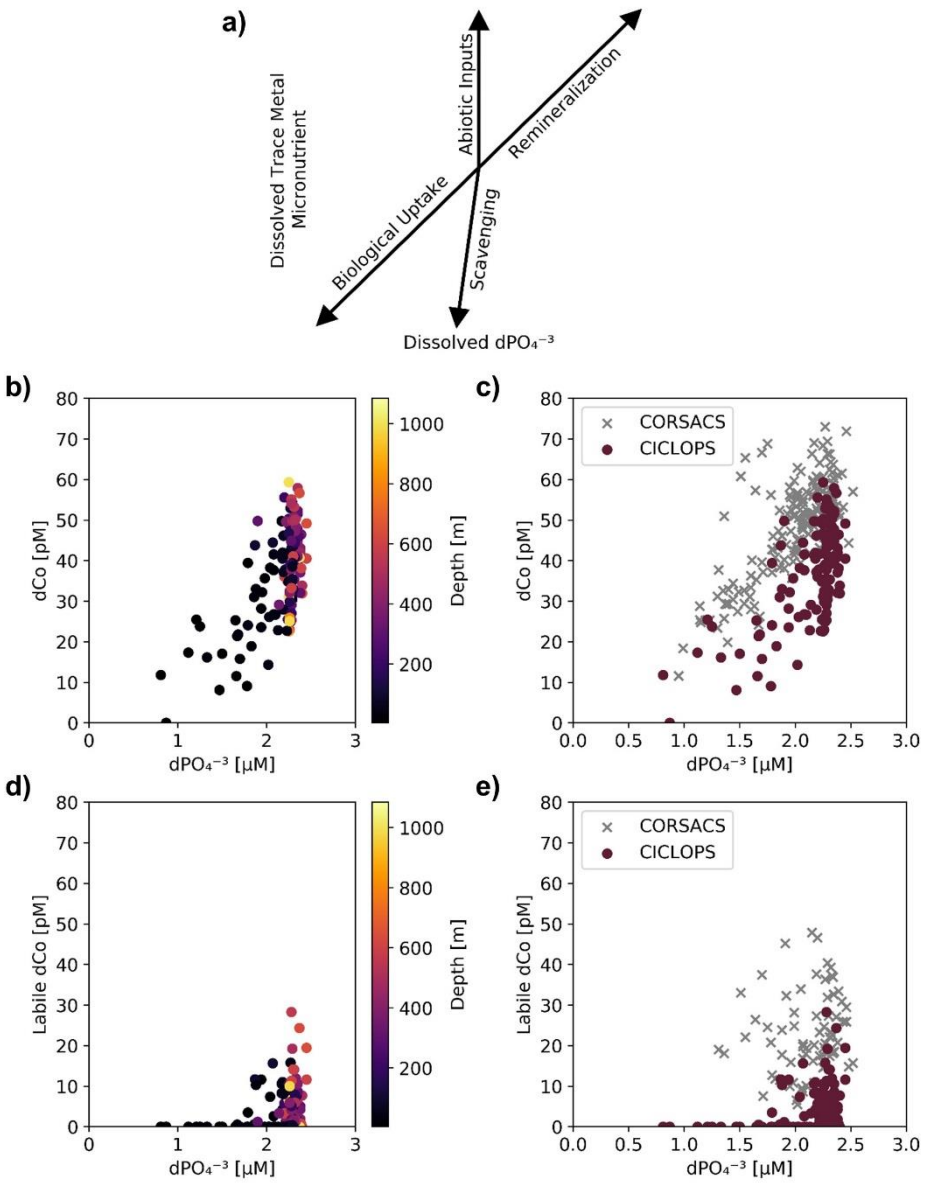

Figure 6. (a) A vector schematic of the relationship between dPO_4^{3-} and dissolved trace metals like dCo, and how the various marine processes can affect their distribution and environmental stoichiometry. Adapted from Noble et al. (2008). The CICLOPS (b) dCo vs. dPO_4^{3-} relationship and (d) labile dCo vs. dPO_4^{3-} relationship, plotted by depth. Also shown are the CICLOPS (red) (c) dCo vs. dPO_4^{3-} and (e) labile dCo vs. dPO_4^{3-} samples overlaid with CORSACS (gray) samples.

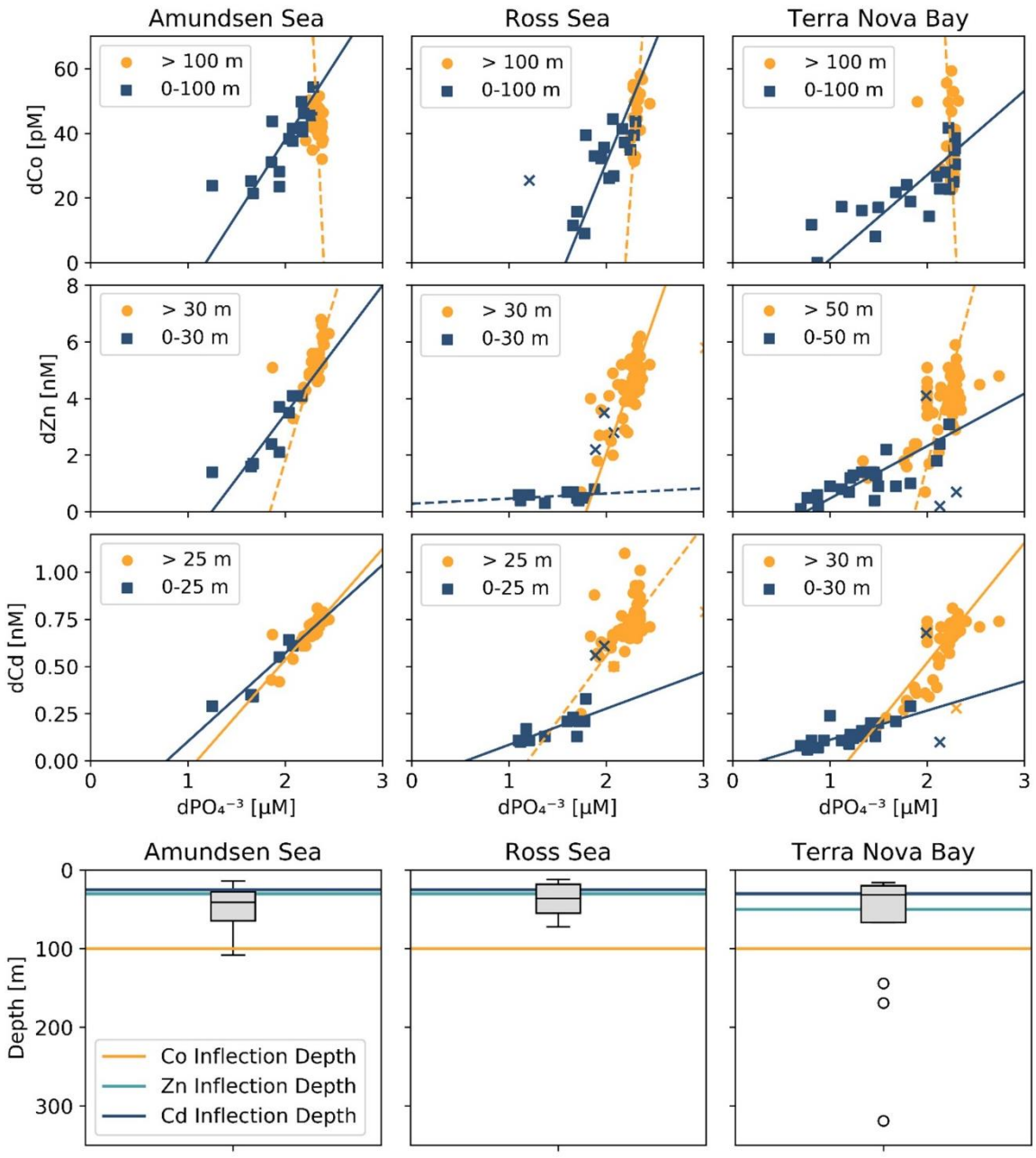

Figure 7. (Top 3 rows) Trace metal : dPO_4^{3-} relationships from the three CICLOPS regions sampled, divided into upper ocean (blue square) and deep ocean (orange circle) bins with a manual depth threshold (or inflection point depth) selected to optimize the linear fit of the upper and deep ocean trends. Regressions with an $R^2 \geq 0.50$ are shown as a solid line, and those with an $R^2 < 0.50$ are shown as a dotted line. The results of the linear regressions are given in Table 3. Regression outliers are marked with an 'x'. (Bottom row) The inflection point depths assigned to dCo, dZn and dCd relationships are shown compared to a box and whiskers plot of the mixed layer depths, with mixed layer depth outliers marked with an 'o'.

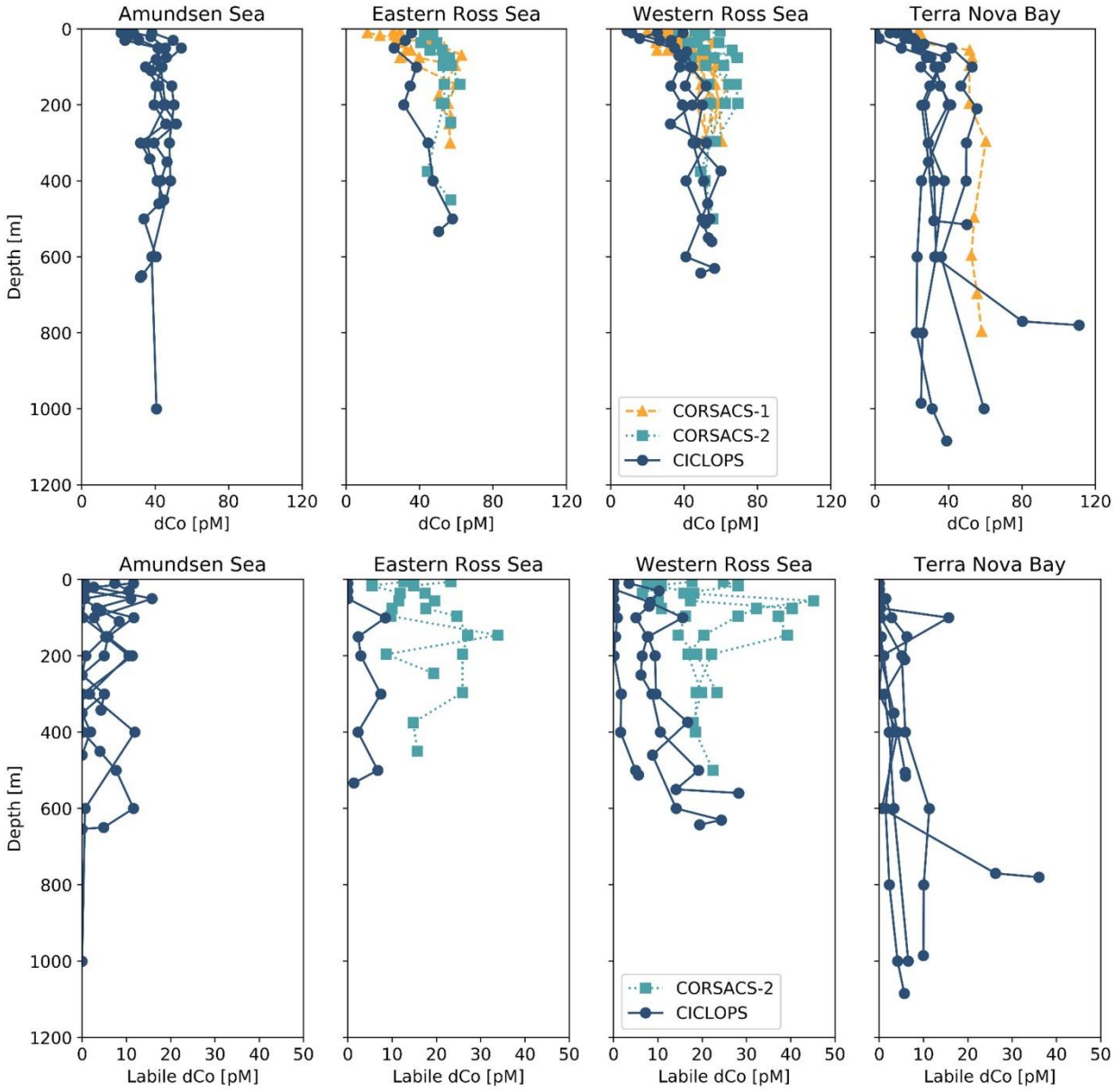

Figure 8. Dissolved Co and labile dCo depth profiles from the CORSACS-1 (NBP0601; December 27, 2005 – January 23, 2006), CORSACS-2 (NBP0608; November 8, 2006 – December 3, 2006) and CICLOPS (NBP-1801; December 11, 2017 – March 3, 2018) expeditions in the 4 regions sampled by the CICLOPS expedition: Terra Nova Bay, the Western Ross Sea, the Eastern Ross Sea and the Amundsen Sea. The Eastern and Western Ross Sea stations are defined by being either east or west of the 175 ºE longitudinal, respectively. The CORSACS expeditions did not extend to the Amundsen Sea, and no labile dCo was reported from the CORSACS-1 expedition. dCo data from the CORSACS expeditions was reported in (Saito et al. 2010) and is accessible at https://www.bco-dmo.org/dataset/3367.

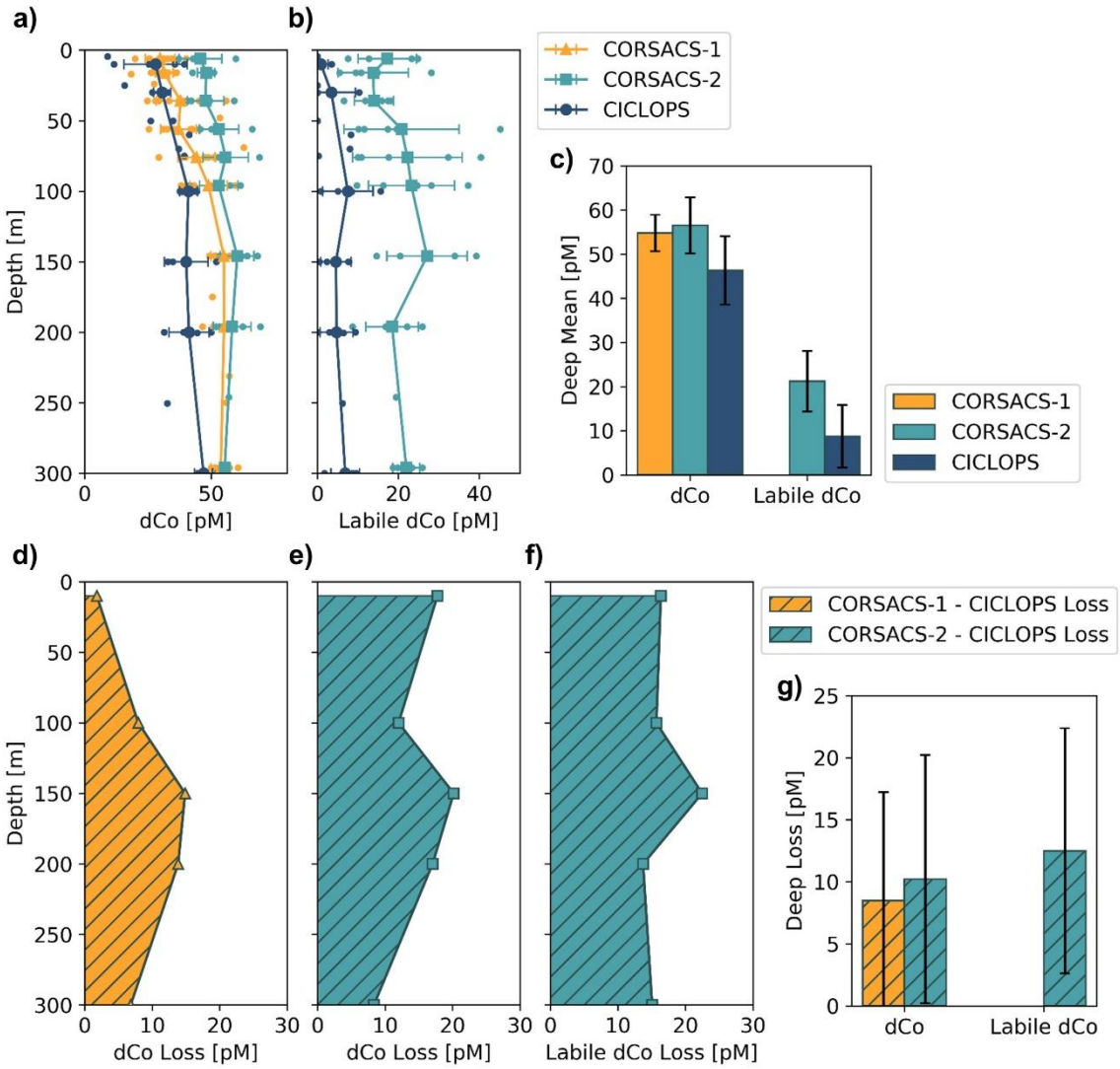

Figure 9. Mean depth profiles of dCo (a) and labile dCo (b) from the Ross Sea from three sampling seasons, including the expeditions: CORSACS-1 (Summer 2005/2006), CORSACS-2 (Spring 2006) and CICLOPS (Summer 2017/2018). Observed profiles values are plotted as unconnected dots, and the mean profile is plotted for each depth at which at least three samples were analyzed. (c) The mean deep (≥ 100 m) dCo and labile dCo concentrations for stations in the Ross Sea on each expedition. The mean difference in the dCo (d, e) and labile dCo (f) profiles between the CORSACS and CICLOPS expeditions where sample depths were within 5 m of each other. (g) The mean deep (≥ 100 m) dCo and labile dCo concentration loss for stations in the Ross Sea. Error bars denote one standard deviation from the mean. No labile dCo data is available for the CORSACS-1 expedition. Mean values, loss values, and the results of independent t-tests to determine the significance of the deep dCo loss are given in Table 4.

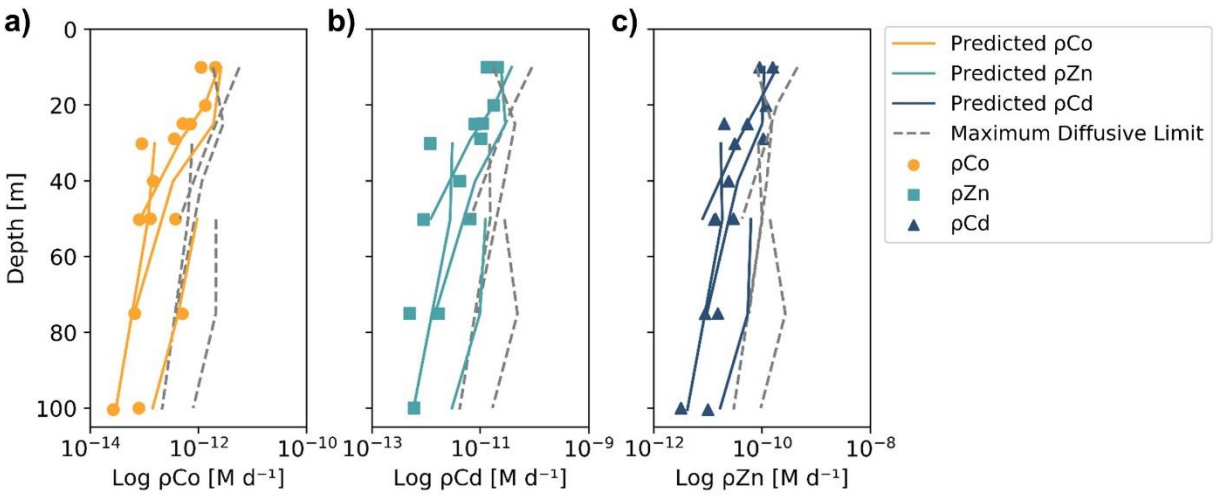

Figure 10. Observed (markers) and predicted (solid lines) trace metal uptake rate (ρ) profiles for Co (a) Cd (b) and Zn (c) from Stations 11, 20, 22 and 57. The maximum diffusive limit profiles (dashed lines) are shown as an estimate of the physical limits of metal diffusion through uptake transporters. The predicted uptake rates were tuned to best fit the observed uptake rate trends by using a V_{max} value of 4 µmol (mol C^{-1}) d^{-1}, and the maximum diffusion limit estimation assumed a speciation of 0.01% labile metals.

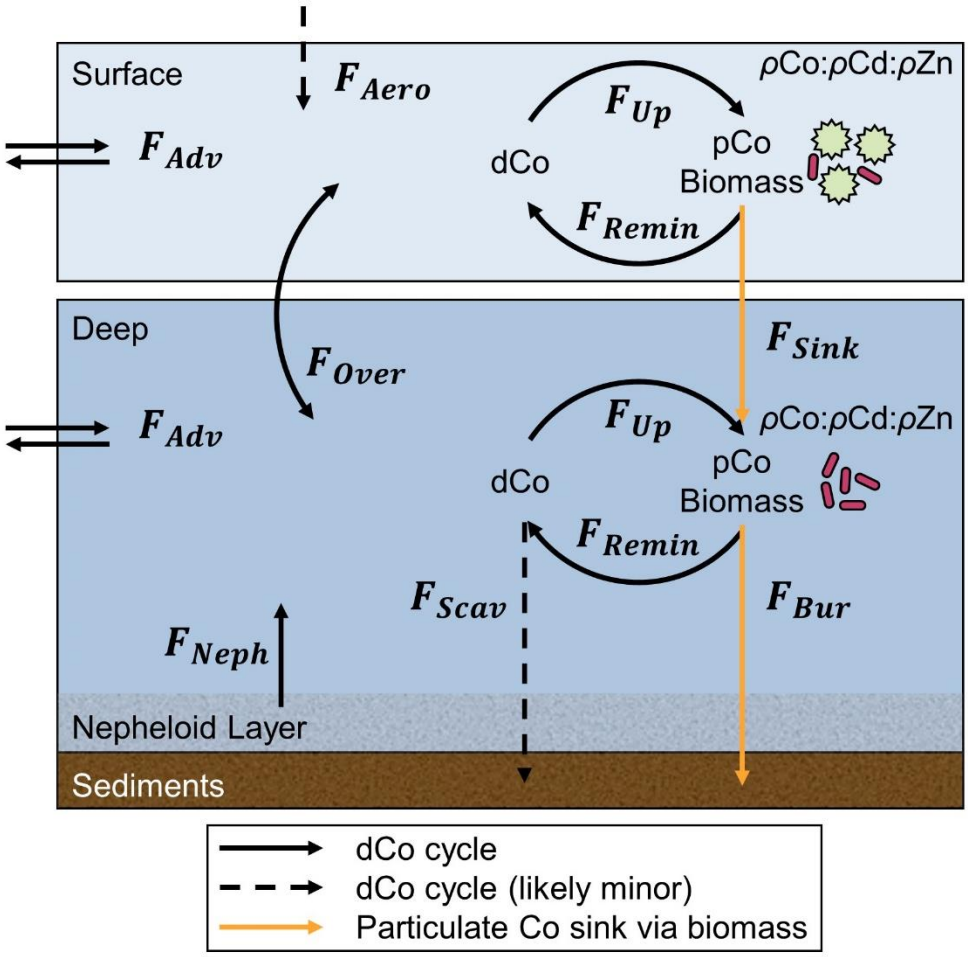

Figure 11. A schematic of the dCo cycle (black) and select processes of the particulate Co (pCo) cycle (orange) presented as a simplified two-box model. Net fluxes of the dCo cycle include sources from aerosol deposition (F_{Aero}), bottom sediments and the nepheloid layer (F_{Neph}), and scavenging to Mn-oxides particles (F_{Scav}) which likely represents a minor flux in the coastal Antarctic seas. Internal cycling fluxes include horizontal advection (F_{Adv}), water column overturning or mixing (F_{Over}), biological uptake (F_{Up}) and remineralization of pCo (F_{Remin}). Fluxes of pCo shown here include sinking biomass from the surface into the deep ocean (F_{Sink}) and pCo burial into sediments along the seafloor (F_{Bur}). The biological uptake of dCo is influenced by the relative stoichiometric uptake of Co, Zn and Cd (ρCo : ρCd : ρZn) among the microbial community. Differential equations that describe and quantify these fluxes are presented in Appendix I.

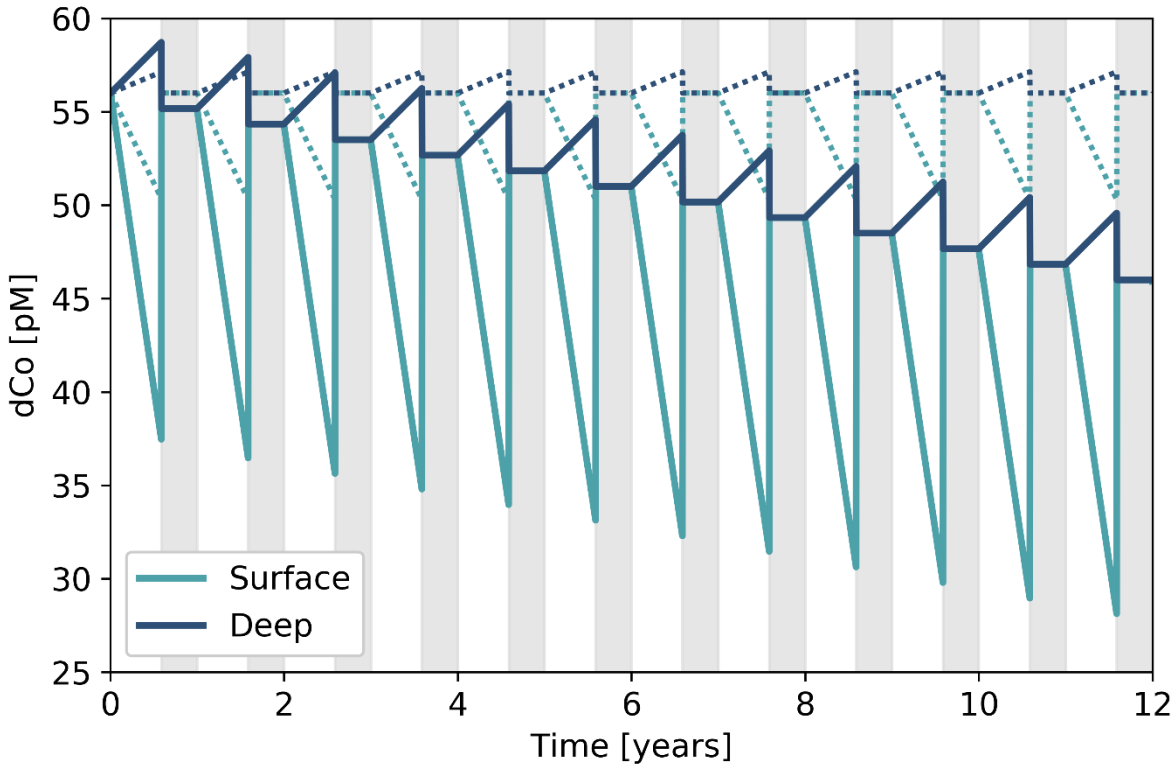

Figure 12. Results of the two-box model illustrating a potential mechanism for the loss of the dCo inventory over time. Gray boxes represent the winter season when the surface and deep boxes mix. The dotted lines represent a system at steady state, where the dCo inventory stays consistent annually. The solid lines represent a system exhibiting dCo loss, where increased Co uptake rates in both the surface and deep ocean result in an annually decreasing dCo inventory. The initial deep dCo concentration was 56 pM, which approximates the mean deep dCo concentrations observed on CORSACS-1 and CORSACS-2. Over 12 years, the dCo loss model depicts the loss of 0.83 pM $year^{-1}$ to end at a deep dCo inventory of 46 pM, the mean deep dCo concentration observed on CICLOPS.

Chapter 5.

Scaling anthropogenic cobalt perturbation: the vulnerability of marine and biological systems following the rise of lithium-ion batteries

Rebecca Chmiel[a,b] & Mak Saito[b]

[a] MIT/WHOI Joint Program in Oceanography/Applied Ocean Science and Engineering, Woods Hole, MA, USA
[b] Department of Marine Chemistry and Geochemistry, Woods Hole Oceanographic Institution, Woods Hole, MA, USA

5.1 Abstract

Cobalt is simultaneously an essential micronutrient for many organisms, a heavy metal ecotoxin, and a critical commodity for modern technologies, including lithium-ion batteries used in personal electronic devices and many electric vehicles. The demand for cobalt has sharply increased over the past decade, and the rate of cobalt extraction via mining has followed suit. Here, we estimate the inventories of the natural cobalt cycle through the Earth systems of the lithosphere, biosphere and hydrosphere, as well as the inventories and fluxes of cobalt through the human system of the anthroposphere. Our findings suggest that the scale of cobalt cycling through the anthroposphere (10^9 mol Co yr^{-1}) is an order of magnitude higher than the total source of cobalt to the oceans (10^8 mol Co yr^{-1}) and around the same magnitude as is estimated to be in the inventories of the hydrosphere and biosphere (10^9–10^{10} mol Co yr^{-1}). Disposal from the anthroposphere into the natural cobalt cycle has the potential to disrupt the biosphere and the hydrosphere, which are vulnerable to perturbation due to their low natural inventories of cobalt. Such perturbations have already been observed in the Arctic and Antarctic seas, where the cascading effects of global climate change have resulted in significant changes to the dissolved cobalt inventory. Improvements to heavy metal and lithium-ion battery disposal infrastructure, innovations to reduce the cost of lithium-ion battery recycling, and policies or incentives to support battery recycling are imperative to help to mitigate cobalt pollution and its effects throughout the Earth system spheres.

5.2 Introduction

Cobalt is an important global commodity used in batteries, superalloys, magnets, catalysts, pigments, and other technologies (Cobalt Institute, 2021; Sun et al., 2019). Notably, cobalt is used as the metallic cathode of many lithium-ion batteries for personal electronic devices like laptops and smartphones, as well as for most types of electric vehicle batteries. As of 2020, batteries were responsible for 57% of cobalt's global consumption (Cobalt Institute, 2021). The prominent use of cobalt in electric vehicle batteries positions the metal as a critical commodity for a sustainable energy revolution that prominently features electric vehicles as a solution for low-carbon transportation. Global demand for cobalt is predicted to increase by a factor of 10–20 or more by 2050, putting pressure on the global supply chain of mined cobalt (Deetman et al., 2018).

Additionally, cobalt is a bioactive metal used by organisms in a variety of metalloenzymes and natural organometallic compounds. Most notably a cobalt atom is the metallic cofactor for vitamin B_{12}, which is essential for many microbes and animals (Bertrand et al., 2013; Hodgkin et al., 1957). At higher concentrations than typically observed in the natural environment, cobalt becomes a heavy metal ecotoxin, and the recent growth of cobalt use in modern technologies has concentrated the heavy metal within landfill waste at levels high enough to potentially negatively impact ecosystem and human health (Kang et al., 2013).

Here, we describe an anthropogenic cobalt cycle using similar vocabulary as we use to describe metal biogeochemical cycles, putting its fluxes and inventories in perspective with the natural cobalt cycle. Several recent industrial ecology studies have analyzed the anthropogenic use of cobalt (Godoy León et al., 2020; Harper et al., 2012; Sun et al., 2019), and this paper aims to complement such studies by placing the metal's anthropogenic flux into the context of natural elemental cycles and inventories to highlight the serious risk that this historically unprecedented accumulation and disposal of large quantities of cobalt poses to Earth systems.

5.3 Estimating global cobalt inventories of natural Earth systems

The global inventories of cobalt within the lithosphere, hydrosphere and biosphere were estimated via simple calculations using values from previously published studies (Fig. 1; Table 1). The estimates are intended to be simple calculations to approximate the relative orders of magnitude of the cobalt cycling within global pools (Fig. 2). When multiple estimates are made for the same inventory using different methods or literature values, the estimates are presented as

a range. See the Appendix J for a more detailed breakdown of the values these estimates are derived from.

5.3.1 Cobalt in the lithosphere

The lithospheric inventory of crustal cobalt was estimated as a sum of the continental and oceanic crust inventories, where each crusts' total volume (Schubert and Sandwell, 1989), average density (Carlson and Raskin, 1984; Christensen and Mooney, 1995) and approximate cobalt concentration (Reimann and de Caritat, 1998) were used to calculate a reasonable value of the cobalt inventory within the Earth's crust. The continental crust contained the majority of lithospheric cobalt (9×10^{18} mol) compared to the oceanic crust (8×10^{17} mol), driven by the greater mass of the continental crust despite the higher concentration of cobalt in the oceanic crust compared to the continental crust (45 mg Co kg^{-1} and 22 mg Co kg^{-1}, respectively) (Reimann and de Caritat, 1998). In total, the lithosphere contains ~1×10^{19} mol cobalt, the largest cobalt inventory on Earth and nine orders of magnitude above the next largest cobalt reservoir, the hydrosphere.

Of that inventory, 2×10^{12} mol of cobalt are estimated to be *global resources* – material that can be potentially extracted from the Earth. Since 83% of cobalt's global resource is located on the seafloor, which is not currently accessible by commercial mining operations due to the current cost and technological limitations of seafloor mining (Sharma, 2011; USGS, 2021), only 1×10^{11} mol cobalt is estimated to be part of the *global reserve* – material that is currently economically feasible to extract (USGS, 2021), although innovative mining projects like seafloor mining are aimed at extracting additional Co resources in the deep ocean over the next decade (see Sect. 5.4.1).

5.3.2 Cobalt in the hydrosphere

Cobalt in the hydrosphere can be found in the dissolved phase in marine and inland waters. Particulate cobalt is also present in the hydrosphere as biomass (plankton) and particulate mineral phases and is assumed to be part of the biosphere and lithosphere, respectively. In the oceans, particulate cobalt is present at concentrations ≤ 1% of dissolved cobalt concentrations (Chmiel et al., 2022; Hawco et al., 2016; Noble et al., 2017). The marine cobalt inventory was estimated in two ways: (1) by assuming steady state, the net source flux of cobalt into the oceans multiplied by

the residence time of marine cobalt (Hawco et al., 2018) provides an approximation of the marine inventory of 8×10^{10} mol cobalt; (2) (Reimann and de Caritat, 1998) estimated a marine cobalt inventory of 4×10^{9} kg cobalt, or 7×10^{10} mol cobalt. Both estimates of the marine cobalt inventory are in excellent agreement. The inventory of cobalt in terrestrial groundwater was estimated via the global volume of fresh groundwater (Oelkers et al., 2011) multiplied by an approximate value of cobalt concentration in groundwater (Reimann and de Caritat, 1998), for a value of 1×10^{10} mol. The inventory of above-ground freshwater was determined by summing the inventories of global ice, lakes, and rivers and streams, which were in turn estimated by multiplying the volume of each freshwater reservoir (Oelkers et al., 2011) by their approximate cobalt concentration (Barbante et al., 1997; Reimann and de Caritat, 1998), and for the ice inventory – including ice caps and glaciers – by the approximate density of ice (Huss, 2013). This method estimates an ice inventory of 2×10^{9} mol, a lake inventory of 8×10^{7} mol, and a rivers and streams inventory of 7×10^{6} mol, for an estimated above-ground freshwater inventory of 2×10^{9} mol cobalt.

These hydrosphere estimates reveal that the oceans, which account for the vast majority of the hydrosphere (97% by volume), also contain the largest cobalt inventory ($7–8 \times 10^{10}$ mol). Notably, although the volumes of global freshwater reservoirs are orders of magnitude smaller than that of the ocean, the cobalt inventory of both groundwater (1×10^{10} mol) and above-ground freshwater (2×10^{9} mol) are significant on a global scale due to their higher concentrations of cobalt relative to the metal-scarce oceans. Together, groundwater and above-ground freshwater account for only 3% of the hydrosphere by volume, but ~14% of the hydrosphere's cobalt inventory.

5.3.3 Cobalt in the biosphere

The cobalt inventory of the biosphere was estimated as a sum of the prokaryotic inventory (archaea and bacteria) and the eukaryotic inventory (plants, including eukaryotic algae, protists, fungi and animals). The prokaryotic inventory was determined by multiplying global prokaryotic biomass (Bar-On et al., 2018) by the cobalt : carbon ratio of both *Prochlorococcus* (1.2×10^{-7} mol Co : mol C) and *Synechococcus* (8×10^{-8} mol Co : mol C) (Sunda and Huntsman, 1995), marine phytoplankton that are among the most abundant prokaryotes on Earth, for an inventory of $5\text{-}8 \times 10^{8}$ mol. When the same calculation used the cobalt : carbon ratio determined from *Pseudoalteromonas*, a common marine heterotroph that exhibited a high cobalt stoichiometry in

culture experiments (1.2×10^{-3} mol Co : mol C) (Mazzotta et al., 2020), the prokaryotic cobalt inventory estimate was four orders of magnitude higher (7×10^{12} mol Co). This value is likely unrealistic as a global estimate, but exemplifies the highly plastic nature of cobalt stoichiometry among microorganisms (see Chapter 3), and the tendency of cells to absorb high amounts of cobalt when environmentally exposed to higher concentrations of the metal.

Similarly, the eukaryotic inventory was determined by multiplying the eukaryotic biomass (Bar-On et al., 2018), of which 96% by weight is composed of plants, by the minimum and maximum cobalt concentrations observed in land plants (Nagajyoti et al., 2010) and trees (Kirchner et al., 2008), along with a general carbon : dry plant weight conversion of 0.4 (Ho, 1976). The resulting eukaryotic cobalt inventory estimate of $1\text{-}16 \times 10^9$ mol displays a wide range of error due to the high variability of plant cobalt composition. This difference is likely regional due to soil conditions because plants do not require any form of cobalt including vitamin B_{12}, and are cycling cobalt through the biosphere without actively using the metal for their metabolic processes.

The total cobalt inventory of the biosphere was estimated to be $2\text{-}17 \times 10^9$ mol cobalt. The wide range and likely high error of this estimate is due to the wide range of cobalt measurements in biota and tendency of cobalt to be passively cycled in organisms. Additional measurements of heavy metals in a variety of organisms would help to improve this estimate.

5.4 Cobalt in the anthroposphere

The anthroposphere describes the portion of Earth's environment that is influenced by humans and human-made systems. It includes resources, energy and information as they are obtained from other environmental spheres, refined and utilized by humans, and eventually disposed of as waste (Baccini and Brunner, 2019). The fields of industrial ecology and biogeochemistry have characterized the Earth system spheres in similar ways – as complex, cyclical systems with fluxes, inventories (or "stocks"), internal cycling and time-dependent processes. Material Flow Analysis (MFA) describes and quantifies resource flow through the anthroposphere, resulting in an output similar to an elemental biogeochemical cycle. Studies that use MFA to examine anthropogenic cobalt are able to quantify the flux of cobalt mining, refining, product use, recycling, and disposal on a global scale (Table 2) (Harper et al., 2012; Sun et al., 2019).

5.4.1 Cobalt mining and use

From 2005 to 2020, the rate of cobalt mined globally (i.e. the flux into the human economy) has more than doubled from 1.1×10^9 to 2.5×10^9 mol cobalt per year (Cobalt Institute, 2021; Harper et al., 2012; Sun et al., 2019). The estimated inventory of cobalt in-use in 2005 was 3.7×10^9 mol cobalt (Harper et al., 2012), which is ~3% of global cobalt reserves. This number is likely much higher today, as the amount of cobalt present in electric vehicle batteries has been increasing by ~5% every year since at least 2013 (Cobalt Institute, 2021).

As of 2020, 70% of cobalt mined globally was sourced from the Democratic Republic of the Congo (DRC) (Cobalt Institute, 2021). The DRC also contains 48% of global cobalt reserves, meaning that there is a strong potential for future cobalt mining growth in this region compared to other nations, particularly if the demand for cobalt continues to increase worldwide (Al Barazi et al., 2017). Many electric vehicle battery manufacturers like Tesla are trying to distance themselves from cobalt sourced from the DRC batteries because of exploitative working practices, child labor, and unsafe working conditions (Calma, 2020).

The increasingly high demand for cobalt has amplified interest in deep-sea mining, which seeks to collect cobalt, manganese and rare earth elements (REEs) from metal-rich manganese nodules, thin seabed crusts, and seafloor massive sulfides (Hein et al., 2013). As yet, mining in these locations is technologically challenging, expensive, and fraught with geopolitical concerns as most of the deposits exist in international waters (Hallgren and Hansson, 2021; Sharma, 2011). Mining the seafloor also has potential environmental consequences for the deep-sea ecosystem, much of which has only recently been discovered or still remains unexplored (Husain, 2018). Seafloor mining is expected to greatly disturb hydrothermal and deep-sea ecosystems (Orcutt et al., 2020) and generate large plumes of sediment enriched in toxic heavy metals in the surrounding ocean (Drazen et al., 2020; Fuchida et al., 2017). Weighing the potential development and proliferation of renewable technologies like efficient electric vehicle batteries against the potential degradation of this unique ecosystem highlights the importance of caution and the need for sustainable mining practices in this emerging resource sector.

5.4.2 Cobalt disposal and recycling

The anthropogenic cobalt cycle is currently not in steady state, with more material mined from the lithosphere than is recycled or removed from the anthroposphere. Disposal is historically

lower than the refined flux, which reflects both the growth of cobalt that is currently in-use as well as the systemic "hoarding" of non-active products that are no longer in use but have not yet been disposed (Godoy León et al., 2020).

The recycling of cobalt is about an order of magnitude lower than the mining and refining fluxes, accounting for ~13% of disposed cobalt in 2015. The Cobalt Institute estimates that 1.8×10^8 mol of cobalt were recycled in 2020, 65% of which came from batteries (Cobalt Institute, 2021). This amount is quite low despite the high value of cobalt because of the difficulty of recycling lithium-ion batteries; isolating the various components of a lithium-ion battery is challenging and energy-intensive, resulting in a cobalt recycling process that is currently more expensive than mining new resources (Skeete et al., 2020). Much of the cobalt recycled from batteries cannot currently be re-incorporated into new batteries, and instead must be "downcycled", or incorporated into other products that do not require cobalt to function (Godoy León et al., 2020). To develop a sustainable electric vehicle fleet, additional technological development of the cobalt recycling process is necessary to ensure the recovered cobalt can be reused in new batteries.

Notably, the flux of cobalt out of the anthroposphere via disposal to landfills or recycling is currently on the order of 10^9 mol per year, which is an order of magnitude higher than the total source of cobalt to the oceans (5.9×10^8 mol Co yr^{-1}) (Hawco et al., 2018), about the same order of magnitude or one higher than the total flux of cobalt entering the biosphere from primary production ($4–24 \times 10^8$ mol Co yr^{-1}), and only one order of magnitude smaller than the entire subduction and crustal growth fluxes of cobalt through the lithosphere (9×10^{10} and $4–5 \times 10^{10}$ mol Co yr^{-1}, respectively; see Appendix J for flux calculations). While the lithospheric inventory is large, the inventories of the hydrosphere and biosphere are both small, on the order of 10^9 and 10^{10} mol, and further increases in the disposal flux of cobalt from the anthroposphere could substantially perturbate these systems.

5.5 Implications for Earth systems

Anthropogenic cobalt waste deposited into the natural Earth system spheres poses a threat to environments with naturally low cobalt inventories. Although much of the disposed cobalt will eventually become re-incorporated back into the lithosphere, a portion of cobalt waste should be expected to enter the hydrosphere and biosphere via pollution from mining, disposal, combustion,

and various other pathways. The low inventories of cobalt in the biosphere and hydrosphere leave them particularly vulnerable to such heavy metal pollution, particularly on a local and regional scale.

Cobalt waste from improper disposal of batteries into a landfill would be expected to enter terrestrial environment first, leeching into the soil before contaminating the biosphere and hydrosphere. A study on leaching from lithium-ion battery casings under landfill conditions concluded that the batteries may contribute hazardous levels of cobalt and other heavy metal pollutants to the surrounding environment, potentially impacting both human and ecosystem health (Kang et al., 2013). Leeching in the soil and terrestrial environment would then provide a pathway for cobalt contamination to enter the local watershed, groundwater and biosphere, which are particularly vulnerable to perturbation. Additionally, the predicted increases in cobalt mining would be expected to increase the flux of cobalt and heavy metals into the surrounding environments, polluting ecosystems and negatively impacting human health (Van Geen et al., 1997). In the DRC, the soils and rivers surrounding cobalt mining locations are polluted with cobalt and other heavy metals (Sovacool, 2019), and cobalt and uranium levels were found to be elevated in the blood and urine of mineworkers and local children due to mining dust inhalation (Banza Lubaba Nkulu et al., 2018).

Cobalt is a necessary micronutrient for many organisms, but it is also a heavy metal that can become toxic to organisms at higher concentrations. Many transporters of heavy metals across a cell membrane are general divalent cation transporters, and their metal uptake is determined by environmental metal concentrations and the binding affinities of each metal to the transporter (Irving and Williams, 1948; Roane et al., 2015). Thus, high concentrations of heavy metals, particularly at different ratios than the organism has adapted to live at, can "clog" the transporter via competitive inhibition and effectively starve the organism of necessary nutrients. In addition, because cobalt is also a micronutrient, anthropogenic cobalt inputs to the environment could cause ecological shifts in populations – such as phytoplankton bloom composition – that can affect regional ecosystems and their biogeochemical cycles (Bertrand et al., 2007; Browning et al., 2017; Granéli and Haraldsson, 1993). Even small changes in the availability of cobalt to the biosphere could affect community composition because ecosystems are carefully tuned to ratios of dissolved metals, whether they are functioning as a toxin or a micronutrient, and organisms in the biosphere have evolved over deep time to best adapt to their metallic environments (Saito et al., 2003). The

biosphere and hydrosphere both have relatively low concentrations of cobalt within their relatively large earth system spheres, leaving these reservoirs vulnerable to potentially toxic levels of cobalt perturbation on a local or regional scale.

5.5.1 Implications for the marine environment

Although the marine cobalt inventory accounts for the majority of cobalt in the hydrosphere, cobalt tends to be one of the scarcest elemental nutrients in the ocean, especially in the surface open ocean where cobalt can be found in the 1 to 10 parts per trillion (picomolar) concentration range (Hawco et al., 2018; Saito et al., 2017). Globally, the surface ocean contains an inventory of ~3×10^9 mol cobalt with major fluxes into and out of the system on the order of 10^8 mol Co yr^{-1} (Fig. 3). If only a fraction of the disposed cobalt waste, whose flux is on the order of 10^9 mol Co yr^{-1}, were to find its way into the surface ocean, it would represent a significant perturbation to the existing inventory of cobalt, likely increasing bio-uptake of cobalt by phytoplankton, potentially to toxic levels, altering the metal ratios of marine ecosystems and plankton community composition, and increasing the flux of cobalt to the deep ocean, although on timescales far too slow to be useful for enhancement of mining activities (Dunlea et al., 2015).

Over the past century, the marine cobalt inventory has been shown to be vulnerable to anthropogenic change from causes unrelated to metal waste disposal. The Arctic Ocean has displayed an alarming increase in cobalt concentrations over the past decades that has been linked to thawing permafrost (Bundy et al., 2020). Warming ocean temperatures are creating larger and more intense regions of low oxygen in the ocean, which is predicted to increase cobalt inventories in both the Atlantic and Pacific Oceans (Chmiel et al., 2022; Noble et al., 2012, 2017). Anthropogenic sources of metal aerosols from fossil fuel combustion are being deposited into the surface ocean and increasing the marine cobalt inventory (Noble et al., 2017). Finally, in the Southern Ocean, the inventory of cobalt appears to be decreasing due to increased biological use of cobalt as vitamin B_{12} (Chmiel et al., 2022).

5.6 Where do we go from here?

Terrestrial, freshwater and marine environments may all face increasing exposure and environmental impact due to the extraordinary increase of cobalt within the human economy, arising from terrestrial mining, future deep-sea mining and unsuitable waste disposal. The fate and

transport of disposed materials and their biological, ecological and biogeochemical impacts are not yet understood and further study is needed. The surface ocean is particularly vulnerable to global change because of its low cobalt inventory and thus high perturbation potential of anthropogenic inputs, and is already experiencing inventory disturbances from global climate change. As more cobalt-containing batteries are created, used, and disposed of, particularly when the first few fleets of electric vehicle batteries reach the end of their lifespan, the amount of cobalt disposed in landfills is expected to increase.

Due to the high material cost of cobalt and human rights concerns of DRC cobalt mining, many electric vehicle manufacturers have been moving towards cobalt-free lithium-ion batteries. Major electric vehicle manufacturers like Tesla and Ford are moving to decrease or eliminate cobalt from their vehicle battery cathodes, and recent innovations in lithium iron phosphate (LIP) batteries – which contain no cobalt – have made this possible (Ford Motor Company, 2022; Holman, 2022; Morris, 2020). LIP batteries have many advantages compared to cobalt-containing lithium-ion batteries, including lower costs and improved safety, but are not currently as energy dense as cobalt-containing electric vehicle batteries, although future innovation may improve their energy output (Yang et al., 2021). An industry-wide shift away from cobalt cathodes in electric vehicle batteries may indicate that we are at or near a point of "peak cobalt" use, and cobalt production and use may become steady or decline rather than continue to rise as predicted by Deetman et al. (2018). If true, this would signify that over the next decade or two, global disposal of cobalt-containing batteries will be at an all-time high as the first initial fleets of electric vehicles are retired, reinforcing the urgent need for updated and widespread battery disposal and recycling infrastructure.

Recycling cobalt in lithium-ion batteries is an ideal solution to address its increasing disposal rates and to stave off various environmental impacts. The United States, the United Nations, and the European Union have all expressed formal interest in incentivizing or requiring lithium-ion battery recycling, but none have introduced any official policies thus far other than designating proper disposal methods of the batteries as hazardous waste (Steen et al., 2017; UNCTAD, 2020; United States Department of Energy, 2019). China is the only nation currently undergoing large-scale lithium-ion battery recycling, and as of 2018, China requires battery manufacturers to collect and recycle used lithium-ion batteries (Stanway, 2018).

As our society continues to consume cobalt as a critical global commodity, we must prioritize the management of heavy metals while working towards innovative solutions to recovering and recycling the resources already present within the anthroposphere. Geoscientists should continue to monitor cobalt and other heavy metal inventories and work towards establishing baseline cobalt concentrations in the environment so they can trace and identify new perturbations in metal biogeochemical cycles. Communities and policymakers should work towards efficient and incentivized battery recycling, adopting policies to better manage the cobalt inventory, and mitigating the risk of heavy metal pollution to the hydrosphere and biosphere.

References

Baccini, P. and Brunner, P. H.: Metabolism of the Anthroposphere: Analysis, Evaluation, Design, 2nd ed., MIT Press, Cambridge, MA., 2019.

Banza Lubaba Nkulu, C., Casas, L., Haufroid, V., De Putter, T., Saenen, N. D., Kayembe-Kitenge, T., Musa Obadia, P., Kyanika Wa Mukoma, D., Lunda Ilunga, J. M., Nawrot, T. S., Luboya Numbi, O., Smolders, E. and Nemery, B.: Sustainability of artisanal mining of cobalt in DR Congo, Nat. Sustain., 1, 495–504, doi:10.1038/s41893-018-0139-4, 2018.

Bar-On, Y. M., Phillips, R. and Milo, R.: The biomass distribution on Earth, Proc. Natl. Acad. Sci., 115(25), 6506–6511, doi:10.1073/pnas.1711842115, 2018.

Al Barazi, S., Naher, U., Vetter, S., Schutte, P., Liedtke, M., Baier, M. and Franken, G.: Cobalt from the DR Congo - potential, risks, and significance for the global cobalt market (translated, original in German), Hannover. [online] Available from: https://www.bgr.bund.de/SharedDocs/GT_Produkte/Commodity_Top_News/CTN_genTab_DE.html, 2017.

Barbante, C., Bellomi, T., Mezzadri, G., Cescon, P., Scarponi, G., Morel, C., Jay, S., Van De Velde, K., Ferrari, C. and Boutron, C. F.: Direct determination of heavy metals at picogram per gram levels in Greenland and Antarctic snow by double focusing inductively coupled plasma mass spectrometry, J. Anal. At. Spectrom., 12, 925–931, doi:10.1039/a701686g, 1997.

Bertrand, E. M., Saito, M. A., Rose, J. M., Riesselman, C. R., Lohan, M. C., Noble, A. E., Lee, P. A. and DiTullio, G. R.: Vitamin B12 and iron colimitation of phytoplankton growth in the Ross Sea, Limnol. Oceanogr., 52(3), 1079–1093, doi:10.4319/lo.2007.52.3.1079, 2007.

Bertrand, E. M., Moran, D. M., McIlvin, M. R., Hoffman, J. M., Allen, A. E. and Saito, M. A.: Methionine synthase interreplacement in diatom cultures and communities: Implications for the persistence of B12 use by eukaryotic phytoplankton, Limnol. Oceanogr., 58(4), 1431–1450, doi:10.4319/lo.2013.58.4.1431, 2013.

Browning, T. J., Achterberg, E. P., Rapp, I., Engel, A., Bertrand, E. M., Tagliabue, A. and Moore, C. M.: Nutrient co-limitation at the boundary of an oceanic gyre, Nature, 551(7679), 242–246, doi:10.1038/nature24063, 2017.

Bundy, R. M., Tagliabue, A., Hawco, N. J., Morton, P. L., Twining, B. S., Hatta, M., Noble, A., Cape, M. R., John, S. G., Cullen, J. T. and Saito, M. A.: Elevated sources of cobalt in the

Arctic Ocean, Biogeosciences, 17, 4745–4767, doi:https://doi.org/10.5194/bg-2020-84, 2020.
Calma, J.: Tesla to make EV battery cathodes without cobalt, The Verge, 22nd September [online] Available from: https://www.theverge.com/2020/9/22/21451670/tesla-cobalt-free-cathodes-mining-battery-nickel-ev-cost, 2020.
Carlson, R. L. and Raskin, G. S.: Density of the ocean crust, Nature, 311, 555–558, doi:10.1038/311555a0, 1984.
Chmiel, R., Lanning, N., Laubach, A., Lee, J.-M., Fitzsimmons, J., Hatta, M., Jenkins, W. J., Lam, P. J., Mcilvin, M., Tagliabue, A. and Saito, M. A.: Major processes of the dissolved cobalt cycle in the North and equatorial Pacific Ocean, Biogeosciences, 19, 2365–2395 [online] Available from: https://doi.org/10.5194/bg-19-2365-2022, 2022.
Christensen, N. I. and Mooney, W. D.: Seismic velocity structure and composition of the continental crust: a global view, J. Geophys. Res., 100(B7), 9761–9788, doi:10.1029/95JB00259, 1995.
Cobalt Institute: 'State of the Cobalt market' report 2020. [online] Available from: www.cobaltinstitute.org, 2021.
Deetman, S., Pauliuk, S., van Vuuren, D. P., van der Voet, E. and Tukker, A.: Scenarios for Demand Growth of Metals in Electricity Generation Technologies, Cars, and Electronic Appliances, Environ. Sci. Technol., 52, 4950–4959, doi:10.1021/acs.est.7b05549, 2018.
Drazen, J. C., Smith, C. R., Gjerde, K. M., Haddock, S. H. D., Carter, G. S., Choy, C. A., Clark, M. R., Dutrieux, P., Goetze, E., Hauton, C., Hatta, M., Koslow, J. A., Leitner, A. B., Pacini, A., Perelman, J. N., Peacock, T., Sutton, T. T., Watling, L. and Yamamoto, H.: Midwater ecosystems must be considered when evaluating environmental risks of deep-sea mining, PNAS, 117(30), 17455–17460, doi:10.1073/pnas.2011914117, 2020.
Dunlea, A. G., Murray, R. W., Sauvage, J., Pockalny, R. A., Spivack, A. J., Harris, R. N. and Hondt, S. D.: Cobalt-based age models of pelagic clay in the South Pacific Gyre, Geochemistry, Geophys. Geosystems, 16(8), 2694–2710, doi:10.1002/2015GC005892.Received, 2015.
Ford Motor Company: Ford Releases New Battery Capacity Plan, Raw Materials Details to Scale EVs; On Track to Ramp to 600K Run Rate by '23 and 2M+ by '26, Leveraging Global Relationships [Press release], , 21st July [online] Available from: https://media.ford.com/content/dam/fordmedia/North America/US/2022/07/21/Ford-EV-Plan-Update-English.pdf, 2022.
Fuchida, S., Yokoyama, A., Fukuchi, R., Ishibashi, J. I., Kawagucci, S., Kawachi, M. and Koshikawa, H.: Leaching of Metals and Metalloids from Hydrothermal Ore Particulates and Their Effects on Marine Phytoplankton, ACS Omega, 2(7), 3175–3182, doi:10.1021/acsomega.7b00081, 2017.
Van Geen, A., Adkins, J. F., Boyle, E. A., Nelson, C. H. and Palanques, A.: A120 yr record of widespread contamination from mining of the Iberian pyrite belt, Geology, 25(4), 291–294, doi:10.1130/0091-7613(1997)025<0291:AYROWC>2.3.CO;2, 1997.
Godoy León, M. F., Blengini, G. A. and Dewulf, J.: Cobalt in end-of-life products in the EU, where does it end up? - The MaTrace approach, Resour. Conserv. Recycl., 158(September 2019), 104842, doi:10.1016/j.resconrec.2020.104842, 2020.
Granéli, E. and Haraldsson, C.: Can increased leaching of trace metals from acidified areas influence phytoplankton growth in coastal waters?, Ambio, 22(5), 308–311, 1993.
Hallgren, A. and Hansson, A.: Conflicting narratives of deep sea mining, Sustainability, 13(9),

5261, doi:10.3390/su13095261, 2021.
Harper, E. M., Kavlak, G. and Graedel, T. E.: Tracking the metal of the goblins: Cobalt's cycle of use, Environ. Sci. Technol., 46(2), 1079–1086, doi:10.1021/es201874e, 2012.
Hawco, N. J., Ohnemus, D. C., Resing, J. A., Twining, B. S. and Saito, M. A.: A dissolved cobalt plume in the oxygen minimum zone of the eastern tropical South Pacific, Biogeosciences, 13(20), 5697–5717, doi:10.5194/bg-13-5697-2016, 2016.
Hawco, N. J., Lam, P. J., Lee, J. M., Ohnemus, D. C., Noble, A. E., Wyatt, N. J., Lohan, M. C. and Saito, M. A.: Cobalt scavenging in the mesopelagic ocean and its influence on global mass balance: Synthesizing water column and sedimentary fluxes, Mar. Chem., 201(March 2017), 151–166, doi:10.1016/j.marchem.2017.09.001, 2018.
Hein, J. R., Mizell, K., Koschinsky, A. and Conrad, T. A.: Deep-ocean mineral deposits as a source of critical metals for high- and green-technology applications: Comparison with land-based resources, Ore Geol. Rev., 51, 1–14, 2013.
Ho, L. C.: Variation in the carbon/dry matter ratio in plant material, Ann. Bot., 40(165), 163–165, 1976.
Hodgkin, D. C., Kamper, J., Lindsey, J., MacKay, M., Pickworth, J., Robertson, J. H., Shoemaker, C. B., White, J. G., Prosen, R. J. and Trueblood, K. N.: The Structure of Vitamin B12 I. An Outline of the Crystallographic Investigation of Vitamin B12, Proc. R. Soc. Lond. A. Math. Phys. Sci., 242(1229), 228–263, 1957.
Holman, J.: Almost half of Tesla EVs produced in Q1 had no nickel, cobalt in battery, S&P Glob. Commod. Insights, 21st April [online] Available from: https://www.spglobal.com/commodityinsights/en/market-insights/latest-news/energy-transition/042122-almost-half-of-tesla-evs-produced-in-q1-had-no-nickel-cobalt-in-battery, 2022.
Husain, F.: The Deepest Paradox: Seafloor Mining and Its Future, Massachusetts Institute of Technology., 2018.
Huss, M.: Density assumptions for converting geodetic glacier volume change to mass change, Cryosph., 7, 877–887, doi:10.5194/tc-7-877-2013, 2013.
Irving, H. and Williams, R. J. P.: Order of stability of metal complexes, Nature, 162, 746–747, 1948.
Kang, D. H. P., Chen, M. and Ogunseitan, O. A.: Potential Environmental and Human Health Impacts of Rechargeable Lithium Batteries in Electronic Waste, Environ. Sci. Technol., 47, 5495–5503, doi:10.1021/es400614y, 2013.
Kirchner, P., Biondi, F., Edwards, R. and Mcconnell, J. R.: Variability of trace metal concentrations in Jeffrey pine (Pinus jeffreyi) tree rings from the Tahoe Basin, California, USA, J. For. Res., 13, 347–356, doi:10.1007/s10310-008-0093-5, 2008.
Mazzotta, M. G., Mcilvin, M. R. and Saito, M. A.: Metallomics Characterization of the Fe metalloproteome of a ubiquitous marine heterotroph, Pseudoalteromonas (BB2-AT2): multiple bacteriogerritin copies enable significant Fe storage, Metallomics, 12(5), 654–667, doi:10.1039/d0mt00034e, 2020.
Morris, J.: Tesla's Shift To Cobalt-Free Batteries Is Its Most Important Move Yet, Forbes, 11th July [online] Available from: https://www.forbes.com/sites/jamesmorris/2020/07/11/teslas-shift-to-cobalt-free-batteries-is-its-most-important-move-yet/?sh=79ac546346b4, 2020.
Nagajyoti, P. C., Lee, K. D. and Sreekanth, T. V. M.: Heavy metals, occurrence and toxicity for plants: A review, Environ. Chem. Lett., 8, 199–216, doi:10.1007/s10311-010-0297-8,

2010.
Noble, A. E., Lamborg, C. H., Ohnemus, D. C., Lam, P. J., Goepfert, T. J., Measures, C. I., Frame, C. H., Casciotti, K. L., DiTullio, G. R., Jennings, J. and Saito, M. A.: Basin-scale inputs of cobalt, iron, and manganese from the Benguela-Angola front to the South Atlantic Ocean, Limnol. Oceanogr., 57(4), 989–1010, doi:10.4319/lo.2012.57.4.0989, 2012.
Noble, A. E., Ohnemus, D. C., Hawco, N. J., Lam, P. J. and Saito, M. A.: Coastal sources, sinks and strong organic complexation of dissolved cobalt within the US North Atlantic GEOTRACES transect GA03, Biogeosciences, 14(11), 2715–2739, doi:10.5194/bg-14-2715-2017, 2017.
Oelkers, E. H., Hering, J. G. and Zhu, C.: Water: Is there a global crisis?, Elements, 7(3), 157–162, doi:10.2113/gselements.7.3.157, 2011.
Orcutt, B. N., Bradley, J. A., Brazelton, W. J., Estes, E. R., Goordial, J. M., Huber, J. A., Jones, R. M., Mahmoudi, N., Marlow, J. J., Murdock, S. and Pachiadaki, M.: Impacts of deep-sea mining on microbial ecosystem services, Limnol. Oceanogr., 65, 1489–1510, doi:10.1002/lno.11403, 2020.
Reimann, C. and de Caritat, P.: Chemical Elements in the Environment - Factsheets for the Geochemist and Environmental Scientist, Springer-Verlag, Berlin, Germany., 1998.
Roane, T. M., Pepper, I. L. and Gentry, T. J.: Microorganisms and Metal Pollutants, in Environmental Microbiology, edited by I. L. Pepper, C. P. Gerba, and T. J. Gentry, pp. 415–439., 2015.
Saito, M. A., Sigman, D. M. and Morel, M. M. F.: The bioinorganic chemistry of the ancient ocean: the co-evolution of cyanobacterial metal requirements and biogeochemical cycles at the Archean-Proterozoic boundary?, Inorganica Chim. Acta, 356, 308–318, doi:10.1016/S0020-1693(03)00442-0, 2003.
Saito, M. A., Noble, A. E., Hawco, N., Twining, B. S., Ohnemus, D. C., John, S. G., Lam, P., Conway, T. M., Johnson, R., Moran, D. and McIlvin, M.: The acceleration of dissolved cobalt's ecological stoichiometry due to biological uptake, remineralization, and scavenging in the Atlantic Ocean, Biogeosciences, 14(20), 4637–4662, doi:10.5194/bg-14-4637-2017, 2017.
Schubert, G. and Sandwell, D.: Crustal volumes of the continents and of oceanic and continental submarine plateaus, Earth Planet. Sci. Lett., 92, 234–246, doi:10.1016/0012-821X(89)90049-6, 1989.
Sharma, R.: Deep-sea mining: Economic, technical, technological, and environmental considerations for sustainable development, Mar. Technol. Soc. J., 45(5), 28–41, doi:10.4031/MTSJ.45.5.2, 2011.
Skeete, J., Wells, P., Dong, X., Heidrich, O. and Harper, G.: Beyond the EVent horizon: Battery waste , recycling , and sustainability in the United Kingdom electric vehicle transition, Energy Res. Soc. Sci., 69(May), 101581, doi:10.1016/j.erss.2020.101581, 2020.
Sovacool, B. K.: The precarious political economy of cobalt: Balancing prosperity, poverty, and brutality in artisanal and industrial mining in the Democratic Republic of the Congo, Extr. Ind. Soc., 6(3), 915–939, 2019.
Stanway, D.: China puts responsibility for battery recycling on makers of electric vehicles, Reuters [online] Available from: https://www.reuters.com/article/us-china-batteries-recycling/china-puts-responsibility-for-battery-recycling-on-makers-of-electric-vehicles-idUSKCN1GA0MG, 2018.

Steen, M., Lebedeva, N., Di Persio, F. and Boon-Brett, L.: EU Competitiveness in Advanced Li-ion Batteries for E-Mobility and Stationary Storage Applications – Opportunities and Actions, Luxembourg., 2017.

Sun, X., Hao, H., Liu, Z., Zhao, F. and Song, J.: Tracing global cobalt flow: 1995–2015, Resour. Conserv. Recycl., 149, 45–55, doi:10.1016/j.resconrec.2019.05.009, 2019.

Sunda, W. G. and Huntsman, S. A.: Cobalt and zinc interreplacement in marine phytoplankton: Biological and geochemical implications, Limnol. Oceanogr., 40(8), 1404–1417, doi:10.4319/lo.1995.40.8.1404, 1995.

UNCTAD: Commodities at a glance: Special issue on strategic battery raw materials, Geneva. [online] Available from: https://unctad.org/system/files/official-document/ditccom2019d5_en.pdf, 2020.

United States Department of Energy: Research Plan to Reduce, Recycle, and Recover Critical Materials in Lithium-Ion Batteries, Washington, D.C. [online] Available from: https://www.energy.gov/sites/prod/files/2019/07/f64/112306-battery-recycling-brochure-June-2019 2-web150.pdf, 2019.

USGS: Cobalt: Mineral Commodity Summaries., 2021.

Yang, X. G., Liu, T. and Wang, C. Y.: Thermally modulated lithium iron phosphate batteries for mass-market electric vehicles, Nat. Energy, 6, 176–185, doi:10.1038/s41560-020-00757-7, 2021.

Tables

Table 1. Estimates of the cobalt inventories within the four major Earth spheres. A description of estimate calculations can be found in the Appendix J. Conversion between moles of cobalt (mol Co) and kg cobalt uses cobalt's molar mass of 58.933 g mol^{-1}.

Sphere	Inventory Estimate [mol Co]	Inventory Estimate [kg Co]
Lithosphere		
Continental	9×10^{18}	5×10^{17}
Oceanic	8×10^{17}	5×10^{16}
Total	1×10^{19}	6×10^{17}
Global Reserve[a]	1×10^{11}	7×10^{9}
Hydrosphere		
Marine	$7 - 8 \times 10^{10}$	$4 - 5 \times 10^{9}$
Above-ground Freshwater	2×10^{9}	1×10^{8}
Groundwater	1×10^{10}	6×10^{8}
Total	$8 - 9 \times 10^{10}$	5×10^{9}
Biosphere		
Prokaryotic[b]	$5 - 8 \times 10^{8}$	$3 - 5 \times 10^{7}$
Eukaryotic	$1 - 16 \times 10^{9}$	$6 - 90 \times 10^{7}$
Total	$2 - 17 \times 10^{9}$	$9 - 100 \times 10^{7}$
Anthroposphere		
In Use[c]	4×10^{9}	2×10^{8}

[a] From USGS Mineral Commodity Summaries (2020).
[b] The prokaryotic biomass estimate could be as high as 7×10^{12} mol Co (or 4×10^{11} kg Co) using a higher cobalt : carbon estimate from Mazzotta et al. (2020), although this value is likely globally unrealistic.
[c] From Harper et al. (2012).

Table 2. Summary of fluxes through the anthroposphere from two material flow analysis studies in 2005 and 2015, and from a 2020 industry report. Note that each study referenced (and therefore each yearly estimate column) used different global records and methodologies to quantify the flux of cobalt.

	Inventory	**Flux [mol Co yr^{-1}]**		
	[mol Co]	**2005[a]**	**2015[b]**	**2020[c]**
Global Reserves[d]	1.2×10^{11}			
Mined		1.1×10^{9}	2.1×10^{9}	2.5×10^{9}
Refined		9.2×10^{8}	1.6×10^{9}	2.2×10^{9}
In Use[a]	3.7×10^{9}	9.0×10^{8}		
Disposed		4.7×10^{8}	1.2×10^{9}	
Recycled		1.6×10^{8}	1.9×10^{8}	1.8×10^{8}

[a] From Harper et al. (2011).
[b] From Sun et al. (2019).
[c] From the Cobalt Institute report (2021).
[d] From USGS Mineral Commodity Summaries (2020).

Figures

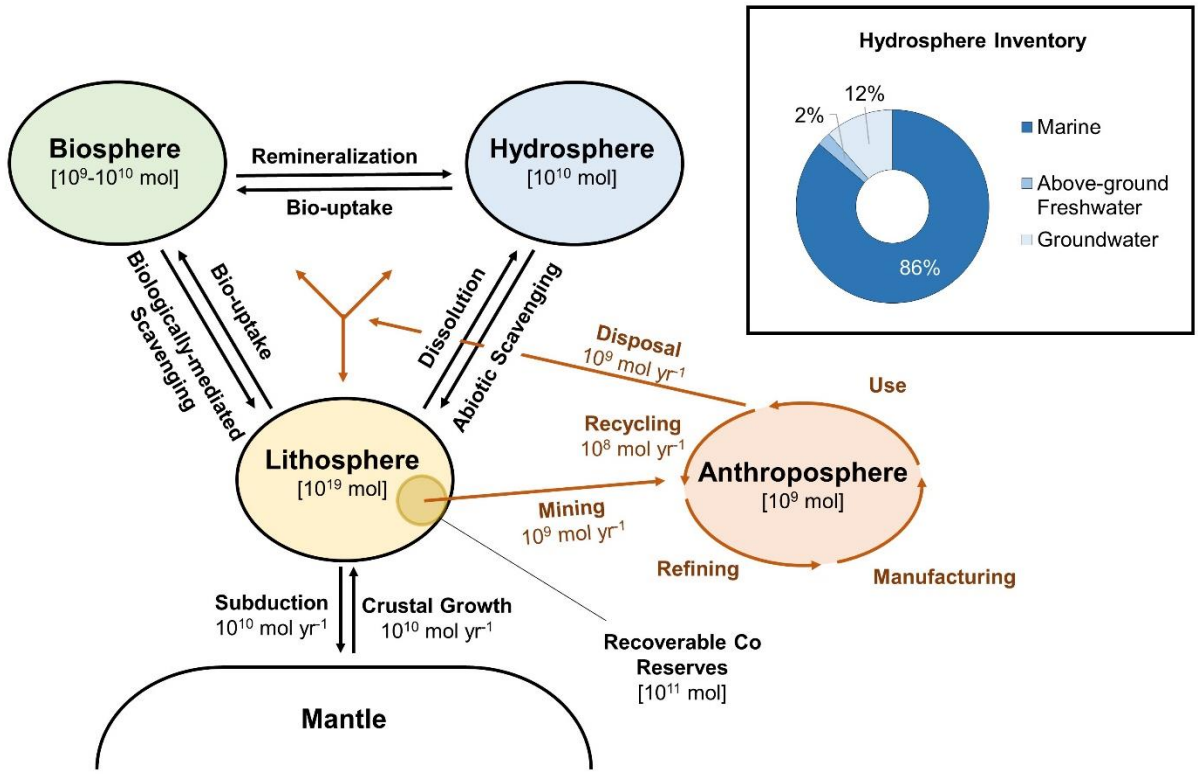

Figure 1. Spheres of the global cobalt cycle, not to scale. The anthropogenic cobalt cycle is shown in orange. The order of magnitude of each cobalt inventory is given in brackets in units of moles (mol) cobalt, and the order of magnitude of select cobalt fluxes are in units of mol cobalt per year.

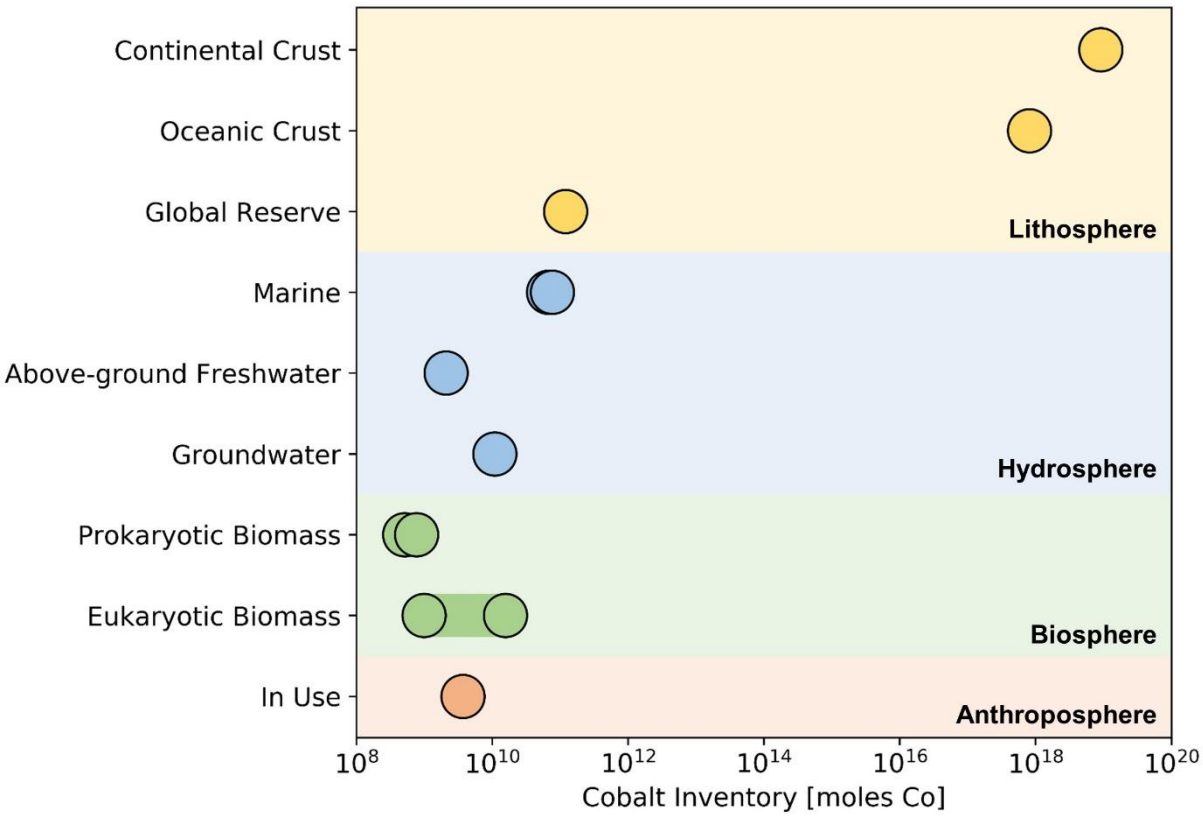

Figure 2. Log-scale estimates of the cobalt inventories within the four major Earth spheres. Note that cobalt estimates in microorganisms are highly plastic and depend upon environmental cobalt concentrations. The prokaryotic biomass estimate could be as high as 7×10^{12} mol Co using a higher cobalt : carbon estimate from Mazzotta et al. (2020), although this value is likely globally unrealistic.

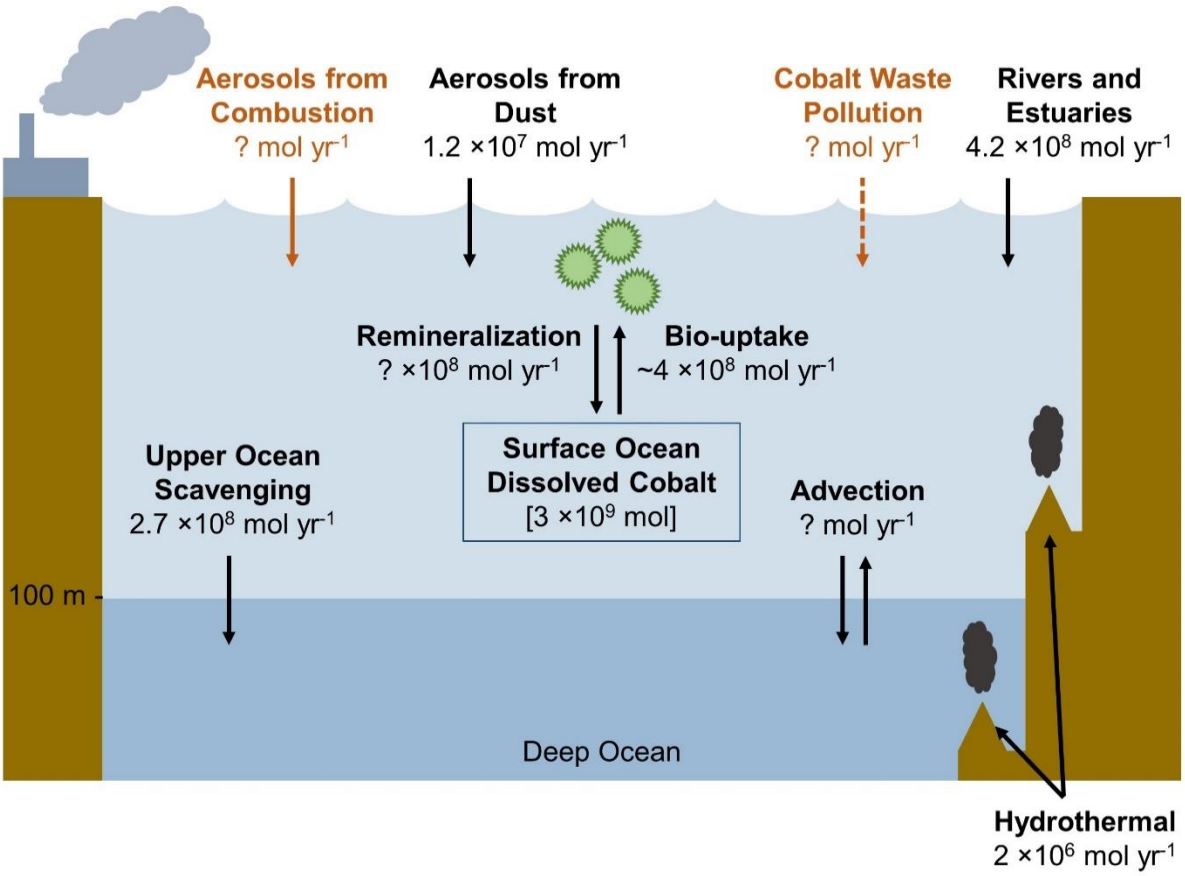

Figure 3. Schematic of cobalt fluxes within the surface ocean (depth ≤ 100 m). Anthropogenic cobalt sources are shown in orange. All cobalt fluxes are given in units of moles of cobalt per year.

Chapter 6.

Conclusions

This dissertation examined the marine and global cobalt cycle, interrogating open questions in the study of biogeochemistry concerning dissolved cobalt distributions, cobalt use by marine microorganisms, and the potential for the perturbation of the cobalt cycle due to global change in the Anthropocene. Chapters 2, 3 and 4 described expeditions that filled key holes in our mapping of global dissolved cobalt distributions in the North and equatorial Pacific Ocean (GP15 and ProteOMZ expeditions), as well as in the Amundsen Sea and Terra Nova Bay (CICLOPS expedition). These ocean transects of high-resolution dissolved cobalt inventory and cobalt speciation establish baseline datasets that are among the most significant contributions that this dissertation provides to the field of trace metal biogeochemistry. The power of establishing baseline measurements of trace metal distributions was exemplified in Chapter 4, where previous baseline data from the CORSACS expeditions was used to reveal a significant perturbation to the Ross Sea cobalt cycle, possibly as the result of anthropogenic global climate change.

Chapters 3 and 4 explored how cobalt was being used by marine microorganisms on a community-scale, and how the coupling of the particulate and dissolved phases of the cobalt cycle are deeply entwined in the processes of cobalt biological uptake by phytoplankton and cobalt remineralization. These chapters explored the complexity and high variability of cobalt stoichiometry among marine plankton, particularly as it related to and was controlled by the dissolved zinc inventory and other key nutrients like phosphate, nitrate, iron and vitamin B_{12}.

A major take-away of this dissertation, as well as of many explorations of biogeochemistry, is that the Earth's elemental cycles are intricately connected in ways that can be challenging to predict until a system is disrupted. The perturbation of the carbon cycle by the burning of fossil fuels for energy or of the nitrogen cycle by the industrial fixation of N_2 for use in agricultural fertilizers represent major disturbances of elemental cycles that, over the past couple centuries, have threatened to surpass Earth's "planetary boundaries", which define the safe operating limits of humanity (Rockstrom et al., 2009). The carbon cycle itself is so deeply entwined within Earth's biological, geological and atmospheric systems that anthropogenic perturbations to carbon

biogeochemistry have cascaded throughout Earth's systems, and one would be hard pressed to identify a single elemental cycle that remains unaffected by global climate change. Rising global temperatures has initiated ocean deoxygenation, shifting limits of species' habitability, and the widespread melting of the polar ice caps, among other effects, and these in turn have triggered cascading changes within other elemental cycles, including the cobalt cycle.

Over the past 50 years, the oceans have experienced deoxygenation and increasing volumes of oxygen minimum zones (OMZs) due to warming ocean temperatures and the subsequent decrease in the solubility of oxygen (Matear and Hirst, 2003; Stramma et al., 2008). This deoxygenation is expected to continue as ocean temperatures increase, and with it, the redox environment of the waters within the newly expanded OMZs will change, seriously altering the biogeochemistry of redox-sensitive elements. As quantified in Chapter 2, dissolved cobalt inventories within OMZs are expected to increase as the inhibition of manganese-oxide particle formation in low-oxygen environments would reduce a major geochemical sink of marine cobalt, allowing the dissolved phase of the metal to build up within OMZ waters (Chmiel et al., 2022; Hawco et al., 2016; Noble et al., 2012, 2017). This effect would primarily impact subtropical OMZs in the Atlantic, Pacific and Indian Oceans, where some of the strongest global oxygen minima can be found off of coastal upwelling systems.

Dissolved cobalt concentrations have also been increasing in the Arctic Ocean, where melting permafrost environments have increased the flux of dissolved and particulate cobalt to the upper ocean (Bundy et al., 2020). In contrast, Chapter 4 discussed a decreasing dissolved cobalt inventory in coastal Antarctic seas, potentially driven by the melting of the Antarctic ice shelves, increased fluxes of iron to coastal Antarctica, and the alleviation of iron limitation. The polar regions have exhibited opposite trends in their changing dissolved cobalt inventories, but both appear linked to higher temperatures and melting polar ice that is changing the regions' ecosystems and trace element cycles.

As discussed in Chapter 5, the flux of cobalt into the anthroposphere via terrestrial mining, driven by the increased use of cobalt in the lithium-ion batteries of personal electronics and electric vehicles, has dramatically risen over the past decade. Currently, the flux of cobalt through the anthroposphere was found to be the same order of magnitude as the global inventory of dissolved cobalt in the surface ocean, and was only one order of magnitude lower than the inventory of dissolved cobalt in the global oceans. Modern lithium-ion battery disposal and recycling

infrastructure is not currently prepared to handle the rising influx of cobalt battery waste, resulting in a substantial threat of perturbation to the natural cobalt cycling processes of the hydrosphere and biosphere.

Compared to many other trace metals used in the metabolisms of marine life, the relatively low inventories of cobalt throughout the marine environment result in the cobalt cycle's high vulnerability to perturbation. Dissolved cobalt concentrations are often below 20 pM in the surface ocean and rarely above 200 pM throughout the pelagic ocean. Cobalt is often the scarcest bioactive nutrient in marine environments where other micronutrients like iron and zinc are typically observed in nanomolar ranges. Low cobalt inventories and subsequent vulnerability to perturbation could mean that cobalt becomes one of the first micronutrients whose marine biogeochemical cycle is disrupted on a scale that results in significant inventory change when an environmental disruption occurs. Thus, changes in source or sink fluxes, such as an increased source of trace metals to the surface ocean from melting polar ice, that may be negligible to other micronutrient inventories may significantly disrupt the small marine cobalt inventory. The timescales of processes are important to consider, and the cobalt inventory may be perturbed on a shorter timescale, while nutrients with larger inventories may be impacted on a longer timescale if the magnitude of the perturbation is proportional.

Changes in the regional inventories of dissolved cobalt, whether as a net increase or a net decrease, are likely to impact the biology and stoichiometry of the marine microbes that utilize cobalt, as well as the relative uptake of trace metals with a similar atomic size and charge, such as cadmium and zinc. In regions like the Arctic and expanding OMZs where dissolved cobalt concentrations are increasing, plankton with flexible metabolisms that can substitute cobalt in place of zinc for proteins like carbonic anhydrase are likely to be favored in bloom communities (Kellogg et al., 2022; Sunda and Huntsman, 1995), while in the Antarctic where cobalt concentrations appear to be decreasing alongside evidence of vitamin B_{12} and zinc stress, plankton that can express the vitamin B_{12}-independent MetE gene may be favored over those limited to the vitamin B_{12}-dependent MetH gene (Bertrand et al., 2013; Helliwell, 2017; Rao et al., In review; Rodionov et al., 2003). In both situations, microbial life that exhibit flexible trace metal metabolisms that are able to thrive in a wide range of trace metal conditions are best prepared to succeed as the availability of trace nutrients change.

References

Bertrand, E. M., Moran, D. M., McIlvin, M. R., Hoffman, J. M., Allen, A. E. and Saito, M. A.: Methionine synthase interreplacement in diatom cultures and communities: Implications for the persistence of B12 use by eukaryotic phytoplankton, Limnol. Oceanogr., 58(4), 1431–1450, doi:10.4319/lo.2013.58.4.1431, 2013.

Bundy, R. M., Tagliabue, A., Hawco, N. J., Morton, P. L., Twining, B. S., Hatta, M., Noble, A., Cape, M. R., John, S. G., Cullen, J. T. and Saito, M. A.: Elevated sources of cobalt in the Arctic Ocean, Biogeosciences, 17, 4745–4767, doi:https://doi.org/10.5194/bg-2020-84, 2020.

Chmiel, R., Lanning, N., Laubach, A., Lee, J.-M., Fitzsimmons, J., Hatta, M., Jenkins, W. J., Lam, P. J., Mcilvin, M., Tagliabue, A. and Saito, M. A.: Major processes of the dissolved cobalt cycle in the North and equatorial Pacific Ocean, Biogeosciences, 19, 2365–2395 [online] Available from: https://doi.org/10.5194/bg-19-2365-2022, 2022.

Hawco, N. J., Ohnemus, D. C., Resing, J. A., Twining, B. S. and Saito, M. A.: A dissolved cobalt plume in the oxygen minimum zone of the eastern tropical South Pacific, Biogeosciences, 13(20), 5697–5717, doi:10.5194/bg-13-5697-2016, 2016.

Helliwell, K. E.: The roles of B vitamins in phytoplankton nutrition: new perspectives and prospects, New Phytol., 216, 62–68, doi:10.1111/nph.14669, 2017.

Kellogg, R. M., Moosburner, M. A., Cohen, N. R., Hawco, N. J., McIlvin, M. R., Moran, D. M., DiTullio, G. R., Subhas, A. V., Allen, A. E. and Saito, M. A.: Adaptive responses of marine diatoms to zinc scarcity and ecological implications, Nat. Commun., 13, doi:10.1038/s41467-022-29603-y, 2022.

Matear, R. J. and Hirst, A. C.: Long-term changes in dissolved oxygen concentrations in the ocean caused by protracted global warming, Global Biogeochem. Cycles, 17(4), 1125, doi:10.1029/2002gb001997, 2003.

Noble, A. E., Lamborg, C. H., Ohnemus, D. C., Lam, P. J., Goepfert, T. J., Measures, C. I., Frame, C. H., Casciotti, K. L., DiTullio, G. R., Jennings, J. and Saito, M. A.: Basin-scale inputs of cobalt, iron, and manganese from the Benguela-Angola front to the South Atlantic Ocean, Limnol. Oceanogr., 57(4), 989–1010, doi:10.4319/lo.2012.57.4.0989, 2012.

Noble, A. E., Ohnemus, D. C., Hawco, N. J., Lam, P. J. and Saito, M. A.: Coastal sources, sinks and strong organic complexation of dissolved cobalt within the US North Atlantic GEOTRACES transect GA03, Biogeosciences, 14(11), 2715–2739, doi:10.5194/bg-14-2715-2017, 2017.

Rao, D., Fussy, Z., Moran, D. M., McIlvin, M. R., Allen, A. E., Follows, M. J. and Saito, M. A.: Flexible B12 ecophysiology of Phaeocystis antarctica to a fusion B12-independent methionine synthase with widespread homologues, PNAS [In review].

Rockstrom, J., Steffen, W., Noone, K., Lambin, E., Lenton, T. M., Scheffer, M., Folke, C., Schellnhuber, H. J., Wit, C. A. De, Hughes, T., Leeuw, S. Van Der, Rodhe, H., Snyder, P. K., Costanza, R., Svedin, U., Falkenmark, M., Karlberg, L., Corell, R. W., Fabry, V. J., Hansen, J., Walker, B., Liverman, D., Richardson, K., Crutzen, P. and Foley, J.: Planetary Boundaries: Exploring the Safe Operating Space for Humanity, Ecol. Soc., 14(2), 32, 2009.

Rodionov, D. A., Vitreschak, A. G., Mironov, A. A. and Gelfand, M. S.: Comparative genomics of the vitamin B12 metabolism and regulation in prokaryotes, J. Biol. Chem., 278(42),

41148–41159, doi:10.1074/jbc.M305837200, 2003.
Stramma, L., Johnson, G. C., Sprintall, J. and Mohrholz, V.: Expanding Oxygen-Minimum Zones in the Tropical Oceans, Science (80-.)., 320(May), 655–658, 2008.
Sunda, W. G. and Huntsman, S. A.: Cobalt and zinc interreplacement in marine phytoplankton: Biological and geochemical implications, Limnol. Oceanogr., 40(8), 1404–1417, doi:10.4319/lo.1995.40.8.1404, 1995.

Appendices

Appendix A. Additional interpretation of the dCo vs. O_2 relationship

Table A1. Two-way regression statistics for the dCo vs. O_2 relationship in the three Pacific OMZs, separated by O_2 concentration (shown in Fig. A1c, g, k). In the North Pacific OMZ, samples at and below 500 m depth were included in the regression, and in the ETNP and ETSP, samples at and below 150 m depth were included. Note that R^2 values of the regressions were particularly low within the North Pacific and low-[O_2] ETNP.

OMZ	Stations included	Latitudinal range	$[O_2] < 50\ \mu mol\ kg^{-1}$			$50 \leq [O_2] \leq 150\ \mu mol\ kg^{-1}$		
			dCo : O_2 [$\mu M : mol\ kg^{-1}$]	R^2	n	dCo : O_2 [$\mu M : mol\ kg^{-1}$]	R^2	n
North Pacific	3–18	55 to 22° N	-6.4 ± 4.5	0.03	75	-0.23 ± 0.12	0.05	69
ETNP	20–25	14.25 to 5° N	-2.8 ± 1.8	0.09	26	-0.58 ± 0.10	0.54	28
ETSP	29–34	0° N to 7.5° S	-2.1 ± 0.6	0.47	13	-0.63 ± 0.07	0.65	38

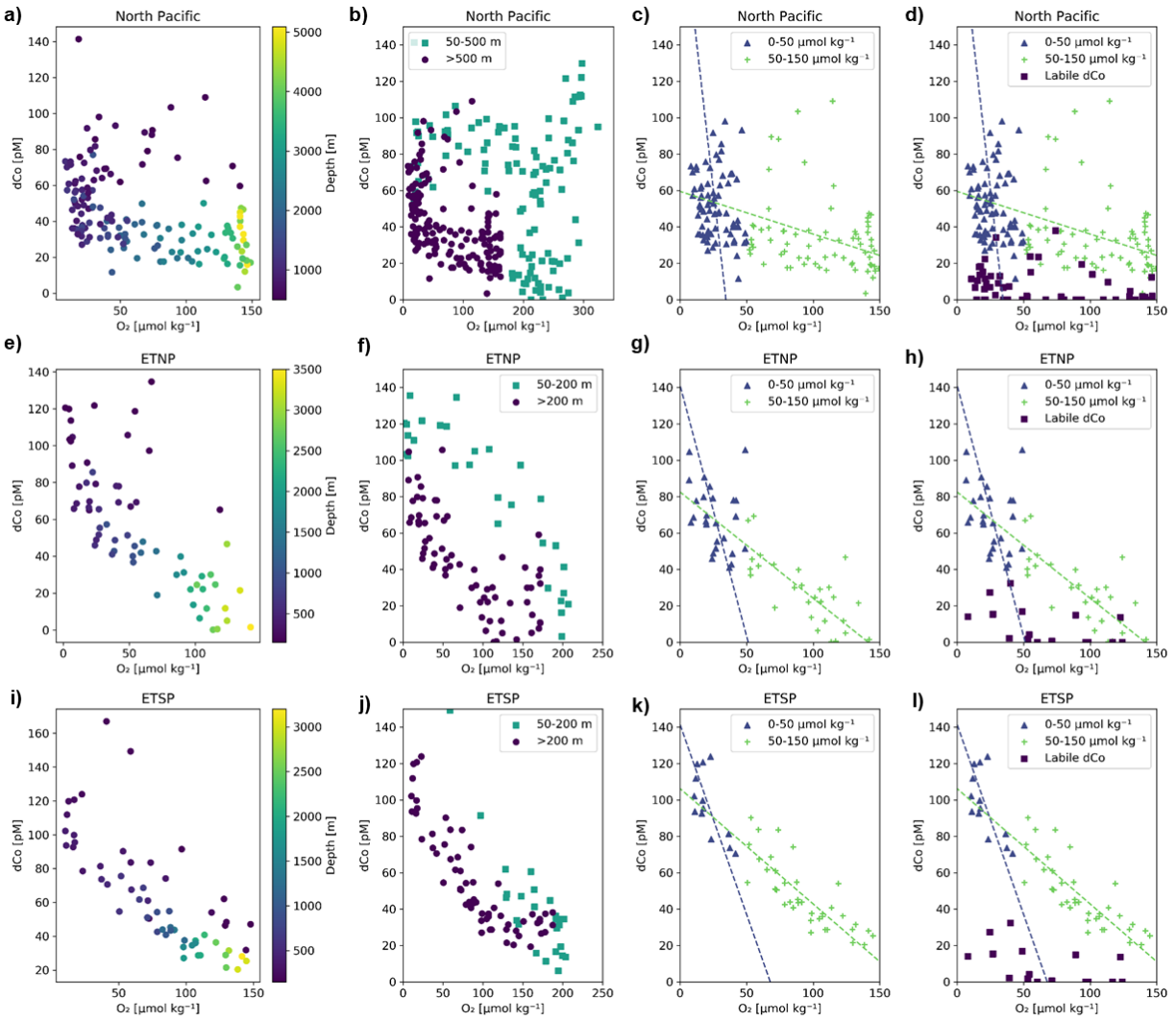

Figure A1. Interpretations of the dCo : O_2 relationship in the North Pacific (a–d; Stations 3–18), ETNP (e–h; Stations 20–25) and ETSP (i–l; Stations 29–34). Subplots (a), (e) and (i) show dCo vs. O_2 where depth $\geq$ 500 m in the North Pacific and depth $\geq$ 200 m in the ETNP and ETSP. Subplots (b), (f) and (j) include shallower samples above the 500 m depth threshold in the North Pacific and 200 m depth threshold in the ETNP and ETSP. Subplots (c), (g) and (k) separate the dCo vs. O_2 correlations by O_2 concentration, with lower [O_2] samples (<50 µmol kg^{-1}) displaying more negative slopes than samples where $50 \leq [O_2] \leq 150$ µmol kg^{-1}. This trend suggests that low-[O_2] samples, which tend to occur at shallower depths, are affected by more vertical processes like remineralization and scavenging at the boundaries of the OMZ core compared to mid-[O_2] samples, which are affected by more horizontal processes of advection and mixing. Two-way regression statistics are given in Table A1 above. Subplots (d), (h) and (l) include labile dCo concentrations and suggest that labile dCo might be more prevalent in the low-[O] samples and could be scavenged in more oxic waters. The labile dCo concentrations appear to be affected by additional processes in the North Pacific.

Appendix B. Dissolved Co distributions from coastal Alaskan sources

Trace metal samples, including dCo samples were collected from the Alaskan Coast and Kodiak Island between September 6 and September 10, 2019 by the Charette and Fitzsimmons laboratories. This fieldwork was aimed at quantifying sources of trace metals to the Alaskan Shelf and coastal marine environments from rivers, estuaries and groundwater fluxes. Here, we present the total dCo and labile dCo results from this fieldwork.

Methods

All dCo samples were filtered using a 60 mL plastic syringe and an attached 0.2 µm filter, then stored in an acid-washed 60 mL LDPE bottle and stored at 4 °C until analysis in the laboratory between October 23 and November 7, 2019 (Fig. B1; Table B1). Shelf samples were collected offshore of Kodiak Island, east of Women's Bay, using a deck hose. Estuary samples were collected from Women's Bay using a well pump. River water samples were collected using a well pump from two locations on Kodiak Island (Salonie Creak and Buskin River) and from three locations on the Alaskan mainland near the city of Anchorage, AK (Susitna River, Matanuska River and Knik River). Groundwater samples from Kodiak Island were collected using a pushpoint and peripump along the Buskin River beach and in Kalsin Bay.

Total dCo and labile dCo concentrations were determined by the Saito laboratory at the Woods Hole Oceanographic Institution (WHOI) using cathodic stripping voltammetry (CSV) as described in Sect. 2.3.2. The CSV methodology is tuned to respond best to saline samples with scarce levels of dCo – less than ~200 pM – as is common throughout the pelagic marine environment, and these more terrestrial samples needed to be diluted with low-dCo seawater prior to analysis. The seawater dilution consisted of non-UV-irradiated seawater from the surface Equatorial Pacific, which contained negligible (~0 pM) concentrations of dCo when measured alone. Samples were diluted by a factor of 1/11 (1 mL sample), 1/110 (0.1 mL sample), or 1/22 (0.5 mL sample) to reach a final analysis volume of 11 mL (Table B2).

Results

The dCo concentrations observed along the Alaskan Coast from the 2019 fieldwork ranged from values of 202 pM in the groundwater of Kalsin Bay to as high as 7182 pM in the Women's Bay estuary (Table B2). On average, dCo concentrations were lowest in groundwater (330 ± 110

pM) and highest in the estuary samples (4900 ± 1600 pM; Table B3). The average dCo concentrations observed along the shelf (620 ± 600 pM) are comparable to the surface of most coastal GP15 station, (Station 1; 576 pM). The freshwater endmember predicted by the dCo : salinity relationship observed in GP15's Station 1 was 13.3 ± 0.4 nM, which is an order of magnitude higher than the river or estuary dCo averages observed in the 2019 fieldwork, suggesting that the linear dCo : salinity relationship observed offshore at Station 1 likely did not persist as a linear relationship in more coastal and estuarine environments.

The results of the labile dCo analysis were often difficult to interpret; in 2 of the 5 estuary samples and 4 of the 5 river samples, measured labile dCo values exceeded total dCo values, which was almost certainly the result of a sample storage or analysis artifact since by definition, the labile dCo fraction cannot exceed the total dCo fraction. In some cases, the higher labile dCo values were close to the total dCo concentration and may have been the result of higher analytical error due to the necessity of sample dilution, as with samples E2 (7182 pM dCo and 7810 pM labile dCo), R4 (822 pM dCo and 859 pM labile dCo) and R5 (441 pM dCo and 460 pM labile dCo). However, some labile dCo values were an order of magnitude higher than the measured total dCo concentrations, including sample R2, whose labile dCo value (3943 pM) was over 5 times greater than the measured dCo value (679 pM). This discrepancy could be due to the labile sample's longer equilibration time with the DMG artificial ligand compared to the UV-irradiated total dCo samples, which may have allowed additional Co in the colloidal form to bind with the strong ligand and seemingly increase the labile dCo measurement. Alternatively, the strong humic material likely present in the estuary and river samples and/or the samples low salinity may have affected the electrode instrument's accuracy, since the method is not well tuned to the measurement of freshwater or samples with high organic carbon concentrations more typical to terrestrial environments. It would be best to interpret all labile dCo concentration values presented here, including the samples with an acceptable labile dCo : total dCo value of < 1, as best estimates of the labile dCo concentrations in these environments.

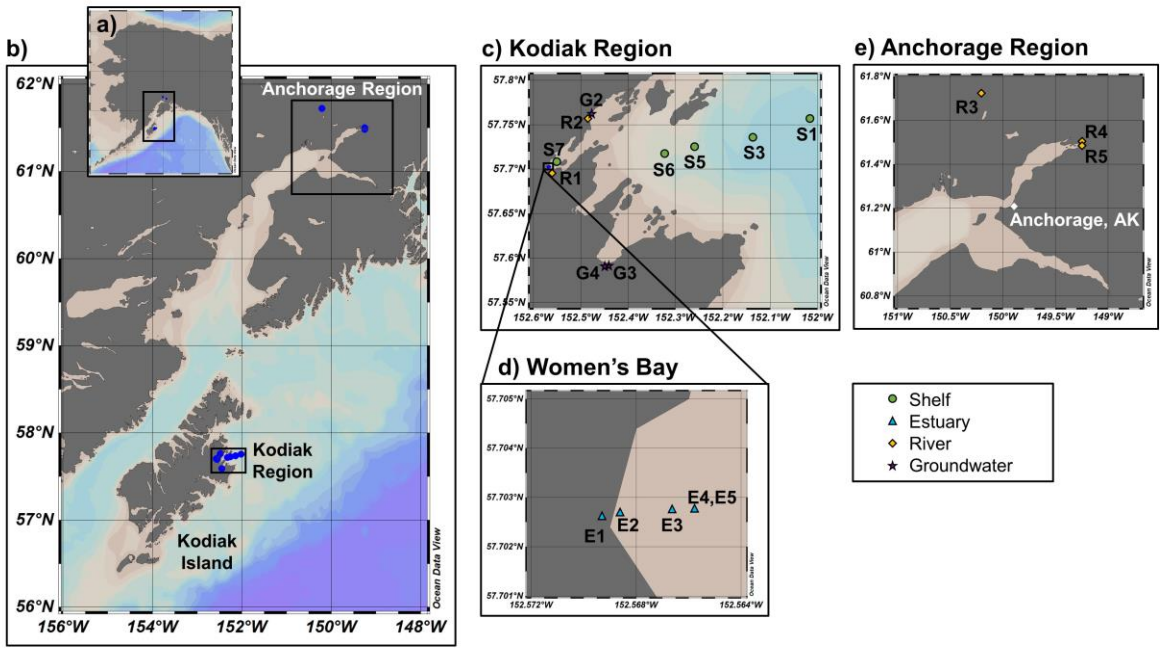

Figure B1. Map of stations where dCo samples were collected from along the Alaskan Coast and Kodiak Island (a, b). Samples were collected from the shelf offshore of Kodiak Island (c), the Women's Bay estuary on Kodiak Island (d), 5 rivers on Kodiak Island and mainland Alaska near the city of Anchorage (c,e), and groundwater on Kodiak Island (c). Note that samples E4 and E5 share a station location and differ by depth (see Table B1). Stations marked with a blue circle are shown in more detail in an inset.

Table B1. Sample locations and additional sampling information for trace metal fieldwork in coastal Alaska in September, 2019. Most samples were collected on Kodiak Island. All estuary samples were collected from Women's Bay. Dates are given in month/day/year format.

Sample Type	Sample ID	Latitude	Longitude	Date	Time [Local]	Depth [m]	Salinity [PSU]	Location Notes
Shelf	S1	57.7554	-152.0184	9/6/2019	8:23	1.0	30.19	Most pelagic shelf station
	S3	57.73521667	-152.1386833	9/6/2019	10:00	1.0	31.76	
	S5	57.72445	-152.26105	9/6/2019	11:45	1.0	32.13	
	S6	57.71785	-152.3255333	9/6/2019	12:20	1.0	31.68	
	S7	57.70811667	-152.5490667	9/6/2019	13:33	1.0	30.62	Most coastal shelf station
Estuary	E1	57.70259	-152.56937	9/7/2019	12:33	0.2	1.83	
	E2	57.70269	-152.5686	9/7/2019	12:54	0.2	2.99	
	E3	57.70274	-152.5666	9/7/2019	13:25	0.4	7.77	
	E4	57.70275	-152.56578	9/7/2019	13:50	0.5	12.28	
	E5	57.70275	-152.56578	9/7/2019	16:00	1.0	15.97	Bottom depth sample, same location as E4
River	R1	57.6964809	-152.5608328	9/7/2019	10:07	1.0	0.04	Salonie Creek
	R2	57.75616	-152.4836	9/8/2019	12:23	0.2	0.45	Buskin River
	R3	61.7214154	-150.2070422	9/10/2019	10:30	0.2	0.07	Susitna River
	R4	61.501252	-149.2508464	9/10/2019	14:18	0.2	0.11	Matanuska River
	R5	61.4832632	-149.2514167	9/10/2019	15:30	0.2	0.09	Knik River
Groundwater	G2	57.7612	-152.47687	9/8/2019	10:00	0.3	0.06	Biskin River beach
	G3	57.58925	-152.44531	9/8/2019	15:45	0.3	22.34	Kalsin Bay, tidal creek
	G4	57.5887	-152.44821	9/8/2019	16:00	0.3	14.92	Kalsin Bay, tidal creek

Table B2. Total dCo and labile dCo results from the 2019 fieldwork along the Alaskan Coast and Kodiak Island. Sample volumes of 1 mL, 0.5 mL or 0.1 mL were diluted to a total analysis volume of 11 mL, resulting in dilution factors of 1/11, 1/22 and 1/110, respectively. Sample analysis that were not diluted are reported with a dilution factor of 'n/a'. Labile dCo results with a '*' contained higher labile dCo measured values than total dCo values (labile dCo : total dCo > 1), which is likely the result of a storage or instrumental artifact.

Sample	Total dCo Analysis		Labile dCo Analysis		Labile dCo : Total dCo
	Dilution Factor	Total dCo [pM]	Dilution Factor	Labile dCo [pM]	
S1	1/11	302	n/a	76	0.25
S3	1/11	252	n/a	108	0.43
S5	1/11	494	n/a	170	0.34
S6	1/11	376	n/a	131	0.35
S7	1/11	1673	1/11	1198	0.72
E1	1/110	5832	1/110	10060*	> 1
E2	1/110	7182	1/110	7810*	> 1
E3	1/110	4030	1/110	3568	0.89
E4	1/22	3480	1/22	2197	0.63
E5	1/22	3921	1/22	2870	0.73
R1	1/11	688	1/11	1845*	> 1
R2	1/11	679	1/11	3943*	> 1
R3	1/11	520	1/11	471	0.91
R4	1/11	822	1/11	859*	> 1
R5	1/11	441	1/11	460*	> 1
G2	1/11	417	--	--	--
G3	1/11	371	n/a	101	0.27
G4	1/11	202	n/a	72	0.36

Table B3. Average total dCo and labile dCo concentrations from the 4 sample types collected from Kodiak Island and the Alaskan Coast. Labile dCo values that exceeded total dCo values were excluded from this analysis.

Sample Type	Average dCo [pM]	n	Average Labile dCo [pM]	n
Shelf	620 ± 600	5	340 ± 480	5
Estuary	4900 ± 1600	5	2900 ± 700	3
River	630 ± 150	5	--	
Groundwater	330 ± 110	3	86 ± 20	2

Appendix C. Protein sampling metadata

Table C1. Protein sampling information for the GP15 surface transect, which collected the 0.2–3 µm particulate fraction. Dates and times are reported in GMT (local time zone: GMT -10).

Station	Latitude	Longitude	DateTime Started	DateTime Ended	Liters Filtered
1	56.06	-156.96	09/26/2018 11:10	09/26/2018 12:24	14.6
3	55.08	-155.72	09/27/2018 22:34	09/28/2018 00:59	35
4	55.08	-155.72	09/29/2018 22:18	09/30/2018 00:41	42.4
5	53.68	-153.80	09/25/2018 05:32	09/25/2018 07:48	35.4
6	52.00	-152.00	10/2/2018 01:50	10/2/2018 04:34	38.9
8	47.00	-152.00	10/5/2018 22:10	10/6/2018 00:19	37.2
10	42.00	-152.00	10/8/2018 22:44	10/9/2018 00:36	39.7
12	37.00	-152.00	10/11/2018 23:33	10/12/2018 02:09	45.6
14	32.00	-152.00	10/14/2018 22:20	10/15/2018 01:12	38.7
15	29.50	-152.00	10/16/2018 00:32	10/16/2018 02:12	41.9
16	27.00	-152.00	10/17/2018 05:05	10/17/2018 07:59	44.5
18	22.00	-152.00	10/20/2018 04:56	10/20/2018 09:22	48.4
19	17.50	-152.00	10/28/2018 01:54	10/28/2018 03:42	48.4
21	11.00	-152.00	10/31/2018 05:44	10/31/2018 10:46	45.6
23	7.53	-152.02	11/3/2018 07:43	11/3/2018 10:47	45.8
25	5.02	-152.02	11/5/2018 12:34	11/5/2018 15:54	52.3
27	2.50	-152.01	11/7/2018 13:05	11/7/2018 17:15	58
29	0.00	-152.01	11/10/2018 03:53	11/10/2018 07:55	49.9
31	-2.50	-152.00	11/12/2018 05:14	11/12/2018 09:18	57.2
33	-5.00	-152.00	11/14/2018 08:42	11/14/2018 13:12	39
35	-10.50	-152.00	11/17/2018 08:48	11/17/2018 13:02	47.4
37	-15.00	-152.00	11/19/2018 20:28	11/20/2018 00:41	53.8
39	-19.99	-152.10	11/22/2018 23:31	11/23/2018 04:02	47.2

Appendix D. Upper ocean dCo and pCo sections of previously characterized transects

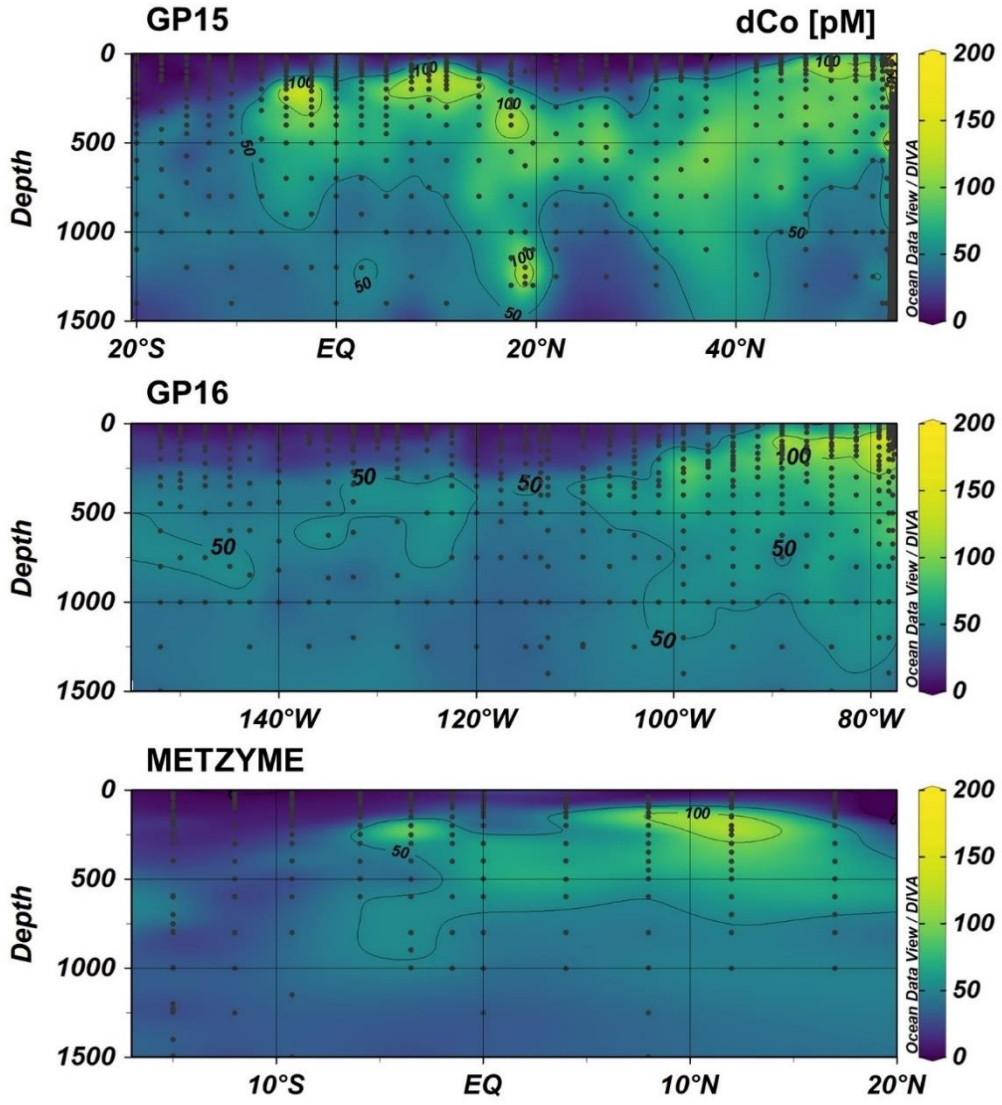

Figure D1. Upper and intermediate ocean (≤ 1500 m) transects of dissolved Co along the GP15, GP16 and METZYME expeditions. DIVA gridding was used to interpolate between data points. These dCo sections were originally published and characterized in Chmiel et al., (2022), Hawco et. al., (2016), and Hawco et. al., (2020), respectively.

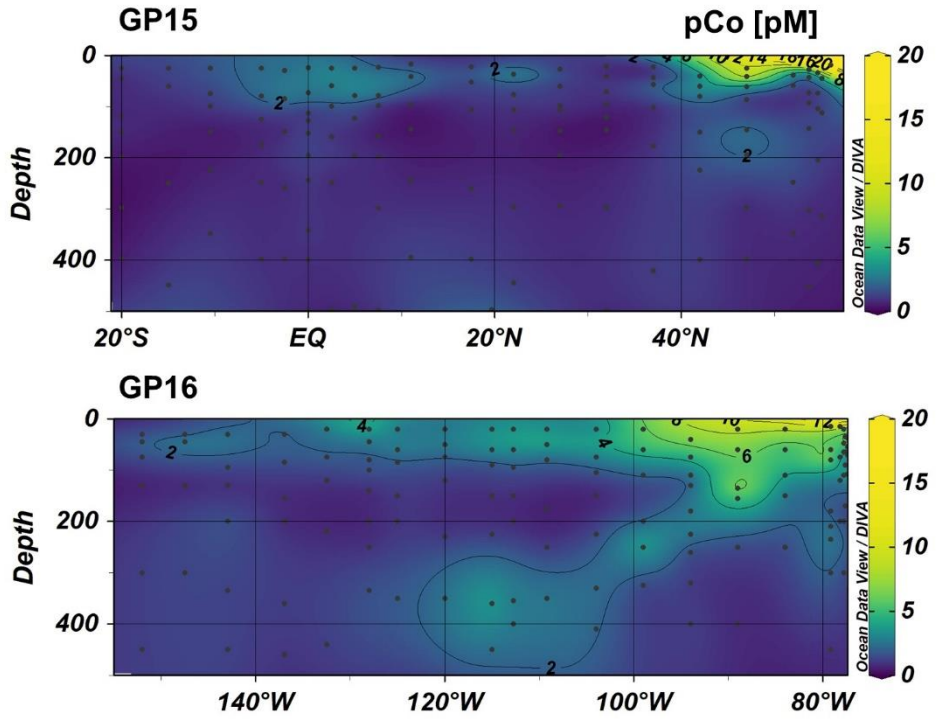

Figure D2. Upper ocean (≤ 500 m) transects of particulate Co along the GP15 and GP16 expeditions. DIVA gridding was used to interpolate between data points. These pCo sections were originally published and characterized in Chmiel et al., (2022), Hawco et. al., (2016), and Lam et. al., (2018).

Appendix E. Dissolved Co : PO_4^{3-} slope tables

Table E1. Dissolved Co : PO_4^{3-} regression statistics from the GP15 expedition. The depth threshold refers to the deepest sample depth included in the regression analysis that best maximizes the R^2 value of the dCo vs. dPO_4^{3-} correlation, and all sample depths above the depth threshold were included in the regression. Stations whose maximum R^2 values were below 0.7 are marked with an '*', and their associated dCo : dPO_4^{3-} slopes should not be interpreted as meaningful values.

Station	Latitude	Longitude	Depth Threshold [m]	dCo : dPO_4^{3-} Slope [µmol : mol]	R^2	n
1	56.1	-157.0	85	-430 ± 88	0.77	7
2	55.6	-156.3	150	-112 ± 70	0.34*	5
3	55.1	-155.7	500	49 ± 20	0.45*	7
4	54.7	-155.2	70	72 ± 41	0.30*	7
5	53.7	-153.8	90	55 ± 12	0.78	6
6	52.0	-152.0	90	42.2 ± 8.9	0.82	5
7	49.5	-152.0	70	108 ± 13	0.94	5
8	47.0	-152.0	90	173 ± 47	0.73	5
9	44.5	-152.0	90	110 ± 13	0.93	6
10	42.0	-152.0	100	117 ± 7.6	0.98	6
12	37.0	-152.0	250	80.8 ± 5.4	0.95	11
13	34.5	-152.0	125	138 ± 12	0.95	6
14	32.0	-152.0	300	88 ± 13	0.83	9
15	29.5	-152.0	900	23 ± 1.7	0.94	12
16	27.0	-152.0	300	96.6 ± 7.8	0.95	8
17	24.5	-152.0	300	66.4 ± 5.4	0.95	8
18	22.0	-152.0	600	32.9 ± 2.3	0.95	10
18.3	19.7	-154.5	1100	30.1 ± 9.6	0.66*	5
18.6	18.9	-155.3	1250	50 ± 21	0.44*	7
19	17.5	-152.0	400	50.8 ± 3.7	0.94	12
20	14.3	-152.0	180	52.3 ± 3.3	0.97	7
21	11.0	-152.0	200	40.5 ± 2.6	0.96	10
22	9.2	-152.0	120	55.8 ± 3	0.98	6
23	7.5	-152.0	160	60 ± 8	0.89	7
25	5.0	-152.0	250	55 ± 10	0.77	9
27	2.5	-152.0	160	62.8 ± 6.9	0.91	8
29	0.0	-152.0	115	209 ± 14	0.97	6
31	-2.5	-152.0	180	97.8 ± 6.4	0.97	8
33	-5.0	-152.0	125	279 ± 12	0.99	6
34	-7.5	-152.0	320	32.9 ± 2.3	0.96	9
35	-10.5	-152.0	300	31.5 ± 4.3	0.85	9
36	-12.8	-152.0	650	17.7 ± 1.6	0.92	11
37	-15.0	-152.0	350	46.9 ± 3.9	0.93	11
38	-17.5	-152.0	800	27.8 ± 3.5	0.84	12
39	-20.0	-152.0	700	27.7 ± 3.4	0.81	16

Table E2. Dissolved Co : PO_4^{3-} regression statistics from the ProteOMZ expedition. The depth threshold refers to the deepest sample depth included in the regression analysis that best maximizes the R^2 value of the dCo vs. dPO_4^{3-} correlation, and all sample depths above the depth threshold were included in the regression. Stations whose maximum R^2 values were below 0.7 are marked with an '*', and their associated dCo : dPO_4^{3-} slopes should not be interpreted as meaningful values.

Station	Latitude	Longitude	Depth Threshold [m]	dCo : dPO_4^{3-} Slope [µmol : mol]	R^2	n
1	17.0	-155.5	249	34.1 ± 1.4	0.99	6
4	10.0	-156.0	124	38.5 ± 1.8	0.99	5
5	8.0	-156.0	124	43.9 ± 0.3	1.00	5
7	10.0	-145.0	155	34.8 ± 8	0.76	6
8	10.0	-140.0	120	37.5 ± 2.5	0.98	5
9	9.0	-140.0	150	34.7 ± 3	0.96	5
10	8.0	-140.0	150	44.2 ± 9.8	0.80	5
11	4.0	-140.0	598	36.2 ± 7.2	0.66*	13
12	0.0	-139.8	140	56.5 ± 6.8	0.92	6
13	-4.2	-142.2	200	70.8 ± 4.5	0.98	5
14	-10.6	-146.3	299	26.4 ± 3.2	0.91	7

Table E3. Dissolved Co : PO_4^{3-} regression statistics from the GP16 expedition. The depth threshold refers to the deepest sample depth included in the regression analysis that best maximizes the R^2 value of the dCo vs. dPO_4^{3-} correlation, and all sample depths above the depth threshold were included in the regression. Stations whose maximum R^2 values were below 0.7 are marked with an '*', and their associated dCo : dPO_4^{3-} slopes should not be interpreted as meaningful values.

Station	Latitude	Longitude	Depth Threshold [m]	dCo : dPO_4^{3-} Slope [µmol : mol]	R^2	n
1	-12.0	-79.2	79.9	70.3 ± 2.8	0.99	6
2	-12.0	-77.4	69.9	64 ± 3.4	0.99	5
3	-12.0	-77.7	50.4	54.3 ± 3.2	0.98	5
4	-12.0	-77.8	111	74 ± 32	0.52*	5
5	-12.0	-78.2	75.6	68 ± 13	0.84	5
6	-12.0	-81.5	95.1	54.7 ± 6.6	0.93	5
7	-12.0	-84.0	80.2	103.6 ± 7.7	0.97	5
8	-12.0	-86.5	161.2	35.3 ± 5.9	0.85	6
9	-12.0	-89.0	100.4	59 ± 14	0.79	5
10	-12.0	-91.5	300.6	23.4 ± 5.7	0.67*	8
11	-12.0	-94.0	319.9	27.9 ± 5.8	0.64*	13
12	-13.0	-96.5	300.9	22.6 ± 3.3	0.84	9
13	-14.0	-99.0	399.7	28.4 ± 2.8	0.90	11
14	-15.0	-101.5	124.5	143 ± 14	0.95	5
15	-16.0	-104.0	150.2	175 ± 12	0.97	6
16	-15.4	-106.5	399.7	22 ± 2	0.93	10
17	-15.0	-109.2	385.7	19.6 ± 1.1	0.97	10
18	-15.0	-112.8	354.6	19.8 ± 2.2	0.91	8
20	-15.0	-113.5	499.9	19.1 ± 1.9	0.91	11
21	-14.8	-115.0	361.3	20.7 ± 1.1	0.98	9
22	-14.4	-117.5	750.3	17.5 ± 2.3	0.83	12
23	-14.0	-120.0	351.7	18.2 ± 0.7	0.98	10
24	-13.3	-122.5	500.9	25 ± 4.4	0.75	11
25	-12.5	-125.0	150.3	95.9 ± 8.2	0.95	7
26	-11.7	-128.0	1501.8	17.7 ± 2.3	0.81	14
27	-11.7	-130.0	100.4	-103 ± 29	0.72	5
28	-11.6	-132.5	440.2	23.9 ± 1.7	0.95	11
29	-11.6	-135.0	625.4	19.1 ± 1.6	0.93	11
30	-11.6	-137.0	1249.7	11.7 ± 0.8	0.98	6
31	-11.3	-140.0	440.7	18.4 ± 0.8	0.98	10
32	-11.0	-143.0	199.8	102 ± 22	0.82	5
33	-10.9	-145.0	300.9	24.3 ± 1.5	0.97	8
34	-10.8	-147.5	150.9	54.3 ± 4.3	0.96	6
35	-10.2	-150.0	750.6	22.4 ± 1.2	0.97	12
36	-10.5	-152.0	800.4	17.7 ± 1.3	0.94	12

Table E4. Dissolved Co : PO_4^{3-} regression statistics from the METZYME expedition. The depth threshold refers to the deepest sample depth included in the regression analysis that best maximizes the R^2 value of the dCo vs. dPO_4^{3-} correlation, and all sample depths above the depth threshold were included in the regression.

Station	Latitude	Longitude	Depth Threshold [m]	dCo : dPO_4^{3-} Slope [µmol : mol]	R^2	n
1	17.0	-154.4	600	25 ± 3.5	0.82	11
2	12.0	-155.5	225	48 ± 2.7	0.97	9
3	8.0	-156.0	150	45.1 ± 3.8	0.97	5
4	4.0	-157.1	150	46.1 ± 5.2	0.93	6
5	0.0	-158.0	499	33.7 ± 4.8	0.82	11
5.5	-1.5	-159.2	150	49.2 ± 9.7	0.84	5
6	-3.5	-160.8	199	71.9 ± 1	1.00	7
7	-6.0	-162.6	249	45.2 ± 2.9	0.97	8
8	-9.3	-165.4	249	28.8 ± 2.2	0.95	9
9	-12.0	-167.6	499	16.4 ± 0.9	0.98	9
10	-15.0	-170.0	595	18.7 ± 1.7	0.95	7
11	-15.0	-171.5	750	18.7 ± 1.2	0.97	8
12	-15.0	-173.1	700	21.2 ± 2.1	0.93	8
13	-15.0	-174.5	399	7.9 ± 2.1	0.75	5

Appendix F. Dissolved Co : PO_4^{3-} ratio tables

Table F1. Dissolved Co : PO_4^{3-} ratio statistics in the surface ocean (≤ 20 m depth) and upper ocean (≤ 500 m depth) from the GP15 expedition. When more than one sample was take from the surface ocean, the sample closer to 20 m depth was selected.

Station	Latitude	Longitude	Surface dCo : dPO_4^{3-} [µmol : mol]	dCo : dPO_4^{3-} Range [µmol : mol]	dCo : dPO_4^{3-} Mean [µmol : mol]	n
1	56.1	-157.0	825	148 - 1279	490 ± 410	7
2	55.6	-156.3	487	53 - 487	140 ± 140	8
3	55.1	-155.7	41	29 - 86	48 ± 20	7
4	54.7	-155.2	79	18 - 127	52 ± 35	14
5	53.7	-153.8	70	23 - 100	59 ± 27	10
6	52.0	-152.0	86	24 - 87	57 ± 27	9
7	49.5	-152.0	69	30 - 83	61 ± 22	9
8	47.0	-152.0	17	17 - 110	52 ± 27	11
9	44.5	-152.0	66	33 - 90	58 ± 17	11
10	42.0	-152.0	23	23 - 94	61 ± 23	10
12	37.0	-152.0	0	0 - 171	67 ± 43	14
13	34.5	-152.0	137	19 - 673	140 ± 190	10
14	32.0	-152.0	--	29 - 862	210 ± 280	9
15	29.5	-152.0	--	40 - 440	160 ± 160	5
16	27.0	-152.0	--	64 - 241	108 ± 66	6
17	24.5	-152.0	0	0 - 442	100 ± 140	8
18	22.0	-152.0	5	0 - 707	140 ± 220	9
18.3	19.7	-154.5	--	29 - 636	190 ± 300	4
18.6	18.9	-155.3	--	534 - 534	533.8 ± 0	1
19	17.5	-152.0	22	22 - 1127	250 ± 320	12
20	14.3	-152.0	28	25 - 202	84 ± 65	10
21	11.0	-152.0	132	23 - 132	63 ± 38	13
22	9.2	-152.0	0	0 - 77	37 ± 24	11
23	7.5	-152.0	1647	17 - 1647	310 ± 530	9
25	5.0	-152.0	156	0 - 203	77 ± 75	14
27	2.5	-152.0	18	18 - 128	56 ± 35	15
29	0.0	-152.0	51	28 - 94	52 ± 18	15
31	-2.5	-152.0	14	14 - 82	44 ± 19	15
33	-5.0	-152.0	5	5 - 80	47 ± 23	15
34	-7.5	-152.0	22	12 - 45	29 ± 11	10
35	-10.5	-152.0	0	0 - 56	27 ± 19	11
36	-12.8	-152.0	0	0 - 85	29 ± 25	10
37	-15.0	-152.0	30	0 - 60	28 ± 17	14
38	-17.5	-152.0	0	0 - 50	15 ± 18	10
39	-20.0	-152.0	0	0 - 586	70 ± 150	14

Table F2. Dissolve Co : PO_4^{3-} ratio statistics in the surface ocean (≤ 20 m depth) and upper ocean (≤ 500 m depth) from the ProteOMZ expedition. When more than one sample was take from the surface ocean, the sample closer to 20 m depth was selected.

Station	Latitude	Longitude	Surface dCo : dPO_4^{3-} [µmol : mol]	dCo : dPO_4^{3-} Range [µmol : mol]	dCo : dPO_4^{3-} Mean [µmol : mol]	n
1	17.0	-155.5	51	20 - 72	45 ± 16	7
4	10.0	-156.0	83	17 - 105	42 ± 31	9
5	8.0	-156.0	48	17 - 48	34 ± 11	10
7	10.0	-145.0	63	18 - 302	62 ± 85	10
8	10.0	-140.0	66	26 - 66	37 ± 13	9
9	9.0	-140.0	107	20 - 107	42 ± 26	9
10	8.0	-140.0	70	23 - 75	42 ± 20	8
11	4.0	-140.0	226	18 - 226	60 ± 59	11
12	0.0	-139.8	80	21 - 80	48 ± 18	12
13	-4.2	-142.2	0	0 - 60	30 ± 19	9
14	-10.6	-146.3	27	14 - 42	24.4 ± 8.7	9

Table F3. Dissolve Co : PO_4^{3-} ratio statistics in the surface ocean (≤ 20 m depth) and upper ocean (≤ 500 m depth) from the GP16 expedition. When more than one sample was take from the surface ocean, the sample closer to 20 m depth was selected.

Station	Latitude	Longitude	Surface dCo : dPO_4^{3-} [µmol : mol]	dCo : dPO_4^{3-} Range [µmol : mol]	dCo : dPO_4^{3-} Mean [µmol : mol]	n
1	-12.0	-79.2	69	27 - 76	53 ± 18	15
2	-12.0	-77.4	43	35 - 52	45.9 ± 5.8	7
3	-12.0	-77.7	56	45 - 67	57.4 ± 6	9
4	-12.0	-77.8	52	28 - 79	48 ± 14	9
5	-12.0	-78.2	55	28 - 71	49 ± 12	11
6	-12.0	-81.5	53	28 - 65	46 ± 13	10
7	-12.0	-84.0	61	20 - 74	43 ± 16	16
8	-12.0	-86.5	47	22 - 64	40 ± 12	10
9	-12.0	-89.0	57	22 - 79	40 ± 16	16
10	-12.0	-91.5	52	24 - 77	40 ± 17	9
11	-12.0	-94.0	31	23 - 79	38 ± 17	16
12	-13.0	-96.5	40	21 - 90	39 ± 21	11
13	-14.0	-99.0	49	32 - 85	52 ± 20	11
14	-15.0	-101.5	39	19 - 67	35 ± 17	11
15	-16.0	-104.0	51	21 - 75	44 ± 18	12
16	-15.4	-106.5	25	21 - 55	35 ± 13	10
17	-15.0	-109.2	28	15 - 42	23.3 ± 8.2	11
18	-15.0	-112.8	14	14 - 40	27 ± 11	9
20	-15.0	-113.5	19	12 - 78	35 ± 23	11
21	-14.8	-115.0	28	12 - 31	23.3 ± 6.4	10
22	-14.4	-117.5	11	11 - 61	32 ± 19	10
23	-14.0	-120.0	17	6 - 24	17.6 ± 4.9	10
24	-13.3	-122.5	21	4 - 90	45 ± 29	10
25	-12.5	-125.0	18	14 - 49	24 ± 12	8
26	-11.7	-128.0	10	0 - 63	31 ± 21	9
27	-11.7	-130.0	6	6 - 47	23 ± 15	6
28	-11.6	-132.5	25	8 - 43	27.6 ± 9.4	11
29	-11.6	-135.0	23	19 - 44	27.6 ± 8.3	10
30	-11.6	-137.0	31	31 - 40	36.6 ± 3.8	4
31	-11.3	-140.0	19	15 - 30	21.3 ± 4.5	10
32	-11.0	-142.9	17	11 - 63	34 ± 23	7
33	-10.9	-145.0	14	4 - 26	18.4 ± 7.4	10
34	-10.8	-147.5	20	19 - 42	32 ± 9.1	9
35	-10.2	-150.0	20	7 - 31	20.2 ± 7.9	11
36	-10.5	-152.0	22	14 - 61	35 ± 17	10

Table F4. Dissolve Co : PO_4^{3-} ratio statistics in the surface ocean (≤ 20 m depth) and upper ocean (≤ 500 m depth) from the METZYME expedition. When more than one sample was take from the surface ocean, the sample closer to 20 m depth was selected.

Station	Latitude	Longitude	Surface dCo : dPO_4^{3-} [µmol : mol]	dCo : dPO_4^{3-} Range [µmol : mol]	dCo : dPO_4^{3-} Mean [µmol : mol]	n
1	17.0	-154.4	18	18 - 115	48 ± 30	10
2	12.0	-155.4	26	26 - 76	45 ± 15	15
3	8.0	-156.0	--	21 - 62	33 ± 13	12
4	4.0	-157.1	--	17 - 49	33 ± 10	10
5	0.0	-158.0	40	17 - 40	29.8 ± 7.3	11
5.5	-1.5	-159.2	16	14 - 42	25.6 ± 9	9
6	-3.5	-160.8	10	10 - 56	26 ± 16	11
7	-6.0	-162.6	8	5 - 32	17.8 ± 8.1	11
8	-9.3	-165.4	3	0 - 22	12.6 ± 7.5	12
9	-12.0	-167.6	0	0 - 17	10.7 ± 6	9
10	-15.0	-170.0	18	13 - 36	20.4 ± 8.5	6
11	-15.0	-171.5	5	5 - 15	10.4 ± 4.5	6
12	-15.0	-173.1	5	5 - 38	22 ± 10	7
13	-15.0	-174.5	6	6 - 25	12.4 ± 8.6	5

Appendix G. Particulate Co : P ratio tables

Table G1. Particulate Co : P ratio statistics in the surface ocean (20–50 m depth) and upper ocean (≤ 500 m depth) from the GP15 expedition. When more than one sample was take from the surface ocean, the sample closer to 50 m depth was selected.

Station	Latitude	Longitude	Surface dCo : dPO_4 [µmol : mol]	dCo : dPO_4 Range [µmol : mol]	dCo : dPO_4 Mean [µmol : mol]	n
1	56.1	-157.0	1807	201 - 2706	1800 ± 1100	4
3	55.1	-155.7	114	114 - 232	178 ± 59	3
4	54.7	-155.2	85	85 - 237	154 ± 62	5
5	53.7	-153.8	89	81 - 299	161 ± 77	7
6	52.0	-152.0	70	70 - 7867	1800 ± 3400	5
8	47.0	-152.0	144	115 - 435	230 ± 120	8
10	42.0	-152.0	165	119 - 488	270 ± 150	6
12	37.0	-152.0	100	76 - 670	240 ± 230	6
14	32.0	-152.0	96	89 - 737	240 ± 260	8
16	27.0	-152.0	102	98 - 448	190 ± 130	7
18	22.0	-152.0	271	156 - 1200	440 ± 410	6
19	17.5	-152.0	130	130 - 1218	440 ± 460	5
21	11.0	-152.0	171	70 - 1193	370 ± 420	6
23	7.5	-152.0	272	143 - 1159	460 ± 370	7
25	5.0	-152.0	290	197 - 715	380 ± 220	5
27	2.5	-152.0	219	195 - 574	300 ± 160	6
29	0.0	-152.0	109	109 - 635	370 ± 190	10
31	-2.5	-152.0	182	148 - 695	330 ± 230	5
33	-5.0	-152.0	175	175 - 814	360 ± 260	6
35	-10.5	-152.0	107	98 - 839	260 ± 290	6
37	-15.0	-152.0	137	137 - 1307	460 ± 570	4
39	-20.0	-152.0	127	122 - 321	167 ± 71	7

Table G2. Particulate Co : P ratio statistics in the surface ocean (20–50 m depth) and upper ocean (≤ 500 m depth) from the GP16 expedition. When more than one sample was take from the surface ocean, the sample closer to 50 m depth was selected.

Station	Latitude	Longitude	Surface dCo : dPO_4 [µmol : mol]	dCo : dPO_4 Range [µmol : mol]	dCo : dPO_4 Mean [µmol : mol]	n
1	-12.0	-79.2	NaN	81 - 248	170 ± 51	8
2	-12.0	-77.4	229	112 - 229	162 ± 56	4
3	-12.0	-77.7	77	77 - 250	143 ± 79	4
4	-12.0	-77.8	172	98 - 210	175 ± 36	7
5	-12.0	-78.2	NaN	119 - 223	172 ± 45	4
7	-12.0	-84.0	286	206 - 357	281 ± 52	6
9	-12.0	-89.0	226	226 - 581	380 ± 140	6
11	-12.0	-94.0	264	264 - 701	440 ± 140	9
13	-14.0	-99.0	292	235 - 850	440 ± 250	6
15	-16.0	-104.0	205	187 - 1427	580 ± 520	7
17	-15.0	-109.2	164	157 - 1525	580 ± 600	7
18	-15.0	-112.8	134	124 - 1104	440 ± 450	7
21	-14.8	-115.0	169	153 - 1844	670 ± 760	7
23	-14.0	-120.0	184	156 - 1879	620 ± 690	7
25	-12.5	-125.0	148	138 - 1241	490 ± 450	7
26	-11.7	-128.0	121	101 - 1052	290 ± 300	9
28	-11.6	-132.5	143	143 - 1055	380 ± 390	5
30	-11.6	-137.0	115	115 - 1068	490 ± 440	6
32	-11.0	-142.9	138	138 - 882	430 ± 320	6
34	-10.8	-147.5	234	136 - 719	320 ± 270	4
36	-10.5	-152.0	88	84 - 865	310 ± 350	6

Table G3. Particulate Co : P ratio statistics in the surface ocean (20–50 m depth) and upper ocean (≤ 500 m depth) from the METZYME expedition. When more than one sample was take from the surface ocean, the sample closer to 50 m depth was selected.

Station	Latitude	Longitude	Surface dCo : dPO_4 [µmol : mol]	dCo : dPO_4 Range [µmol : mol]	dCo : dPO_4 Mean [µmol : mol]	n
1	17.0	-154.4	142	8 - 142	86 ± 41	11
2	12.0	-155.4	102	-15 - 643	140 ± 160	15
3	8.0	-156.0	NaN	75 - 178	137 ± 38	5
4	4.0	-157.1	158	-188 - 204	50 ± 130	10
5	0.0	-158.0	130	32 - 136	96 ± 32	11
6	-3.5	-160.8	132	11 - 183	99 ± 54	9
7	-6.0	-162.6	109	16 - 156	94 ± 41	11
8	-9.3	-165.4	68	-11 - 171	77 ± 43	12
9	-12.0	-167.6	86	21 - 368	113 ± 99	9
10	-15.0	-170.0	99	56 - 113	88 ± 21	6
11	-15.0	-171.5	134	58 - 139	103 ± 35	6
12	-15.0	-173.1	122	3 - 125	86 ± 44	7

Appendix H. Estimating trace metal uptake and maximum rate of dissolution profiles from classic competitive inhibition equations.

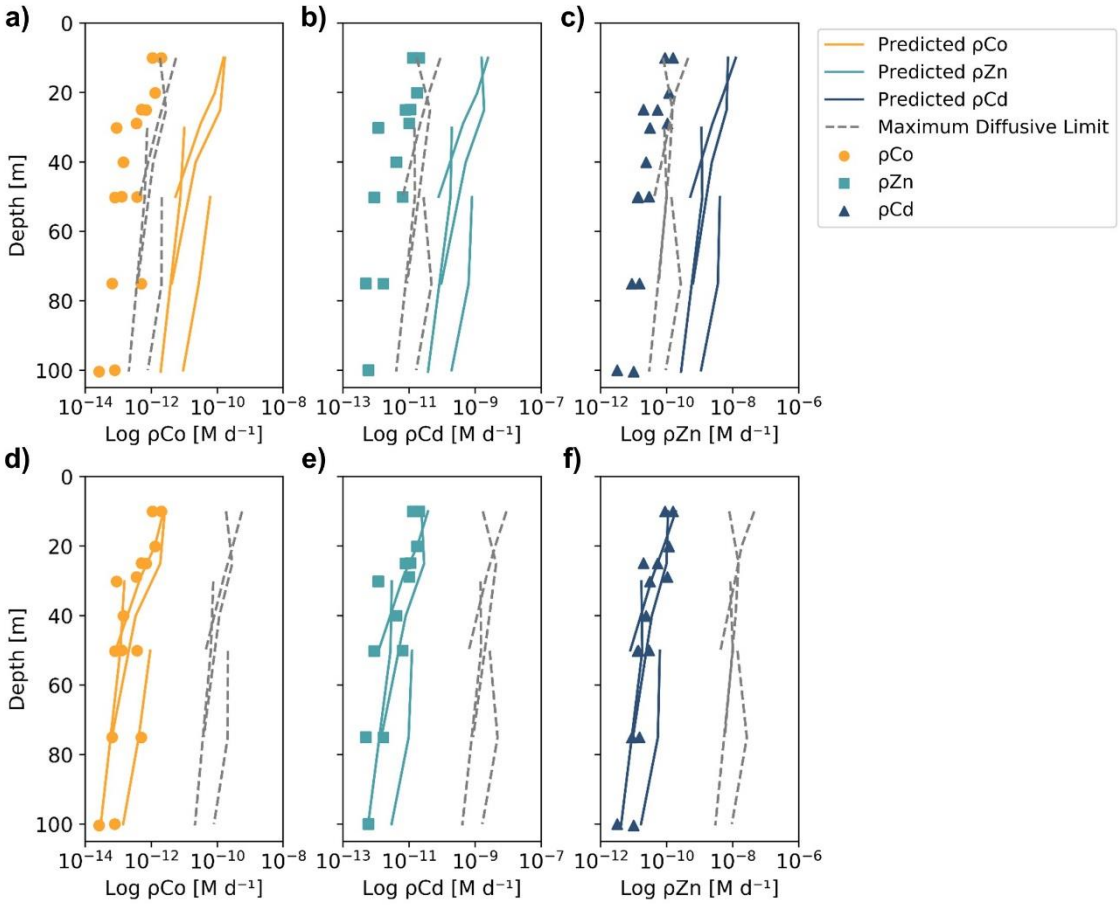

Figure H1. Observed (markers) and predicted (solid lines) trace metal uptake rate (ρM) profiles and the estimated maximum diffusive limit profiles (dashed line) for Co (a,d) Cd (b,e) and Zn (c,f) from Stations 11, 20, 22 and 57, using different equation parameters than those used in Fig. 10. In panels a-c, the predicted uptake rates used a literature V_{max} value of 626 µmol (mol C^{-1}) d^{-1} determined from Zn^{2+} uptake experiments in *Emiliania huxleyi* cultures (Sunda and Huntsman 1992), resulting in predicted uptake rates that were orders of magnitude greater than the observed values. In panels d-e, the estimated maximum diffusive limit profiles assumed that 100% of the dCo, dCd and dZn inventories were labile and 0% were bound to strong organic ligands, resulting in diffusive limits that were also orders of magnitude greater than the observed values. This analysis helps to show how parameter assumptions can greatly influence the predicted uptake rates and illustrates the difficulty of assigning kinetic parameters to environmental analyses.

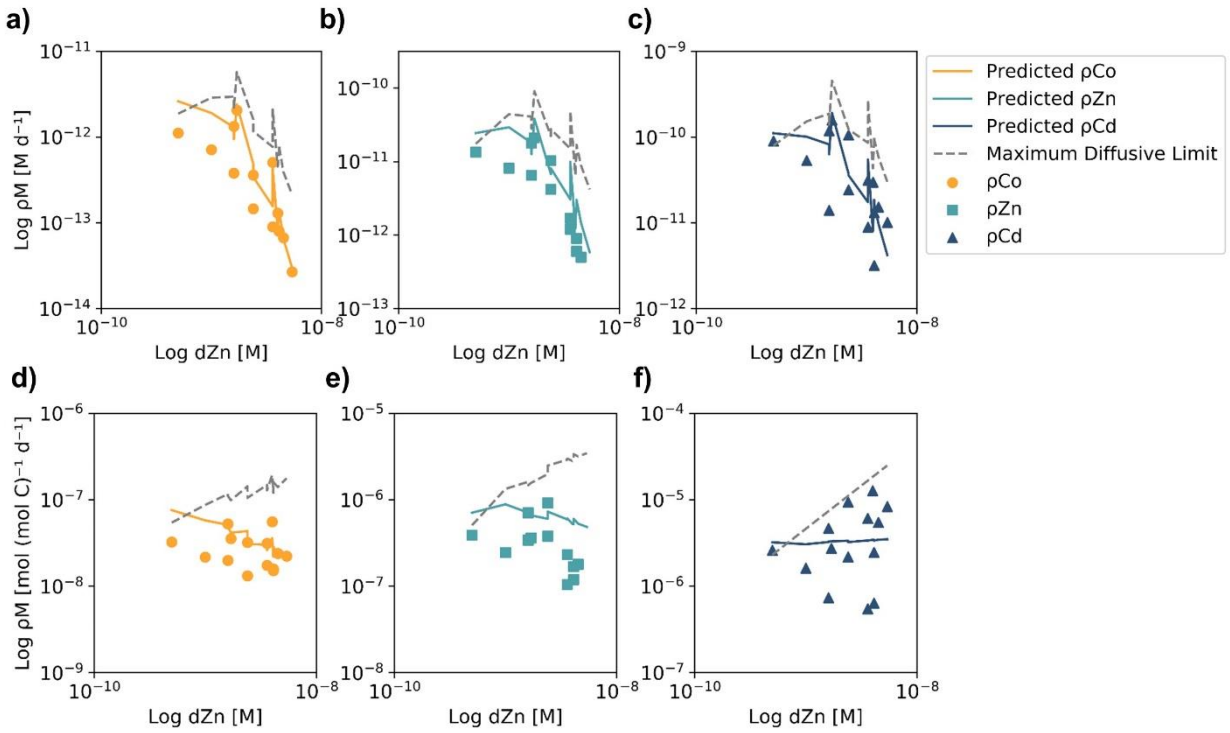

Figure H2. Observed (markers) and predicted (solid lines) trace metal uptake rates (ρM) and the estimated maximum diffusive limit profiles (dashed line) plotted against total dZn concentrations, assuming a V_{max} of 4 µmol (mol C^{-1}) d^{-1} and that 99% of the trace metal inventory was bound to strong organic ligands. Panels a-c show ρM in units of M d^{-1}, which tended to decrease at high dZn concentrations. This is attributable to higher dZn concentrations below the photic zone, where much lower rates of micronutrient uptake occur. Panels d-f show ρM when normalized to biomass using Chl-a concentrations and a C : chl-a ratio of 130 w/w (DiTullio and Smith 1996). The normalized predicted ρZn values are relatively stable over the observed range of dZn concentrations, while the predicted ρCo and ρCd values decrease slightly as dZn increases, suggesting that competitive inhibition of ρCo and ρCd may have occurred at higher dZn concentrations due to the smaller inventories of dCo and dCd compared to dZn.

Appendix I. Description of a two-box model of the dCo cycle in coastal Antarctic seas, and a potential mechanism for deep dCo loss with changing microbial uptake stoichiometry.

The two-box model described below was used to conceptualize the biogeochemical cycling of dCo in the surface and deep ocean. The model describes a 1 m^2 column of water with a total depth of 600 m and a depth threshold between the surface and deep box of 100 m. Within each box, the net change of dCo over time is equivalent to the sum of the source fluxes minus the sum of the sink fluxes:

$$\left(\frac{d[dCo]}{dt}\right)_{Surface} = \frac{\sum(F_i)_{Sources} - \sum(F_i)_{Sinks}}{V_{Surface}}$$

$$\left(\frac{d[dCo]}{dt}\right)_{Deep} = \frac{\sum(F_i)_{Sources} - \sum(F_i)_{Sinks}}{V_{Deep}}$$

where fluxes (F_i) are in units of mols dCo d^{-1}. A summary of the sources and sinks relevant to dCo in coastal Antarctic seas is shown below in Table I1. In the Southern Ocean, we would expect the fluxes of scavenging (F_{Scav}) and aerosol deposition (F_{Aero}) would be relatively negligible, and so these fluxes have been omitted from the model. Additionally, we can assume that horizontal advection is at steady state, and thus the net advection flux is ≈ 0 mols dCo d^{-1}. This gives us the net equations for both boxes:

$$\left(\frac{d[dCo]}{dt}\right)_{Surface} = \frac{F_{Over} + F_{Remin} - F_{Up}}{V_{Surface}}$$

$$\left(\frac{d[dCo]}{dt}\right)_{Deep} = \frac{F_{Remin} + F_{Neph} - F_{Up} - F_{Over}}{V_{Deep}}$$

Table I1: The source and sink fluxes of dCo in the surface and deep ocean boxes. Fluxes are theoretically in units of mols dCo d^{-1}.

Surface Sources		Surface Sinks		Deep Sources		Deep Sinks	
Remineralization	F_{Remin}	Microbial Uptake	F_{Up}	Remineralization	F_{Remin}	Microbial Uptake	F_{Up}
Overturning	F_{Over}	Advection	F_{Adv}	Nepheloid Layer	F_{Neph}	Overturning	F_{Over}
Aerosols	F_{Aero}			Advection	F_{Adv}	Scavenging	F_{Scav}
Advection	F_{Adv}					Advection	F_{Adv}

Uptake fluxes

The flux of dCo incorporation into microbial biomass via uptake by protein transporters can be described using the uptake rates (ρCo) measured by ^{57}Co incubation experiments, where units of pCo are in mols dCo L^{-1} d^{-1}:

$$F_{Up,Surface} = (\rho Co_{Surface} * V_{Surface})$$

$$F_{Up,Deep} = (\rho Co_{Deep} * V_{Deep})$$

Remineralization fluxes

In this model, the remineralization flux of particulate Co in organic matter to dCo is quantified by a Remineralization Factor (RF), which can be applied to the amount of particulate matter present in each box. Typical RF values tend to be between 0.90 and 0.99 (Glover et al. 2011), meaning that between 90% and 99% of all microbial biomass produced tends to be remineralized before sinking out of its respective box. It is not clear that the RFs for the surface and deep box should be represented by the same value, and so we have defined both surface ($RF_{Surface}$) and deep (RF_{deep}) variables here. In the surface ocean, excess Co in un-remineralized biomass will sink into the deep box (F_{Sink}), where it is further able to be remineralized in the deep ocean. In the deep ocean, excess Co in un-remineralized biomass is assumed to flux into the sediments via burial (F_{Bur}), representing a key sink of dCo biomass out of the two-box system. The surface box remineralization flus is represented with a relatively simple equation:

$$F_{Remin,Surface} = RF_{Surface} * F_{Up,Surface}$$

$$F_{Remin,Surface} = RF_{Surface}(\rho Co_{Surface} * V_{Surface})$$

The deep ocean remineralization flux can then be calculated as the sum of the remineralization flux from excess biomass that sinks as particulate Co and biomass generated in the deep ocean:

$$F_{Remin,Deep} = RF_{Deep}\left(F_{Up,\,Surface} - F_{Remin,Surface}\right) + RF_{Deep}(F_{Up,\,Deep})$$

$$F_{Remin,Deep} = RF_{Deep}(\rho Co_{Surface} * V_{Surface} - RF_{Surface}\left(\rho Co_{Surface} * V_{Surface}\right)) + RF_{Deep}\left(\rho Co_{Deep} * V_{Deep}\right)$$

Overturning fluxes

An overturning dCo flux represents the flux of a volume of water from the deep ocean box into the shallow ocean box, and a corresponding flux of the same volume from the shallow ocean box into the deep ocean box for mass conservation. In a dynamic coastal upwelling system like the Ross and Amundsen Seas, the reality of this overturning flux is almost certainly much more complicated, as coastal upwelling processes overlap with meltwater processes and deep water mass formation processes. For the purposes of this two-box model, the flux of dCo via overturning can be estimated as a function of the overturning water flux (F_{Water}) and the dCo concentrations of each box:

$$F_{Over,Surface} = (F_{Water}[dCo]_{Deep} - F_{Water}[dCo]_{Surface})$$

$$F_{Over,Deep} = (F_{Water}[dCo]_{Surface} - F_{Water}[dCo]_{Deep})$$

In the model presented in Sect. 4.5.6, the F_{Water} and both F_{Over} fluxes are assumed to be negligible for the sake of modeling simplicity, but the introduction of a nonzero overturning flux would help to make the seasonal change in the dCo inventory in both the surface and deep oceans nonlinear, as it is currently the only flux in this model that is calculated using the time step's dCo concentrations.

Flux from the nepheloid layer

At several CICLOPS stations, a distinct nepheloid layer was detected as dCo concentration increased sharply at depths immediately above (~10 m) the ocean floor. The nepheloid layer tends to contain high levels of particles moving horizontally along the seafloor, and is likely a significant source of dCo to the surrounding water column. The source of dCo from the nepheloid layer is somewhat unclear; it could be via dissolution of particles suspended within the nepheloid layer or from a porewater flux of dCo out of the sediments. In this model, the flux of deep dCo inputs into the deep ocean, assumed to be from the nepheloid layer, was derived using the Microsoft Excel solver tool, given the parameter that that 10 pM of deep dCo was lost over 12 years. The deep source of dCo was calculated to be 3550 pmol dCo m^{-2} d^{-1}. This value should be considered an adjustable parameter used to tune the model to our conceptual understanding of dCo inventory loss, and not a meaningful calculation of observed Co flux from the deep nepheloid layer, which has yet to be constrained.

The cobalt burial sink

The loss of cobalt from the deep ocean box into the sediments via burial can be quantified with the equation:

$$\left(\frac{d[Co]}{dt}\right)_{Bur} = F_{Sink} + F_{Up,Deep} - F_{Remin,Deep}$$

where F_{Sink} is described by:

$$F_{Sink} = (\rho Co_{Surface} * V_{Surface}) - RF_{Surface}(\rho Co_{Surface} * V_{Surface})$$

This estimate of the loss of dCo due to burial assumes that all biogenic particulate Co that is not remineralized in the surface ocean sinks into the deep ocean, and that all biogenic particulate Co that is not remineralized in the deep ocean is sequestered in sediments and "lost" to the model.

Modeling seasonality: the winter mixed layer

In the Ross and Amundsen Seas, sea ice covers the surface ocean for a larger portion of the year (~ 5 months). During this time, the water column mixes – a process that was modeled by combining the two-box model into one homogenized box after the 7-month bloom season to simulate the winter season. This process can be modeled by a volume-weighted average with the volume of each box.

$$[dCo]_{Winter} = \frac{(V_{Surface} * [dCo]_{Surface}) + (V_{Deep} * [dCo]_{Deep})}{(V_{Surface} + V_{Deep})}$$

Appendix J: Estimating the inventories and fluxes of cobalt in Earth systems

The Lithosphere

The lithosphere consists of the continental crust, oceanic crust and upper mantle; however, this calculation will only quantify the inventory of cobalt in the Earth's crust since the cobalt in the upper mantle is not relevant with respect to the anthroposphere. The inventory of cobalt (Co) in the continental and oceanic lithosphere was estimated by multiplying the volume, density and average cobalt concentration of both the continental crust and oceanic crust (Table J1):

$$I_{Litho} = I_c + I_o$$
$$I_{Litho} = V_c[Co]_c\rho_c + V_o[Co]_o\rho_o$$

Table J1. Parameters used to calculate the Co inventory of the lithosphere.

Parameter	Parameter Description	Value	Reference
	Volume of the crust		
V_c	Continental crust	7,581 x 10^6 km^3	Schubert and Sandwell (1989)
V_o	Oceanic crust	369 x 10^6 km^3	Schubert and Sandwell (1989)
	Density of the crust		
ρ_c	Continental crust	2830 kg m^{-3}	Christensen and Mooney (1995)
ρ_o	Oceanic crust	2890 kg m^{-3}	Carlson and Raskin (1984)
	Co concentration		
$[Co]_c$	In bulk continental crust	25 mg kg^{-1}	Reimann and de Caritat (1998)
$[Co]_o$	In oceanic crust (gabbro and basalt)	45 mg kg^{-1}	Reimann and de Caritat (1998)
	Calculated Co inventory		
I_c	Continetal crust	9.1 x 10^{18} mol	
I_o	Oceanic crust	8.1 x 10^{17} mol	
I_{Litho}	**Total**	**9.9 x 10^{18} mol**	

The flux of Co through the lithosphere was estimated via oceanic crust subduction (net sink) and crustal growth of both the continental and oceanic crust (net source). The estimate of the Co subduction flux was calculated by multiplying the rate of crustal subduction of both the oceanic crust and the marine sediments above the crust by their average Co concentrations:

$$F_{sub\ Co} = F_{sub\ Co,o} + F_{sub\ Co,s}$$

$$F_{sub\ Co} = F_{sub,o}[Co]_o + F_{sub,s}[Co]_s$$

and the estimate of the Co flux into the lithosphere via crustal growth was calculated by multiplying the rate of crustal growth of the oceanic and continental crust by their respective densities and Co concentrations (Table J2):

$$F_{growth\ Co} = F_{growth\ Co,c} + F_{growth\ Co,o}$$
$$F_{growth\ Co} = F_{growth,c}[Co]_c\rho_c + F_{growth,0}[Co]_o\rho_o$$

Table J2. Parameters used to calculate the annual flux of Co from the lithosphere via oceanic subduction and into the lithosphere via crustal growth.

Parameter	Parameter Description	Value	Reference
	Subduction rate of the oceanic crust		
$F_{sub,\ o}$	Oceanic crust	7 x 10^{16} g yr^{-1}	Staudacher and Allegre (1988)
$F_{sub,\ s}$	Oceanic sediments	1.3 x 10^{16} g yr^{-1}	Staudacher and Allegre (1988)
	Growth rate of the continental crust		
$F_{growth,\ c}$	Continental crust minimum	3 km^3 yr^{-1}	Dhuime et al. (2018)
	Continental crust maximum	4.7 km^3 yr^{-1}	Dhuime et al. (2018)
$F_{growth,\ o}$	Young oceanic ridges	18.1 km^3 yr^{-1}	Cogne and humbler (2004)
	Density of the crust		
ρ_c	Continental crust	2830 kg m^{-3}	Christensen and Mooney (1995)
ρ_o	Oceanic crust	2890 kg m^{-3}	Carlson and Raskin (1984)
	Co concentration		
$[Co]_o$	In oceanic crust (gabbro and basalt)	45 mg kg^{-1}	Reimann and de Caritat (1998)
$[Co]_s$	In pelagic marine sediments	0.016 weight %	Goldberg and Arrhenius (1958)
$[Co]_c$	In bulk continental crust	25 mg kg^{-1}	Reimann and de Caritat (1998)
	Calculated subduction flux of cobalt		
$F_{sub\ Co,\ o}$	From oceanic crust	5.3 x 10^{10} mol yr^{-1}	
$F_{sub\ Co,\ s}$	From oceanic sediments	3.5 x 10^{10} mol yr^{-1}	
$F_{sub\ Co}$	**Total**	**8.9 x 10^{10} mol yr^{-1}**	
	Calculated flux of cobalt into new crustal growth		
$F_{growth\ Co,\ c}$	Continental crust minimum	3.6 x 10^{9} mol yr^{-1}	
	Continental crust maximum	5.6 x 10^{9} mol yr^{-1}	
$F_{growth\ Co,\ o}$	Young oceanic ridges	4.0 x 10^{10} mol yr^{-1}	
$F_{growth\ Co}$	**Total minimum**	**4.4 x 10^{10} mol yr^{-1}**	
	Total maximum	**4.6 x 10^{10} mol yr^{-1}**	

The Hydrosphere

The Earth's hydrosphere accounts for the cycling of both the oceans (~97%) and terrestrial freshwater (~3%), including glacial ice, lakes, streams, rivers and groundwater (Table J3). The marine dissolved Co inventory was estimated using two studies: a study by Hawco et al. (2018) estimated the global marine Co flux to be 5.9×10^8 mol yr^{-1} from its major sources (rivers, dust deposition, hydrothermal, etc.). This study also predicts a marine Co residence time of 130 years, allowing for an estimation of the marine Co inventory of 7.7×10^{10} mol using the equation:

$$\text{Inventory} = \text{Flux} \times \text{Residence Time}.$$

This inventory estimate is in excellent agreement with Reimann and de Caritat's (1998) estimate of 4.0×10^9 kg Co, or 6.7×10^{10} mol Co in the ocean inventory.

The above-ground freshwater Co inventory, including ice, lakes, rivers and streams, was estimated by multiplying the volume of each reservoir by its density (assumed 1 kg L^{-1} for liquid freshwater) and by a representative estimate of its cobalt concentration (Table J4):

$$I_{Reservoir} = V[Co]\rho$$

Table J3. Parameters used to calculate the global Co inventories of above-ground freshwater (glaciers and ice caps, lakes, rivers and streams) and groundwater.

Parameter	Value	Reference
Reservoir volume (V)		
Glaciers and ice caps	2.41×10^{7} km^3	Oelkers et al. (2011)
Lakes	9.10×10^{4} km^3	Oelkers et al. (2011)
Rivers and Streams	2.12×10^{3} km^3	Oelkers et al. (2011)
Groundwater	1.05×10^{7} km^3	Oelkers et al. (2011)
Reservoir density (ρ)		
Glaciers and ice caps	0.85 kg L^{-1}	Huss (2013)
Lakes, rivers, streams, groundwater	1 kg L^{-1}	
Co concentration ([Co])		
Glaciers and ice caps	5.80×10^{-12} g g^{-1} ice	Barbante et al. (1997)
Lakes	5.30×10^{-5} mg L^{-1}	Reimann and de Caritat (1998)
Rivers and Streams	2.00×10^{-4} mg L^{-1}	Reimann and de Caritat (1998)
Groundwater	6.15×10^{-5} mg L^{-1}	Reimann and de Caritat (1998)
Calculated Co inventory (I)		
Glaciers and ice caps	2.0×10^{9} mol Co	
Lakes	8.2×10^{7} mol Co	
Rivers and Streams	7.2×10^{6} mol Co	
Groundwater	1.1×10^{10} mol Co	

The Biosphere

The cobalt inventory of the biosphere was estimated as a sum of the prokaryotic inventory (archaea and bacteria) and the eukaryotic inventory (plants, protists, fungi and animals). The prokaryotic inventory was determined by multiplying prokaryotic biomass by the Co : C ratio of both *Prochlorococcus* and *Synechococcus*, marine phytoplankton that are among the most abundant prokaryotes on Earth, for an inventory of 5-8 × 10^8 mol Co. When the same calculation used the cobalt : carbon ratio determined from *Pseudoalteromonas*, a common marine heterotroph that exhibited a high cobalt stoichiometry in culture experiments (1.2×10^{-3} mol Co : mol C), the prokaryotic cobalt inventory estimate was four orders of magnitude higher (7×10^{12} mol Co). This extraordinarily high estimate of global prokaryotic cobalt reveals the plasticity and variability of cobalt quotas among microorganisms and difficulties of estimating global biological inventories using only a few representative species. This *Pseudoalteromonas*-derived inventory estimate was excluded from the total biosphere inventory range.

Similarly, the eukaryotic inventory was determined by multiplying the eukaryotic biomass, of which 96% by weight is composed of plants, by the minimum and maximum cobalt concentrations observed in land plants and trees, along with a general carbon : dry plant weight conversion of 0.4 (Ho, 1976). The resulting eukaryotic Co inventory estimate of 1-16 × 10^9 mol Co displays a wide range of error due to the high variability of plant cobalt composition (Table J4).

An estimate of the flux of Co into the biosphere via global primary production was calculated by multiplying global productivity in units of gigatons (Gt) carbon by the Co : C ratio of marine cyanobacteria (for prokaryotes) and terrestrial plants (for eukaryotes), which make up the majority of eukaryotic biomass on Earth (Table J5).

Table J4. Parameters used to calculate the global inventories of the prokaryotic and eukaryotic biosphere, assuming a general carbon : dry plant weight conversion factor of 0.4 (Ho 1976).

Parameter	Value	Reference
Global Biomass		
Prokaryotic	77 Gt C	Bar-On et al. (2018)
Eukaryotic	468 Gt C	Bar-On et al. (2018)
Co:C		
Prokaryotic (marine cyanobacteria)	8 - 12 x 10^{-8} mol:mol	Hawco et al. (2020) and Sunda and Huntsman (1995)
Prokaryotic (*Pseudoalteromonas*)	1.16 x 10^{-3} mol:mol	Mazzotta et al. (2018)
Eukaryotic (plants)	2.5 - 40 x 10^{-8} mol:mol	Nagajyoti et al. (2010) and Kirchner et al. (2008)
Calculated I_{Co}		
Prokaryotic	5 - 8 x 10^8 mol	
Prokaryotic (high)*	7 x 10^{12} mol	
Eukaryotic	1 - 16 x 10^9 mol	
Total	**1.5 - 17 x 10^9 mol**	

* A maximum (high) calculation of the prokaryotic cobalt inventory is included here using the higher (and likely globally unrealistic) cobalt : carbon ratio from Mazzotta et al. (2018). This inventory estimate was excluded from the total biosphere inventory range.

Table J5. Parameters used to calculate the global primary productivity flux of Co to the biosphere, assuming a general carbon : dry plant weight conversion factor of 0.4 (Ho 1976).

Parameter	Value	Reference
Global Productivity		
Terrestrial	56.4 Gt C yr^{-1}	Field et al. (1998)
Marine	48.5 Gt C yr^{-1}	Field et al. (1998)
Co:C		
Terrestrial (plants)	2.5 - 40 x 10^{-8} mol:mol	Nagajyoti et al. (2010) and Kirchner et al. (2008)
Marine (cyanobacteria)	8 - 12 x 10^{-8} mol:mol	Hawco et al. (2020) and Sunda and Huntsman (1995)
Productivity Flux of Cobalt		
Terrestrial	1.2 - 19 x 10^{8} mol yr^{-1}	
Marine	3.2 - 4.8 x 10^{8} mol yr^{-1}	
Total	4.4 - 24 x 10^{8} mol yr^{-1}	

Appendix J References

Bar-On, Y. M., Phillips, R. and Milo, R.: The biomass distribution on Earth, Proc. Natl. Acad. Sci., 115(25), 6506–6511, doi:10.1073/pnas.1711842115, 2018.

Barbante, C., Bellomi, T., Mezzadri, G., Cescon, P., Scarponi, G., Morel, C., Jay, S., Van De Velde, K., Ferrari, C. and Boutron, C. F.: Direct determination of heavy metals at picogram per gram levels in Greenland and Antarctic snow by double focusing inductively coupled plasma mass spectrometry, J. Anal. At. Spectrom., 12, 925–931, doi:10.1039/a701686g, 1997.

Carlson, R. L. and Raskin, G. S.: Density of the ocean crust, Nature, 311, 555–558, doi:10.1038/311555a0, 1984.

Christensen, N. I. and Mooney, W. D.: Seismic velocity structure and composition of the continental crust: a global view, J. Geophys. Res., 100(B7), 9761–9788, doi:10.1029/95JB00259, 1995.

Cogné, J. P. and Humler, E.: Temporal variation of oceanic spreading and crustal production rates during the last 180 My, Earth Planet. Sci. Lett., 227, 427–439, doi:10.1016/j.epsl.2004.09.002, 2004.

Dhuime, B., Hawkesworth, C. J., Delavault, H. and Cawood, P. A.: Rates of generation and destruction of the continental crust: Implications for continental growth, Philos. Trans. R. Soc. A Math. Phys. Eng. Sci., 376, 20170403, doi:10.1098/rsta.2017.0403, 2018.

Field, C. B., Behrenfeld, M. J., Randerson, J. T. and Falkowski, P.: Primary production of the biosphere: Integrating terrestrial and oceanic components, Science (80-.)., 281(5374), 237–240, doi:10.1126/science.281.5374.237, 1998.

Goldberg, E. D. and Arrhenius, G. O. S.: Chemistry of Pacific pelagic sediments, Geochim. Cosmochim. Acta, 13(2–3), 153–212, doi:10.1016/0016-7037(58)90046-2, 1958.

Hawco, N. J., Lam, P. J., Lee, J. M., Ohnemus, D. C., Noble, A. E., Wyatt, N. J., Lohan, M. C. and Saito, M. A.: Cobalt scavenging in the mesopelagic ocean and its influence on global mass balance: Synthesizing water column and sedimentary fluxes, Mar. Chem., 201(March 2017), 151–166, doi:10.1016/j.marchem.2017.09.001, 2018.

Hawco, N. J., McIlvin, M. M., Bundy, R. M., Tagliabue, A., Goepfert, T. J., Moran, D. M., Valentin-Alvarado, L., DiTullio, G. R. and Saito, M. A.: Minimal cobalt metabolism in the marine cyanobacterium prochlorococcus, Proc. Natl. Acad. Sci., 117(27), 15740–15747, doi:10.1073/pnas.2001393117, 2020.

Ho, L. C.: Variation in the carbon/dry matter ratio in plant material, Ann. Bot., 40(165), 163–165, 1976.

Huss, M.: Density assumptions for converting geodetic glacier volume change to mass change, Cryosph., 7, 877–887, doi:10.5194/tc-7-877-2013, 2013.

Kirchner, P., Biondi, F., Edwards, R. and Mcconnell, J. R.: Variability of trace metal concentrations in Jeffrey pine (Pinus jeffreyi) tree rings from the Tahoe Basin, California, USA, J. For. Res., 13, 347–356, doi:10.1007/s10310-008-0093-5, 2008.

Mazzotta, M. G., Mcilvin, M. R. and Saito, M. A.: Metallomics Characterization of the Fe metalloproteome of a ubiquitous marine heterotroph, Pseudoalteromonas (BB2-AT2): multiple bacteriogerritin copies enable significant Fe storage, Metallomics, 12(5), 654–667, doi:10.1039/d0mt00034e, 2020.

Nagajyoti, P. C., Lee, K. D. and Sreekanth, T. V. M.: Heavy metals, occurrence and toxicity for plants: A review, Environ. Chem. Lett., 8, 199–216, doi:10.1007/s10311-010-0297-8, 2010.

Oelkers, E. H., Hering, J. G. and Zhu, C.: Water: Is there a global crisis?, Elements, 7(3), 157–162, doi:10.2113/gselements.7.3.157, 2011.

Reimann, C. and de Caritat, P.: Chemical Elements in the Environment - Factsheets for the Geochemist and Environmental Scientist, Springer-Verlag, Berlin, Germany., 1998.

Schubert, G. and Sandwell, D.: Crustal volumes of the continents and of oceanic and continental submarine plateaus, Earth Planet. Sci. Lett., 92, 234–246, doi:10.1016/0012-821X(89)90049-6, 1989.

Staudacher, T. and Allègre, C. J.: Recycling of oceanic crust and sediments: the noble gas subduction barrier, Earth Planet. Sci. Lett., 89(2), 173–183, doi:10.1016/0012-821X(88)90170-7, 1988.

Sunda, W. G. and Huntsman, S. A.: Cobalt and zinc interreplacement in marine phytoplankton: Biological and geochemical implications, Limnol. Oceanogr., 40(8), 1404–1417, doi:10.4319/lo.1995.40.8.1404, 1995.